Utah State University

DigitalCommons@USU

8-2021

Attitude and Reflection Parameter Estimation of Resident Space Objects Using Ground-Based Photometry

Arun J. Bernard
Utah State University

Follow this and additional works at: https://digitalcommons.usu.edu/etd

 Part of the Aerospace Engineering Commons

ATTITUDE AND REFLECTION PARAMETER ESTIMATION OF RESIDENT

SPACE OBJECTS USING GROUND-BASED PHOTOMETRY

by

Arun J. Bernard

A dissertation submitted in partial fulfillment
of the requirements for the degree

of

DOCTOR OF PHILOSOPHY

in

Aerospace Engineering

Approved:

_____   _____
David K. Geller, Ph.D.   Doug Hunsaker, Ph.D.
Major Professor   Committee Member

_____   _____
Geordie Richards, Ph.D.   Ludger Scherliess, Ph.D.
Committee Member   Committee Member

_____   _____
Randy Christensen, Ph.D.   D. Richard Cutler, Ph.D.
Committee Member   Interim Vice Provost
                                       of Graduate Studies

UTAH STATE UNIVERSITY
Logan, Utah

2021

ABSTRACT

Attitude and Reflection Parameter Estimation of Resident Space Objects Using

Ground-based Photometry

by

Arun J. Bernard, Doctor of Philosophy

Utah State University, 2021

Major Professor: David K. Geller, Ph.D.
Department: Mechanical and Aerospace Engineering

There are currently thousands of objects orbiting Earth, and this number is only going to increase. Larger number of satellites will require that operators have a greater knowledge of the state their assets. Electro-optical telescopes are currently being used to observe and track many of these objects. These telescopes can also be used to determine the attitude and reflection parameters of spacecraft using ground-based photometry, or the measure of the brightness of an object as viewed by a telescope on Earth. The time series of these photometry measurements are called lightcurves. The purpose of this research is to use lightcurves to determine the attitude and reflection parameters of space objects of known shape with enough accuracy that these estimates can be used to predict the short-term attitude of the objects. Included in this research is the comparison of different attitude estimation algorithms, an in-depth analysis of the different variables affecting the ability to obtain accurate attitude estimates using lightcurves, an analysis of the benefits of using a one or two observatories to collect measurements, and the proposal and evaluation of different methods for accounting for the uncertainty in shape model reflection parameters.

(271 pages)

PUBLIC ABSTRACT

Attitude and Reflection Parameter Estimation of Resident Space Objects Using

Ground-based Photometry

Arun J. Bernard

There are currently thousands of objects orbiting Earth, and this number is only going to increase. Larger number of satellites will require that operators have a greater knowledge of the state their assets. Electro-optical telescopes are currently being used to observe and track many of these objects. When using these telescopes to take images of satellites, they often appear as dots in the image. Depending on the surface properties of the satellite, and its orientation at a given time, the dots in the image can appear brighter or dimmer. Photometry measurements are a quantification of how bright the object appears. The time series of these photometry measurements are called lightcurves. The purpose of this research is to use lightcurves to determine the orientation (i.e. attitude), and surface reflection parameters of space object. Included in this research is the comparison of different attitude estimation algorithms, an in-depth analysis of the different variables affecting the ability to obtain accurate attitude estimates using lightcurves, an analysis of the benefits of using a one or two observatories to collect measurements, and the proposal and evaluation of different methods for accounting for the uncertainty in shape model reflection parameters.

ACKNOWLEDGMENTS

This dissertation is the culmination of a lifetime of learning, and it would not have been made possible without support from many different sources along the way. I'd now like to take the time to acknowledge those who have helped me in getting to where I am today.

First of all, I would like to thank my major professor, Dr. David Geller, who has been patient and understanding as I have labored to complete this work throughout this whole process. This dissertation would not have been possible without his support and guidance.

Next, I'd like to thank the Utah NASA Space Grant Consortium for sponsoring this work. The support I received allowed me to work on a meaningful project that I enjoyed.

I would also like to thank the members of my committee. Each of them has helped me to learn things that have helped me get to where I am today. I am grateful for the time and effort they have invested in order to help me complete my degree.

I am also grateful for Dr. Kohei Fujimoto for giving me my first chance to do academic research and helping me get started along the line of research that has resulted in this dissertation.

In addition, I would like to thank my fellow members of the Space Awareness, Guidance, and Navigation (SAGN) lab, especially Dr. Akhter Mahmud Nafi, Dr. Simon Shuster, and Dr. Rachit Bhatia. Their friendship and their help in discussing my ideas have been invaluable these past few years.

I would also like to take the time to acknowledge my parents and siblings for all the love an support they have given me throughout my life.

I would like to thank Leah Crockett, Jared Cummings, Lauren Stachitus, and Cynthia Throop for their aid in preparing this dissertation. I'd like to give a special thank you to Kathleen Crockett for the time and effort she has spent in proofreading and helping me in getting this dissertation ready. This dissertation would not be at the level it is at now without her thorough review.

vi

Finally, I would like to thank my loving wife, Mariah. She has been willing to put up with a lot in order for me to get my degree. I am eternally grateful for her support and all that she has done to help me get to where I am today. I would also like to acknowledge my children, Deirdre and Zeke. They are the motivation that has pushed me to completing this degree.

<div style="text-align: right;">Arun Bernard</div>

CONTENTS

x

LIST OF TABLES

LIST OF FIGURES

ACRONYMS

ACS	attitude control system
BFF	body fixed frame
BLO	Bear Lake Observatory
BPF	bootstrap particle filter
BRDF	Bidirectional reflectance distribution function
CCD	charged coupled device
DCM	direction cosine matrix
DOF	degrees of freedom
ECEF	Earth-centered Earth-fixed
ECI	Earth-centered inertial
ECRV	exponentially correlated random variable
EKF	extended Kalman filter
EO	electro-optical
GEO	geosynchronous orbit
GEODSS	Ground-based Electro-Optical Deep Space Surveillance
GRP	generalized Rodrigues parameters
HAMR	high area-to-mass ratio
IP	impoverishment problem
KF	Kalman filter
LLA	latitude longitude altitude
LEO	low-Earth orbit
LVLH	local vertical local horizontal

MMAE	multiple model adaptive estimation
MCMC	Monte Carlo Markov chain
MEKF	modified extended Kalman filter
PF	particle filter
PDF	probability density function
RHS	right-hand side
RSO	resident space object
RSS	root sum squared
SSA	space situational awareness
SRP	solar radiation pressure
UKF	unscented Kalman filter
UPF	unscented particle filter
USU-STAR	Utah State University Space Situational Awareness Telescope for Astrodynamics Research

CHAPTER 1

INTRODUCTION

Earth is orbited by thousands of man-made resident space objects (RSOs) larger than 10 cm. With the current development rate of space assets, this number will increase with a commensurate surge in the risk to existing and future space assets [1]. The potential risk posed by these objects is mitigated through space situational awareness (SSA).

SSA is the ability to obtain and utilize knowledge about the local space environment; this encompasses observation and tracking, characterization, identification, and threat assessment of the objects surrounding the planet. SSA allows for governments and space operators to take action by either moving their spacecraft using a collision avoidance maneuver or working to remove debris that pose a large threat to space resources.

To maximize utility, the observational data for an object should include information on both the spacecraft's orbit and its spatial orientation, or attitude, as these dynamics are coupled; a spacecraft's orbital position and velocity influence its attitude and vice versa. The combination of attitude and orbital dynamics support SSA by allowing for the identification of observed objects, predicting the future behavior of objects, and for object recovery and/or disposal.

Generally, the observation of RSOs is realized with data collected through radar systems or using electro-optical (EO) sensors, or telescopes. In recent years, much emphasis has been given to the use of EO sensors in tracking space objects for two reasons. First, EO sensors are capable of tracking objects in higher orbital regimes (e.g., geostationary orbits), than what radar is capable of achieving. Second, EO sensors can be a cheaper alternative to radar systems [2].

Observations of RSOs realized with an EO sensor are typically nonresolved images of the spacecraft; the features of the spacecraft are not discernible in the image. Rather, RSOs appear as bright dots or streaks. How bright an object appears in an image, or its apparent

magnitude, is a function of the object's orientation, shape, size, and material properties. Thus, using light curves, or the time history of an object's apparent magnitude, one or more of these parameters may be estimated [3]. This approach has long been used in the attitude and shape estimation of asteroids [4], and in recent years has been utilized for RSOs [5]. Notwithstanding all of the recent work that has been completed in extending the capabilities of determining the attitude and shape of an object using light curves, there still remains a technical gap in being able to estimate the attitude of the spacecraft well enough that it can be used to predict the future attitude of the spacecraft. Many satellites or RSOs are symmetrical in nature, which creates ambiguities in attitude estimation. Furthermore, even in the case where the shape and materials of the spacecraft are known, the space environment can alter or degrade the materials composing the body of the spacecraft. Thus, in order to accurately track and predict the attitude of the spacecraft, there is a need to be able to estimate the reflection properties of the spacecraft.

1.1 Thesis statement

The thesis of this dissertation is that current estimation algorithms can be improved to provide better estimates of the orientation and reflection properties of a resident space object using novel models for the effects of the reflection properties and light curve measurements from one or more observatories.

1.2 Research scope

This research is limited to estimating the attitude and reflection parameters of artificial, Earth-orbiting satellites with well-defined shape models and light curve measurements from observatories on the ground. In this context, the well-defined shape model refers to having prior knowledge of the number of facets, mass, inertia matrix, and in some cases reflection parameters composing the spacecraft shape model. When estimating the reflection parameters, they are not known perfectly a priori. The estimation of the other listed shape parameters and the spacecraft orbit were not considered in this work.

1.3 Research contributions

The major contributions to this line of research which were identified in carrying out this work are summarized in the following list:

- the proposal and evaluation of three separate models for accounting for the uncertainty in the spacecraft reflection parameters

- a direct comparison of the attitude estimation performance of three separate algorithms: an extended Kalman filter, an unscented Kalman filter, and a bootstrap particle filter

- an in-depth analysis of the different variables and scenario configurations that affect the performance of the filters in estimating the attitude of the spacecraft

- an examination of the effectiveness of using nonsimultaneous photometry measurements for the estimation of the attitude and reflection parameters of the spacecraft

Later chapters provide more details into the context and impact of these key contributions.

1.4 Dissertation overview

The remainder of the dissertation consists of ten additional chapters. Chapter 2 focuses on the literature and previous work that has been completed relevant to this line of research. Chapter 3 provides an overview of spacecraft attitude and the different methods in which it is modeled in this work. Chapters 4 and 5 present the dynamical and measurement models that are used in setting up the different test cases. The next group of chapters is focused on estimation. Chapter 6 presents a general overview of the different estimation algorithms being examined, and Chapters 7 and 8 present the methods by which these algorithms are tailored for the estimation of the spacecraft attitude and reflection parameters, respectively. Finally, The results from the different analyses are presented in Chapters 9 and 10, with a summary of the major findings and potential future work given in Chapter 11.

CHAPTER 2

LITERATURE SURVEY AND RELATED WORK

The purpose of this chapter is to present a brief overview of the literature related to the topics discussed in this dissertation. This is done both to provide background information and to establish context and the novel contributions of this dissertation.

2.1 Dynamics

The space environment is very different from any environment on Earth. Thus, it is of interest to examine the special dynamics experienced by objects orbiting the planet. This section serves as a brief introduction into both the orbital and the attitude dynamics of a spacecraft.

2.1.1 Orbital dynamics

Orbital motion is the motion of an object about another object due to the forces of gravity. A great stride in the understanding of orbital motion came in the seventeenth century when Sir Isaac Newton solved the two-body problem. This breakthrough allowed for the mathematics of orbital motion to be generally understood. The equations for two-body motion are shown below.

$$\dot{\bar{r}} = \bar{v} \tag{2.1}$$

$$\ddot{\bar{r}} = -\frac{\mu}{|\bar{r}|^3}\bar{r} \tag{2.2}$$

Even today, modern orbital trajectories can be described using two-body motion with perturbations added. These perturbations can include third-body perturbations, perturbations due to a nonspherical Earth, solar radiation pressure, and atmospheric drag. Many

of these perturbations are well-known, and information on them can be found in a number of astrodynamics texts such as in [6, 7]. For high-accuracy orbit models, spacecraft attitude information must be used in conjunction with position and velocity information. Perturbations due to atmospheric drag and solar radiation pressure are a function of the projected area of the spacecraft in a given direction. As the spacecraft's projected areas will change in accord with its orientation, the spacecraft attitude plays a major part in accurately determining the location of the spacecraft.

2.1.2   Attitude dynamics

As the attitude of the spacecraft can greatly affect the orbital dynamics of the spacecraft, so too, can the orbital motion affect the attitude. The dynamics governing spacecraft attitude are dependent upon the angular velocity, ω, of the spacecraft, which in turn is a function of the torques experienced by the spacecraft, as shown below in Eq. 2.3 and in Eq. 4.13.

$$\dot{\boldsymbol{q}} = \frac{1}{2}\boldsymbol{\omega} \otimes \boldsymbol{q} \tag{2.3}$$

$$\dot{\boldsymbol{\omega}} = \boldsymbol{I}^{-1}[\boldsymbol{T} - \bar{\boldsymbol{\omega}} \times \boldsymbol{I}\bar{\boldsymbol{\omega}}] \tag{2.4}$$

In the above equations, $\boldsymbol{q}$ is the quaternion attitude representation, $\boldsymbol{I}$ is the moment of inertia, and $\boldsymbol{T}$ is the sum of the torques on the spacecraft. In [8] a number of external torques that affect spacecraft are presented. These torques include gravity gradient torques, magnetic field torques, and torques due to atmospheric drag and radiation pressure. The torques due to the gravity gradient, nonspherical Earth, and solar radiation pressure are functions of the spacecraft's position, and the drag torque is a function of the spacecraft's position and velocity.

2.2   Light curve inversion

For most cases, whenever there is light or another form of radiation impinging upon an object, whatever amount of radiation that is not absorbed or passed through is reflected. This reflection is dependent upon the shape and orientation of the object. Specifically speaking of light, for a given illumination source the amount of light that is reflected by the object and that can be perceived by an observer changes as the object's orientation changes. Also affecting this reflection is the shape of the object. A round object will reflect in a different manner than a flat plate.

As the reflected light of an object is a function of its shape and attitude, it is possible to estimate these by observing how this light reflection changes over time. The change of the apparent brightness or magnitude over time constitutes what is known as a light curve. The process of extracting information from these light curves is called light curve inversion. The extraction of both the shape and attitude of the object as well as the surface parameters of the object is called, in this paper, the complete inversion process. The extraction of one of these components would be a partial inversion process. The light curve inversion process involves using some initial attitude or shape information or initial guesses for these and then using a filter or optimization process to determine the correct estimate of the unknown parameters. The different estimation techniques and approaches used in literature will be presented in section 2.4.

Traditionally, light curves have been used to estimate the shape and attitude of asteroids. In [4] it is shown that the complete light curve inversion process can yield rotation period, pole directions, and shape of the asteroid; however, man-made spacecraft present additional challenges to the light curve inversion process. In [9], Holzinger et al. present some of these additional challenges: RSOs are often symmetric, which leads to ambiguities in the RSO attitude estimates. Also, spacecraft are controlling their own attitudes, which means that there are nonzero torques acting on the spacecraft. Furthermore, depending on the orbital regime in which the RSO resides, it may only be visible to an observer for a short period of time. This means that there may be little available data for the extraction

of the shape and attitude of the RSO.

However, despite the challenges that result when working with satellites, much work has been accomplished in the past twenty years that has made great strides toward using light curves for estimating satellite parameters. The following sections will present the recent developments that allow application of light curve inversion to RSOs.

2.2.1 Attitude and shape estimation

When using light curve measurements, the ability to determine the attitude of the spacecraft is directly linked to the shape of the spacecraft and its reflection parameters. Thus, when looking at an unknown object, some assumptions, or guesses, about these parameters must be made. Typically this involves having some sort of a shape model with fixed reflection properties that is used as part of the state of the system, and that is refined through correlating the shape model and attitude with the light curve measurements. However, in [10], methods are presented for estimating either shape or attitude when the other is known. This section of this work will focus on the combination of attitude and shape estimation, while the following two sections will focus on separated attitude and shape estimation, respectively.

When referring to the shape in this paper, the shape model is meant to be the physical properties of the object such as size, mass, and features. The material and physical reflection properties of the object are not included in this definition of shape. Some of the work dealing with the estimation of reflection parameters can be found in both the shape and attitude determination works. With this definition in mind, there have been numerous papers demonstrating the feasibility of the inversion process to determine these parameters (i.e. size, mass, features). The following subsections discuss some of the physical parameters of the spacecraft that are able to be determined using photometry, or the measurement of light or brightness.

Mass and albedo area

In [11], Linares et al. demonstrate that it is possible to estimate the mass of a spacecraft along with its attitude and angular rates when the photometric data is combined with astrometric angles-only data. These astrometric angles data consist of right ascension and declination, two angles that can be combined over time to estimate the orbit of a spacecraft. These angle measurements can be easily obtained along with the apparent magnitude from a charged coupled device (CCD) image when using an EO sensor. The perturbing force of solar radiation pressure is a function of the area-to-mass ratio of the spacecraft, and it is also a function of the albedo area of the spacecraft. Through analysis of the orbit and reflectance of the object, the authors were able to obtain estimates for the mass of the object as well as the albedo area of the spacecraft.

The mass calculations were further developed in reference [12], where the solar radiation pressure is set up to match the reflectance function of the spacecraft. In reference [13] this work is further applied to different orbital regimes, specifically at determining the mass of high area-to-mass ratio (HAMR) objects. For both of these cases, a rectangular, six-sided shape model was used for the simulations.

Inertia matrix

In [14] Linares et al. demonstrate that the scaled inertia matrix and the principal directions of a spacecraft can be determined through use of light curve and angles data from an EO sensor. However, as the material properties of the spacecraft and its complete attitude aren't known, the full inertia matrix is not able to be estimated. However, the method employed was able to estimate the scaled inertia within 1% and determine the directions of the principal moments of inertia to within 5 degrees.

Size

In her doctoral dissertation [15], Henderson uses a variety of estimation techniques to determine the length, height, and width of a box-type satellite in multiple orbital regimes using angles and photometric measurements. In the course of her work, it is shown that these parameters are estimated very well.

Shape feature estimation

In addition to determining the physical parameters such as the size and the mass of the spacecraft, much work has been done to determine the actual shape features of the spacecraft. Typically, a shape model of a spacecraft is made up of flat plates, or facets. In [16], Linares et al. use what are called the control points of the facets to extract a convex shape model for the spacecraft. The results show that for a simple cuboid shape model, the shape parameters, or distance from the origin to the control points, converge well for the different points that are visible to the observer. Some of the shape parameters were unobservable, as certain portions of the spacecraft were not able to be viewed by the observer location.

Other works for determining the shape and attitude of an RSO involve using multiple model estimation approaches. This approach involves having a number of different shape models that could represent the actual shape model of the spacecraft being observed. These models are processed in parallel, after which a weighting scheme is applied so that the model that best matches the actual measurements of the spacecraft is selected. Linares et al. in [3] use this approach with a number of simple regular polygon or cubic prisms. Their results show that the method will choose the true shape model when that model is part of the total possible models. However, when the exact model is not one of the possible models, the filter will still select a model that, while not exactly matching the true shape model, is still similar in form to the truth.

Wetterer et al. in [17] also use a multiple-model estimation approach, with spacecraft being represented as different bus shapes with solar panels on either side. This work demonstrated that the correct shape model and reflection parameters can be estimated when the

hypothesized shape and attitude models are similar to the truth models.

A more recent approach to shape and attitude estimation is the use of Monte Carlo Markov chains (MCMC) to estimate the attitude and shape of the spacecraft. In [18], Linares and Crassidis use an adaptive Hamiltonian Monte Carlo Markov chain approach to perform Bayesian estimation of the shape and attitude parameters of the spacecraft. The paper expresses that this method is preferable, as it can estimate all of the parameters at the same time without knowing what the other parameters are.

All work presented thus far has utilized a terrestrial approach for the determination of the satellite shape model. In reference [19], however, Bradley and Axelrad use a space-based sensor approach for determining the shape and rotation pole directions of spacecraft. Their work utilizes the algorithms developed for determining the shape and attitude of asteroids [4]. The results showed low errors in the estimates of convex bodies like rocket bodies and CubeSats, but it didn't perform as well for box-wing-shaped or HAMR objects.

As can be seen, much work has been realized in determining the attitude and the shape of the spacecraft. However, despite all of these advancements, there is still work to be accomplished. Most of these papers used only very simple prismatic shapes for their simulations. Actual spacecraft vary in their size and shape, and so other shape models need to be considered. The proposed work includes expanding the complexity of shape models used in light curve inversion and creating a library of shape models as used on actual spacecraft.

2.2.2 Attitude estimation from light curves

Attitude determination of a spacecraft using light curve measurements without shape estimation falls into one of two categories. The first is determining the attitude of an RSO independent of its shape, and the second is the case when the shape of the spacecraft is known. Each of these is presented in the subsections below.

Shape-independent attitude determination

In reference [10], Hall et al. give some of the methods of shape-independent attitude determination. The first method is the analysis of the synodic modulations in the light curve measurements to determine the spin rate period of the satellite. According to this paper, this is typically accomplished through a Fourier fit of the data similar to what is done in [20] by Früh and Schildknecht. The other methods presented by Hall et al. are analyzing the glints of the spacecraft, seeing the variation of the light curve from a single facet as the spacecraft flies overhead, and finally by performing stabilized object attitude tests. Typically these methods are much less commonly used than the attitude determination with some sort of shape estimate as was presented in the previous section and in the following section.

Attitude determination with known shape model

This section discusses the methods of determining a satellite's attitude when the shape model of the RSO is known. In many cases, even though the shape of the spacecraft is known, some uncertainty often remains in the reflection or surface parameters of the space-craft, and so these parameters must also be estimated. Jah and Madler in [21] show that the attitude and reflectance properties could be estimated. In [9], a method for determining the attitude is presented by Holzinger et al. for both a completely known shape model and one with estimated physical parameters for facet areas and reflection parameters that create a bias in the apparent magnitude calculations.

Coder et al. in [22] further the work of [9] by incorporating a radiometric measurement noise model, a correlated process noise model, and implementation of a marginalized particle filter, which reduces the problem to a 3 degree-of-freedom (DOF) estimation problem. Other methods of attitude estimation are typically for the full 6DOF estimation.

Most of the work that has been presented for determining the attitude of a spacecraft has involved the spacecraft being represented by a simplified facet model with defined reflection parameters for the different facets. However, in [1], a different approach of using virtual reality tools to simulate the light curve measurements is demonstrated. Simulated light curves are compared to actual light curves of satellites, and the difference between

the two curves is minimized using optimization techniques. Additionally, the simulated measurements are simulated in three different passbands to show the ability of simultaneous measurements to improve the estimates of the RSO attitude.

Finally, another contribution to understanding how light curve measurements can be used for the attitude determination of a satellite is presented by Hinks et al. in [23]. A static observability analysis of the RSO's attitude errors and reflection model parameters is presented. This work can be used to determine how well the attitude of a satellite may be observable for a given measurement. Indeed, Dianetti et al. in [24] expanded on this work to develop an adaptive filter for orbit determination that would also include light curve measurements for attitude determination when available. Knowing how well a solution can be obtained is very important in understanding the limitations of a given work.

2.2.3   Shape determination using light curves

While it is common for light curves to be used to determine the shape of an RSO or spacecraft, most of the approaches taken also involve obtaining some estimate for the attitude of the RSO. However, it is possible to obtain estimates for the shape of the craft without any attitude information. Hall et al. in [10] present a method of doing this using a distribution of brightness measurements for different phase angles between the Sun and the satellite. In [25] Fulcoly et al. utilize this approach to determine the distribution for some basic shapes of a satellite. It is also important to note that this method involves the observation of satellites from multiple observation points; thus, it may be costly to implement.

Attitude independent shape estimation of a spacecraft is also shown by Calef et al. in [26]. Photometric signals from a light source and thermal imaging are used to determine the shape of a satellite. These measurements are then used to estimate the albedo area of the satellite. This albedo estimate is then exploited to solve what is called the Minkowski problem to determine the three-dimensional shape of the object.

2.2.4   Surface reflection parameter estimation

As was discussed in Chapter 1, a major component of the research is this work is related to the estimation of the surface parameters affecting the manner in which light is reflected by a spacecraft. This section presents the relevant work related to using photometric measurements to estimate the surface reflection properties of spacecraft.

In [27], Kurcharski et al. developed an approach which utilized direct mapping of the spacecraft surface and high-definition photometry to determine if the surfaces were impacted by orbital debris. With the high-definition photometry, if the surface parameters were changed by an impact, there would be a resultant change in the reflected light and the number of electrons detected by the sensor. Thus they were able to determine anomalies due to impact.

Another approach is to estimate the surface parameters for bidirectional reflectance distribution function. These models are discussed in more detail in the next section, but the underlying principle is that there are different parameters in a model that can determine how the light is reflected by the spacecraft.

Wetterer et al. in [28] used combined angles and photometry measurements to estimate reflection parameters for the Ashikhmin–Shirley BRDF model along with a number of other state parameters. Holzinger et al. in [9] developed a bias model to account for uncertainties in the reflection parameters for the Cook–Torrance BRDF model, which is the same BRDF model used in this work.

2.3   Reflection models

Estimating the shape or attitude of an RSO involves some knowledge or simulation of the reflection properties of said object. Bidirectional reflectance distribution functions (BRDFs) are used to accurately model these parameters. A BRDF is used to model the reflection of an object by considering two directions: the direction of the illumination source and the direction of the observer viewing the reflected light from the object. For simulation purposes, the aerospace community has utilized BRDF models developed for implementation in computer graphic visualizations. In [29] it is explained that the different BRDF

models can be organized into two groups: those based on empirical data that have been collected and those that are based on the physical reflectance properties of the objects. Two of the more commonly used models for light curve measurement simulation are the Ashikhmin–Shirley model [30], which falls into the former category, and the Cook–Torrance BRDF model [31], which falls into the latter.

The BRDF operates by determining the weighted combination of the specular and diffuse reflectance of the given objects. Specular reflection is the directional dependence reflection that occurs when a light impinges upon a smooth surface. Diffusive reflectance is when the light is scattered due to light hitting a rough surface. In this case, the light is reflected as a distribution. The BRDF models determine a method of combining these types of reflection with some sort of weighting to emphasize the strength of the diffusive or specular reflectance.

The Ashikhmin–Shirley BRDF model [30] was developed to incorporate the advantages of other empirical models that had been developed previously. The benefits of this model include the fact that it is anisotropic and is easy to implement into Monte Carlo simulations. This model uses a Lambertian diffusive reflectance term; the light hitting the object is scattered equally in all directions. This model was used in a number of works including [11].

The Cook–Torrance model [31] was developed to provide rendering information for objects based on the physical reflection parameters of an object such as the index of refraction or area of a facet. The model includes factors for self-shadowing of satellites and rough surfaces and for a geometric attenuation factor. As with the Ashikhmin–Shirley model above, this model utilizes a Lambertian diffuse reflectance term in combination with a specular term. This model was used by Holzinger et al. in [9].

In her dissertation work, Henderson [15] performed a shape and attitude observability and sensitivity analysis using a number of different BRDF models. Her work found that of the ones tested, the Ashikhmin–Shirley, Cook–Torrance, and He–Torrance [32] models were best suited for use in the complete inversion problem. Ceniceros et al. in [33] moved beyond sole simulation and performed a comparison of three BRDF models with measurements of

geostationary orbit (GEO) objects taken using EO telescopes. The three models tested were the Ashikhmin–Shirley model, the Cook–Torrance model, and the Ashikhmin–Premoze model [34]. The report found that the Cook–Torrance model best matched the actual light curves and magnitude measurements of the satellites tested.

2.4 Estimation algorithms and concepts

As spacecraft attitude and shape are not directly measured using light curve measurements, some form of an estimation algorithm must be employed to estimate these parameters. Two commonly employed methods are using particle filters (PF) and Kalman filters (KF). The following sections serve to explain these different methods and their variations.

2.4.1 Particle filter

A particle filter is a recursive estimation method designed to be able to obtain the posterior probability distribution function (PDF) of a state that is being estimated using sensor measurements. Particle filters are especially useful for nonlinear systems that deviate from Gaussian distributions in the dynamics and measurement models. The PF operates by first creating a distribution of particles that are then propagated forward in time using the system dynamics. The particles that more closely match the truth model are kept and multiplied, and those that are less likely to be a match to the truth state are thrown away. With a sufficient number of particles, the PDF of the truth state can be obtained. With an infinite number of particles, it is theoretically possible to perfectly estimate any state. However, the computation cost increases with the number of particles used. Thus, as shown in [35], the difficulty with PFs is the ability to design a PF that will correctly determine the estimated state while using a minimal number of particles.

While PFs are a useful tool in state estimation, there are some drawbacks associated with them. These drawbacks include the computational cost of implementing PFs, the degradation of the particles forming the state estimate, and the possibility of filter divergence. Large numbers of particles are needed to perform accurate state estimation; increasing the number of particles increases the computational cost of estimation. In addition,

in throwing out particles with unlikely state estimates, the PFs may suffer from particle degradation due to what is called the "impoverishment problem (IP)." The IP is what occurs when the number of particles has been reduced to the extent that there is no longer a sufficient number of particles to estimate the state. The IP often leads to filter divergence, as the particles are concentrated in one area instead of encapsulating a distribution large enough to include the truth state.

However, despite the challenges associated with PFs, the capability and versatility in estimation have led to the development of different methods to mitigate these possible problems. Some of these approaches will be discussed in the next sections.

Bootstrap particle filter

The bootstrap particle filter (BPF) was developed by Gordon et al. in [36]. This filter first samples the given distribution to place the particles such that they represent the current PDF. Then the particles are propagated forward in time, and when a measurement is available, the filter assigns weights and determines the particles of highest likelihood. Then after this, it uses what is called a resampling algorithm. This involves the reassigning of particle values based on those particles that have the largest weights so that the same number of particles is kept at each update phase of the filter. Additionally, particle "roughening" can be employed to aid in prevention of the IP through furthering the distribution of the particles, typically by adding noise to the system. The BPF was used in reference [9] for RSO attitude inversion using light curve measurements and in reference [15] for satellite state and shape estimation.

Unscented particle filter

In reference [37], Du et al. use an unscented particle filter (UPF) where spacecraft attitude inversion is performed. The UPF combines parts of the unscented Kalman filter (UKF) (see section 2.4.2 for more information on this filter) with a particle filter to aid in resolving the impoverishment problem. It is explained that this combination of filters is better able to perform than just one of the filters on its own.

Particle filter with Monte Carlo Markov chain resampling

Another approach to aid in the impoverishment problem is presented in reference [38]. There it is suggested that Monte Carlo Markov chain (MCMC) methods can be used for filter resampling to better match the actual PDF of the truth model. In this approach, MCMC is used to better sample the data based on the current PDF. The improved resampling works to better match the new estimate with the truth model.

2.4.2   Kalman filters

A Kalman filter (KF) is another form of recursive estimation technique developed in the 1960s that is able to perform optimal state estimation of linear systems based on measurement data. The Kalman filter takes place in two parts. The first part is the propagation stage where the current state estimate is propagated forward in time. This propagated estimate is then updated, when measurement data is available, through the calculation of a gain that is weighted by the accuracy of the measurement. The advantages of the Kalman filter are that it is more computationally efficient than other estimation methods like PFs, it is able to process all measurements regardless of their precision to the state estimate variables, it is an optimal estimation system, and Kalman filters don't require all previous data to be kept in storage like other methods such as batch filters.

However, despite the many advantages of the Kalman filter, its application is limited to linear systems (linear dynamics and measurement models). Other methods have been developed to be able to process data with nonlinear dynamics and measurements. Two of these methods are the extended Kalman filter (EKF) and the unscented Kalman filter. These filters are further explained in the following sections.

Extended Kalman filter

The extended Kalman filter is a version of the KF that is very useful for state estimation when the system is governed by nonlinear dynamics and measurements. As explained in reference [35], the underlying assumption of the EKF is that at each step the system

dynamics and measurements can be linearized about the current state estimate and covariance using a first-order Taylor series approximation. The linearized estimate is then used to update the state and covariance estimates. While not optimal like the linear KF, the EKF is very commonly used and brings some of the other advantages of the KF for the state estimation of nonlinear systems. However, the EKF only works well when the linearized models are close approximations of the nonlinear models. When this is not the case or when the systems are not well represented by Gaussian distributions, then other filtering options should be considered.

Unscented Kalman filter

Many papers such as [12, 13, 15] utilize UKF formulations for performing light curve inversion. The UKF is advantageous to use in situations when the linearized dynamics and measurements of the EKF don't accurately represent the nonlinearized system. According to Crassidis and Junkins in [35], some of advantages of the UKF include a lower expected error, and matching higher-order expansions, better than what may be obtained with the EKF.

The UKF operates by selecting a number of points, called sigma points, from the state covariance matrix. These sigma points are then used to propagate the current state estimate. This update is then refined through the use of Kalman gain like what is done in other KF formulations. The use of the sigma points in this filter allows it to better represent the actual distribution of the state variables, resulting in a better overall estimation.

2.4.3   Batch estimation

Batch estimation methods involve the determination of a solution based on all of the previous measurements. In [35] it is explained that one of the advantages of batch estimation methods includes the ability to obtain state estimates with more accuracy than sequential estimation methods. It is further explained that some of the disadvantages of batch estimation techniques are that with some batch estimation formulations it is difficult to include model uncertainty, and as batch processing methods require that all of the

measurements be stored, these techniques are not ideal for real-time application.

Henderson in [15] uses batch estimation techniques in conjunction with a UKF to better estimate the shape parameters of a satellite. The process involved using the UKF to estimate the state variables of the spacecraft and then refining these estimates with a batch filter once a certain number of measurements had been reached. The work concluded that the batch estimation technique in conjunction with the UKF performed better than the UKF on its own. Thus, there is some potential for utilizing batch estimation in solving the light curve inversion problem.

2.4.4   Multiple model adaptive estimation

Multiple model adaptive estimation (MMAE) is a filtering technique that runs a number of filters with different models or initial conditions in parallel; likelihood functions and weights are employed to estimate the truth state from the different models. In [3, 17] the MMAE approach is utilized with different spacecraft shape models to determine which models better match the light curve measurements. This method shows a lot of potential for use in shape estimation. Many spacecraft can be categorized into a few different shape classes. These classes could then be employed in an MMAE framework to obtain good estimates of the spacecraft shape.

2.5   Contributions of proposed research

As can be seen from the previous sections, there has been a large amount of work dedicated to improving the amount of usable data that can be extracted from satellite light curves. The proposed research seeks to add to this already established wealth of knowledge. The technical contributions of the proposed research include a direct comparison of the attitude estimation performance of three separate algorithms: an extended Kalman filter, an unscented Kalman filter, and a bootstrap particle filter; an in-depth analysis of the different variables and scenario configurations that affect the performance of the filters in estimating the attitude of the spacecraft; and an examination of the effectiveness of using nonsimultaneous photometry measurements for the estimation of the attitude and reflection

parameters of the spacecraft.

CHAPTER 3

ATTITUDE REPRESENTATIONS

The attitude of an object is its orientation relative to some predefined reference frame. A reference or coordinate frame is a set of orthonormal basis vectors that can be used to help describe other vectors. Attitude is often defined in terms of the transformation from one reference frame to another. For example, spacecraft attitude is often defined in terms of the transformation between a frame fixed to the center of Earth and another coordinate frame that is fixed to the body of the spacecraft. There are multiple ways in which these frame transformations can be expressed, including direction cosine matrices (DCM), Euler angles, Euler axes/angles, rotation vectors, Rodrigues parameters, and quaternions.

The different methods listed above are examples of attitude representations, and each has pros and cons associated with it. The choice of which attitude representation to use is often problem-specific. Thus, it is important to understand when one representation might be preferable over another. The following sections provide a brief overview of the afore-mentioned attitude representations along with some of the transformations to go between different representations.

Note that the discussion in the following sections is not intended to be a comprehensive list of the different attitude representations and their properties. Rather, the intent of these sections is to provide enough background information about the attitude representations and their transformations that the use of these representations in the later development of equations and algorithms can be better understood.

3.1 Direction cosine matrix

One of the most commonly used methods to define attitude is a direction cosine matrix. However, before an overview of DCMs can be given, it is imperative to first provide a brief overview of vectors. A vector is an object that is defined by a magnitude and a direction.

Vectors exist independently of coordinate frames. It is often useful to express a vector in terms of the basis vectors defining a coordinate frame. For example, in a Cartesian frame, a vector can be coordinatized by the projection of the components into $\boldsymbol{e}_x$, $\boldsymbol{e}_y$, and $\boldsymbol{e}_z$ directions

$$\boldsymbol{v}_{xyz} = \begin{bmatrix} v_1\boldsymbol{e}_x \\ v_2\boldsymbol{e}_y \\ v_3\boldsymbol{e}_z \end{bmatrix} = v_1\boldsymbol{e}_x + v_2\boldsymbol{e}_y + v_3\boldsymbol{e}_z \tag{3.1}$$

where the individual scalar components, v_n, are found using $\boldsymbol{v} \cdot \boldsymbol{e}_n$. Similarly, if there is a second coordinate frame with different basis vectors as shown in Fig. 3.1, then the same vector could be coordinatized in terms of those basis vectors.

$$\boldsymbol{v}_{x'y'z'} = \begin{bmatrix} v_{1'}\boldsymbol{e}_{x'} \\ v_{2'}\boldsymbol{e}_{y'} \\ v_{3'}\boldsymbol{e}_{z'} \end{bmatrix} = v_{1'}\boldsymbol{e}_{x'} + v_{2'}\boldsymbol{e}_{y'} + v_{3'}\boldsymbol{e}_{z'} \tag{3.2}$$

Direction cosine matrices are transformations that change one set of basis vectors to another set of basis vectors. The direction cosine term is due to the fact that the elements of the matrix compose the cosine of the angle between the different basis vectors. For the two coordinate frames of Fig. 3.1, the transformation matrix between the xyz frame and the $x'y'z'$ frame is the following.

$$A_{xyz \to x'y'z'} = \begin{bmatrix} \boldsymbol{e}_{x'} \cdot \boldsymbol{e}_x & \boldsymbol{e}_{x'} \cdot \boldsymbol{e}_y & \boldsymbol{e}_{x'} \cdot \boldsymbol{e}_z \\ \boldsymbol{e}_{y'} \cdot \boldsymbol{e}_x & \boldsymbol{e}_{y'} \cdot \boldsymbol{e}_y & \boldsymbol{e}_{y'} \cdot \boldsymbol{e}_z \\ \boldsymbol{e}_{z'} \cdot \boldsymbol{e}_x & \boldsymbol{e}_{z'} \cdot \boldsymbol{e}_y & \boldsymbol{e}_{z'} \cdot \boldsymbol{e}_z \end{bmatrix} \tag{3.3}$$

The opposite transformation is the transpose of the DCM. This is due to the fact that direction cosine matrices are orthonormal matrices: the transpose of the matrix is equivalent
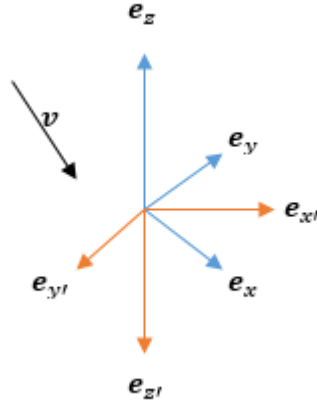
Fig. 3.1: Illustration of a vector and coordinate frames with different basis vectors

to its inverse. The magnitude of the individual rows and columns of the DCM are unity. Thus, the DCM to go from the $x'y'z'$ to the xyz frame is

$$A_{x'y'z'\rightarrow xyz} = (A_{xyz\rightarrow x'y'z'})^T = \begin{bmatrix} \boldsymbol{e}_{x'} \cdot \boldsymbol{e}_x & \boldsymbol{e}_{y'} \cdot \boldsymbol{e}_x & \boldsymbol{e}_{z'} \cdot \boldsymbol{e}_x \\ \boldsymbol{e}_{x'} \cdot \boldsymbol{e}_y & \boldsymbol{e}_{y'} \cdot \boldsymbol{e}_y & \boldsymbol{e}_{z'} \cdot \boldsymbol{e}_y \\ \boldsymbol{e}_{x'} \cdot \boldsymbol{e}_z & \boldsymbol{e}_{y'} \cdot \boldsymbol{e}_z & \boldsymbol{e}_{z'} \cdot \boldsymbol{e}_z \end{bmatrix} \tag{3.4}$$

A vector coordinatized in one frame can be transformed so that it is coordinatized in a different one using the DCM.

$$\boldsymbol{v}_{x'y'z'} = A_{xyz\rightarrow x'y'z'}\boldsymbol{v}_{xyz} \tag{3.5}$$

It is important to note that these transformations are strictly changing the basis vectors or coordinate reference frame used to describe the vector. This is sometimes referred to as a passive transformation. With a passive transformation, actual direction and magnitude of the vector remain unchanged, unlike an active transformation where the vector itself is rotated. In addition, here the DCM was shown as being a 3 x 3 matrix, but the same principles can easily be scaled up to higher dimensional matrices and vectors.

Direction cosine matrices are commonly used for attitude representation because they are able to operate on vectors and can be used to incorporate multiple rotations without a need to convert to any other representations. Eq. 3.5 shows an example of how a DCM can be used to change the frame in which a vector is represented. Multiple rotations can be incorporated by cascading DCMs. Eq. 3.6 below illustrates how this is done.

$$A_{xyz \to uvw} = A_{x'y'z' \to uvw} A_{xyz \to x'y'z'} \tag{3.6}$$

As can be seen from the equation, here the DCM for the conversion from the xyz frame to the $x'y'z'$ is combined with the transformation from the $x'y'z'$ frame to the uvw to get the transformation from the xyz frame to the uvw frame. The ability to cascade DCMs makes it easy to define or find the transformations between many different coordinate systems.

Despite direction cosine matrices being so versatile in their utility, they are generally not the attitude representation of choice for estimation purposes due to their size. DCMs contain nine different elements that have to be stored and used in computations. However, due to the orthonormal constraints of the DCM, there are only three independent elements. This means that other representations might be preferable for attitude estimation, especially in those cases where the memory available to the filter is limited.

The following sections provide an overview of some of the other attitude representations along with the advantages and disadvantages associated with each of them.

3.2   Euler angles

Euler angles are a commonly used method to express attitude, as it is a method that is straightforward for a person to understand and visualize. An Euler angle sequence is a sequence of rotations about the frame basis vectors. For example a 3-2-1 Euler angle sequence gives the right-handed rotation of the coordinate axes first about the z-axis, then the new y-axis, and then finally a rotation about the new x-axis to get the final new set of coordinate axes. Pitch, yaw, and roll angles that are commonly used with aircraft are an

example of an Euler angle sequence.

There are a total of 12 possible Euler angle sequences. There are six symmetrical sequences such as 3-1-3, and six asymmetrical sequences such as a 1-2-3 sequence. A full set of the different rotation sequences and their transformation to direction cosine matrices is presented in Markley and Crassidis [8] and Schaub and Junkins [39].

One of the reasons that Euler angles aren't commonly employed for attitude estimation is that every Euler angle sequence has some rotations that result in singularities in representing the attitude of the spacecraft. This occurs when the rotation axes of the first and third rotations align. The conversion from the direction cosine matrix to the Euler angles is undefined. When considering the control of the spacecraft, this singularity is often referred to as gimbal lock. This occurs when the second rotation angle is 0 or 180 degrees for the symmetrical sequences or 90 or 270 degrees for the asymmetrical sequences.

In this work, Euler angles are only used to define the initial attitude of the spacecraft. All of these initial attitudes are presented in a 3-2-1 Euler sequence. The direction cosine matrix for rotations of ϕ about the z-axis, θ about the y-axis, and ψ about the x-axis is [8]

$$A_{321}(\phi, \theta, \psi) = \begin{bmatrix} c_\theta c_\phi & c_\theta s_\phi & -s_\theta \\ -c_\psi s_\phi + s_\psi s_\theta c_\phi & c_\psi c_\phi + s_\psi s_\theta s_\phi & s_\psi c_\theta \\ s_\psi s_\phi + c_\psi s_\theta c_\phi & -s_\psi c_\phi + c_\psi s_\theta s_\phi & c_\psi c_\theta \end{bmatrix} \tag{3.7}$$

where the c and s are used to represent the cosine and sine of the subscripted angles.

3.3 Euler axis/angle representation

In the previous section, Euler angle sequences comprising multiple rotations about basis vectors were presented. However, it is possible to combine all of these rotations into a single rotation about some axis. The unit vector axis of rotation $\hat{e}$ and the magnitude or angle of the rotation about this axis, θ, are the Euler axis and angle.

The Euler axis/angle can be computed from an attitude matrix in the following manner [8].

$$\theta = \cos^{-1}\left(\frac{\text{tr}(A) - 1}{2}\right) \tag{3.8}$$

$$\hat{e} = \frac{1}{2\sin\theta}\begin{bmatrix} A_{23} - A_{32} \\ A_{31} - A_{13} \\ A_{12} - A_{21} \end{bmatrix} \tag{3.9}$$

This is clearly undefined for the cases where θ is 0 or 180 degrees. If the angle is 0 degrees, then there is no rotation and the axis of rotation is undefined. If the angle of rotation is 180 degrees then the axis of rotation can be found by normalizing any nonzero column of the matrix $\frac{A + I_{3\times3}}{2}$. This is due to the fact that all of the columns of this matrix are parallel to the axis of rotation [8].

$$\hat{e}\hat{e}^T = \frac{A + I_{3\times3}}{2} \tag{3.10}$$

Also of note is that a given Euler axis/angle is not unique in representing an attitude. The same attitude could be achieved by performing the opposite rotation about the opposite of the axis $A(\hat{e}, \theta) = A(-\hat{e}, -\theta)$.

To obtain the attitude DCM from the Euler axis/angle of rotation, Eq. 3.11 can be employed [40]. Note that in the equation, c_θ and s_θ are used to, respectively, represent the cosine and sine of the rotation angle, θ.

$$A(\theta, \hat{e}) = \begin{bmatrix} c_\theta + (1 - c_\theta)e_1^2 & (1 - c_\theta)e_1e_2 + s_\theta e_3 & (1 - c_\theta)e_1e_3 - s_\theta e_2 \\ (1 - c_\theta)e_2e_1 - s_\theta e_3 & c_\theta + (1 - c_\theta)e_2^2 & (1 - c_\theta)e_2e_3 + s_\theta e_1 \\ (1 - c_\theta)e_1e_3 - s_\theta e_2 & (1 - c_\theta)e_2e_3 + s_\theta e_1 & c_\theta + (1 - c_\theta)e_3^2 \end{bmatrix} \tag{3.11}$$

The Euler axis/angle representation is useful for expressing or analyzing rotations over large angles. In addition, if rotating about the same axis, successive rotations can be incorporated by summing the angles to give the new rotation. However, there is not a manner of expressing the rotation about a different axis in this representation. In this case the Euler axes/angles would have to be converted to some other form of attitude representation such as DCMs or quaternions and then combined to give the new rotation.

The next two sections present attitude representations that are different ways of packaging the Euler axis/angle into a separate form in order to achieve distinct properties.

3.4   Rotation vector

The rotation vector attitude representation combines the Euler axis/angle into a single three-element vector. It is found by computing the product of the Euler axis and angle [8].

$$\boldsymbol{\theta} = \theta \hat{\boldsymbol{e}} \tag{3.12}$$

The rotation vector is a common choice for representing the error between two different attitude states or other small-angle rotations. The product between $\hat{\boldsymbol{e}}$ and θ eliminates the undefined case of the rotation axis when the rotation angle is zero. However, like the Euler axis/angle representation, the nonparallel rotations are not able to be combined in this representation, and the rotation vector cannot operate on vectors directly. Any of these operations would require converting to some other form of representing the attitude.

The conversion from a rotation vector to a DCM is given by

$$A = \exp\left(-[\boldsymbol{\theta}\times]\right) \tag{3.13}$$

where the exp is a matrix exponential, and the $[\boldsymbol{x}\times]$ notation denotes the skew-symmetric cross-product matrix formed from the vector. This transformation is somewhat more computationally expensive than other transformations. Due to this and the fact that this conversion would be necessary to operate on vectors, the rotation vector is used here only in describing the error states in filter performance and not as the general attitude representation used for the spacecraft attitude.

3.5 Quaternion

A quaternion is a four-element unit vector that is widely used for describing the attitude of an object. Attitude quaternions contain a scalar component and a vector component as shown in the following equation.

$$\boldsymbol{q} = \begin{bmatrix} q_1 \\ \boldsymbol{q}_{2:4} \end{bmatrix} \tag{3.14}$$

Like the Euler axis/angle representation and the rotation vector, these terms contain information on the axis and the magnitude angle of rotation (adapted from) [8].

$$\boldsymbol{q} = \begin{bmatrix} \cos\frac{\theta}{2} \\ \sin\frac{\theta}{2}\hat{\boldsymbol{e}} \end{bmatrix} \tag{3.15}$$

Note that some references have the scalar element as the fourth element of the quaternion instead of the first, so when looking at a reference involving quaternions, it is important to note how the author defines them. Reference [8] is one such reference where the scalar component is the fourth element. When an equation is listed as being adapted from this

book, it is saying that the equations have been modified to conform with the notation of this work, which has the scalar component as the first component of the quaternion.

One of the main advantages to using quaternions for attitude representation is that they are free from the singularities present in other types of attitude representations. In addition, the transformation from quaternion to a direction cosine matrix does not require any trigonometric functions, as can be seen below (adapted from) [8].

$$A(q) = (q_1^2 - |\boldsymbol{q}_{2:4}|^2)I_{3\times3} - 2q_1[\boldsymbol{q}_{2:4}\times] + 2\boldsymbol{q}_{2:4}\boldsymbol{q}_{2:4}^T \tag{3.16}$$

$$= \begin{bmatrix} q_1^2 + q_2^2 - q_3^2 - q_4^2 & 2(q_2q_3 + q_1q_4) & 2(q_2q_4 - q_1q_3) \\ 2(q_2q_3 - q_1q_4) & q_1^2 - q_2^2 + q_3^2 - q_4^2 & 2(q_3q_4 + q_1q_2) \\ 2(q_2q_4 + q_1q_3) & 2(q_3q_4 - q_1q_2) & q_1^2 - q_2^2 - q_3^2 + q_4^2 \end{bmatrix} \tag{3.17}$$

Further benefits of quaternions include the ability to transform three-element vectors between coordinate frames, and the means to cascade quaternions for successive rotations. This is advantageous, as other representations require a conversion to a DCM before this can be done. However, before these benefits can be fully explained, it is first requisite to define some of the general properties pertaining to quaternion attitude representation. These fundamental properties are presented in the following section with the proceeding sections explaining the details of these transformations.

3.5.1 Quaternion properties

A quaternion is a four-element vector, but with a unit norm constraint. This means that there are only three independent elements contained in a quaternion. Due to its formulation, quaternions are similar to the Euler axis/angle representation in that a given attitude is not uniquely represented. With any attitude matrix A, the attitude can be represented as a quaternion $\boldsymbol{q}$ or as $-\boldsymbol{q}$. The identity quaternion for the case where there is no transformation is defined as

$$\boldsymbol{q} = \begin{bmatrix} 1 \\ 0 \\ 0 \\ 0 \end{bmatrix} \tag{3.18}$$

The identity quaternion is the product of a quaternion multiplication with a quaternion and its conjugate q^*. The conjugate is the quaternion that defines the transformation opposite to that of the original quaternion. For a quaternion that represents the transformation from the x frame to the y frame:

$$\left(\boldsymbol{q}_{x \to y}\right)^* = \boldsymbol{q}_{y \to x} = \begin{bmatrix} \cos\frac{\theta}{2} \\ -\sin\frac{\theta}{2}\hat{\boldsymbol{e}} \end{bmatrix} \tag{3.19}$$

Essentially the conjugate can be found by negating the vector portion of the original quaternion. There are two operations for performing quaternion multiplication, which are referred to as either the cross or the dot form of quaternion multiplication. These are defined in the following equations for two arbitrary quaternions called $\boldsymbol{q}$ and $\boldsymbol{p}$ [8]

$$\boldsymbol{q} \otimes \boldsymbol{p} = [\boldsymbol{q}\otimes]\boldsymbol{p} = \begin{bmatrix} q_1 & -\boldsymbol{q}_{2:4}^T \\ \boldsymbol{q_{2:4}} & q_1 I_{3\times3} - [\boldsymbol{q}_{2:4}\times] \end{bmatrix} \boldsymbol{p} \tag{3.20}$$

$$\boldsymbol{q} \odot \boldsymbol{p} = [\boldsymbol{q}\odot]\boldsymbol{p} = \begin{bmatrix} q_1 & -\boldsymbol{q}_{2:4}^T \\ \boldsymbol{q_{2:4}} & q_1 I_{3\times3} + [\boldsymbol{q}_{2:4}\times] \end{bmatrix} \boldsymbol{p} \tag{3.21}$$

The two forms of quaternion multiplication are not commutative,

$$\boldsymbol{q} \otimes \boldsymbol{p} \neq \boldsymbol{p} \otimes \boldsymbol{q} \tag{3.22}$$

$$\boldsymbol{q} \odot \boldsymbol{p} \neq \boldsymbol{p} \odot \boldsymbol{q} \tag{3.23}$$

but rather the forms are related to each other in the following manner.

$$\boldsymbol{q} \otimes \boldsymbol{p} = \boldsymbol{p} \odot \boldsymbol{q} \tag{3.24}$$

The cross form of the quaternion multiplication is the only form of quaternion used in the subsequent equations of this work, but it is important to understand the different forms and their relationship, because some software packages will have functions that perform quaternion multiplication without specifying the type. Either form of the quaternion multiplication operations between a quaternion and its conjugate will result in the identity quaternion.

Now that the different properties of the quaternion have been established, the use of quaternions for coordinate frame transformations can now be addressed.

3.5.2 Quaternion transformation

Quaternions are much like DCMs in that they can operate on vectors directly without having to convert to another attitude representation. This property allows for the quaternion kinematics to be expressed in a very straightforward manner (see Chapter 4 for more information). To operate on a vector, the vector is first transformed into a quaternion form. For some three-dimensional vector $\boldsymbol{v}$, the quaternion formed by the vector is

$$\boldsymbol{q_v} = \begin{bmatrix} 0 \\ \boldsymbol{v} \end{bmatrix} \tag{3.25}$$

With a vector in this form, the frame in which the vector is coordinatized can be changed using only a quaternion and its conjugate. The following equation illustrates the method to transform a vector from some arbitrary x frame to another arbitrary y coordinate frame.

$$\begin{bmatrix} 0 \\ \boldsymbol{v}^y \end{bmatrix} = \boldsymbol{q}_{x \to y} \otimes \begin{bmatrix} 0 \\ \boldsymbol{v}^x \end{bmatrix} \otimes \boldsymbol{q}_{y \to x} \tag{3.26}$$

In addition to the ability to be used in changing the coordinate system of a vector, multiple quaternions can be cascaded together like DCMs to create new quaternions that represent a different transformation. An example of this is shown in the following equation.

$$\boldsymbol{q}_{x \to z} = \boldsymbol{q}_{y \to z} \otimes \boldsymbol{q}_{x \to y} \tag{3.27}$$

In the previous equation the resultant quaternion is the transformation between some arbitrary x coordinate frame and another arbitrary z coordinate frame.

Due to the properties and abilities of the quaternion, it is a very good choice for representing the attitude of an object. The quaternion is able to do many of the operations of a DCM while maintaining fewer parameters, which makes computations more efficient. Furthermore, unlike some of the other representations, quaternions are free from singularities and have very straightforward kinematics that make them simple to propagate forward in time. For this reason, the quaternion is the main attitude representation used here for the global attitude of a spacecraft.

3.6 Generalized Rodrigues parameters

The final attitude representation to be discussed is the generalized Rodrigues parameters (GRPs). The GRPs are a generalized version of the standard Rodrigues parameters, or Gibbs vector, and the modified Rodrigues parameters that are commonly encountered

in the literature. At their core, Rodrigues parameters constitute a method of mapping a four-dimensional quaternion sphere into a three-dimensional hyperplane [40], [41]. As with other three-dimensional representations, there are singularities that may occur. The Gibbs vector has a singularity at rotations of 180 degrees, the modified Rodrigues parameters have one at 360 degrees, and the GRPs allow for the singularity to be set between 180 and 360 degrees [42]. Here the GRPs are used in the filter attitude error state to avoid singularities (as the errors will be small) and because the error covariance is the same to the first order for both GRPs and quaternions [3].

A quaternion can be expressed as a GRP using the following equation (adapted from) [42]:

$$\boldsymbol{\theta} = f \frac{\boldsymbol{q}_{2:4}}{a + q_1} \tag{3.28}$$

where a is a parameter from 0 to 1, and f is a scale factor commonly set to $f = (2(1+a))$ [3]. The Gibbs vector can be found by setting $a = 0$ and $f = 1$, and the modified Rodrigues parameter can be found by setting $a = f = 1$. Computing quaternions from GRPs can be done using the following equations (adapted from) [42].

$$q_1 = \frac{-a\|\boldsymbol{\theta}\|^2 + f\sqrt{f^2 + (1 - a^2)\|\bar{\boldsymbol{\theta}}\|^2}}{f^2 + \|\boldsymbol{\theta}\|^2} \tag{3.29}$$

$$\boldsymbol{q}_{2:4} = f^{-}1 \left[a + q_1 \right] \boldsymbol{\theta} \tag{3.30}$$

$$\boldsymbol{q} = \begin{bmatrix} q_1 \\ \boldsymbol{q}_{2:4} \end{bmatrix} \tag{3.31}$$

3.7   Summary

This purpose of this chapter is to provide some background material on attitude and some of the different representations that are available. There are many different types of attitude representations, and they can all be useful depending on the context in which they are used. Subsequent chapters build on this material in explaining the different coordinate

reference frames that are used and how the different attitude representations fit into the algorithms for estimating the attitude and reflection parameters of a spacecraft. In general, due to the ease of implementing the kinematics and other properties, the quaternion is the main attitude representation used in this work.

CHAPTER 4

COORDINATE FRAMES, DYNAMICS, AND PERTURBATION MODELS

The purpose of this chapter is to define all of the coordinate frames, dynamics models, and perturbations models that are used in this work to model the motion of spacecraft in orbit.

4.1 Coordinate frames

A coordinate frame is a reference from which coordinates can be specified to define the location of some object. Common coordinate frames include Cartesian, cylindrical, and spherical coordinate frames. The use of different coordinate frames allows for the motion or position of objects to be described in a way that can promote understanding. Typically coordinate frames are defined by three mutually orthogonal vectors. This is done so that the vectors can serve as basis vectors such that a linear combination of these basis vectors can be used to describe any point in space.

Coordinate frames can either be inertial or accelerating. An inertial coordinate frame is any frame that is not accelerating. The frame may be translating at a constant rate, but it is cannot be accelerating. Any rotating coordinate frame experiences angular acceleration and thus is not an inertial frame.

Vectors are used to describe location and motion of objects in a coordinate frame. However, vectors are strictly a magnitude and direction that exist independently of a coordinate frame, so to make it easier to describe the location of objects, vectors are coordinatized into a specific reference frame. Vectors coordinatized in a given coordinate frame can be coordinatized in a different reference frame by multiplying the vector by passive rotation matrices.

There are six degrees of freedom (DOF) that are used to describe the motion of a spacecraft. These are broken down into three DOF for describing the translational motion

of the satellite in its orbit, and three DOF for describing the rotational motion of the satellite. Multiple coordinate systems can be defined to aid in describing this motion of the satellite. In this work only the following coordinate systems will be used in describing the orbital motion of the satellite: the Earth-centered inertial (ECI) frame, the Earth-centered Earth-fixed frame (ECEF), the local vertical local horizontal frame (LVLH), and the latitude longitude altitude (LLA) reference frame. The rotational motion of the satellite is described using a satellite body fixed frame (BFF). Each of these frames is discussed in greater detail in the sections below.

4.1.1 Earth-centered inertial frame

The Earth-centered inertial frame is one of the most commonly used reference frames to describe the motion of a satellite. It is used by placing the coordinate frame at the center of Earth. The x-axis is aligned with the first point of Aries (Υ), which is the direction of the vernal equinox (the point where the Sun crosses Earth's equatorial plane when passing from negative to positive declination), the z-axis is aligned with the pole of Earth, and the y-axis is aligned to complete the right-handed triad of basis vectors.

As explained in [43], while not truly inertial, the frame is considered inertial for many applications if these directions are taken at a specific epoch. A common reference epoch that is used is J2000, though it has seen a decline in popularity in recent years. In later sections, this frame will be referenced as the inertial frame and denoted by the letter I in ECI.

4.1.2 Earth-centered Earth-fixed frame

The Earth-centered Earth-fixed coordinate frame is a rotating frame that is fixed to Earth. In this case the z-axis is aligned with Earth's pole, and the x- and y-axes are aligned with specified locations on Earth's body. Typically the intersection of the equator and the prime meridian is used to define the x-axis direction, and the y-axis direction is found by completing the triad. As Earth moves about, the data defining these directions relative to the inertial frame change periodically. The transformation from ECI to ECEF or vice versa

is presented in [43]

4.1.3   Latitude longitude altitude

Latitude, longitude, and altitude (LLA) are three coordinates that can be used to map a location onto the surface of Earth. Latitude is an elevation-type angle that gives the location of the satellite above the equator. Positive latitude corresponds to locations north of the equator, and negative longitude corresponds to locations south of the equator. Longitude is an azimuthal-type angle that tells the location of the object relative to the prime meridian, which passes through Greenwich, England. Positive values are for those locations east of the prime meridian, and negative values are west. Altitude is the measure of the distance of the location above sea level.

Typically when discussing latitude, longitude, and altitude, one is referring to geodetic latitude. As Earth is an oblate object rather than a sphere, the geodetic latitude is measured from the equator to an imaginary vector that is perpendicular to the local tangent of the geographic location and intersects the equatorial plane. Geocentric latitude is the latitude measured from the equatorial plane to the position vector of the location relative to the center of Earth.

It is common practice to define ground stations or observatories in terms of LLA. However, when dealing with satellites, it is often more practical to determine the position of these observatories in an Earth-centered frame. The following equation from [44] is a method to convert the latitude, longitude, altitude of a ground location to a position vector in the ECI frame.

$$
\boldsymbol{R} = \left[\frac{R_e}{\sqrt{1 - (2f - f^2)\sin^2\phi}} + H \right] \cos\phi \left(\cos\theta\hat{\boldsymbol{i}} + \sin\theta\hat{\boldsymbol{j}} \right)
$$
$$
+ \left[\frac{R_e(1-f)^2}{\sqrt{1 - (2f - f^2)\sin^2\phi}} + H \right] \sin\phi\hat{\boldsymbol{k}} \quad (4.1)
$$

Here R_e is the radius of Earth, f is the flattening factor of Earth, ϕ is the geodetic latitude, θ is the local sidereal time (which is a function of longitude), and H is the altitude of the ground location.

4.1.4 Local vertical local horizontal (LVLH)

The local vertical local horizontal frame is defined such that one of the axes is aligned with the radial direction of the spacecraft (local vertical), another pointing in the direction of the angular momentum of the orbit, and the final component pointing in the direction of the local horizontal of the spacecraft. This frame of reference is commonly used to orient spacecraft for ground communications or to report on the results of orbit determination, as the results can be expressed with errors given in the radial, along-track, and cross-track components of its orbit.

As the LVLH frame is aligned with the position vector of the spacecraft, it is a rotating reference frame. So for noncircular orbits, the transformation from the inertial frame to the LVLH frame must be computed at every time step. For circular orbits the rotation rate of the frame can be set to the mean motion of the spacecraft. The following equations outline the process of converting from the ECI frame to the LVLH frame. First, the elements of the transformation matrix are computed using the inertial position, velocity, and angular momentum vectors.

$$\hat{\boldsymbol{i}}_x = \frac{\bar{\boldsymbol{h}} \times \boldsymbol{r}}{|\bar{\boldsymbol{h}} \times \boldsymbol{r}|} \tag{4.2}$$

$$\hat{\boldsymbol{i}}_y = \frac{\boldsymbol{r} \times \boldsymbol{v}}{|\boldsymbol{r} \times \boldsymbol{v}|} = \frac{\bar{\boldsymbol{h}}}{|\bar{\boldsymbol{h}}|} \tag{4.3}$$

$$\hat{\boldsymbol{i}}_z = \frac{\boldsymbol{r}}{|\boldsymbol{r}|} \tag{4.4}$$

With these directions defined, it is then possible to define the direction cosine matrix to go from the inertial to the LVLH frame:

$$A_{I \to LVLH} \begin{bmatrix} \boldsymbol{i}_x^T \\ \boldsymbol{i}_y^T \\ \boldsymbol{i}_z^T \end{bmatrix} \tag{4.5}$$

Using this DCM, it is also possible to define a similar coordinate frame that has a nadir-pointing component instead of pointing in the direction of the position vector. This is defined as

$$A_{I \to R} \begin{bmatrix} \boldsymbol{i}_x^T \\ -\boldsymbol{i}_y^T \\ -\boldsymbol{i}_z^T \end{bmatrix} \tag{4.6}$$

4.1.5 Body fixed frame

When dealing with a spacecraft and attitude, it is often helpful to discuss these items in terms of the body fixed frame (BFF), sometimes referred to as the body frame. The BFF is attached to the spacecraft, and it rotates as the satellite does. Spacecraft attitude is described by the rotation of a reference frame to the body frame of the spacecraft. The different means of describing spacecraft attitude are presented in Chapter 3.

4.2 Dynamics and perturbation models

Spacecraft dynamics are used to describe the motion of a spacecraft by defining the forces and torques acting on the spacecraft. This motion can be broken up into two parts, the translational, or orbital, motion of the spacecraft, and the rotational motion of the

spacecraft. The orbital motion describes how a satellite moves around the body it is orbiting, and the rotational motion is how the satellite body is spinning or moving while in its orbit. The models for each of these kinds of motion are described in the following section.

4.2.1 Orbital dynamics

Orbital motion is the motion of an object relative to another body. This work focuses only on objects in orbit around Earth. The governing differential equations for the orbital motion of an object are shown in Eqs. 4.7 and 4.8.

$$\dot{\boldsymbol{r}} = \boldsymbol{v} \tag{4.7}$$

$$\ddot{\boldsymbol{r}} = \dot{\boldsymbol{v}} = -\frac{\mu}{|\boldsymbol{r}|^3}\boldsymbol{r} + \boldsymbol{a}_d \tag{4.8}$$

Here $\boldsymbol{r}$ is the position of the object, $\boldsymbol{v}$ is the velocity of the object, μ is the gravitational parameter of Earth, and $\boldsymbol{a}_d$ is the sum of the disturbing forces acting on the object. If Earth were just a point mass, then the differential equations above would simply reduce to the two-body problem, where the satellite experiences acceleration due solely to the uniform gravitational force of Earth.

This is not the case in real life, as Earth is not a point mass, and forces such as atmospheric drag, solar radiation pressure, and third-body gravitational forces perturb the orbit of the satellite. These perturbations are often coupled with the attitude of the object. However, this work focuses on estimating the attitude of the satellite with the assumption that the orbital motion of the spacecraft is perfectly known. Thus, when performing analysis in simulation, only perturbations due to a nonspherical Earth are accounted for, and the acceleration of the object is caused by the gravitational force of Earth as shown in the equations below.

$$\dot{\boldsymbol{r}} = \boldsymbol{v} \tag{4.9}$$

$$\ddot{\boldsymbol{r}} = \boldsymbol{a}_{gravity} \tag{4.10}$$

Here $\boldsymbol{a}_{gravity}$ is the acceleration due to the gravity of Earth, which takes into account the actual gravitational potential of the planet.

Gravitational forces

The planet Earth is a nonspherical planet, and thus the gravitational force on an orbiting object is not constant. It varies from location to location. The gravitational force acting on the object at any given time is dependent upon the gravitational potential. From [45] it is shown that Earth's gravitational potential can be modeled using spherical harmonics as shown below

$$U = \frac{GM_e}{r} \sum_{n=0}^{\infty} \sum_{m=0}^{n} \frac{R_e^n}{r^n} P_n m \left(\sin \phi\right) \left(C_{nm} \cos m\lambda + S_{nm} \sin m\lambda\right) \tag{4.11}$$

where λ is the longitude, ϕ is the geocentric latitude, and the coefficients c_{nm} and S_{nm} describe Earth's mass distribution. For simulation purposes, these gravitational coefficients were found using the GEM-T1 gravity model in [46]. When performing analysis in simulation, a gravity model up to J4 was used.

4.2.2   Attitude dynamics

The general differential equations for the rotational motion of a spacecraft using quaternion representations of attitude are presented below.

$$\dot{q}_{I \to b} = \frac{1}{2} \begin{bmatrix} 0 \\ \boldsymbol{\omega}^b \end{bmatrix} \otimes q_{I \to b} \tag{4.12}$$

$$\dot{\boldsymbol{\omega}}^b = J^{-1}[\boldsymbol{T} - \boldsymbol{\omega}^b \times J\boldsymbol{\omega}^b] + \boldsymbol{\eta} \tag{4.13}$$

In the above equations, $\boldsymbol{\omega}$ is the angular velocity and J is the inertia matrix of the spacecraft. The term $\boldsymbol{T}$ is the sum of the torques acting on the spacecraft, including gravity gradient, aerodynamic drag, and control torques, and $\boldsymbol{\eta}$ is a random angular acceleration term with power spectral density, Q_η.

Equations 4.12 and 4.13 are the full rotational dynamics equations for any space object. However, satellites are often capable of maintaining their own attitude through an attitude control system. In these cases, the control systems are designed to reject any disturbance torques and maintain the desired attitude. In the simulation, a controlled satellite will maintain its attitude as either an inertial hold, where its attitude stays fixed, or rotating at a constant rate. The differential equations that describe this controlled motion are presented below.

$$\dot{q}_{I \to b} = \frac{1}{2} \begin{bmatrix} 0 \\ \boldsymbol{\omega}^b \end{bmatrix} \otimes q_{I \to b} \tag{4.14}$$

$$\dot{\boldsymbol{\omega}}^b = \boldsymbol{0} \tag{4.15}$$

However, objects such as space debris or satellites without attitude control systems are subject to all of the perturbing torques, and so their motion is governed by Eqs. 4.12 and 4.13. Different torques being modeled to simulate the actual space environment torques are

presented in the following sections.

Solar radiation pressure

The radiation from the Sun exerts pressure on spacecraft that can cause disturbances to the orbit and attitude of the spacecraft. This is especially true for objects with a high area-to-mass ratio. This pressure is known as solar radiation pressure (SRP). In low-Earth Orbits (LEOs), the spacecraft disturbances are dominated by gravity and atmospheric drag; however, in higher orbits, the disturbances due to SRP have a much greater effect on the dynamics of the spacecraft.

The torque due to SRP is found by breaking the satellite shape into different plates, or facets, calculating the force acting on each of these plates, and then summing up the moments of these forces acting on the center of pressure of the different facets. From [8], the force due to SRP acting on a plate of the spacecraft can be given as

$$\boldsymbol{F}_{SRP} = -P_{SR}A_i \left[2 \left(\frac{\mathcal{R}_d^i}{3} + \mathcal{R}_s^i \cos\theta_{SRP}^i \right) \hat{\boldsymbol{n}}^b + (1 - \mathcal{R}_s^i)\hat{\boldsymbol{s}}^b \right] max(\cos\theta_{SRP}^i, 0) \qquad (4.16)$$

In the above equation, i is used to denote properties specific to a given facet; P_{SR} is the solar radiation pressure; A is the area of the plate; $\hat{\boldsymbol{n}}^b$ is the unit normal of the plate in the body frame; $\hat{\boldsymbol{s}}^b$ is the unit normal of the Sun vector in the body frame, $\cos\theta_{SRP} = \hat{\boldsymbol{n}} \cdot \hat{\boldsymbol{s}}$; and $\mathcal{R}_d$ and $\mathcal{R}_s$ are, respectively, the diffuse and specular reflection coefficients of the plate. These two parameters can be written in terms of the specular diffuse weighting term ξ that is used in later chapters for the measurement model and reflection parameter estimation.

$$\mathcal{R}_d = \xi \qquad (4.17)$$

$$\mathcal{R}_s = 1 - \xi \qquad (4.18)$$

The torque that acts on the spacecraft is then calculated as

$$\boldsymbol{T}_{SRP} = \sum_{i=1}^{N} \boldsymbol{r}_{cm}^{i} \times \boldsymbol{F}_{SRP}^{i} \tag{4.19}$$

where $\boldsymbol{r}_{cm}^{i}$ is the vector from the spacecraft center of mass to the center of pressure from SRP acting on the individual plate.

As it is sunlight acting on the spacecraft that induces torque on the spacecraft, the torque due to SRP is not calculated at a time when the satellite is in eclipse. In these instances the component $\boldsymbol{T}$ in Eq. 4.13 is the sum of the remaining external torques acting on the spacecraft.

4.2.3   Gravity gradient torques

Gravity gradient torques are torques due to the gravity field acting on a spacecraft. As the different portions of the spacecraft experience different gravity fields, a torque is induced.

The gravity gradient torque can be calculated using the following equation from [47].

$$T_{gg}^{b} = \frac{3\mu}{|\boldsymbol{r}^{b}|^{5}} \left[\boldsymbol{r}^{b} \times \left(J\boldsymbol{r}^{b} \right) \right] \tag{4.20}$$

In the above equation, $\boldsymbol{r}^{b}$ is the orbital position vector of the spacecraft coordinatized in the body frame, μ is the standard gravitational parameter of Earth, and J is the inertia matrix of the spacecraft.

4.2.4   Atmospheric drag

In Curtis [44] it is explained that the altitude where "space" begins is 100 km above Earth. The majority of Earth's atmosphere is contained in the region below this altitude. However, spacecraft in low altitudes travel at sufficiently high velocities that the very low densities of the atmosphere in space can still affect the motion of the spacecraft and perturb its trajectory. The different molecules composing the planet's atmosphere impinge on the

spacecraft, resulting in the application of this force in the direction opposite the velocity of the spacecraft. This force is called the atmospheric drag force.

The atmospheric drag force, or drag, is a function of the density of the atmosphere, the spacecraft's drag coefficient, mass, velocity, and projected area in the direction of the velocity vector.

To determine the projected area of the satellite, the satellite shape is assumed to be convex and divided into a number of facets of differing areas, A_i, and unit normal vectors, $\hat{\boldsymbol{n}}_i$. Section 5.2 of this work provides more detail about how this is done.

A simple model for the drag force acting on a satellite is given by

$$\boldsymbol{F}_{aero}^{I} = \sum_{i=1}^{N} -\frac{1}{2}\rho(C_{D,i}A_i)|\boldsymbol{v}|^2\,(\hat{\boldsymbol{v}} \cdot \hat{\boldsymbol{n}}_i)\,\hat{\boldsymbol{n}}^b \tag{4.21}$$

where i refers to the individual facets used to make up the spacecraft, ρ is the atmospheric density, C_D is the drag coefficient, A_i is the area of the facet, $\boldsymbol{v}$ is the orbital velocity vector of the object, and $\hat{\boldsymbol{n}}$ is the unit normal of the individual facet.

For the simulation, an exponential model from [8] is utilized for the calculation of the atmospheric density, ρ.

$$\rho = \rho_0 e^{-\frac{h-h_0}{H}} \tag{4.22}$$

where p_0 and h_0 are reference density and height, H is the scale height, and h is the altitude of the spacecraft. The given reference, [8], presents a table where these values are tabulated based on the value of h.

The acceleration due to drag can be found by dividing the force due to drag by the mass of the spacecraft, and the torque due to drag is

$$T_{drag} = \sum_{i=1}^{N} \boldsymbol{r}_{cm}^{i} \times \boldsymbol{F}_{aero,i}^{b} \tag{4.23}$$

4.3   Summary

This chapter provides a brief overview of the different coordinate frames that are used in this work. In addition, it defines the dynamics models for both the orbital and rotational motion of the spacecraft. This presentation of the dynamics includes an overview of the different perturbing accelerations and disturbance torques acting on the spacecraft.

CHAPTER 5

MEASUREMENT AND SHAPE MODEL

When taking images of satellites using electro-optical sensors, there are two kinds of images that can be obtained. The first are resolved images, where the different features of the spacecraft are discernible, and the second are unresolved images. In unresolved images, depending on the setup, the satellite will appear as either a dot or a streak in the image. How bright the object appears in the image is the apparent magnitude of the object. Figure 5.1 is an example of three images of the same satellite (circled in red, and the other objects are background stars) with different apparent magnitudes.
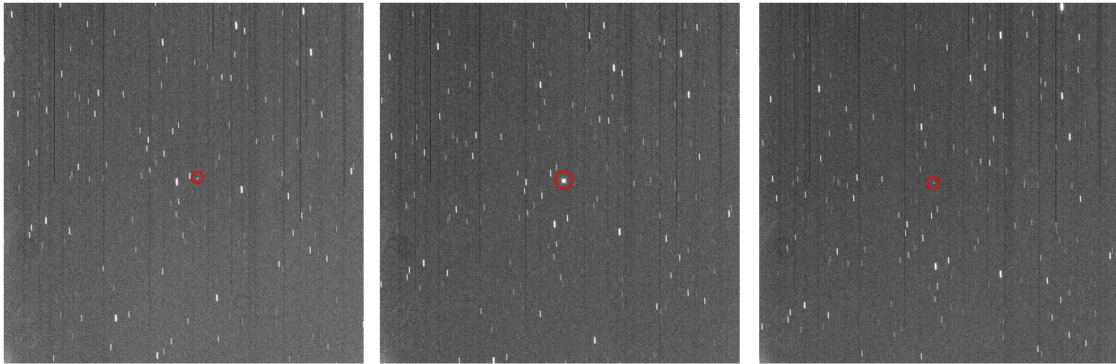
Fig. 5.1: Three successive images of a satellite in geostationary orbit taken by USU-STAR at the Bear Lake Observatory

The three images of the satellite were taken with 30 seconds between images. It is clear that the apparent magnitude of the satellite is different in all three of the images. The object is brightest in the center frame, and much dimmer in the other two. How bright an object appears is a function of the shape of the object, the material properties of the spacecraft, and the orientation of the object relative to both the light source (the Sun) and the observatory.

The premise of this research is that compiling the time history of the object brightness, or photometry measurements, into a lightcurve can provide sufficient information to enable the estimation of the attitude and some of the reflection properties of the spacecraft. The purpose of this chapter is to provide an overview of the measurement model used for simulating the apparent magnitude measurements that are employed in the attitude estimation process. The following sections will provide more detail into the models used, specifically the measurement model, the reflection model, and the spacecraft shape model.

5.1   Apparent magnitude

The magnitude of an object is a measure of how bright the object appears to an observer. While *aboslute* magnitude is how bright an object would appear from a set distance of ten parsecs, *apparent* magnitude is how bright the object appears relative to some reference at the actual distance between the observer and object [48]. Ten parsecs is approximately 32.62 light years.

The early applications of photometry were to determine the relative brightness of celestial objects such as planets and stars [49]. According to Brian D. Warner [50], a magnitude of 1 was given to the brightest stars and a value of 6 was to given to those that were the most dim. Later Edmund Halley discerned that stars with a value of 1 were about 100 times brighter than stars with a magnitude of 6 [50]. In 1856 Norman Pogson came forward with a magnitude scale where a difference of 5 corresponds exactly to one object being 100 times brighter than another [51]. This is the basis for the scale still in use today. The apparent magnitude relative to some reference can be found using the following equation [48]

$$M_{sat} - M_{ref} = -2.5 \log_{10} \left(\frac{I_{sat}}{I_{ref}} \right) \tag{5.1}$$

where M_{sat} is the apparent magnitude of the spacecraft.

In the previous equation, the terms I_{sat} and I_{ref} are the power flux seen by the observer for the satellite and the reference, respectively. In practice when using a telescope, the reference is some standard star of known magnitude that was chosen for this purpose [50],

[48]. In simulation, however, one is free to choose the reference, and the apparent magnitude can be found in terms of the Sun, which results in the following equation [9]

$$M_{sat} = -2.5 \log_{10} \left(\frac{I_{sat}}{I_{sun}} \right) - 26.74 \tag{5.2}$$

where I_{sun} is the average illumination intensity of the Sun at a given distance. There are some key characteristics associated with the magnitude measurement. The first is that the lower the magnitude value, the brighter the object appears in the image; likewise, the larger the value, the dimmer the object appears. Another key feature is that due to the logarithmic nature of the magnitude measurement, a difference of 5 in magnitude corresponds to the brighter object being 100 times brighter than the dimmer object. This means that if there is a magnitude difference of 1 between two objects, one object is 2.5119 ($\sqrt[5]{100}$) times brighter than the other.

From Holzinger et al. [9] the photometric flux of the spacecraft over wavelengths Λ as viewed by an observer can be written as

$$I_{sat} = \frac{1}{\boldsymbol{v}_r^T \boldsymbol{v}_r} \int_{\Lambda} I_{sun}\left(\boldsymbol{s}, \lambda\right) \mathcal{R} d\lambda \tag{5.3}$$

where $\mathcal{R}$ describes the reflected intensity density in the direction of the observer at the frequency of the given wavelength, λ, $\boldsymbol{v}_r$ is the position vector from the object to the observer, and $\boldsymbol{s}$ is the position vector from the object to the Sun. They further explain that finding the term $\mathcal{R}$ can be difficult and can be approximated using a shape model. To simplify calculations, the satellite shape is represented by a series of flat plates or facets. Each facet is defined by an area, A_i, and a unit normal vector, $\hat{\boldsymbol{n}}_i$. Using the facet representation, the reflection can be calculated for each of the individual facets and then summed to give the total reflection. Figure 5.2 illustrates the reflection geometry for an individual facet.
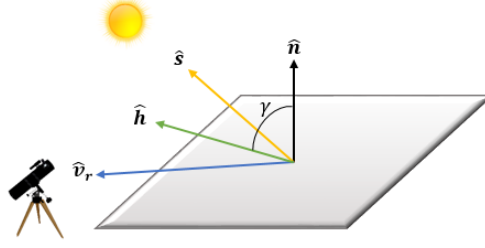
Fig. 5.2: Reflection geometry for a given facet of the spacecraft shape model

In the figure, the vector $\hat{\boldsymbol{v}}_r$ is the satellite-to-observer unit vector, $\hat{\boldsymbol{s}}$ is the object-to-Sun unit vector, $\hat{\boldsymbol{h}}$ is the bisector of these two vectors, and $\hat{\boldsymbol{n}}_i$ is the unit normal of the facet. With the faceted shape model assumption, the photometric flux can be written as

$$I_{sat} = \frac{1}{\boldsymbol{v}_r^T \boldsymbol{v}_r} \int_\Lambda I_{sun}\left(\boldsymbol{s}, \lambda\right) \sum_{i=1}^{N_f} A_{i,vis} \mathcal{R}_i\left(\hat{v}_r^b, \hat{s}^b, p_i,\right) d\lambda \tag{5.4}$$

where the index i is to denote the individual facets composing the shape model, the term p encompasses the physical reflection properties of the facet, and A_{vis} is the visible projected area of the facet, which for a convex shape model is found using the following equation,

$$A_{i,vis} = A_i * \max\left((\hat{\boldsymbol{n}}_i \cdot \hat{\boldsymbol{v}}_i), 0\right) * \max\left((\hat{\boldsymbol{n}}_i \cdot \hat{\boldsymbol{s}}_i), 0\right) \tag{5.5}$$

Equation 5.5 is adapted from the work of Holzinger et al. [9]. This equation makes it so that if a facet is not illuminated or visible to the observer, then it won't contribute to the computation of the apparent magnitude measurement.

Now if it is further assumed that the light reflects equally over the particular wavelength band of interest, then Eq. 5.4 can be further reduced to:

$$I_{sat} = \frac{1}{\boldsymbol{v}_r^T \boldsymbol{v}_r} I_{sun}\left(\boldsymbol{s}\right) \sum_{i=1}^{N_f} A_{i,vis} \mathcal{R}_i\left(\hat{v}_r^b, \hat{s}^b, p_i,\right) \tag{5.6}$$

With the spacecraft being approximated using a facet shape model, the reflectance term has reduced to a summation of the reflectance of the individual facets. The models used for the reflectance function are presented in the following section.

5.1.1 Bidirectional reflectance distribution function

A bidirectional reflectance distribution function (BRDF) is a model that is used to describe the reflection from a facet surface given the direction of the impinging light and the direction of the observer viewing the reflected light. A brief overview of some of the BRDF models commonly used in the aerospace community is given in section 2.3. This section explains the different components of the Cook–Torrance BRDF [31], a physical-property-based BRDF that has been shown to be a good choice for lightcurve inversion [15], [33].

With the Cook–Torrance BRDF the reflection is found for each individual facet and then summed to give the total reflectance of the satellite. For reference, the reflection geometry of a facet is shown in Fig. 5.2. The total reflectance is a weighted combination of both a specular and a diffuse reflection component as shown in the following equation.

$$\mathcal{R}_i = \xi_i \mathcal{R}_{d,i} + (1 - \xi_i)\mathcal{R}_{s,i} \tag{5.7}$$

The term ξ is the specular/diffuse weight of the facet. The diffuse reflection is modeled using a Lambertian reflection model where light reflects equally in all directions. The amount of light that is reflected is governed by the diffuse albedo term a, and the orientation of the facet relative to the light source.

$$\mathcal{R}_{d,i} = \frac{a_i(\hat{\boldsymbol{n}}_i^b \cdot \hat{\boldsymbol{s}}^b)}{\pi} \tag{5.8}$$

The specular reflection is determined using the following equation.

$$\mathcal{R}_{s,i} = \frac{F_i}{4} \frac{D_i}{(\hat{\boldsymbol{n}}_i^b \cdot \hat{\boldsymbol{s}}^b)} \frac{G_i}{(\hat{\boldsymbol{n}}_i^b \cdot \hat{\boldsymbol{v}}^b)} \tag{5.9}$$

Here F is the Fresnel equation, D is the facet slope distribution function, and G is the geometric attenuation factor of each facet. Each of these terms will be described below with the accompanying equations.

The Fresnel equation, F, is used to describe the reflectance of electromagnetic radiation on the surface of an object.

$$F = \frac{1(g_i - c)^2}{2(g_i + c)^2} \left[1 + \frac{(c(g_i + c) - 1)^2}{(c(g_i + c) + 1)^2} \right] \tag{5.10}$$

$$c = \hat{\boldsymbol{v}}^b \cdot \hat{\boldsymbol{h}}^b, \quad g_i^2 = n_i^2 + c^2 - 1 \tag{5.11}$$

$$n_i = \frac{1 + \sqrt{F_{0,i}}}{1 - \sqrt{F_{0,i}}} \tag{5.12}$$

In the above equations, $F_{0,i}$ is the Fresnel equation at zero angle of incidence, and n_i is the index of refraction.

The facet slope distribution function, D, is a term that is used to determine the specular reflection due to a rough surface. According to Cook et al. [31], the slope distribution represents how much of the surface of the facet is oriented in the direction of the bisector $\hat{\boldsymbol{h}}_i$. To calculate this term, the Beckmann distribution function [52] is used. For the observer to best view the specular reflection of a perfectly smooth surface, the facet unit normal has to be aligned with the bisector defined in Fig. 5.2. The Beckmann distribution is a function of the angle γ between the bisector and the unit normal, and the slope of the roughness of the surface, m. This distribution term, D, is calculated as follows

$$D = \frac{1}{\pi m_i^2 cos^4 \gamma_i} e^{-\left(\frac{tan^2 \gamma_i}{m_i^2} \right)} \tag{5.13}$$

where

$$\gamma_i = cos^{-1}(\hat{\boldsymbol{n}}_i^b \cdot \hat{\boldsymbol{h}}^b) \tag{5.14}$$

The final term in Eq. 5.9 is the geometric attenuation factor, G. This term accounts for the self-shadowing of the surface microfacets due to roughness.

$$G = min \left\{ 1, \frac{2cos\gamma_i(\hat{\boldsymbol{n}}^b \cdot \hat{\boldsymbol{v}}_r^b)}{(\hat{\boldsymbol{v}}_r^b \cdot \hat{\boldsymbol{h}}^b)}, \frac{2cos\gamma_i(\hat{\boldsymbol{n}}^b \cdot \hat{\boldsymbol{s}}^b)}{(\hat{\boldsymbol{v}}_r^b \cdot \hat{\boldsymbol{h}}^b)} \right\} \tag{5.15}$$

More information about this term can be found in references [53] and [54].

In implementing these equations in simulation, a simplifying assumption is made for the diffuse albedo term, $a_i = F_{0,i}$. For justification of this assumption refer to references [9] and [31]. Under this assumption, there are four physical shape parameters that directly affect the power flux computed using Eq. 5.6 and thus the apparent magnitude measurement of Eq. 5.2. These parameters are the area of facet, A; the microfacet slope parameter, m; the diffuse albedo term, a; and the specular/diffuse weighting term, ξ. As these parameters directly affect the measurements that are obtained, they must be taken into account when setting up the shape model used for the analysis. In addition, the limits to the values that these parameters can take on must also be considered: the area, A, must be positive; ξ is on the interval $[0, 1]$; a is on the interval $(0, 1)$ if used for $F_{0,i}$; and m is restricted to $(0, 1]$ [9]. The parameters for each of the different facets composing the shape model need to conform to these limits.

5.2 Shape model

The amount of light that an object reflects at any given time is a strong function of the shape of the object. The size, the physical properties, and the form of the object all play a role in how the light is reflected. It was shown in section 2.2 that there are many instances of shape parameters being estimated using lightcurve data. In this work, the focus is on estimating the attitude of a spacecraft with a known shape model. This section provides an overview of how the shape model is defined so that it can be compatible with the measurement model explained in the previous sections and with the estimation algorithms explained in later chapters.

As previously stated, Eq. 5.6 is based on the assumption of a faceted shape model. This applies for a general faceted model, for both convex and nonconvex shapes. As Eq. 5.5 simplifies the calculation of the visible area of the facets, the shape models here are restricted to convex shapes. A convex shape is one where all of the diagonals from one point to another are contained within the shape, and the interior angles are less than 180 degrees. An example of both a convex and a nonconvex shape is given in Fig. 5.3.
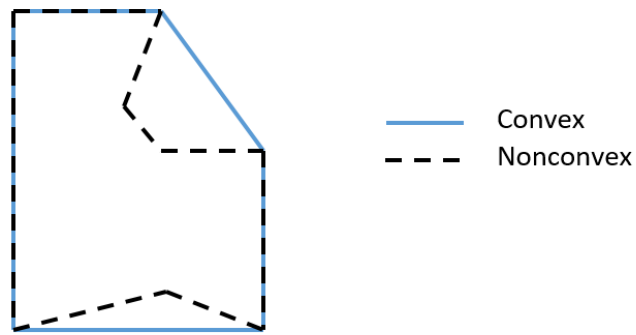
Fig. 5.3: Convex and nonconvex shapes

Common three-dimensional shapes such as boxes or cylinders which can be used to model buses or rocket bodies can be represented using a facet shape model as shown in Fig. 5.4. In the figure, the circular part of the cylinder has been represented using ten facets (more or fewer facets could be used if desired). Those ten facets, along with the top and bottom faces of the cylinder, would be the facet model used for that object.
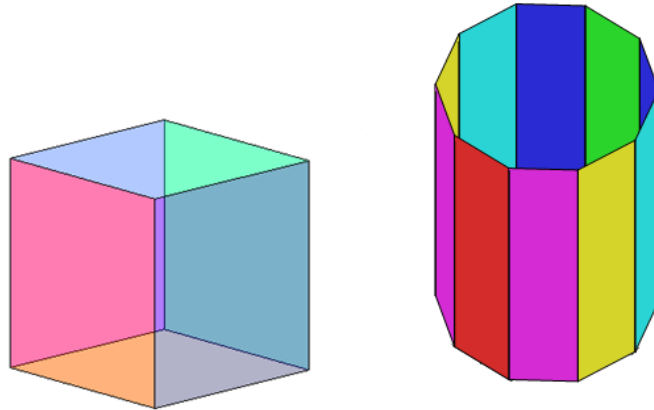
Fig. 5.4: Facet representations of a cube and a cylinder

For each facet a number of parameters need to be defined: the area of the facet, the unit normal vector in the object body frame, and the reflection parameters from the previous section. If the perturbation models from the previous chapter are employed, then the location of the center of pressure from the object center of mass along with the drag coefficients of the facets must also be included.

With the shape, reflection, and apparent magnitude measurement models defined in this chapter, there is sufficient information to simulate photometric measurements of a resident space object. The next chapters delve into how these measurements can be used to provide an estimate of the attitude of the spacecraft.

CHAPTER 6

ESTIMATION METHODS

Estimation methods exist because it is impossible to perfectly model real-world systems. For any real system there are errors in the models used for the dynamics, random perturbations, measurement errors, etc. Invariably there will be some errors that remain unmodeled or other uncertainties associated with the system. This inability to perfectly capture a system has led to the advent of many estimation techniques. By utilizing different estimation algorithms it is possible to obtain an estimate of the true system parameters with some quantified measure of the uncertainty associated with that estimate.

However, not every problem can be solved using the same estimation technique. Trying to account for different factors such as nonlinear dynamics and measurements, and complicated systems, has resulted in an abundance of different estimation techniques. Each one has associated benefits and drawbacks. The purpose of this chapter is to provide an overview of some of the more commonly used estimation techniques and a brief overview of some of the pros and cons associated with these techniques. The following filters will be discussed in this chapter: Kalman filters, including both the extended Kalman filter (EKF) and the unscented Kalman filter (UKF), and the bootstrap particle filter (BPF), including the standard BPF as well as a variation that is designed to improve BPF performance.

However, before discussing the specific filters, a brief overview of some of the key elements common between the different filters will be presented.

6.1 Filter elements

At its core, each of these different filters is designed to provide information about some value that is not precisely known. The values being estimated by the filter are called the state variables. Information about the state is gained by processing measurements related to the state with some known uncertainty. Processing these measurements allows for increasing

the information related to the state or, in other words, decreasing the uncertainty of the state. Furthermore, these filters do this while also accounting for random terms that may make it so that the uncertainty increases. The following sections very briefly discuss these different elements of the estimation process so that the later presentation of these estimation algorithms can be better understood. References [55] and [35] provide a much more detailed presentation of the elements touched upon here.

6.1.1   State

For every estimation algorithm there needs to be something that is being estimated. As mentioned above, these variables are called the state variables. The state variables can consist of a single value like the range to an object or can be a larger vector like the full position vector of an object. For the filters in this chapter, all of the state variables are combined into a single $n \times 1$ vector, $\boldsymbol{x}$.

Typically, the idea is to be able to estimate the state as it changes in time or as it evolves. Thus, along with the state, it is necessary to define the dynamics models that show how the state evolves in time. These dynamics models all depend on the physics of the system. In addition to constants, or the state variables, the state dynamics might also include terms such as a control and process noise, in which case the dynamics would be of the following form.

$$\dot{\boldsymbol{x}} = f(\boldsymbol{x}, \boldsymbol{u}, \boldsymbol{w}) \tag{6.1}$$

In the above equation, the term $\boldsymbol{u}$ is the control vector, and the term $\boldsymbol{w}$ is the process noise. Controls are described below, and noise is presented in the following section.

A control is some input into the system that can be used to influence how the system behaves. An example might be adjusting the gas pedal in a car to change the speed of a vehicle. If a control is being used, then it should be included in the dynamics of the estimation algorithm. Some dynamics models may not require the use of a control in the estimation algorithms, in which cases the control can be left out. This is generally not the

case with noise.

6.1.2 Noise

Noise is changes in a system that make it difficult to completely define the system deterministically or without uncertainty. Noise is part of what defines a stochastic process. Generally noise is expressed as random changes due to environmental or other factors that affect the accuracy of the models used in predicting the future values of the state. Noise may be uncorrelated in time so that each value is not related to the value before or after, or it may be correlated in time or some other manner. For a better discussion of noise see [55]. In this work, the term process noise refers to the random noise that causes fluctuations to the state dynamics, and measurement noise refers to the the uncertainties in measuring some value.

6.1.3 Measurements

In an estimation process, measurements are used in order to provide additional information about the state. In order to be effective in updating the state estimates, the measurements should be a function of the state. However, like with the dynamics, measurements aren't perfect, and so the uncertainty in the measurement needs to be taken into account in order to provide a better estimate of the state distribution.

6.1.4 Distribution

The overarching goal of the estimation algorithms in this work is to obtain a probabilistic idea of the state value within in some range. The idea is to use the filter to get the uncertainty in the state estimates as small as possible or to shrink the distribution. As time goes on, noise will generally increase the uncertainty in the estimate, and the measurements will help to reduce it. For the extended and unscented Kalman filters that will be presented in the later sections, the filters estimate the state in terms of a Gaussian distribution that is defined through a mean estimate and covariance matrix. The mean describes an area of high probability of where the value lies, while the covariance matrix describes the spread of

the distribution in the state space. The smaller the uncertainties defined by the covariance matrix, the better the knowledge of the state variable.

Now that some of the basic elements of a filter have been defined, the different estimation algorithms can be discussed.

6.2   Kalman filters

The Kalman filter (KF) is a recursive estimation technique that was developed by Rudolf Kálmán in the 1960s [56]. Despite being less restricted in its original formulation, the Kalman filter has come to be accepted as being best suited for linear, Gaussian systems [57]. Maybeck [55] extends this in saying that the Kalman filter is useful in cases where the system can be described through linear dynamics and the measurement and state errors are Gaussian. The Kalman filter provides an analytic approach to calculating the optimal state estimate conditioned on the available observations, or measurements.

The implementation of a Kalman filter takes place in two parts. The first part is the propagation stage where the current state estimate is propagated forward in time. This propagated estimate is then updated, when measurement data is available, through the calculation of a gain that is weighted by the accuracy of the measurement. The KF is capable of processing all measurements, regardless of their precision, in order to update the state estimate variables. As it is recursive, a record of all the prior measurements doesn't need to be maintained. This fact combined with its analytic formulation make the Kalman filter straightforward to implement on a computer and computationally inexpensive compared to other estimation schemes.

However, despite the many advantages of the Kalman filter, its application is limited to linear systems (linear dynamics and measurement models) for best operations. Other methods, building on the KF, have been developed to be able to process data with nonlinear dynamics and measurements. Two of these methods are the extended Kalman filter (EKF) and the unscented Kalman filter (UKF). These filters are further explained in the following sections.

6.2.1 Extended Kalman filter

The extended Kalman filter is a version of the KF that is very useful for state estimation when the system is governed by nonlinear dynamics and measurements. As explained in reference [35], the underlying assumption of the EKF is that at each step the system dynamics and measurements can be linearized about the current state estimate, or other reference trajectory, and covariance using a first-order Taylor series approximation. The true state and the state estimated are related to each other through a small-error vector.

$$\boldsymbol{x} = \hat{\boldsymbol{x}} + \delta\boldsymbol{x} \tag{6.2}$$

The EKF uses the standard formulation of the KF with error vector $\delta\boldsymbol{x}$ and the linearized system evaluated at the reference trajectory in order to update the estimate of the error vector. This updated error vector is then used to correct the state estimate and update the covariance matrix.

While not optimal like the standard KF, the EKF is very commonly used and brings some of the other advantages of the KF for the state estimation of nonlinear systems. However, the EKF only works well when the linearized models are close approximations of the nonlinear models. When this is not the case, or when the systems are not well-represented by Gaussian distributions, other filtering options should be considered.

The equations for implementing an extended Kalman with continuous dynamics and discrete measurements are shown in the following sections. For every given system, there is some state vector $\boldsymbol{x}$ that is to be estimated. The dynamics of the state are given as a function of the state variables, any controls operating on the state, and noise to represent unmodeled perturbations. It is assumed that any possible controls ($\boldsymbol{u}$) and noise ($\boldsymbol{w}$) terms are strictly added to the state dynamics as shown below.

$$\dot{\boldsymbol{x}}(t) = f(\boldsymbol{x}, t) + B(t)\boldsymbol{u}(t) + G(t)\boldsymbol{w}(t) \tag{6.3}$$

In Eq. 6.3 the matrices B and G are matrices that map the controls and the noise to the state variables. The noise is assumed to be zero mean, Gaussian, and white with strength Q as shown in the following equation

$$E[\boldsymbol{w}(t)\boldsymbol{w}(t')] = Q\delta(t - t') \tag{6.4}$$

where δ refers to the Dirac delta function.

The linearized system dynamics are

$$\delta\dot{\boldsymbol{x}}(t) = F(t)\delta\boldsymbol{x}(t) + B(t)\boldsymbol{u}(t) + G(t)\boldsymbol{w}(t) \tag{6.5}$$

The F matrix, the Jacobian, represents the linearized dynamics evaluated at the current state estimate.

$$F = \left.\frac{\partial f(\boldsymbol{x}, t)}{\partial \boldsymbol{x}}\right|_{\hat{x}} \tag{6.6}$$

With the nonlinear and linearized systems defined, the different steps of the Kalman filter can be explained.

Initialization

The EKF requires an initial estimate of the state and its uncertainty. In other words the filter is initialized with the best estimate of the first and second moments of the state probability density function (PDF) or distribution. Moments are terms that describe the statistics of a distribution [55]. The first and second moments refer to the mean and covariance matrix.

$$\hat{\boldsymbol{x}}_0 = E[\boldsymbol{x}_0], \qquad P_{\boldsymbol{x}_0} = E[(\boldsymbol{x}_0 - \hat{\boldsymbol{x}}_0)((\boldsymbol{x}_0 - \hat{\boldsymbol{x}}_0)^T] \tag{6.7}$$

In the above equation, the operator $E[\cdot]$ is the expected value, or expectation of the argument. It is the average value of the argument that you would get if you measured the value repeatedly [55].

Propagation/time update equations

The following equations outline the differential equations for propagating both the state estimate and the covariance matrix. As the state estimate is the expected value of the filter design model (Eq. 6.3), the noise term does not appear in the following equation. This is due to the noise being zero mean. In addition, it is important to note that with the EKF, the nonlinear dynamics are used in the propagation of the state estimate.

$$\dot{\hat{\boldsymbol{x}}}(t) = f(\hat{\boldsymbol{x}}, t) + B(t)\boldsymbol{u}(t) \tag{6.8}$$

$$\dot{P}(t) = F(t)P(t) + P(t)F(t)^T + G(t)Q(t)G(t)^T \tag{6.9}$$

Using these differential equations, the estimate and covariance matrix can be propagated until a measurement becomes available.

Measurement update equations

Whenever a measurement is available, it is used to update the propagated state estimate. This pre-update estimate is called the a priori state estimate and is signified with "-" as the superscript. For a measurement to be useful in gaining information about the state, it must be a function of the state that is being estimated. This is shown mathematically in the following equation.

$$\tilde{\boldsymbol{y}}_k = h(\boldsymbol{x}_k) + \boldsymbol{\nu}_k \tag{6.10}$$

Here the subscript k refers to discrete measurements taking place at some time t_k, and the term $\boldsymbol{\nu}$ is the noise associated with the measurement. The measurement noise is assumed to be Gaussian and white, meaning uncorrelated in time. As the measurements that are being processed are discrete values and are not considered continuous, the strength, R, of the measurement noise is given as

$$E[\boldsymbol{\nu}_i \boldsymbol{\nu}_j^T] = R\delta(t_i - t_j) \tag{6.11}$$

where in this instance δ is the Kroenecker delta function.

The first step to processing the measurement at a time $t = k$ is to first compute the measurement geometry vector at the given time, H_k, as shown in the equation below.

$$H_k = \frac{\partial h}{\partial \boldsymbol{x}}\Big|_{\hat{x}_k^-} \tag{6.12}$$

The measurement geometry vector is the linearized measurement function h evaluated at the current state estimate. In addition to being used as part of the EKF, the measurement geometry vector can also provide some insight into the relationship between the state and the measurement. As the measurement is linearized about the state, examination of the measurement geometry vector shows in which direction information about the state can be obtained. Indeed, it is for this reason that this vector is used in determining when a system is observable or can be estimated with the given measurements (see [35], or [55]). With the measurement geometry vectors computed, it is then possible to calculate the Kalman gain.

$$K_k = P_k^- H_k^T \left(H_k P_k^- H_k^T + R_k\right)^{-1} \tag{6.13}$$

The Kalman gain is used to correct the state estimate by scaling the difference between the measurement and the computed measurement from the a priori state estimate.

$$\hat{\boldsymbol{y}}_k = h(\hat{\boldsymbol{x}}_k) \tag{6.14}$$

The corrections to the a priori state estimate can then be computed.

$$\delta\hat{\boldsymbol{x}}_k^+ = K_k \left(\tilde{\boldsymbol{y}}_k - \hat{\boldsymbol{y}}_k\right) \tag{6.15}$$

These corrections can then be applied to update the state to find the a posteriori estimate.

$$\hat{\boldsymbol{x}}_k^+ = \hat{\boldsymbol{x}}_k^- + \delta\hat{\boldsymbol{x}}_k^+ \tag{6.16}$$

The a posteriori covariance matrix is also computed using the Kalman gain. There are two forms to the computation of this covariance matrix. Here the Joseph form of the covariance matrix ix used, as it ensures that the covariance matrix is positive semi-definite [55].

$$P_k^+ = (I - K_k H_k)\, P_k^- = (I - K_k H_k)\, P_k^-\, (I - K_k H_k)^T + K_k R K_k^T \tag{6.17}$$

Table 6.1 provides a summary of these equations for the extended Kalman filter.

Table 6.1: Continuous discrete EKF algorithm

State and error vecs.	$\boldsymbol{x}, \quad \delta\boldsymbol{x}$
Model	$\dot{\boldsymbol{x}}(t) = f(\boldsymbol{x},t) + B(t)\boldsymbol{u}(t) + G(t)\boldsymbol{w}(t) \qquad \boldsymbol{w}(t) \sim N(\boldsymbol{0}, Q(t))$ $\delta\dot{\boldsymbol{x}}(t) = F(t)\delta\boldsymbol{x}(t) + B(t)\boldsymbol{u}(t) + G(t)\boldsymbol{w}(t) \qquad F = \left.\frac{\partial f(\boldsymbol{x},t)}{\partial \boldsymbol{x}}\right|_{\hat{x}}$ $\tilde{\boldsymbol{y}}_k = h(\boldsymbol{x}_k) + \boldsymbol{\nu}_k \qquad\qquad\qquad \boldsymbol{\nu}_k \sim N(0, R_k)$
Initialize	$\hat{\boldsymbol{x}}_0 = E\{\boldsymbol{x}_0\}$ $P_0 = E\{(\boldsymbol{x}_0 - \hat{\boldsymbol{x}}_0)(\boldsymbol{x}_0 - \hat{\boldsymbol{x}}_0)^T\}$
Propagation	$\dot{\hat{\boldsymbol{x}}}(t) = f(\hat{\boldsymbol{x}}, t)$ $\dot{P}(t) = F(t)P(t) + P(t)F(t)^T + G(t)Q(t)G(t)^T$
Update	$K_k = P_k^- H_k^T \left(H_k P_k^- H_k^T + R_k\right)^{-1}$ $H_k(\hat{\boldsymbol{x}}_k) = \left.\frac{\partial h}{\partial \boldsymbol{x}}\right|_{\hat{x}_k^-}$ $\delta\hat{\boldsymbol{x}}_k^+ = K_k(\tilde{\boldsymbol{y}}_k - h(\hat{\boldsymbol{x}}_k))$ $\hat{\boldsymbol{x}}_k^+ = \hat{\boldsymbol{x}}_k^- + \delta\hat{\boldsymbol{x}}_k^+$ $P_k^+ = (I - K_k H_k)\, P_k^-\, (I - K_k H_k)^T + K_k R_k K_k^T$

6.2.2   Unscented Kalman filter

The unscented Kalman filter (UKF) is another Kalman filtering approach that is suited for nonlinear systems. This filter is also called a sigma point filter, [57] or a linear regression filter, [58] due to the method in which it operates. Unlike the EKF, which approximates the dynamics and the measurement model using a first-order Taylor series expansion, the UKF approximates the (posterior) distribution of the state using a Gaussian density [58]. This is accomplished by deterministically selecting a set of sample points from the covariance of the matrix and then using the points to obtain estimates about the statistical distribution of the state estimate. As these points are taken from the covariance matrix, they are sometimes referred to as sigma points.

The premise of the UKF is that it is better to approximate the distribution of these points than to approximate the dynamics [59]. The filter sigma points completely capture the mean and the covariance of the system, and when they are propagated through the state dynamics are second-order accurate for any nonlinear system with errors only in the higher-order terms [57]. Both the state propagation and the measurement calculation use the full nonlinear dynamics of the system.

Some of the benefits associated with using the UKF over other filters is that the UKF may better represent the true covariance of the state variables. Oftentimes the extended Kalman filter may underestimate or not truly capture the true covariance [57]. In these instances, the UKF may provide more accurate information. Furthermore, the UKF is also easy to implement on a computer. The sigma points are selected deterministically, and only matrix and vector computations are required. A third benefit of the UKF is that Jacobians do not need to be calculated, which is useful for cases when the Jacobians may be difficult to determine due to complex dynamics or measurement models.

However, there are some downsides to using the UKF as well. First, as the Jacobians are not calculated, the insights that can be obtained from the measurement geometry vector are lost. Second, as the UKF propagates the sigma points through the full nonlinear dynamics and measurement equations, it may require more computational power than the EKF. A

third point to consider about the UKF is that it remains best suited for systems that are well represented by the first and second moments, Gaussian systems for example. Multimodal or strongly skewed systems may not perform well with a UKF.

The driving mechanism for the UKF is the unscented transform of the system. The unscented transform, developed by Julier and Uhlman [59], uses the mean and the covariance matrix of the state to determine the location for the sigma points. These points are then weighted and put through the full nonlinear dynamics. The new state statistics are then calculated. However, the standard unscented transform can drive the covariance matrix to be nonpositive semi-definite, so most often the scaled unscented transform is used to maintain the positive semidefinite nature of the covariance matrix [60]. The scaled unscented transform replaces the original set of sigma points with a transformed set scaled by a parameter α while maintaining the same mean and covariance of the estimate. The scaling is controlled by three tuning parameters, α, β, and κ.

The parameter α is a term between 0 and 1 that is used to control the spread of the sigma points. The smaller the value of α, the lesser the effect of the nonlocal terms on the state estimate. The second term, β, is used to incorporate prior knowledge of the higher order moments of the distribution [57]. The term β is nonnegative [57], and $\beta = 2$ is a good choice for an initial guess for β [35], as it is for a Gaussian prior distribution [60], $\beta \geq 0$. The third term, $\kappa \geq 0$ is used to ensure that the covariance matrix is positive semi-definite.

The following sets of equations illustrate how these tuning parameters are used with the state estimate, $\hat{\boldsymbol{x}}$, and covariance matrix P_x to determine the sigma point locations and their respective weights for use in the UKF.

$$\boldsymbol{\chi}_0 = \hat{\boldsymbol{x}}, \qquad\qquad i = 0 \qquad\qquad (6.18)$$

$$\boldsymbol{\chi}_i = \hat{\boldsymbol{x}} + \sqrt{(L + \lambda)P_x}, \qquad\qquad i = 1, ..., L \qquad\qquad (6.19)$$

$$\boldsymbol{\chi}_i = \hat{\boldsymbol{x}} - \sqrt{(L + \lambda)P_x}, \qquad\qquad i = L + 1, ..., 2L \qquad\qquad (6.20)$$

Here $\hat{\boldsymbol{x}}$ is the state estimate, P_x is the state covariance matrix, L is length of the augmented state vector used in the filter, and λ is given by

$$\lambda = \alpha^2(L + \kappa) - L. \tag{6.21}$$

In the above equations, the notation $\sqrt{A}$ is used to denote a matrix M such that $MM^T = A$. This can be computed using the Cholesky decomposition. It can be seen that the 0th sigma point is the original mean of the estimate. Different weights are computed for this sigma point and the other sigma points as shown below.

$$\mathfrak{w}_0^{(m)} = \frac{\lambda}{L + \lambda} \qquad\qquad i = 0 \tag{6.22}$$

$$\mathfrak{w}_0^{(c)} = \frac{\lambda}{L + \lambda} + (1 - \alpha^2 + \beta) \qquad\qquad i = 0 \tag{6.23}$$

$$\mathfrak{w}_i^{(m)} = \mathfrak{w}_i^{(c)} = \frac{1}{2(L + \lambda)} \qquad\qquad i = 1, ..., 2L \tag{6.24}$$

In these equations, the (c) refers to weights on the covariance matrix, and the (m) refers to weights on the mean.

The following sections outline the steps needed to implement the unscented Kalman filter. The equations for the UKF follow those of Van Der Merwe in [57].

Initialization

To match the formulation of the EKF, the equations for the UKF will be presented for a system with continuous nonlinear dynamics and discrete measurements.

The system dynamics are shown in the following equation

$$\dot{\boldsymbol{x}}(t) = f(\boldsymbol{x}, t) + B(t)\boldsymbol{u}(t) + G(t)\boldsymbol{w}(t) \tag{6.25}$$

where the matrices B and G are matrices that map the controls and the noise to the state variables, and the noise is assumed to be zero mean, Gaussian, and white with strength Q.

$$E[\boldsymbol{w}(t)\boldsymbol{w}(t')] = Q\delta(t - t') \tag{6.26}$$

The term δ is the Dirac delta function. The measurement function is given as

$$\tilde{\boldsymbol{y}}_k = h(\boldsymbol{x}_k) + \boldsymbol{\nu}_k \tag{6.27}$$

Here the term $\boldsymbol{\nu}$ is the noise associated with the measurement strength, R, given as

$$E[\boldsymbol{\nu}_i\boldsymbol{\nu}_j^T] = R\delta(t_i - t_j) \tag{6.28}$$

where in this instance δ is the Kroenecker delta function.

Starting with the initial estimate and covariance, an augmented state and covariance matrix are formed; the augmented states are the mean and covariance for both process and measurement noise. Assuming that the noise terms are white and uncorrelated with the state, the filter can then be initialized in the following manner.

$$\hat{\boldsymbol{x}}_0 = E[\boldsymbol{x}_0], \qquad \hat{\boldsymbol{x}}_0^a = E[\boldsymbol{x}^a] = E\begin{bmatrix} \hat{\boldsymbol{x}}_0 & \mathbf{0} & \mathbf{0} \end{bmatrix}^T \tag{6.29}$$

$$P_{x_0} = E[(\boldsymbol{x}_0 - \hat{\boldsymbol{x}}_0)((\boldsymbol{x}_0 - \hat{\boldsymbol{x}}_0)^T], \qquad P_0^a = E\left[(\boldsymbol{x}_0^a - \hat{\boldsymbol{x}}_0^a)(\boldsymbol{x}_0^a - \hat{\boldsymbol{x}}_0^a)^T\right] = \begin{bmatrix} P_{x_0} & 0 & 0 \\ 0 & Q_d & 0 \\ 0 & 0 & R \end{bmatrix} \tag{6.30}$$

The superscripts in the above equations are used to refer to the components of the state and covariance matrices that are being referenced. Terms with a superscript $(\cdot)^a$ refer to the entire augmented state and covariance matrix. The term Q_d is the covariance of the process noise. At a given moment in time it can be calculated as

$$Q_d = \frac{Q}{\Delta t} \tag{6.31}$$

Now using the augmented state and covariance matrix, the sigma points may be calculated by applying equations 7.51–7.53 and adding the state estimate to the columns of the $\sqrt{P}$ terms.

$$\boldsymbol{\chi}^a_{k-1} = \left[\hat{\boldsymbol{x}}^a_{k-1} \quad \hat{\boldsymbol{x}}^a_{k-1} + \gamma\sqrt{P^a_{k-1}} \quad \hat{\boldsymbol{x}}^a_{k-1} - \gamma\sqrt{P^a_{k-1}} \right] \tag{6.32}$$

$$\gamma = \sqrt{L + \lambda} \tag{6.33}$$

$$\lambda = \alpha^2(L + \kappa) - L \tag{6.34}$$

The term $\boldsymbol{\chi}^a_{k-1}$ is now an $L \times (2L + 1)$ matrix containing the sigma point components for the state, the process noise, and the measurement noise as shown below. Each individual sigma point is a column in the matrix and comprises these three parts.

$$\boldsymbol{\chi}^a = \begin{bmatrix} \boldsymbol{\chi}^x \\ \boldsymbol{\chi}^w \\ \boldsymbol{\chi}^\nu \end{bmatrix} \tag{6.35}$$

Propagation/time update equations

With the sigma points defined, the next step is to propagate the sigma point state components forward in time using the full nonlinear dynamics of the system (Eq. 6.25). However, it is common in the literature to use the discrete notation to show the time intervals between the sigma points (references [35], [3], and [42] all use the discrete notation for the UKF). Thus, the differential equations, or the equivalent discrete difference equations, may be used for propagating the sigma point states. If the differential equations are used, they would just be used to propagate the state to the discrete time intervals used in the filter. It is important to note that the noise used in propagating the states isn't a random perturbation, rather, it is the specific process noise components belonging to the ith sigma point.

$$\boldsymbol{\chi}^x_{k|k-1} = f\left(\boldsymbol{\chi}^x_{k-1}, \boldsymbol{\chi}^w_{k-1}, u_{k-1}\right) \tag{6.36}$$

After the sigma points have been propagated, the weights are applied, and a new estimate and covariance matrix are calculated.

$$\hat{\boldsymbol{x}}_k^- = \sum_{i=0}^{2L} \mathfrak{w}_i^{(m)} \boldsymbol{\chi}_{i,k|k-1}^x \tag{6.37}$$

$$P_{x_k}^- = \sum_{i=0}^{2L} \mathfrak{w}_i^{(c)} \left(\boldsymbol{\chi}_{k|k-1}^x - \hat{\boldsymbol{x}}_k^- \right) \left(\boldsymbol{\chi}_{k|k-1}^x - \hat{\boldsymbol{x}}_k^- \right)^T \tag{6.38}$$

If no measurements are available, then the process repeats using the new state and covariance to find the sigma points.

Measurement update equations

If a measurement is available at the given time, it is processed in the following manner. First, the expected measurement for each of the sigma points is found using the full non-linear measurement equation (6.27) with noise terms coming from the measurement noise components of the specific sigma point. Assuming that the noise is added linearly to the measurement function, this would be

$$\boldsymbol{Y}_{i,k|k-1} = h\left(\boldsymbol{\chi}_{i,k-1}^x \right) + \boldsymbol{\chi}_{i,k-1}^\nu \tag{6.39}$$

If the measurement noise is not strictly added linearly, but is a nonlinear component in the measurement function, then the individual sigma point measurement noise component would be used in the equation where the measurement noise is usually applied.

The individual expected measurements for the different sigma points are then combined with the weighting scheme to find a mean expected measurement.

$$\hat{\boldsymbol{y}}_k^- = \sum_{i=0}^{2L} \mathfrak{w}_i^{(m)} \boldsymbol{Y}_{i,k|k-1} \tag{6.40}$$

Then using this term and the mean state estimate, the measurement covariance and the state and measurement cross-covariance can be calculated.

$$P_{\tilde{y}_k} = \sum_{i=0}^{2L} \mathfrak{w}_i^{(c)} \left(\boldsymbol{Y}_{k|k-1} - \hat{\boldsymbol{y}}_k^- \right) \left(\boldsymbol{Y}_{k|k-1} - \hat{\boldsymbol{y}}_k^- \right)^T \tag{6.41}$$

$$P_{x_k y_k} = \sum_{i=0}^{2L} \mathfrak{w}_i^{(c)} \left(\boldsymbol{\chi}_{k|k-1}^x - \hat{\boldsymbol{x}}_k^- \right) \left(\boldsymbol{Y}_{k|k-1} - \hat{\boldsymbol{y}}_k^- \right)^T \tag{6.42}$$

Then using these terms, the Kalman gain is calculated.

$$K_k = P_{x_k y_k} P_{\tilde{y}_k}^{-1} \tag{6.43}$$

With the Kalman gain, the a posteriori state estimate and covariance matrix are found:

$$\hat{\boldsymbol{x}}_k^+ = \hat{\boldsymbol{x}}_k^- + K_k(\tilde{y}_k - \hat{y}_k^-) \tag{6.44}$$

$$P_{x_k}^+ = P_{x_k}^- - K_k P_{\tilde{y}_k} K_k^T \tag{6.45}$$

A summary of the equations needed to implement the UKF is presented in Table 6.2.

6.3 Particle filters

A particle filter (PF) is a recursive estimation method designed to be able to obtain the posterior probability density function (PDF) of a state that is being estimated using sensor measurements [35]. Particle filters are especially useful for nonlinear systems that deviate from Gaussian distributions in the dynamics and measurement models. The PF operates by first creating a distribution of particles that are then propagated forward in time using the system dynamics. The particles that more closely match the truth model are kept and multiplied, and those that are less likely to be a match to the truth state are thrown away. With a sufficient number of particles, the PDF of the truth state can be obtained. With an infinite number of particles, it is theoretically possible to perfectly estimate any state. However, the computation cost increases with the number of particles used. Thus, as shown

Table 6.2: UKF algorithm for controlled spacecraft propagation and time update

State	$\boldsymbol{x}$
Model	$\dot{\boldsymbol{x}}(t) = f(\boldsymbol{x}, t) + B(t)\boldsymbol{u}(t) + G(t)\boldsymbol{w}(t) \quad \boldsymbol{w}(t) \sim N(\boldsymbol{0}, Q(t))$ $\tilde{\boldsymbol{y}}_k = g(\boldsymbol{x}_k, \boldsymbol{\nu}_k) \qquad\qquad \boldsymbol{\nu}_k \sim N(0, R_k)$
Initialize	$\hat{\boldsymbol{x}}_0 = E[\boldsymbol{x}_0], \qquad \hat{\boldsymbol{x}}_0^a = E[\boldsymbol{x}^a] = E\begin{bmatrix} \hat{\boldsymbol{x}}_0 & \boldsymbol{0} & \boldsymbol{0} \end{bmatrix}^T$ $P_{x_0} = E[(\boldsymbol{x}_0 - \hat{\boldsymbol{x}}_0)((\boldsymbol{x}_0 - \hat{\boldsymbol{x}}_0)^T]$ $P_0^a = E\left[(\boldsymbol{x}_0^a - \hat{\boldsymbol{x}}_0^a)(\boldsymbol{x}_0^a - \hat{\boldsymbol{x}}_0^a)^T\right] = \begin{bmatrix} P_{x_0} & 0 & 0 \\ 0 & Q_d & 0 \\ 0 & 0 & R \end{bmatrix}$
Draw sigma points	$\boldsymbol{\chi}_{k-1}^a = \begin{bmatrix} \hat{\boldsymbol{x}}_{k-1}^a & \hat{\boldsymbol{x}}_{k-1}^a + \gamma\sqrt{P_{k-1}^a} & \hat{\boldsymbol{x}}_{k-1}^a - \gamma\sqrt{P_{k-1}^a} \end{bmatrix}$ $\gamma = \sqrt{L + \lambda}$ $\lambda = \alpha^2(L + \kappa) - L$
Propagation	$\boldsymbol{\chi}_{k|k-1}^x = f\left(\boldsymbol{\chi}_{k-1}^x, \boldsymbol{\chi}_{k-1}^w, u_{k-1}\right)$
Time update	$\hat{\boldsymbol{x}}_k^- = \sum_{i=0}^{2L} \mathfrak{w}_i^{(m)} \boldsymbol{\chi}_{i,k|k-1}^x$ $P_{x_k}^- = \sum_{i=0}^{2L} \mathfrak{w}_i^{(c)} \left(\boldsymbol{\chi}_{k|k-1}^x - \hat{\boldsymbol{x}}_k^-\right)\left(\boldsymbol{\chi}_{k|k-1}^x - \hat{\boldsymbol{x}}_k^-\right)^T$
Measurement update	$\boldsymbol{Y}_{i,k|k-1} = g\left(\left(\boldsymbol{\chi}_{i,k-1}^x\right)^-, \boldsymbol{\chi}_{i,k-1}^\nu\right)$ $\hat{\boldsymbol{y}}_k^- = \sum_{i=0}^{2L} \mathfrak{w}_i^{(m)} \boldsymbol{Y}_{i,k|k-1}$ $P_{\tilde{y}_k} = \sum_{i=0}^{2L} \mathfrak{w}_i^{(c)} \left(\boldsymbol{Y}_{i,k|k-1} - \hat{\boldsymbol{y}}_k^-\right)\left(\boldsymbol{Y}_{i,k|k-1} - \hat{\boldsymbol{y}}_k^-\right)^T$ $P_{x_k y_k} = \sum_{i=0}^{2L} \mathfrak{w}_i^{(c)} \left(\boldsymbol{\chi}_{i,k-1}^x - \hat{\boldsymbol{x}}_k^-\right)\left(\tilde{\boldsymbol{y}}_{k|k-1} - \hat{\boldsymbol{y}}_k^-\right)^T$ $K_k = P_{x_k y_k} P_{\tilde{y}_k}^{-1}$ $\hat{\boldsymbol{x}}_k^+ = \hat{\boldsymbol{x}}_k^- + K_k(\tilde{\boldsymbol{y}}_k - \hat{\boldsymbol{y}}_k^-)$ $P_{x_k}^+ = P_{x_k}^- - K_k P_{\tilde{y}_k} K_k^T$

in [35], the difficulty with PFs is the ability to design a PF that will correctly determine the estimated state and use only a minimal number of particles.

While PFs are a useful tool in state estimation, there are some drawbacks associated with them. These drawbacks include the computational cost of implementing PFs, the degradation of the particles forming the state estimate, and the possibility of filter divergence. Large numbers of particles are needed to perform accurate state estimation; increasing the number of particles increases the computational cost of estimation. In addition, in throwing out particles with unlikely state estimates, the PFs may suffer from particle degradation due to what is called the "impoverishment problem" (IP). The IP is what occurs when the weights are not very well distributed, and so the filter narrows in on a solution space of only one or two particles. This results in obtaining an erroneous answer that is output with very high certainty. The number of particles has been reduced to the extent that there is no longer a sufficient number of particles to estimate the state. The IP often leads to filter divergence, as the particles are concentrated in one area instead of encapsulating a distribution large enough to include the truth state.

However, despite the challenges associated with particle filters, their ability and versatility in estimation has led to the development of different methods to mitigate these problems. The following section provides an example of a commonly used particle filter and highlights one of these methods.

6.3.1 Bootstrap particle filter

The bootstrap particle filter (BPF), also known as a sample importance sampling filter, was developed by Gordon et al. [36]. This filter operates by first sampling a given distribution to place a specified number of particles such that they represent the PDF from which they were drawn. The particles are propagated forward in time, and when a measurement is available the filter assigns weights and determines the particles of highest likelihood. The particles are then resampled. This involves the reassigning of particle values based on those particles that have the largest weights so that the same number of particles is kept at each update phase of the filter, and they are concentrated in the region(s) of

greatest likelihood. With time, the particles may concentrate in regions of just one or two distinct values, losing the diversity of the particles and becoming impoverished. To mitigate this, an additional step called particle "roughening" can be employed to aid in prevention of the IP through furthering the distribution of the particles, typically by adding noise to the system. The BPF was used in reference [9] for RSO attitude inversion using light curve measurements and in reference [15] for satellite state and shape estimation.

Initialization

Unlike the EKF and the UKF, the BPF isn't used to obtain a single value for the state estimate. One can be obtained from the BPF, but the output of the BPF at each time step is really an estimation of the state distribution. If things are working properly, the statistics of the BPF distribution should closely match that of the truth value being estimated. However, in order to do this, each of the different particles of the BPF must have some estimate of the state, and these states are propagated according to the state dynamics.

$$\dot{\boldsymbol{x}}(t) = f(\boldsymbol{x}, t) + B(t)\boldsymbol{u}(t) + G(t)\boldsymbol{w}(t) \tag{6.46}$$

where the matrices B and G are matrices that map the controls and the noise to the state variables, and the noise is assumed to be zero mean, Gaussian, and white with strength Q:

$$E[\boldsymbol{w}(t)\boldsymbol{w}(t')] = Q\delta(t - t') \tag{6.47}$$

The term δ is the Dirac delta function.

The measurement function is given as

$$\tilde{\boldsymbol{y}}_k = h(\boldsymbol{x}_k) + \boldsymbol{\nu}_k \tag{6.48}$$

Here the term $\boldsymbol{\nu}$ is the noise associated with the measurement with strength, R, given as

$$E[\boldsymbol{\nu}_i\boldsymbol{\nu}_j^T] = R\delta(t_i - t_j) \tag{6.49}$$

where in this instance δ is the Kroenecker delta function.

The first step to running the BPF is to create a distribution of particles sampled from the PDF used to model the state at the starting time. The number of particles needed is one of the tuning parameters of the filter. The computational cost increases with the number of particles, so it is desirable to use as few particles as necessary to accurately estimate the state parameters.

After the particles have been drawn, the other parts for implementing the BPF include the propagation, update, and resampling of the particles. Some texts such as [35] include a fourth step of roughening the particles. This step is an optional fourth step that adds process noise to the particles to help prevent impoverishment.

Propagation/time update equations

As there are no assumptions or linearizations made with the bootstrap particle filter, the particles are propagated using the full nonlinear dynamics.

$$\boldsymbol{x}^{(j)}(t) = f\left(\boldsymbol{x}^{(j)(t),t}\right) + B(t)\boldsymbol{u}(t) + G(t)\boldsymbol{w}(t) \tag{6.50}$$

Here the superscript j is used to denote the jth particle.

Unlike the UKF, where the noise is the deterministic value taken from the covariance of the process noise, the noise applied in the propagation of the particle is random white noise of the same strength as the actual dynamics (or a conservative estimate if the true strength of the noise is unknown).

At desired intervals a new mean estimate and covariance matrix can be calculated using the following equations. (Here the discrete notation is used, as the time updates take place at specific times.)

$$\hat{\boldsymbol{x}}_k = \sum_{j=1}^{N} \mathfrak{W}_k^{(j)} \boldsymbol{x}_k^{(j)} \tag{6.51}$$

$$\tilde{\boldsymbol{x}}_k = \boldsymbol{x}_k^{(j)} - \hat{\boldsymbol{x}}_k \tag{6.52}$$

$$P_k \approx \sum_{j=1}^{N} \mathfrak{W}_k^{(j)} \tilde{\boldsymbol{x}}_k^{(j)} \left(\tilde{\boldsymbol{x}}_k^{(j)} \right)^T \tag{6.53}$$

In the above equations, $\mathfrak{W}$ refers to the weights of the individual particles. When there are no measurements available to assign the weights, then the particles are all weighted equally with $\mathfrak{W} = 1/N$ where N is the number of particles, and the mean estimate and covariance reduce to just the standard statistical method for calculating the mean and covariance. However, when measurements are available, the particle weighting is handled differently.

Update

The update portion of the BPF operates by using some criteria to apply a weighting scheme to all of the individual particles. These weights are then normalized such that they sum to one. With the normalized weights, the new mean and covariance are calculated, and the particles can then be resampled and roughened. Oftentimes the observed measurement is used to create the weighting scheme as explained in the following equations.

Whenever a measurement is available, the first step is to compute the expected measurement for each of the particles from the measurement model. As with the UKF, the full nonlinear measurement model is used to calculate the expected measurements. However, unlike the UKF, no measurement noise is added to the expected measurement of the particles.

$$\hat{\boldsymbol{y}}_k^{(j)} = h \left(\boldsymbol{x}_k^{(j)} \right) \tag{6.54}$$

The weights can then be calculated by passing the difference between the observed measurement and the calculated measurement for each of the particles into the PDF used to model the measurement distribution. If the measurement distribution is assumed to be Gaussian, this would be accomplished as follows

$$\boldsymbol{\mathfrak{w}}_k^{(j)} = \tilde{\boldsymbol{y}}_k - \hat{\boldsymbol{y}}_k^{(j)} \tag{6.55}$$

$$\tilde{\mathfrak{w}}_k^{(j)} = \frac{1}{(2\pi)^{\frac{n}{2}} |R_k|^{\frac{1}{2}}} \exp\left[\frac{(\boldsymbol{\mathfrak{w}}_k^{(j)})^T R_k^{-1} \boldsymbol{\mathfrak{w}}_k^{(j)}}{2} \right] \tag{6.56}$$

where n is the number of states.

These weights are then normalized.

$$\mathfrak{W}_k^{(j)} = \frac{\tilde{\mathfrak{w}}_k^{(j)}}{\sum_{j=1}^{N} \tilde{\mathfrak{w}}_k^{(j)}} \tag{6.57}$$

The next step involves resampling the particles so that the particles with the highest likelihood are kept, and those that are least likely are rejected. However, by definition, this will change the distribution of the particles and the corresponding statistics. These statistics should thus be calculated before the particles are resampled. The following equations show how the mean and covariance are calculated.

$$\hat{\boldsymbol{x}}_k = \sum_{j=1}^{N} \mathfrak{W}_k^{(j)} \boldsymbol{x}_k^{(j)} \tag{6.58}$$

$$\tilde{\boldsymbol{x}}_k = \boldsymbol{x}_k^{(j)} - \hat{\boldsymbol{x}}_k \tag{6.59}$$

$$P_k \approx \sum_{j=1}^{N} \mathfrak{W}_k^{(j)} \tilde{\boldsymbol{x}}_k^{(j)} \left(\tilde{\boldsymbol{x}}_k^{(j)} \right)^T \tag{6.60}$$

Resampling

Resampling is a process that is used after obtaining the weights from the measurements to redistribute the particles around the areas of greatest likelihood while maintaining the same number of total particles. While one may choose to do so, it is not necessary to resample the particles after every measurement update. The intended purpose of resampling is to remove the particles that are not contributing much to the knowledge of the state and focus on the particles that are. A measure of this is called the effective sample size N_{eff}. This term essentially represents the number of samples with large weights that are contributing to a better knowledge of the state.

From [35], an approximation of the effective size is

$$N_{eff} \approx 1 / \sum_{1}^{N} (\mathfrak{w}_k^{(j)})^2 \tag{6.61}$$

A value of $N_{eff} \approx 1$ means that the there are a few particles with a significant weight, and a value of $N_{eff} \approx N$ means that almost all of the particles are weighted at about the same level. Typically in the cases where N_{eff} is small, there is a lack of diversity, and particle resampling may help the overall estimation process and help prevent impoverishment. If the number is large, then resampling the particles may not be as effective. With the BPF there is no set method to determine how many samples are needed at any given time to accurately represent the state, and so it is a matter of judgment and tuning to determine how many particles are needed and what level of N_{eff} should determine when the particles are resampled.

There are many different approaches to resampling the particles. Reference [35] lists four different approaches: multinomial resampling, systematic resampling, stratified resampling, and residual resampling. The following is the multinomial resampling algorithm presented by Gordon et al. [36].

To resample the particles N, random samples u_i are drawn from a uniform distribution over $(0,1]$. The cumulative sum of the particle weights is used to determine which values to keep and which to multiply. As shown here, the ith particle would have its state vector replaced by the state of the Mth particle corresponding to

$$\sum_{j=0}^{M-1} \mathfrak{W}^{(j)} < u_i < \sum_{j=0}^{M} \mathfrak{W}^{(j)} \tag{6.62}$$

This is used to loop through and reassign the values of the different particles so that the larger weights are more prevalent than the smaller weights.

The multinomial resampling algorithm shown in Table 6.3 is adapted from the algorithm presented in [35, p. 283] as it is set up for implementation in code.

Table 6.3: Multinomial resampling algorithm for BPF

1)	Initialize a cumulative sum of the weights $z^{(i)} = \sum_{j=1}^{i} W^{(j)}$, $z^{i=N} = 1$
2)	Draw N independent uniform samples $u^{(i)}$ on the interval (0,1]
3)	FOR $j = 1 : N$
	set $i = 1$
	WHILE $z^{(i)} < u^{(j)}$
	$i \leftarrow i + 1$
	END WHILE
	Replace $\boldsymbol{x}^{(j)}$ with $\boldsymbol{x}^{(i)}$
	END FOR
	The term $\leftarrow$ signifies replacing the value
4)	Weights are reset to $\frac{1}{N}$

Roughening

Over time, solely resampling can lead to degeneracy and the impoverishment problem. The filter narrows in on a solution space of only one or two particles. This results in obtaining an erroneous answer that is output with very high certainty. To rectify this,

an additional step called particle roughening is used to add more diversity to the particle distribution.

Particle roughening works by adding artificial noise to the system. Small jitters are added so that the particle states are not all concentrated in a single region. It is performed after resampling and before integrating the state of the particles to the next time step. The following method for particle roughening is taken from [35].

To implement this roughening, the artificial noise, c, used to diversify the particle distribution is drawn from a Gaussian distribution, $N(0, \mathcal{J}_k)$. The matrix $\mathcal{J}_k$ is a diagonal matrix where the diagonal elements comprise $\sigma_1^2...\sigma_n^2$. The lth standard deviation is given by

$$\sigma_l = \mathcal{G}E_l N^{-1/n} \tag{6.63}$$

where E_l is the length of the interval between the maximum and minimum values of this component (before roughening), n is the dimension of the state space, and N is the number of particles. $\mathcal{G}$ is a tuning parameter that is used to determine how much noise is needed. With the proper tuning of $\mathcal{G}$ and the process noise, the BPF is a general tool that can be used to estimate the state for many different applications.

Tables 6.4–6.6 summarize the equations needed to implement the BPF. Note that these equations are shown as having the particle drawn from a normal distribution and having the measurements updated using a normal distribution to assign the weights. This is done to be consistent with and match the EKF and UKF. In actuality, the initial distribution, could be created from any distribution and there are numerous ways to assign the particles weights. The choice of distributions depends on the individual problem being solved.

6.4   Summary

This chapter provided an overview of three different filters, the extended Kalman filter, the unscented Kalman filter, and the bootstrap particle filter. For each of the filters, the pros and cons were presented. Finally, general forms of the algorithms were shown so that

Table 6.4: BPF algorithm for controlled spacecraft propagation and time update

State	$\boldsymbol{x}$
Model	$\dot{\boldsymbol{x}}(t) = f(\boldsymbol{x}, t) + B(t)\boldsymbol{u}(t) + G(t)\boldsymbol{w}(t) \quad \boldsymbol{w}(t) \sim N(\mathbf{0}, Q(t))$ $\tilde{\boldsymbol{y}}_k = h(\boldsymbol{x}_k) + \boldsymbol{\nu}_k) \qquad\qquad \boldsymbol{\nu}_k \sim N(0, R_k)$
Initialize	$\hat{\boldsymbol{x}}_0 = E\left[\boldsymbol{x}_0\right] \quad P_0 = E\left[(\boldsymbol{x}_0 - \hat{\boldsymbol{x}}_0)(\boldsymbol{x}_0 - \hat{\boldsymbol{x}}_0)^T\right]$ $\mathfrak{W}_0^{(j)} = \frac{1}{N}$
Draw particles	$\boldsymbol{x}_0^{(j)} \sim N\left(\hat{\boldsymbol{x}}_0, (P_0)\right)$
Propagation	$\boldsymbol{x}^{(j)}(t) = f\left(\boldsymbol{x}^{(j)(t),t}\right) + B(t)\boldsymbol{u}(t) + G(t)\boldsymbol{w}(t)$
Time update	$\hat{\boldsymbol{x}}_k = \sum_{j=1}^{N} \mathfrak{W}_k^{(j)} \boldsymbol{x}_k^{(j)}$ $\tilde{\boldsymbol{x}}_k = \boldsymbol{x}_k^{(j)} - \hat{\boldsymbol{x}}_k$ $P_k \approx \sum_{j=1}^{N} \mathfrak{W}_k^{(j)} \tilde{\boldsymbol{x}}_k^{(j)} \left(\tilde{\boldsymbol{x}}_k^{(j)}\right)^T$

Table 6.5: Measurement update equations for attitude BPF with controlled spacecraft

Calculate expected measurements	$\hat{\boldsymbol{y}}^{(j)} = h(\hat{\boldsymbol{x}}^{(j)})$
Calculate weights	$\mathfrak{w}_k^{(j)} = \tilde{\boldsymbol{y}}_k - \hat{\boldsymbol{y}}_k^{(j)}$ $\tilde{\mathfrak{w}}_k^{(j)} = \frac{1}{(2\pi)^{\frac{n}{2}} |R_k|^{\frac{1}{2}}} \exp\left[\frac{\mathfrak{w}_k^{(j)T} R_k^{-1} \mathfrak{w}_k^{(j)}}{2}\right]$ $\mathfrak{W}_k^{(j)} = \frac{\tilde{\mathfrak{w}}_k^{(j)}}{\sum_{j=1}^{N} \tilde{\mathfrak{w}}_k^{(j)}}$
Measurement update	$\hat{\boldsymbol{x}}_k = \sum_{j=1}^{N} \mathfrak{W}_k^{(j)} \boldsymbol{x}_k^{(j)}$ $\tilde{\boldsymbol{x}}_k = \boldsymbol{x}_k^{(j)} - \hat{\boldsymbol{x}}_k$ $P_k \approx \sum_{j=1}^{N} \mathfrak{W}_k^{(j)} \tilde{\boldsymbol{x}}_k^{(j)} \left(\tilde{\boldsymbol{x}}_k^{(j)}\right)^T$
Calculate N_{eff}	$N_{eff} \approx 1/\sum_1^N (\mathfrak{w}_k^{(j)})^2$
Resample Using algorithm in Table 6.3 (optional)	
Particle roughening using algorithm in Table 6.6 (optional)	

Table 6.6: Particle roughening for BPF

Compute ith component σ_l	$E_{l,i} = max(\underline{\boldsymbol{x}}_i^{(j)}) - min(\underline{\boldsymbol{x}}_i^{(j)})$ $\sigma_{l,i} = \mathcal{G}E_l N^{-1/n}$
Compute noise	$\mathcal{J}_k = diag\left(\left[\sigma_{l,1}^2 \ldots \sigma_{l,n}\right]\right)$ $\boldsymbol{c}_k^{(j)} \sim N(0, \mathcal{J}_k)$
Update states	$\boldsymbol{x}_{roughened,k}^{(j)} = \boldsymbol{x}_{resampled,k}^{(j)} + \boldsymbol{c}_k^{(j)}$

the different filters could be implemented for real-world applications.

CHAPTER 7

QUATERNION ATTITUDE REPRESENTATION ESTIMATION ALGORITHMS

In Chapter 6 the general algorithms of the continuous-discrete extended Kalman filter, the unscented Kalman filter, and the bootstrap particle filter were presented. The framework presented there can be applied to a number of different applications. However, there are two main reasons why slight modifications of these algorithms are necessary for the applications presented in this work. The first is that quaternions are used for the spacecraft attitude representation, and the second is the way in which the dynamics are formulated for the cases of satellites with controlled and uncontrolled attitudes.

Using quaternions for the attitude representation is desirable, as it allows for avoiding singularities common to other representations. Recall from Chapter 3 that the attitude of an object can be reduced to three independent elements. The four-element quaternion also contains only three independent elements, as it must maintain a unit norm. Many estimation algorithms compute an additive update to be applied to the current state estimate, or in the case of multiple point filters like the bootstrap particle filter (BPF) and the unscented Kalman filter (UKF), calculating the mean and covariance at a given time requires a weighted summation of the individual states. These additive terms can violate the unit norm constraint of the quaternion. To avoid this, the three-element error vector $\delta\boldsymbol{\theta}$ is calculated and used to update the quaternion estimate. Here, generalized Rodrigues parameters, GRPs, are used for this three-element error vector. The equations to transform between quaternions and GRPs are shown below,

$$\boldsymbol{\theta} = f\frac{\boldsymbol{q}_{2:4}}{a + q_1} \tag{7.1}$$

where a is a parameter from 0 to 1, and f is a scale factor commonly set to $f = (2(1+a))$ [3]. Computing quaternions from GRPs can be done using the following equations.

$$q_0 = \frac{-a\|\boldsymbol{\theta}\|^2 + f\sqrt{f^2 + (1 - a^2)\|\bar{\boldsymbol{\theta}}\|^2}}{f^2 + \|\boldsymbol{\theta}\|^2} \tag{7.2}$$

$$\boldsymbol{q}_{2:4} = f^{-1}\,[a + q_1]\,\boldsymbol{\theta} \tag{7.3}$$

$$q = \begin{bmatrix} q_1 \\ \boldsymbol{q}_{2:4} \end{bmatrix} \tag{7.4}$$

Error GRPs are used for this error vector representation, as the state error covariance matrix is invariant to first order when using either quaternions or GRPs [3] [40]. Notwithstanding this benefit, even GRPs can have singularities, and so the quaternion is used to define the spacecraft attitude.

For simulations, determining the effectiveness of an estimation algorithm requires defining the truth model that is used to gauge filter performance. Recall from Chapter 4 that the equations for modeling the attitude dynamics of a spacecraft are

$$\dot{q}_{I \to b} = \frac{1}{2} \begin{bmatrix} 0 \\ \boldsymbol{\omega}^b \end{bmatrix} \otimes q_{I \to b} \tag{7.5}$$

$$\dot{\boldsymbol{\omega}}^b = J^{-1}[\boldsymbol{T} - \boldsymbol{\omega}^b \times J\boldsymbol{\omega}^b] + \boldsymbol{\eta} \tag{7.6}$$

with the strength of the white noise, Q_η, defined below.

$$E\left[\boldsymbol{\eta}(t)\boldsymbol{\eta}(t')^T\right] = Q_\eta \delta\left(t - t'\right) \tag{7.7}$$

These are continuous dynamics, and so the above delta function is the Dirac delta function.

The equations above govern the rotational motion of a spacecraft. In this work they are used as the equations comprising the truth and filter design models for the estimation algorithms pertaining to the uncontrolled spacecraft presented in this chapter. The models

for the controlled spacecraft are adapted from these.

In section 4.2.2 it was stated that some of the satellites being examined are equipped with an attitude control system (ACS). This means the satellite will generally follow a commanded trajectory. However, no ACS operates perfectly. There are random perturbations that need to be rejected and biases that need to be corrected. This means that at a given time there is some amount (determined by the ability of the ACS) in which the true attitude of the satellite differs from the commanded attitude. To model this, the satellite attitude is propagated forward in time without noise, and then discrete noise is applied at the time where a measurement is available. This is expressed in the following dynamics model for the controlled satellite.

$$\dot{\boldsymbol{q}}_{I \to b} = \frac{1}{2} \begin{bmatrix} 0 \\ \boldsymbol{\omega}^b \end{bmatrix} \otimes \boldsymbol{q}I \to b \tag{7.8}$$

$$\dot{\boldsymbol{\omega}}^b = \boldsymbol{0} \tag{7.9}$$

The true attitude at times of measurement is computed at discrete intervals by perturbing the commanded attitude values by some small amount as shown in the equation

$$\boldsymbol{q}_{I \to b} = \delta \boldsymbol{q}(\boldsymbol{\zeta}) \otimes \boldsymbol{q}^*_{I \to b} \tag{7.10}$$

where for the truth model

$$\delta \boldsymbol{q}(\boldsymbol{\zeta}) = \begin{bmatrix} 1 \\ \boldsymbol{\zeta}/2 \end{bmatrix} \tag{7.11}$$

Here $\boldsymbol{\zeta}$ is a discrete noise term with strength given by $E[\boldsymbol{\zeta}_i \boldsymbol{\zeta}_j^T] = Q_{\boldsymbol{\zeta}} \delta(t_i - t_j)$ where δ is the Kronecker delta function.

This approach for modeling the process noise in the system is atypical for the models used in most filters, and so the algorithms have to be adjusted to account for this. The following sections demonstrate how to utilize the different filters from Chapter 6 with the adjustments for using the quaternion for the spacecraft attitude representation and for the cases of the controlled and uncontrolled spacecraft.

Before discussing the specifics of the algorithms of the different filters, there are some items that need to be established beforehand to improve clarity. First, as there are only three independent elements in a quaternion, and a three-element representation is used when computing state updates, the covariance matrix associated with the attitude states is a 3×3 matrix. So when expanding out the state vector with other terms, the full state vector will be an $n \times 1$ vector while the covariance matrix will be an $(n-1) \times (n-1)$ matrix. Second, it is important to note that the dynamics models associated with the attitude and angular velocity are both the truth models and the filter design models. Finally, the measurement model is fully explained in (Chapter 5), and so it is not presented again here.

7.1 Multiplicative extended Kalman filter

With the standard formulation of the extended Kalman filter shown in section 6.2.1, the state update after processing the measurement information is additive (see Eq. 6.16). With the quaternion as a state variable, the EKF update of the state at time t_k using this formulation would be

$$\hat{\boldsymbol{q}}^{+}(t_k) = \hat{\boldsymbol{q}}^{-}(t_k) + \delta\hat{\boldsymbol{q}}(t_k) \tag{7.12}$$

where

$$\delta\hat{\boldsymbol{q}}(t_k) = K_k(\tilde{\boldsymbol{y}}_k - h(\hat{\boldsymbol{x}}_k)) \tag{7.13}$$

Looking at the above equations, it is clear that there is a possibility that the update to the state may result in a violation to the unit norm constraint of the quaternion. To mitigate this, a different form of the Kalman filter that uses a multiplicative update is utilized. This form of the Kalman filter is called the multiplicative extended Kalman filter

(MEKF).

With the standard EKF, it is assumed that the truth state is different from the state estimate by only a small perturbation, $\boldsymbol{x} = \delta\boldsymbol{x} + \hat{\boldsymbol{x}}$. The dynamics and measurements are linearized about the current estimate to determine the value of $\delta\boldsymbol{x}$ that is then used to update the state estimate. The MEKF operates in a similar manner except that it is assumed that the error between the estimated state and the truth state can be represented as a small-angle rotation that is multiplied with the quaternion estimate rather than an additive perturbation.

$$\boldsymbol{q} = \delta\boldsymbol{q}(\delta\boldsymbol{\theta}) \otimes \hat{\boldsymbol{q}} \tag{7.14}$$

Here $\delta\boldsymbol{\theta}$ is the three-component small-angle rotation between the estimated state and thetruth state. As quaternions only have three independent values, the small-angle error can be transformed to a quaternion representation and use quaternion multiplication to obtain a new state estimate without violating the unit norm constraint of the quaternion. The following sections show how the MEKF is utilized for the controlled and uncontrolled satellite attitude cases.

7.1.1   Satellite with controlled attitude

When the satellite ACS is functioning properly, it is designed to maintain the commanded attitude of the satellite to within a certain tolerance. Disturbance torques and other perturbations are rejected by the control system. However, the control system isn't perfect, and so it will be continuously making minor adjustments to ensure that the attitude is aligned with the commanded attitude. To represent this in a computer simulation, there needs to be some commanded trajectory that is perturbed very slightly at discrete points to represent the truth model, and then a filter model is used in estimating these state parameters.

Model

The state vector comprises the satellite attitude quaternion and the angular velocity of the satellite.

$$\boldsymbol{x} = \begin{bmatrix} \boldsymbol{q}_{I \to b} \\ \boldsymbol{\omega}^b \end{bmatrix} \tag{7.15}$$

The state estimate is

$$\hat{\boldsymbol{x}} = \begin{bmatrix} \hat{\boldsymbol{q}}_{I \to b} \\ \hat{\boldsymbol{\omega}}^b \end{bmatrix} \tag{7.16}$$

The state error vector is

$$\delta\boldsymbol{x} = \begin{bmatrix} \delta\boldsymbol{\theta} \\ \delta\boldsymbol{\omega} \end{bmatrix} \tag{7.17}$$

With the state related to the state estimate by

$$\boldsymbol{q} = \delta\boldsymbol{q}(\delta\boldsymbol{\theta}) \otimes \hat{\boldsymbol{q}} \tag{7.18}$$

$$\boldsymbol{\omega}^b = \hat{\boldsymbol{\omega}}^b + \delta\boldsymbol{\omega} \tag{7.19}$$

The dynamics equations for this model are shown in Eqs. 7.8–7.10. This approach to modeling the dynamics and the process noise ensures that the covariance doesn't grow over time due to process noise like what may occur with a random walk. Please note that it may sometimes be necessary to add in some small artificial process noise to "open up" the filter so that it will still apply information from new measurements, but that this is an optional step for filter performance and not necessarily part of the algorithm.

The measurement model for the filter is the apparent magnitude measurement from Chapter 5.

$$\tilde{\boldsymbol{y}}_k = h\left(\boldsymbol{x}_k, t_k\right) + \boldsymbol{\nu}_k = \boldsymbol{M}_{sat}(\boldsymbol{x}_k, t_k) + \boldsymbol{\nu}_k \tag{7.20}$$

With the covariance of the measurements defined as

$$E\left[\boldsymbol{\nu}(j)\boldsymbol{\nu}(k)^T\right] = R\delta[t_j - t_k] \tag{7.21}$$

where the delta function is the Kroenecker delta function.

Note: the measurements are left as a vector to account for the case where multiple measurements are taken at the same time and are being processed together.

Propagation/time update equations

The state estimate is propagated using the nonlinear dynamics of the system.

$$\begin{bmatrix} \dot{\hat{\boldsymbol{q}}}_{I \to b} \\ \dot{\hat{\boldsymbol{\omega}}}^b \end{bmatrix} = \begin{bmatrix} \frac{1}{2} \begin{bmatrix} 0 \\ \hat{\boldsymbol{\omega}}^b \end{bmatrix} \otimes \hat{\boldsymbol{q}}_{I \to b} \\ 0 \end{bmatrix} \tag{7.22}$$

The differential equation for propagating the covariance matrix is

$$\dot{P} = FP + PF^T \tag{7.23}$$

Here F is the matrix of the linearized dynamics (for derivation refer to Appendix A.1).

$$F = \begin{bmatrix} [-\boldsymbol{\omega}\times] & I_{3\times3} \\ 0_{3\times3} & 0_{3\times3} \end{bmatrix}\bigg|_{\hat{\boldsymbol{x}}} \tag{7.24}$$

If the integration step size is sufficiently small, the covariance may also be propagated at discrete times using the state transition matrix.

$$P_{k+1} = \Phi_k P_k \Phi_k^T \tag{7.25}$$

Where Φ is the state transition matrix found from the linearized dynamics of the system, it can be calculated as

$$\Phi = e^{F\Delta t} \tag{7.26}$$

Measurement update equations

With the controlled satellite attitude, the covariance matrix doesn't increase over time. Hence, there are no terms associated with the noise in Eqs. 7.23 and 7.25. However, there is still some uncertainty that needs to be accounted for with the slight perturbations added to the commanded quaternion to get the truth model. As this is discrete and is removed from the commanded trajectory, this added noise needs to be accounted for in the measurement update.

The covariance of the measurement at the update times is equal to

$$R_{d,k} = R_k + H_k G_k Q_{\zeta,k} G_k^T H_k^T \tag{7.27}$$

Where R is the measurement noise of the apparent magnitude measurement, Q_ζ is the value for the covariance of the attitude control system, G maps this noise to the state, and H is the measurement geometry vector. The expected measurement from the state estimate is

$$\hat{\boldsymbol{y}}_k = h_k(\hat{\boldsymbol{x}}_k^-, t_k) \tag{7.28}$$

$$H_i = \frac{\partial h}{\partial \boldsymbol{x}}\big|_{\hat{\boldsymbol{x}}_i^-} \tag{7.29}$$

The Kalman gain, error state estimate, and the covariance update are then

$$K_k = P_k^- H_k^T \left(H_k P_k^- H_k^T + R_{d,k} \right)^{-1} \tag{7.30}$$

$$\delta \hat{\boldsymbol{x}}_k^+ = \begin{bmatrix} \delta \hat{\boldsymbol{\theta}}^+ \\ \delta \hat{\boldsymbol{\omega}}^+ \end{bmatrix} = K_k (\tilde{\boldsymbol{y}}_k - \hat{\boldsymbol{y}}_k) \tag{7.31}$$

$$P_k^+ = (I - K_k H_k) P_k^- \tag{7.32}$$

Or using the Joseph form, the covariance update equation is

$$P_k^+ = (I - K_k H_k) P_k^- (I - K_k H_k)^T + K_k R_{d,k} K_k^T \tag{7.33}$$

The state updates are

$$\hat{\boldsymbol{q}}_k^+ = \delta \boldsymbol{q}_k^+ (\delta \hat{\boldsymbol{\theta}}) \otimes \hat{\boldsymbol{q}}_k^- \tag{7.34}$$

$$\hat{\boldsymbol{\omega}}_k^+ = \hat{\boldsymbol{\omega}}_k^- + \delta \hat{\boldsymbol{\omega}}_k^+ \tag{7.35}$$

Table 7.1 provides a concise summary of the different equations used in utilizing the MEKF for estimating the attitude of a spacecraft with the controlled attitude outlined in this section. The conversion between error GRPs and error quaternions is done using Eqs. 7.2–7.4.

Table 7.1: Continuous discrete MEKF algorithm for controlled spacecraft

State	$\boldsymbol{x} = \begin{bmatrix} \boldsymbol{q}_{I \to b} \\ \boldsymbol{\omega}^b \end{bmatrix}$
Model	$\dot{\boldsymbol{x}} = f(\boldsymbol{x}(t), t) = \begin{bmatrix} \begin{bmatrix} 0 \\ \frac{\boldsymbol{\omega}^b}{2} \end{bmatrix} \otimes \boldsymbol{q}_{I \to b} \\ \boldsymbol{0} \end{bmatrix} \qquad \boldsymbol{\zeta}_k \sim N(\boldsymbol{0}, Q_\zeta)$ $\tilde{\boldsymbol{y}}_k = h(\boldsymbol{x}_k, \boldsymbol{\zeta}_k) + \boldsymbol{\nu}_k \qquad \boldsymbol{\nu}_k \sim N(0, R_k)$
Initialize	$\hat{\boldsymbol{x}}_0 = E\{\boldsymbol{x}_0\}$ $P_0 = E\{(\boldsymbol{x}_0 - \hat{\boldsymbol{x}}_0)(\boldsymbol{x}_0 - \hat{\boldsymbol{x}}_0)^T\}$
Propagation	$\dot{\hat{\boldsymbol{x}}}(t) = f(\hat{\boldsymbol{x}}, t)$ $\dot{P}(t) = F(t)P(t) + P(t)F^T(t)$ $F(t) = \left.\frac{\partial f}{\partial \boldsymbol{x}}\right|_{\hat{x}(t)}$
Update	$K_k = P_k^- H_k^T \left(H_k P_k^- H_k^T + (R_k + H_k G Q_{\zeta,k} G^T H_k^T)\right)^{-1}$ $H_k(\hat{\boldsymbol{x}}_k) = \left.\frac{\partial h}{\partial \boldsymbol{x}}\right|_{\hat{x}_k^-}$ $\delta \hat{\boldsymbol{x}}_k^+ = \begin{bmatrix} \delta \hat{\boldsymbol{\theta}}^+ \\ \delta \hat{\boldsymbol{\omega}}^+ \end{bmatrix} = K_k(\tilde{\boldsymbol{y}}_k - h(\hat{\boldsymbol{x}}_k))$ $P_k^+ = (I - K_k H_k) P_k^- (I - K_k H_k)^T + K_k(R_k + H_k G Q_{\zeta,k} G^T H_k^T) K_k^T$ $\hat{\boldsymbol{q}}_k^+ = \delta \boldsymbol{q}_k^+(\delta \hat{\boldsymbol{\theta}}) \otimes \hat{\boldsymbol{q}}_k^-$ $\hat{\boldsymbol{\omega}}_k^+ = \hat{\boldsymbol{\omega}}_k^- + \delta \hat{\boldsymbol{\omega}}_k^+$

7.1.2 MEKF formulation for satellite with uncontrolled attitude

This section presents the methods of setting up the MEKF to estimate the attitude of a spacecraft that is not equipped with an attitude control system.

The formulation of the MEKF for the case of an uncontrolled satellite is similar to that of the controlled satellite except for the differences in the dynamics and noise models used. The state vector, estimate, and error vector are the same as those presented for the controlled model in Eqs. 7.15–7.17, and are related through Eqs. 7.18 and 7.19.

However, unlike the controlled model, the differential equations for the uncontrolled model are Eqs. 7.5 and 7.6.

The linearized dynamics are

$$\delta\dot{\boldsymbol{x}} = F\delta\boldsymbol{x} + G\boldsymbol{\eta} \tag{7.36}$$

where

$$F = \begin{bmatrix} [-\boldsymbol{\omega}\times] & I_{3\times3} \\ J^{-1}\sum\frac{\partial \boldsymbol{T}}{\partial\boldsymbol{\theta}} & J^{-1}\left[-[J\boldsymbol{\omega}^b\times] + [\boldsymbol{\omega}^b\times]J\right] \end{bmatrix} \tag{7.37}$$

The derivation of the linearized models for the specific torques and the other dynamics is found in Appendix A. The matrix G that maps the noise to the state is

$$G = \begin{bmatrix} 0_{3\times3} \\ I_{3\times3} \end{bmatrix} \tag{7.38}$$

The differential equation for propagating the covariance matrix is

$$\dot{P}(t) = F(t)P(t) + P(t)F^T(t) + G(t)Q_\eta(t)G^T(t) \tag{7.39}$$

If the integration step size is sufficiently small, the covariance matrix may also be propagated discretely using the state transition matrix.

$$P_{k+1} = \Phi_K P_k \Phi_k^T + Q_{\eta d,k} \tag{7.40}$$

As with the controlled case, Φ is the state transition matrix that is equivalent to

$$\Phi = e^{F\Delta t} \tag{7.41}$$

The term $Q_{\eta_d,k}$ is the covariance of process noise and can be found by multiplying the strength of the continuous process noise by the integration time step.

$$Q_{\eta_d} = Q_\eta \Delta t \qquad (7.42)$$

The measurement function is the same for both the controlled and uncontrolled cases. Equation 7.20 is the equation for the apparent magnitude of the spacecraft as viewed from a (the) telescope(s).

The measurement function remains the same as the controlled case. It is the apparent magnitude of the spacecraft as viewed from a (the) telescope(s).

Update equations

The dynamics equations are used to propagate the state forward in time until a measurement is received. When a measurement comes in, the expected measurement and measurement geometry vector are found.

$$\hat{\boldsymbol{y}}_k = h_k(\hat{\boldsymbol{x}}_k^-, t_k) \qquad (7.43)$$

$$H_k = \frac{\partial h}{\partial \boldsymbol{x}}\big|_{\hat{\boldsymbol{x}}_k^-} \qquad (7.44)$$

The Kalman gain, error state estimate, and covariance update are then

$$K_k = P_k^- H_k^T \left(H_k P_k^- H_k^T + R_k \right)^{-1} \qquad (7.45)$$

$$\delta\hat{\boldsymbol{x}}_k^+ = \begin{bmatrix} \delta\hat{\boldsymbol{\theta}}^+ \\ \delta\hat{\boldsymbol{\omega}}^+ \end{bmatrix} = K_k(\tilde{\boldsymbol{y}}_k - \hat{\boldsymbol{y}}_k) \qquad (7.46)$$

$$P_k^+ = (I - K_k H_k) P_k^- (I - K_k H_k)^T + K_k R_k K_k^T \qquad (7.47)$$

Note that in these equations, the Kalman gain and the covariance update use only the regular measurement covariance. The process noise has already been accounted for in the

covariance propagation equations.

The state updates are

$$\hat{\boldsymbol{q}}_k^+ = \delta \boldsymbol{q}_k^+(\delta\hat{\boldsymbol{\theta}}) \otimes \hat{\boldsymbol{q}}_k^- \tag{7.48}$$

$$\hat{\boldsymbol{\omega}}_k^+ = \hat{\boldsymbol{\omega}}_k^- + \delta\hat{\boldsymbol{\omega}}_k^+ \tag{7.49}$$

Table 7.2: Continuous discrete MEKF algorithm for uncontrolled spacecraft

State	$\boldsymbol{x} = \begin{bmatrix} \boldsymbol{q}_{I\to b} \\ \boldsymbol{\omega}^b \end{bmatrix}$
Model	$\dot{\boldsymbol{x}} = f(\boldsymbol{x}(t), t) + G(t)\boldsymbol{\eta}(t) \qquad \boldsymbol{\eta}(t) \sim N(\boldsymbol{0}, Q_\eta(t))$ $\dot{\boldsymbol{q}} = \frac{1}{2}\boldsymbol{q}_\omega \otimes \boldsymbol{q} \qquad \dot{\boldsymbol{\omega}} = J^{-1}\left[\sum T - \boldsymbol{\omega}^b \times J\boldsymbol{\omega}^b\right] + \boldsymbol{\eta}(t)$ $\tilde{\boldsymbol{y}}_k = h\left(\boldsymbol{x}_k\right) + \boldsymbol{\nu}_k \qquad \boldsymbol{\nu}_k \sim N(0, R_k)$
Initialize	$\hat{\boldsymbol{x}}_0 = E\{\boldsymbol{x}_0\}$ $P_0 = E\{(\boldsymbol{x}_0 - \hat{\boldsymbol{x}}_0)(\boldsymbol{x}_0 - \hat{\boldsymbol{x}}_0)^T\}$
Propagation	$\dot{\hat{\boldsymbol{x}}}(t) = f(\hat{\boldsymbol{x}}, t)$ $\dot{P}(t) = F(t)P(t) + P(t)F^T(t) + G(t)Q_\eta(t)G^T(t)$ $F(t) = \frac{\partial f}{\partial \boldsymbol{x}}\big|_{\hat{x}(t)}$
Update	$K_k = P_k^- H_k^T \left(H_k P_k^- H_k^T + R_k\right)^{-1}$ $H_k(\hat{\boldsymbol{x}}_k) = \frac{\partial h}{\partial \boldsymbol{x}}\big|_{\hat{x}_k^-}$ $\delta\hat{\boldsymbol{x}}_k^+ = \begin{bmatrix} \delta\hat{\boldsymbol{\theta}}^+ \\ \delta\hat{\boldsymbol{\omega}}^+ \end{bmatrix} = K_k(\tilde{\boldsymbol{y}}_k - h(\hat{\boldsymbol{x}}_k))$ $P_k^+ = (I - K_k H) P_k^- (I - K_k H)^T + K_k R_k K_k^T$ $\hat{q}_k^+ = \delta q_k^+(\delta\hat{\boldsymbol{\theta}}) \otimes \hat{q}_k^-$ $\hat{\boldsymbol{\omega}}_k^+ = \hat{\boldsymbol{\omega}}_k^- + \delta\hat{\boldsymbol{\omega}}_k^+$

7.2 Unscented Kalman filter

In the literature the UKF is a commonly employed method for performing light curve inversion as the dynamics and measurement model are both very nonlinear. The purpose of this section is to outline how the UKF can be applied to estimate the attitude of a spacecraft

using photometry measurements.

However, before diving into the details of the filters, it is beneficial to first define some of the different terms or expressions used in this section to avoid confusion. To begin, the variable $\boldsymbol{x}$ denotes the state vector; it is a single $n \times 1$ vector. If there is a hat, it denotes an estimate per standard convention. The term $\boldsymbol{\chi}$ will be used to refer to the different sigma points. Superscripts on either $\boldsymbol{x}$ or $\boldsymbol{\chi}$ will often be used to identify specific components of the vector. In some instances there will be terms that consist of an error vector in attitude, and the regular angular velocity. To identify these cases, when it is not clear from the superscripts, an underbar will be used as shown in the following equation.

$$\underline{\boldsymbol{x}} = \begin{bmatrix} \delta\boldsymbol{\theta} \\ \boldsymbol{\omega} \end{bmatrix} \tag{7.50}$$

With these definitions in place, the formulation of the UKF for quaternion attitude estimation can be better understood. The following section presents the general approach to how the UKF is adjusted to accommodate quaternions for the state attitude representation. Then the proceeding sections delve into the further adjustments requisite for the implementation of the controlled and uncontrolled satellite attitude cases.

7.2.1 UKF for general quaternion attitude estimation

In the previous chapter, the general formulation for the unscented Kalman filter was presented. The sigma points were found by adding the state estimate to the columns of the $\sqrt{P}$ terms (where the $\sqrt{P}$ is the Cholesky decomposition of the scaled matrix).

$$\boldsymbol{\chi}_i = \hat{\boldsymbol{x}}, \qquad\qquad\qquad i = 0 \tag{7.51}$$

$$\boldsymbol{\chi}_i = \hat{\boldsymbol{x}} + \sqrt{(L+\lambda)P_x}, \qquad\qquad i = 1, ..., L \tag{7.52}$$

$$\boldsymbol{\chi}_i = \hat{\boldsymbol{x}} - \sqrt{(L+\lambda)P_x}, \qquad\qquad i = L+1, ..., 2L \tag{7.53}$$

The points are then propagated forward in time and then recombined to obtain the new state estimate and covariance matrix.

$$\hat{\boldsymbol{x}}_k^- = \sum_{i=0}^{2L} \mathfrak{w}_i^{(m)} \boldsymbol{\chi}_{i,k|k-1}^x \tag{7.54}$$

$$P_{x_k}^- = \sum_{i=0}^{2L} \mathfrak{w}_i^{(c)} \left(\boldsymbol{\chi}_{k|k-1}^x - \hat{\boldsymbol{x}}_k^- \right) \left(\boldsymbol{\chi}_{k|k-1}^x - \hat{\boldsymbol{x}}_k^- \right)^T \tag{7.55}$$

When measurements are available, a similar process is used where the expected measurement of each sigma point is found and then these are combined with the state values to obtain a new state estimate and covariance matrix as shown in Eqs. 6.40–6.45

With this standard approach to the UKF, it is clear that both defining the sigma points and updating the state and covariance matrix require additions to the state variables. Now when the state contains the quaternion attitude representation, these sums can cause the unit norm constraint of the quaternion to be violated. Thus, similarly to the EKF, the formulation of the UKF must be changed somewhat to keep from violating this constraint. Crassidis and Markley [42] outline how this can be done by employing generalized Rodrigues parameters. This is the general approach followed in this work.

The first step is to define the state that is being estimated. In this case it is the attitude and angular velocity of the spacecraft.

$$\boldsymbol{x} = \begin{bmatrix} \boldsymbol{q}_{I \to b} \\ \boldsymbol{\omega}^b \end{bmatrix} \tag{7.56}$$

The sigma points are defined around the filter state estimate at a given time. The different attitude locations of the sigma points can be expressed in terms of a small rotation

about the "mean," or current estimate quaternion.

$$\boldsymbol{\chi}_i^q = \delta \boldsymbol{q}(\delta \boldsymbol{\theta}) \otimes \hat{\boldsymbol{q}} \tag{7.57}$$

$$\boldsymbol{\chi}_0^q = \hat{\boldsymbol{q}} \tag{7.58}$$

The small rotations are represented using generalized Rodrigues parameter (GRP) error vectors. The choice of GRPs allows for the attitude to be represented using only three parameters and a 6×6 covariance matrix to define the state and allows for the updates to be computed using the traditional summations. The estimated states that the UKF yields are the small rotation from the current estimate and the angular velocity estimate.

$$\hat{\underline{\boldsymbol{x}}} = \begin{bmatrix} \delta \hat{\boldsymbol{\theta}} \\ \hat{\boldsymbol{\omega}} \end{bmatrix} \tag{7.59}$$

As the $\delta \boldsymbol{\theta}$ terms are small rotations away from the state estimate, the value of $\delta \boldsymbol{\theta}$ for χ_0^θ is 0 as the 0th sigma point should match up with the mean.

With GRP representation, the sigma points can be defined as normal. The augmented state vector is defined.

$$\boldsymbol{\chi}^{\underline{a}} = \begin{bmatrix} \boldsymbol{\chi}^{x_\theta} \\ \boldsymbol{\chi}^\eta \\ \boldsymbol{\chi}^\nu \end{bmatrix} \tag{7.60}$$

As opposed to Chapter 6, here the term η is used for the process noise to avoid confusion with the angular velocity, ω. The term ν still refers to the measurement noise.

For the cases where the process and measurement noise are both zero mean, the augmented state vector is initialized to the following:

$$\hat{\underline{x}}_0^a = E\left\{ \begin{bmatrix} x_{\boldsymbol{\theta}} \\ \boldsymbol{\eta} \\ \boldsymbol{\nu} \end{bmatrix} \right\} = \begin{bmatrix} \mathbf{0} \\ \hat{\boldsymbol{\omega}} \\ \mathbf{0} \\ \mathbf{0} \end{bmatrix} \tag{7.61}$$

The sigma points are then drawn from the covariance matrix.

$$\boldsymbol{\chi}_{k-1}^{\mathrm{a}} = \begin{bmatrix} \hat{\boldsymbol{x}}_{k-1}^a & \hat{\boldsymbol{x}}_{k-1}^a + \gamma\sqrt{P_{k-1}^a} & \hat{\boldsymbol{x}}_{k-1}^a - \gamma\sqrt{P_{k-1}^a} \end{bmatrix} \tag{7.62}$$

$$\gamma = \sqrt{L + \lambda} \tag{7.63}$$

$$\lambda = \alpha^2(L + \kappa) - L \tag{7.64}$$

Recall from Chapter 6 that the $\sqrt{P}$ operator in Eq. 7.62 is not the square root of the matrix, but rather the Cholesky decomposition. For Eq. 7.63 the operator is the standard square root.

To propagate the sigma points forward in time, the UKF utilizes the full nonlinear state dynamics. As the dynamics consist of the quaternion kinematics and the angular velocity differential equations, the sigma points must be converted to the full quaternion before propagation. The error GRPs contained in the sigma points are converted to error quaternions using Eqs. 7.2–7.4.

$$\boldsymbol{\chi}_{k-1}^{x_{\boldsymbol{\theta}}} \rightarrow \boldsymbol{\chi}_{k-1}^{x_{\delta q}} \tag{7.65}$$

$$\boldsymbol{\chi}^{x_{\delta q}} = \begin{bmatrix} \delta\boldsymbol{q} \\ \boldsymbol{\omega} \end{bmatrix} \tag{7.66}$$

Then the error quaternions are applied to the state estimate to get the quaternions at the next time step.

$$\boldsymbol{\chi}_{i,k-1}^{q} = \boldsymbol{\chi}_{i,k-1}^{\delta q} \otimes \hat{\boldsymbol{q}}_{k-1} \tag{7.67}$$

$$\boldsymbol{\chi}_{0,k-1}^{q} = \hat{\boldsymbol{q}}_{k-1} \tag{7.68}$$

$$\boldsymbol{\chi}^{x_q} = \begin{bmatrix} \boldsymbol{q} \\ \boldsymbol{\omega} \end{bmatrix} \tag{7.69}$$

The state dynamics may be propagated forward in time using the differential equations. However, it is common in the literature to use the discrete notation to show the time intervals between the sigma points (references [35], [3], and [42] all use the discrete notation for the UKF). The differential equations can still be used; they would just be used to propagate the state to the discrete time intervals used in the filter.

$$\boldsymbol{\chi}_{i,k|k-1}^{x_q} = f(\boldsymbol{\chi}_{i,k-1}^{x_q}, \boldsymbol{\chi}_{i,k-1}^{\eta}) \tag{7.70}$$

After the propagation of the quaternion sigma points, the small rotation sigma point locations are found by doing quaternion multiplication of the other sigma points with the 0th sigma point quaternion (the mean).

$$\boldsymbol{\chi}_{i,k|k-1}^{\delta q} = \boldsymbol{\chi}_{i,k|k-1}^{q} \otimes [\boldsymbol{\chi}_{0,k|k-1}^{q}]^{*} \tag{7.71}$$

In Eq. 7.71 the * denotes the quaternion conjugate. These error quaternions are then converted back to error GRPs using Eq. 7.1 giving $\boldsymbol{\chi}_{i,k|k-1}^{x_\theta}$. The value of the attitude terms in $\boldsymbol{\chi}_{0,k|k-1}^{x_\theta}$ are once again set to zero, as this is the same as the mean, or estimate after propagation. With the error GRPs the state update is then calculated.

$$\hat{\underline{\boldsymbol{x}}}_k^- = \sum_{i=0}^{2L} \mathfrak{w}_i^{(m)} \boldsymbol{\chi}_{i,k|k-1}^{x_\theta} \tag{7.72}$$

$$P_{x_k}^- = \sum_{i=0}^{2L} \mathfrak{w}_i^{(c)} \left(\boldsymbol{\chi}_{k|k-1}^{x_\theta} - \hat{\underline{\boldsymbol{x}}}_k \right) \left(\boldsymbol{\chi}_{k|k-1}^{x_\theta} - \hat{\underline{\boldsymbol{x}}}_k \right)^T \tag{7.73}$$

The estimate calculated in 7.72 is the estimate of the attitude state error from the propagated estimate in GRPs and the updated angular velocity vector. It is not the updated estimate of the quaternion. The new quaternion estimate is found by using Eqs. 7.2–7.4 to convert the error GRP to an error quaternion and then adding the correction to the propagated state estimate (the 0th sigma point) using quaternion multiplication.

$$\hat{\boldsymbol{q}}_k^- = \hat{\boldsymbol{q}}_k^-(\delta\boldsymbol{\theta}) \otimes \boldsymbol{\chi}_{0,k|k-1}^q \tag{7.74}$$

When a measurement is available to process, the expected measurements are calculated using the sigma points after propagation. The measurements are generated using the full quaternion.

$$\boldsymbol{Y}_{k|k-1} = g\left(\boldsymbol{\chi}_{k-1}^{x_q}, \boldsymbol{\chi}_{k-1}^{\nu} \right) \tag{7.75}$$

Here $g(\boldsymbol{x}_k)$ is the measurement function with the addition of any noise terms. For the case of a measurement with an additive noise value, the function $g(\boldsymbol{x}_k)$ would be $g(\boldsymbol{x}_k) = h(\boldsymbol{x}_k) + \boldsymbol{\nu}_k$, with $h(\boldsymbol{x}_k)$ being the measurement model. The individual expected measurements for the different sigma points are then combined with the weighting scheme to find a mean expected measurement.

$$\hat{\boldsymbol{y}}_k^- = \sum_{i=0}^{2L} \mathfrak{w}_i^{(m)} \boldsymbol{Y}_{i,k|k-1} \tag{7.76}$$

Then using this term and the GRP form of the mean state estimate, the measurement covariance and the state and measurement cross-covariance can be calculated.

$$P_{\tilde{y}_k} = \sum_{i=0}^{2L} \mathfrak{w}_i^{(c)} \left(\boldsymbol{Y}_{k|k-1} - \hat{\boldsymbol{y}}_k^- \right) \left(\boldsymbol{Y}_{k|k-1} - \hat{\boldsymbol{y}}_k^- \right)^T \tag{7.77}$$

$$P_{x_k y_k} = \sum_{i=0}^{2L} \mathfrak{w}_i^{(c)} \left(\boldsymbol{\chi}_{k|k-1}^{x_\theta} - \hat{\underline{\boldsymbol{x}}}_k^- \right) \left(\boldsymbol{Y}_{k|k-1} - \hat{\boldsymbol{y}}_k^- \right)^T \tag{7.78}$$

Then using these terms, the Kalman gain is calculated.

$$K_k = P_{x_k y_k} P_{\tilde{y}_k}^{-1} \tag{7.79}$$

With the Kalman gain, the *a posteriori* attitude error state and angular velocity estimates and covariance matrix are found:

$$\hat{\underline{\boldsymbol{x}}}_k^+ = \begin{bmatrix} \delta\hat{\boldsymbol{\theta}}^+ \\ \hat{\boldsymbol{\omega}}^+ \end{bmatrix} = \hat{\underline{\boldsymbol{x}}}_k^- + K_k(\tilde{y}_k - \hat{y}_k^-) \tag{7.80}$$

$$P_{x_k}^+ = P_{x_k}^- - K_k P_{\tilde{y}_k} K_k^T \tag{7.81}$$

and the state estimate of the quaternion is updated.

$$\hat{\boldsymbol{q}}^+ = \delta\hat{\boldsymbol{q}}^+(\delta\hat{\boldsymbol{\theta}}) \otimes \boldsymbol{\chi}_{0,k|k-1}^q \tag{7.82}$$

The previous equations show only the general process related to estimating spacecraft attitude with an unscented Kalman filter. The following sections show the distinctions that are made for the case when the satellite is controlling its own attitude and for the case when the spacecraft is tumbling in an uncontrolled state.

7.2.2   Unscented Kalman for spacecraft with controlled attitude

The main difference between the spacecraft with an active attitude control system and the uncontrolled spacecraft is in the dynamics equations and how the noise is applied. An active ACS system should keep the spacecraft following some prescribed trajectory. The attitude will be maintained within some tolerance dictated by the ACS performance. This means that the covariance of the attitude and angular velocity should not be increasing over time due to process noise. It should remain nearly the same. (There may be some changes due to the dynamics and recombining the sigma points after propagation.)

The dynamics used to describe the controlled satellite with a constant angular velocity are shown in Eqs. 7.8 and 7.9.

From these equations it can be seen that there is no process noise applied to the state during the general propagation. However, if desired a small amount of pseudo process noise can be used in defining the sigma points to help open up the filter and prevent filter saturation. The true process noise is only applied at the times when measurements are available to simulate the error in an attitude control system. In this instance a set of perturbing sigma points can be drawn from the covariance of the noise representing the accuracy of the ACS. These perturbations are then applied to the state before calculating the expected measurements of the sigma points.

When setting up the problem, two augmented covariance matrices may be formed in lieu of the single augmented covariance matrix that is normally used to create the sigma points. The first consists of the covariance of the state variables, zeros for the covariance of the process noise (unless utilizing some additional noise as a tuning parameter to help open up the filter), and the covariance of the measurement noise.

$$
P_0^a = \begin{bmatrix} P_{x_0} & 0 & 0 \\ 0 & 0 & 0 \\ 0 & 0 & R \end{bmatrix}
\tag{7.83}
$$

The second augmented covariance matrix also contains the state and measurement covariance matrices, and in addition contains the covariance matrix for the ADCS.

$$P_{d,0}^a = \begin{bmatrix} P_{x_0} & 0 & 0 \\ 0 & Q_\zeta & 0 \\ 0 & 0 & R \end{bmatrix} \tag{7.84}$$

The sigma points are propagated without process noise, and Eq. 7.70 reduces to the following.

$$\chi_{i,k|k-1}^{x_q} = f(\chi_{i,k-1}^{x_q}) \tag{7.85}$$

If there are no measurements available, the time update equations are carried out as normal. However if measurements are available, small perturbations drawn from the second augmented covariance matrix are applied to the attitude state components after propagation and before calculating the expected measurement of each of the sigma points. As these perturbations are three-element vectors, they are first converted to quaternions before being combined with the attitude state. There are no perturbations on the angular velocity terms.

$$\chi_{i,k-1}^{Q_\theta} \to \chi_{i,k-1}^{Q_{\delta q}} \tag{7.86}$$

$$\left(\chi_{i,k|k-1}^q \right)^- = \chi_{i,k-1}^{Q_{\delta q}} \otimes \chi_{i,k|k-1}^q \tag{7.87}$$

Now with the state propagated and the noise properly applied, the rest of the measurement update equations can be used to find the updated state estimate and covariance matrix.

The expected measurements of each of the sigma points are found:

$$\boldsymbol{Y}_{k|k-1} = g\left(\left(\chi_{i,k|k-1}^{x_q} \right)^-, \chi_{k-1}^\nu \right) \tag{7.88}$$

These are then combined with the weights calculated using Eqs. 6.22–6.24 to obtain a mean expected measurement.

$$\hat{\boldsymbol{y}}_k^- = \sum_{i=0}^{2L} \mathfrak{w}_i^{(m)} \boldsymbol{Y}_{i,k|k-1} \tag{7.89}$$

The sigma points are converted back into the error GRPs by employing Eqs. 7.71 and 7.1. The measurement covariance and the state and measurement cross-covariance matrices can then be calculated.

$$P_{\tilde{y}_k} = \sum_{i=0}^{2L} \mathfrak{w}_i^{(c)} \left(\boldsymbol{Y}_{k|k-1} - \hat{\boldsymbol{y}}_k^-\right) \left(\boldsymbol{Y}_{k|k-1} - \hat{\boldsymbol{y}}_k^-\right)^T \tag{7.90}$$

$$P_{x_k y_k} = \sum_{i=0}^{2L} \mathfrak{w}_i^{(c)} \left(\boldsymbol{\chi}_{i,k|k-1}^{x_\theta} - \hat{\underline{\boldsymbol{x}}}_k^-\right) \left(\boldsymbol{Y}_{k|k-1} - \hat{\boldsymbol{y}}_k^-\right)^T \tag{7.91}$$

Finally, the Kalman gain is found and used to compute the a posteriori state estimate and covariance matrix.

$$K_k = P_{x_k y_k} P_{\tilde{y}_k}^{-1} \tag{7.92}$$

$$\hat{\underline{\boldsymbol{x}}}_k^+ = \begin{bmatrix} \delta\hat{\boldsymbol{\theta}}^+ \\ \hat{\boldsymbol{\omega}}^+ \end{bmatrix} = \hat{\underline{\boldsymbol{x}}}_k^- + K_k(\tilde{\boldsymbol{y}}_k - \hat{\boldsymbol{y}}_k^-) \tag{7.93}$$

$$P_{x_k}^+ = P_{x_k}^- - K_k P_{\tilde{y}_k} K_k^T \tag{7.94}$$

The quaternion state is then updated using Eq. 7.82. This process presents the formulation of the unscented Kalman filter in estimating the attitude of a spacecraft with an ACS that keeps the attitude following a prescribed trajectory.

Table 7.3 provides a summary of the algorithms used for the initialization and time update equations of the state and covariance. The measurement update equations for this case are summarized in Table 7.4.

Table 7.3: UKF algorithm for controlled spacecraft propagation and time update

State	$\boldsymbol{x} = \begin{bmatrix} \boldsymbol{q}_{I \to b} \\ \boldsymbol{\omega}^b \end{bmatrix}, \quad \underline{\boldsymbol{x}} = \begin{bmatrix} \delta\boldsymbol{\theta} \\ \boldsymbol{\omega}^b \end{bmatrix}$
Model	$\dot{\boldsymbol{x}} = f(\boldsymbol{x}(t), t) = \begin{bmatrix} \begin{bmatrix} 0 \\ \frac{\boldsymbol{\omega}^b}{2} \end{bmatrix} \otimes \boldsymbol{q}_{I \to b} \\ \boldsymbol{0} \end{bmatrix} \quad \boldsymbol{\zeta}_k \sim N(\boldsymbol{0}, Q_\zeta)$ $\tilde{\boldsymbol{y}}_k = g(\boldsymbol{x}_k, \boldsymbol{\nu}_k) = h(\boldsymbol{x}_k) + \boldsymbol{\nu}_k \qquad \boldsymbol{\nu}_k \sim N(0, R_k)$
Initialize	$\hat{\boldsymbol{x}}_0 = E\{\boldsymbol{x}_0\} \qquad\qquad \underline{\hat{\boldsymbol{x}}}_0 = E\{\underline{\boldsymbol{x}}_0\}$ $\tilde{\boldsymbol{x}}_0 = [\delta\boldsymbol{\theta}_0^T \quad (\boldsymbol{\omega} - \hat{\boldsymbol{\omega}})^T]^T \qquad P_{x_0} = \{\tilde{\boldsymbol{x}}_0 \tilde{\boldsymbol{x}}_0^T\}$ $\hat{\underline{\boldsymbol{x}}}_0^a = E\{\underline{\boldsymbol{x}}_0^a\} = \begin{bmatrix} \boldsymbol{0} & \hat{\boldsymbol{\omega}}^T & \boldsymbol{0} & \boldsymbol{0} \end{bmatrix}^T$ $P_0^a = \begin{bmatrix} P_{x_0} & 0 & 0 \\ 0 & 0 & 0 \\ 0 & 0 & R \end{bmatrix}, \qquad P_{d,0}^a = \begin{bmatrix} P_{x_0} & 0 & 0 \\ 0 & Q_\zeta & 0 \\ 0 & 0 & R \end{bmatrix}$
GRP sigma points	$\boldsymbol{\chi}_{k-1}^{\underline{a}} = \begin{bmatrix} \hat{\underline{\boldsymbol{x}}}_{k-1}^a & \hat{\underline{\boldsymbol{x}}}_{k-1}^a + \gamma\sqrt{P_{k-1}^a} & \hat{\underline{\boldsymbol{x}}}_{k-1}^a - \gamma\sqrt{P_{k-1}^a} \end{bmatrix}$ $\gamma = \sqrt{L + \lambda}$ $\lambda = \alpha^2(L + \kappa) - L$
Quaternion sigma points	$\boldsymbol{\chi}_{k-1}^{x_\theta} \to \boldsymbol{\chi}_{k-1}^{x_{\delta q}}$ $\boldsymbol{\chi}_{i,k-1}^q = \boldsymbol{\chi}_{i,k-1}^{\delta\boldsymbol{q}} \otimes \hat{\boldsymbol{q}}_{k-1}$
Propagation	$\boldsymbol{\chi}_{i,k|k-1}^{x_q} = f(\boldsymbol{\chi}_{i,k-1}^{x_q})$
Time update	$\boldsymbol{\chi}_{i,k|k-1}^{\delta q} = \boldsymbol{\chi}_{i,k|k-1}^q \otimes [\boldsymbol{\chi}_{0,k|k-1}^q]^*$ $\boldsymbol{\chi}_{i,k-1}^{\delta q} \to \boldsymbol{\chi}_{i,k-1}^\theta$ $\boldsymbol{\chi}_{0,k-1}^\theta = 0_{3 \times 1}$ $\hat{\underline{\boldsymbol{x}}}_k^- = \sum_{i=0}^{2L} \mathfrak{w}_i^{(m)} \boldsymbol{\chi}_{i,k|k-1}^{x_\theta}$ $P_{x_k}^- = \sum_{i=0}^{2L} \mathfrak{w}_i^{(c)} \left(\boldsymbol{\chi}_{k|k-1}^{x_\theta} - \hat{\underline{\boldsymbol{x}}}_k^-\right)\left(\boldsymbol{\chi}_{k|k-1}^{x_\theta} - \hat{\underline{\boldsymbol{x}}}_k^-\right)^T$ $\hat{\boldsymbol{q}}_k^- = \hat{\boldsymbol{q}}_k^-(\delta\hat{\boldsymbol{\theta}}) \otimes \boldsymbol{\chi}_{0,k|k-1}^q$

Table 7.4: Measurement update equations for attitude UKF with controlled spacecraft

Draw sigma points from P_d	$$\boldsymbol{\chi}^a_{k-1} = \left[\hat{\underline{\boldsymbol{x}}}^a_{k-1} \quad \hat{\underline{\boldsymbol{x}}}^a_{k-1} + \gamma\sqrt{P^a_{d,k-1}} \quad \hat{\underline{\boldsymbol{x}}}^a_{k-1} - \gamma\sqrt{P^a_{d,k-1}}\right]$$ $$\gamma = \sqrt{L+\lambda}$$ $$\lambda = \alpha^2(L+\kappa) - L$$
Add in process noise	$$\boldsymbol{\chi}^{Q_\theta}_{i,k-1} \to \boldsymbol{\chi}^{Q_{\delta q}}_{i,k-1}$$ $$\left(\boldsymbol{\chi}^q_{i,k|k-1}\right)^- = \boldsymbol{\chi}^{Q_{\delta q}}_{i,k-1} \otimes \boldsymbol{\chi}^q_{i,k|k-1}$$
Measurement update	$$\boldsymbol{Y}_{k|k-1} = g\left(\left(\boldsymbol{\chi}^{\boldsymbol{x}_q}_{i,k|k-1}\right)^-, \boldsymbol{\chi}^\nu_{k-1}\right)$$ $$\hat{\boldsymbol{y}}^-_k = \sum_{i=0}^{2L} \mathfrak{w}^{(m)}_i \boldsymbol{Y}_{i,k|k-1}$$ $$P_{\tilde{y}_k} = \sum_{i=0}^{2L} \mathfrak{w}^{(c)}_i \left(\boldsymbol{Y}_{k|k-1} - \hat{\boldsymbol{y}}^-_k\right)\left(\boldsymbol{Y}_{k|k-1} - \hat{\boldsymbol{y}}^-_k\right)^T$$ $$P_{x_k y_k} = \sum_{i=0}^{2L} w^{(c)}_i \left(\boldsymbol{\chi}^{x_\theta}_{i,k|k-1} - \hat{\boldsymbol{x}}^-_k\right)\left(\tilde{\boldsymbol{y}}_{k|k-1} - \hat{\boldsymbol{y}}^-_k\right)^T$$ $$K_k = P_{x_k y_k} P^{-1}_{\tilde{y}_k}$$ $$\hat{\underline{\boldsymbol{x}}}^+_k = \hat{\underline{\boldsymbol{x}}}^-_k + K_k(\tilde{\boldsymbol{y}}_k - \hat{\boldsymbol{y}}^-_k)$$ $$P^+_{x_k} = P^-_{x_k} - K_k P_{\tilde{y}_k} K^T_k$$ $$\hat{\boldsymbol{q}}^+ = \hat{\boldsymbol{q}}^+(\delta\hat{\boldsymbol{\theta}}) \otimes \boldsymbol{\chi}^q_{0,k|k-1}$$

7.2.3 Unscented Kalman filter for spacecraft with uncontrolled attitude

For an uncontrolled spacecraft, the formulation of the UKF follows much of the general formulation for the UKF for attitude estimation presented at the beginning of this section. The differences between the formulation for the uncontrolled spacecraft and the controlled spacecraft stem from the dynamics governing the two. The process noise in the uncontrolled case is applied at every propagation step, so only one augmented covariance matrix is needed for the UKF. This section presents how the UKF is formulated for spacecraft with this kind of dynamics.

As before, the state vector consists of the attitude quaternion (q) and the spacecraft angular velocity (ω). The dynamics models consist of the quaternion kinematics and Euler's rotational equation shown in Eqs. 7.5 and 7.6.

The augmented covariance matrix used to define the sigma points consists of the state, process noise, and measurement noise covariance matrices. The covariance of the process

noise $Q_{\eta,d}$ is found by multiplying the strength of the process by the propagation time step $(Q_{\eta_d} = Q_\eta \Delta t)$.

$$P_0^a = \begin{bmatrix} P_{x_0} & 0 & 0 \\ 0 & Q_{\eta,d} & 0 \\ 0 & 0 & R \end{bmatrix} \tag{7.95}$$

The process noise being applied here is different from that applied for the controlled spacecraft. The process noise term for this formulation is an angular acceleration applied in the dynamics. In the controlled case, it was noise that was added to the attitude state.

To use the filter the sigma points are drawn from this augmented covariance matrix as described in the first part of section 7.2. The state is propagated using the state sigma points with the noise terms from the process noise being appropriately applied in the dynamics.

$$\boldsymbol{\chi}_{i,k|k-1}^{x_q} = f(\boldsymbol{\chi}_{i,k-1}^{x_q}, \boldsymbol{\chi}_{i,k-1}^{\eta}) \tag{7.96}$$

The time update and measurement update equations follow the general procedure for utilizing a UKF for spacecraft attitude determination as shown in the beginning part of section 7.2.

7.3   Bootstrap particle filter

As with the extended and unscented Kalman filters, estimating spacecraft attitude with a quaternion representation requires some modification to the general filter algorithm for the BPF from Chapter 6. For the bootstrap particle filter (BPF), the state and covariance matrix is updated at each time step using Eqs. 7.97–7.99s.

Table 7.5: UKF algorithm for uncontrolled spacecraft propagation and time update

State	$\boldsymbol{x} = \begin{bmatrix} \boldsymbol{q}_{I \to b} \\ \boldsymbol{\omega}^b \end{bmatrix}, \quad \underline{\boldsymbol{x}} = \begin{bmatrix} \delta\boldsymbol{\theta} \\ \boldsymbol{\omega}^b \end{bmatrix}$
Model	$\dot{\boldsymbol{x}} = f(\boldsymbol{x}(t), t, \boldsymbol{\eta}(t)) = \begin{bmatrix} \dot{\boldsymbol{q}} \\ \dot{\boldsymbol{\omega}} \end{bmatrix} \quad \boldsymbol{\eta}(t) \sim N(\boldsymbol{0}, Q_\eta(t))$ $\tilde{\boldsymbol{y}}_k = g(\boldsymbol{x}_k, \boldsymbol{\nu}_k) = h(\boldsymbol{x}_k) + \boldsymbol{\nu}_k \quad \boldsymbol{\nu}_k \sim N(0, R_k)$
Initialize	$\hat{\boldsymbol{x}}_0 = E\{\boldsymbol{x}_0\} \qquad \hat{\underline{\boldsymbol{x}}}_0 = E\{\underline{\boldsymbol{x}}_0\}$ $\tilde{\boldsymbol{x}}_0 = [\delta\boldsymbol{\theta}_0^T \quad (\boldsymbol{\omega} - \hat{\boldsymbol{\omega}})^T]^T \quad P_{x_0} = \{\tilde{\boldsymbol{x}}_0 \tilde{\boldsymbol{x}}_0^T\}$ $\hat{\underline{\boldsymbol{x}}}_0^a = E\{\underline{\boldsymbol{x}}_0^a\} = \begin{bmatrix} \boldsymbol{0} & \hat{\boldsymbol{\omega}}^T & \boldsymbol{0} & \boldsymbol{0} \end{bmatrix}^T$ $P_0^a = \begin{bmatrix} P_{x_0} & 0 & 0 \\ 0 & Q_{\eta,d} & 0 \\ 0 & 0 & R \end{bmatrix}$
GRP sigma points	$\boldsymbol{\chi}_{k-1}^a = \begin{bmatrix} \hat{\boldsymbol{x}}_{k-1}^a & \hat{\underline{\boldsymbol{x}}}_{k-1}^a + \gamma\sqrt{P_{k-1}^a} & \hat{\underline{\boldsymbol{x}}}_{k-1}^a - \gamma\sqrt{P_{k-1}^a} \end{bmatrix}$ $\gamma = \sqrt{L + \lambda}$ $\lambda = \alpha^2(L + \kappa) - L$
Quaternion sigma points	$\boldsymbol{\chi}_{k-1}^{x_\theta} \to \boldsymbol{\chi}_{k-1}^{x_{\delta q}}$ $\boldsymbol{\chi}_{i,k-1}^q = \boldsymbol{\chi}_{i,k-1}^{\delta q} \otimes \hat{q}_{k-1}$
Propagation	$\boldsymbol{\chi}_{i,k\|k-1}^{x_q} = f[\boldsymbol{\chi}_{i,k-1}^{x_q}, \boldsymbol{\chi}_{i,k-1}^\eta]$
Time update	$\boldsymbol{\chi}_{i,k\|k-1}^{\delta q} = \boldsymbol{\chi}_{i,k\|k-1}^q \otimes [\boldsymbol{\chi}_{0,k\|k-1}^q]^*$ $\boldsymbol{\chi}_{i,k-1}^{\delta q} \to \boldsymbol{\chi}_{i,k-1}^\theta$ $\boldsymbol{\chi}_{0,k-1}^\theta = 0_{3\times1}$ $\hat{\underline{\boldsymbol{x}}}_k^- = \sum_{i=0}^{2L} \mathfrak{w}_i^{(m)} \boldsymbol{\chi}_{i,k\|k-1}^{x_\theta}$ $P_{x_k}^- = \sum_{i=0}^{2L} \mathfrak{w}_i^{(c)} \left(\boldsymbol{\chi}_{k\|k-1}^{x_\theta} - \hat{\underline{\boldsymbol{x}}}_k^-\right)\left(\boldsymbol{\chi}_{k\|k-1}^{x_\theta} - \hat{\underline{\boldsymbol{x}}}_k^-\right)^T$ $\hat{q}_k^- = \hat{q}_k^-(\delta\hat{\boldsymbol{\theta}}) \otimes \boldsymbol{\chi}_{0,k\|k-1}^q$

Table 7.6: Measurement update equations for attitude UKF with uncontrolled spacecraft

Expected measurements	$\boldsymbol{Y}_{k\|k-1} = g\left(\left(\boldsymbol{\chi}_{i,k\|k-1}^{x_q}\right)^-, \boldsymbol{\chi}_{k-1}^{\nu}\right)$ $\hat{\boldsymbol{y}}_k^- = \sum_{i=0}^{2L} w_i^{(m)} Y_{i,k\|k-1}$
Covariance matrices	$P_{\tilde{y}_k} = \sum_{i=0}^{2L} \mathfrak{w}_i^{(c)} \left(\boldsymbol{Y}_{k\|k-1} - \hat{\boldsymbol{y}}_k^-\right)\left(\boldsymbol{Y}_{k\|k-1} - \hat{\boldsymbol{y}}_k^-\right)^T$
Cross-covariance	$P_{x_k y_k} = \sum_{i=0}^{2L} \mathfrak{w}_i^{(c)} \left(\boldsymbol{\chi}_{i,k\|k-1}^{x_\theta} - \hat{\boldsymbol{x}}_k^-\right)\left(\tilde{\boldsymbol{y}}_{k\|k-1} - \hat{\boldsymbol{y}}_k^-\right)^T$
Kalman gain	$K_k = P_{x_k y_k} P_{\tilde{y}_k}^{-1}$
Update	$\hat{\underline{\boldsymbol{x}}}_k^+ = \hat{\underline{\boldsymbol{x}}}_k^- + K_k(y_k - \hat{y}_k^-)$ $P_{x_k}^+ = P_{x_k}^- - K_k P_{\tilde{y}_k} K_k^T$ $\hat{\boldsymbol{q}}^+ = \hat{\boldsymbol{q}}^+(\delta\hat{\boldsymbol{\theta}}) \otimes \boldsymbol{\chi}_{0,k\|k-1}^q$

$$\hat{\boldsymbol{x}}_k = \sum_{j=1}^{N} \mathfrak{W}_k^{(j)} \boldsymbol{x}_k^{(j)} \tag{7.97}$$

$$\tilde{\boldsymbol{x}}_k = \boldsymbol{x}_k^{(j)} - \hat{\boldsymbol{x}}_k \tag{7.98}$$

$$P_k \approx \sum_{j=1}^{N} \mathfrak{W}_k^{(j)} \tilde{\boldsymbol{x}}_k^{(j)} \left(\tilde{\boldsymbol{x}}_k^{(j)}\right)^T \tag{7.99}$$

As can be seen in Eqs. 7.97–7.99, these updates require summations and differences of the state variables. This means that it is again likely that the quaternion norm constraint could be violated. To prevent this, error GRPs are again utilized to allow the filter to maintain this constraint while still being able to estimate the attitude of the spacecraft. For an additional reference see the work of Linares, Crassidis, and Jah [61]. The general approach taken there is the same as what is presented in that work, but with some slight changes in notation and in the order the information is presented.

The basic procedure for the BPF is the same as what was laid out in Chapter 6, but changes need to be incorporated before calculating the mean and covariance matrix and in roughening the particles after the resampling step. The other portions of the BPF such as assigning weights, using the measurements, and resampling the particles remain the same.

These components of the filter are based on the expected measurement of the state and the index of the particles. Thus, no changes need to be made to those portions of the filter.

The following section provides an overview of how the BPF can be used with a quaternion attitude representation. As with the UKF it is valuable to first define some of the notations used in describing the different parts of this filter.

As with the other filters, $\boldsymbol{x}$ denotes the state vector. A superscript consisting of a letter in parentheses (e.g. $\boldsymbol{x}^{(j)}$) is used for denoting the different particles. An estimate is denoted with a hat per standard convention. As with the UKF, in the course of using the filter there are instances in which the state vector comprises an error vector in attitude and the regular angular velocity. These cases are distinguished by an underbar on the variable as shown in Eq. 7.50.

Now that this notation is established, the adjustments to the BPF algorithm can be shown. The following section will first provide a brief overview of the different changes that need to be made in order to utilize the quaternion for the attitude state representation, and then the proceeding sections will show the further changes required for the controlled and uncontrolled satellite attitude dynamics cases.

7.3.1 BPF for general quaternion attitude estimation

Normally when using the BPF, the covariance matrix is calculated using equations 7.97–7.99. However, as previously stated, these equations will not work when employing quaternions for the attitude state representation. To compute the covariance matrix, the error quaternion between all of the j particles and the quaternion of some ith particle is found.

$$\delta \boldsymbol{q}_e^{(j)} = \boldsymbol{q}^{(j)} \otimes \left(\boldsymbol{q}^{(i)} \right)^* \tag{7.100}$$

Then, the error quaternions are transformed to error GRPs using Eq.7.1. With the attitude in this form the *a priori* state estimate and covariance can be calculated. The following equations are used to show how this is accomplished for a state vector consisting

of the spacecraft attitude and angular velocity.

$$\underline{\boldsymbol{x}} = \begin{bmatrix} \delta\boldsymbol{\theta}^{(j)} \\ \bar{\boldsymbol{\omega}}^{(j)} \end{bmatrix} \tag{7.101}$$

$$\hat{\underline{\boldsymbol{x}}}_k = \sum_{j=1}^{N} \mathfrak{W}_k^{(j)} \underline{\boldsymbol{x}}_k^{(j)} \tag{7.102}$$

$$\tilde{\underline{\boldsymbol{x}}}_k = \begin{bmatrix} \delta\hat{\boldsymbol{\theta}}^{(j)} \\ \boldsymbol{\omega}^{(j)} - \hat{\boldsymbol{\omega}} \end{bmatrix} \tag{7.103}$$

$$P_k \approx \sum_{j=1}^{N} \mathfrak{W}_k^{(j)} \tilde{\underline{\boldsymbol{x}}}_k^{(j)} \left(\tilde{\underline{\boldsymbol{x}}}_k^{(j)} \right)^T \tag{7.104}$$

For the attitude state, Eq. 7.102 calculates the mean of the errors between ith particle and the attitude state of all of the particles. Thus, to get the estimate mean of all the particles, this mean error needs to be combined with ith particle state of Eq. 7.100. This is done by first converting the GRP term back into an error quaternion using 7.2–7.4 and then multiplying this with the previous quaternion used to find the error quaternions.

$$\hat{\boldsymbol{q}} = \delta\hat{\boldsymbol{q}}(\delta\hat{\boldsymbol{\theta}}) \otimes \boldsymbol{q}^{(i)} \tag{7.105}$$

Note that this same process is used to output a mean and covariance matrix for a time update after propagation and also for computing the *a posteriori* state estimate and covariance matrix after the measurement update. The quaternion used to find the error quaternions for the measurement update using Eq. 7.100 could be the quaternion state of any of the particles, or it could be the *a priori* quaternion estimate. The key part is to be consistent in that whichever quaternion is used to calculate the error states in Eq. 7.100 is used again in Eq. 7.105.

In addition, the weights of Eqs. 7.102 and 7.104 could either be the normalized weights found when computing the measurement updates or some other form of weight that yields the estimate. When beginning the filter without measurements, or after resampling the particles, the weights can be set to $1/N$, where N is the number of particles, so that all the particles are weighted equally. Resampling the particles resets the different weights.

In addition to calculating the mean and covariance estimates, the roughening step of the BPF also requires that some adjustments be made to the algorithm. Particle roughening is optional, but it is very useful in improving particle diversity. From Chapter 6, the particle roughening is performed by applying artificial noise to the different states with the standard deviation of the different state components given by

$$\sigma_l = \mathcal{G}E_l N^{-1/n} \tag{7.106}$$

where E_l is the length of the interval between the maximum and minimum values of this component (before roughening), n is the dimension of the state space, and N is the number of particles. The term $\mathcal{G}$ is a tuning parameter that is used to determine how much noise is added.

As E_l is the interval between the maximum and minimum values of the different state components, it becomes difficult to find when utilizing quaternions. This is due to the fact that quaternion representations are not unique, and that the values of the quaternions are normalized. To remedy this, error GRPs are once again employed.

The error quaternions are found by combining the particle quaternion attitude states post-resampling with the *a posteriori* state estimate.

$$\delta \boldsymbol{q}_e = \boldsymbol{q}_{resampled}^{(j)} \otimes \left(\hat{\boldsymbol{q}}^+\right)^* \tag{7.107}$$

These are then converted to error GRPs using Eq. 7.1. The state consisting of the error GRPs and the angular velocity of the spacecraft is used to get the individual noise terms c drawn from $N(0, \mathcal{J})$. Recall that $\mathcal{J}$ is a diagonal matrix comprising the squares of the

different σ_l terms. For the attitude, the individual noise terms are converted to quaternions and combined the individual particle states using quaternion multiplication.

$$q_{roughened}^{(j)} = q(c_\theta)^{(j)} \otimes q_{resampled}^{(j)} \tag{7.108}$$

For the angular velocity the noise values are simply added to the resampled states.

$$\omega_{roughened}^{(j)} = c_\omega + \omega_{resampled}^{(j)} \tag{7.109}$$

With those adjustments and the material presented in Chapter 6, the bootstrap particle filter can be used to estimate the attitude of a spacecraft.

7.3.2 Bootstrap particle filter for spacecraft with controlled attitude

As has been stated with the other filters, the controlled spacecraft is modeled as having a constant angular velocity. It is assumed that the attitude control system is maintaining the spacecraft attitude within some tolerance, and so the state covariance terms aren't growing over time due to process noise. Rather, process noise is applied to the attitude state before processing measurements to simulate the uncertainty of the ACS at that given time. This noise is modeled as Gaussian white noise with a mean of 0 and a covariance Q_ζ that is from the attitude control system. For the BPF, this approach to modeling the noise doesn't result in many changes to the algorithm for attitude estimation. The only changes are that the particles must have this noise added in before computing the measurements, and no noise is added when propagating the states of the particles.

The state being estimated consists of the inertial to body attitude quaternion and the spacecraft body angular velocity vector.

$$x = \begin{bmatrix} q_{I \to b} \\ \omega^b \end{bmatrix} \tag{7.110}$$

The differential equations describing the motion of the spacecraft following a commanded trajectory at a constant angular rate are shown in Eqs. 7.8 and 7.9.

The initial states of the particles are drawn from some specified distribution. For the sake of simplicity, and to better match the other filters, the particles are drawn from a Gaussian distribution described by the initial state estimate $\hat{\boldsymbol{x}}_0$ and the initial covariance matrix P_0.

$$\hat{\boldsymbol{x}}_0^{(j)} \sim N\left(\hat{\boldsymbol{x}}_0, (P_0)\right) \tag{7.111}$$

The particles are then propagated forward in time using the dynamics of the system. No process noise is added to the particles during this propagation phase. When a measurement becomes available, noise representing the accuracy of the ACS is applied to the particles before processing the measurement. This is done by drawing noise samples from $N(0, Q_\zeta)$, converting the samples to quaternions, and then using quaternion multiplication to add the noise into the system.

$$\left(\boldsymbol{q}_k^{(j)}\right)^- = \delta \boldsymbol{q}(\boldsymbol{\zeta})^{(j)} \otimes \boldsymbol{q}_k^{(j)} \tag{7.112}$$

After the noise is applied, the measurement update is the same as for the general particle filter from Chapter 6, with the particle roughening explained in section 7.3. A summary of the different equations needed to implement this filter is found in Tables 7.7–7.9

Table 7.7: BPF algorithm for controlled spacecraft propagation and time update

State	$\boldsymbol{x} = \begin{bmatrix} \boldsymbol{q}_{I \to b} \\ \boldsymbol{\omega}^b \end{bmatrix}, \quad \underline{\boldsymbol{x}} = \begin{bmatrix} \delta\boldsymbol{\theta} \\ \boldsymbol{\omega}^b \end{bmatrix}$
Model	$\dot{\boldsymbol{x}} = f(\boldsymbol{x}(t), t) = \begin{bmatrix} \begin{bmatrix} 0 \\ \frac{\boldsymbol{\omega}^b}{2} \end{bmatrix} \otimes \boldsymbol{q}_{I \to b} \\ \boldsymbol{0} \end{bmatrix} \quad \boldsymbol{\zeta}_k \sim N(\boldsymbol{0}, Q_\zeta)$ $\tilde{\boldsymbol{y}}_k = g(\boldsymbol{x}_k, \boldsymbol{\nu}_k) = h(\boldsymbol{x}_k) + \boldsymbol{\nu}_k \quad \boldsymbol{\nu}_k \sim N(0, R_k)$
Initialize	$\hat{\boldsymbol{x}}_0 = E\{\boldsymbol{x}_0\} \qquad \hat{\underline{\boldsymbol{x}}}_0 = E\{\underline{\boldsymbol{x}}_0\}$ $\tilde{\boldsymbol{x}}_0 = [\delta\boldsymbol{\theta}_0^T \quad (\boldsymbol{\omega} - \hat{\boldsymbol{\omega}})^T]^T \quad P_{x_0} = \{\tilde{\boldsymbol{x}}_0 \tilde{\boldsymbol{x}}_0^T\}$ $\mathfrak{W}_0^{(j)} = \frac{1}{N}$
Draw particles	$\boldsymbol{x}_0^{(j)} \sim N\left(\hat{\boldsymbol{x}}_0, (P_0)\right)$
Propagation	$\dot{\boldsymbol{x}}^{(j)}(t) = f(\boldsymbol{x}^{(j)}(t), t)$
Time update	$\delta\boldsymbol{q}_e^{(j)} = \boldsymbol{q}^{(j)} \otimes \left(\boldsymbol{q}^{(i)}\right)^*$ $\delta\boldsymbol{q}_e \to \delta\boldsymbol{\theta}$ $\hat{\underline{\boldsymbol{x}}}_k = \sum_{j=1}^{N} \mathfrak{W}_k^{(j)} \underline{\boldsymbol{x}}_k^{(j)}$ $\tilde{\underline{\boldsymbol{x}}}_k = \begin{bmatrix} \delta\hat{\boldsymbol{\theta}} \\ \boldsymbol{\omega}^{(j)} - \hat{\boldsymbol{\omega}} \end{bmatrix}$ $P_k \approx \sum_{j=1}^{N} \mathfrak{W}_k^{(j)} \tilde{\underline{\boldsymbol{x}}}_k^{(j)} \left(\tilde{\underline{\boldsymbol{x}}}_k^{(j)}\right)^T$ $\hat{\boldsymbol{q}}_k^- = \hat{\boldsymbol{q}}_k^-(\delta\hat{\boldsymbol{\theta}}) \otimes \boldsymbol{q}^{(i)}$

Table 7.8: Measurement update equations for attitude BPF with controlled spacecraft

Draw noise	$\boldsymbol{\zeta}^{(j)} \sim N(0, Q_{\zeta,k})$
Add in process noise	$\boldsymbol{\zeta}^{(j)} \to \delta \boldsymbol{q}_{\zeta}^{(j)}$ $\left(\boldsymbol{q}_k^{(j)} \right)^- = \delta \boldsymbol{q}_{\zeta}^{(j)} \otimes \boldsymbol{q}_k^{(j)}$
Calculate expected measurements	$\hat{\boldsymbol{y}}^{(j)} = h(\hat{\boldsymbol{x}}^{(j)})$
Calculate weights	$\mathfrak{w}_k^{(j)} = \tilde{\boldsymbol{y}}_k - \hat{\boldsymbol{y}}_k^{(j)}$ $\tilde{\mathfrak{w}}_k^{(j)} = \frac{1}{(2\pi)^{\frac{n}{2}} |R_k|^{\frac{1}{2}}} \exp\left[\frac{\mathfrak{w}_k^{(j)^T} R_k^{-1} \mathfrak{w}_k^{(j)}}{2} \right]$ $\mathfrak{W}_k^{(j)} = \frac{\tilde{\mathfrak{w}}_k^{(j)}}{\sum_{j=1}^N \tilde{\mathfrak{w}}_k^{(j)}}$
Measurement update	$\delta \boldsymbol{q}_e^{(j)} = \boldsymbol{q}^{(j)} \otimes \left(\boldsymbol{q}^{(i)} \right)^*$ $\delta \boldsymbol{q}_e \to \delta \boldsymbol{\theta}$ $\hat{\underline{\boldsymbol{x}}}_k = \sum_{j=1}^N \mathfrak{W}_k^{(j)} \underline{\boldsymbol{x}}_k^{(j)}$ $\tilde{\underline{\boldsymbol{x}}}_k = \begin{bmatrix} \delta \hat{\boldsymbol{\theta}} \\ \boldsymbol{\omega}^{(j)} - \hat{\boldsymbol{\omega}} \end{bmatrix}$ $P_k \approx \sum_{j=1}^N \mathfrak{W}_k^{(j)} \tilde{\underline{\boldsymbol{x}}}_k^{(j)} \left(\tilde{\underline{\boldsymbol{x}}}_k^{(j)} \right)^T$ $\hat{\boldsymbol{q}}_k^+ = \hat{\boldsymbol{q}}_k^+ (\delta \hat{\boldsymbol{\theta}}) \otimes \boldsymbol{q}^{(i)}$
Calculate N_{eff}	$N_{eff} \approx 1 / \sum_1^N (\mathfrak{w}_k^{(j)})^2$
Resample using algorithm in table 6.3 (optional)	
Roughen particles using algorithm in table 7.9 (optional)	

Table 7.9: Particle roughening for attitude BPF

Calculate error GRPs	$\delta \boldsymbol{q}_e = \boldsymbol{q}_{resampled}^j \otimes (\hat{\boldsymbol{q}}^+)^*$ $\delta \boldsymbol{q}_e \to \delta \boldsymbol{\theta}$
Compute ith component σ_l	$E_{l,i} = max(\underline{\boldsymbol{x}}_i^{(j)}) - min(\underline{\boldsymbol{x}}_i^{(j)})$ $\sigma_{l,i} = \mathcal{G} E_l N^{-1/n}$
Compute noise	$\mathcal{J}_k = diag\left(\left[\sigma_{l,1}^2 \dots \sigma_{l,n}\right]\right)$ $\underline{\boldsymbol{c}}_k^{(j)} \sim N(0, \mathcal{J}_k)$ $\underline{\boldsymbol{c}} = \begin{bmatrix} \boldsymbol{c}_\theta \\ \boldsymbol{c}_\omega \end{bmatrix}$
Update state	$\boldsymbol{q}_{roughened}^{(j)} = \boldsymbol{q}(\boldsymbol{c}_\theta)^{(j)} \otimes \boldsymbol{q}_{resampled}^{(j)}$ $\boldsymbol{\omega}_{roughened}^{(j)} = \boldsymbol{c}_\omega^{(j)} + \boldsymbol{\omega}_{resampled}^{(j)}$

7.3.3 Bootstrap particle filter for spacecraft with uncontrolled attitude

With the uncontrolled spacecraft, the BPF formulation follows the basic pattern of the BPF from Chapter 6 with the adjustments for the quaternion attitude representation presented in section 7.3. The dynamics equations for this uncontrolled spacecraft case are those shown in Eqs. 7.5 and 7.6.

In this instance, the noise term $\boldsymbol{\eta}$ is included in the dynamics, and it is added when propagating the spacecraft attitude dynamics for all of the particles.

$$\dot{\boldsymbol{x}}^{(j)}(t) = f(\boldsymbol{x}^{(j)}(t), t, \boldsymbol{\eta}^{(j)}) \tag{7.113}$$

Calculating the mean and covariance matrix and the measurement update for this filter is done in the same manner as has previously been explained.

The algorithms for using the BPF in this manner are presented in tables 7.10 and 7.11.

Table 7.10: BPF algorithm for uncontrolled spacecraft propagation and time update

State	$\boldsymbol{x} = \begin{bmatrix} \boldsymbol{q}_{I \to b} \\ \boldsymbol{\omega}^b \end{bmatrix}, \quad \underline{\boldsymbol{x}} = \begin{bmatrix} \delta\boldsymbol{\theta} \\ \boldsymbol{\omega}^b \end{bmatrix}$
Model	$\dot{\boldsymbol{x}} = f(\boldsymbol{x}(t), t, \boldsymbol{\eta}(t)) = \begin{bmatrix} \dot{\boldsymbol{q}} \\ \dot{\boldsymbol{\omega}} \end{bmatrix} \quad \boldsymbol{\eta}(t) \sim N(\boldsymbol{0}, Q_\eta)$ $\tilde{\boldsymbol{y}}_k = g(\boldsymbol{x}_k, \boldsymbol{\nu}_k) = h(\boldsymbol{x}_k) + \boldsymbol{\nu}_k \quad \boldsymbol{\nu}_k \sim N(0, R_k)$
Initialize	$\hat{\boldsymbol{x}}_0 = E\{\boldsymbol{x}_0\} \qquad \hat{\underline{\boldsymbol{x}}}_0 = E\{\underline{\boldsymbol{x}}_0\}$ $\tilde{\boldsymbol{x}}_0 = [\delta\boldsymbol{\theta}_0^T \quad (\boldsymbol{\omega} - \hat{\boldsymbol{\omega}})^T]^T \quad P_{x_0} = \{\tilde{\boldsymbol{x}}_0 \tilde{\boldsymbol{x}}_0^T\}$ $\mathfrak{W}_0^{(j)} = \frac{1}{N}$
Draw particles	$\boldsymbol{x}_0^{(j)} \sim N\left(\hat{\boldsymbol{x}}_0, \mathrm{diag}(P_0)\right)$
Propagation	$\dot{\boldsymbol{x}}^{(j)}(t) = f(\boldsymbol{x}^{(j)}(t), t, \boldsymbol{\eta}^{(j)}), \quad \boldsymbol{\eta}(t) \sim N(0, Q_\eta)$
Time update	$\delta\boldsymbol{q}_e^{(j)} = \boldsymbol{q}^{(j)} \otimes \left(\boldsymbol{q}^{(i)}\right)^*$ $\delta\boldsymbol{q}_e \to \delta\boldsymbol{\theta}$ $\hat{\underline{\boldsymbol{x}}}_k = \sum_{j=1}^N \mathfrak{W}_k^{(j)} \underline{\boldsymbol{x}}_k^{(j)}$ $\tilde{\underline{\boldsymbol{x}}}_k = \begin{bmatrix} \delta\hat{\boldsymbol{\theta}} \\ \boldsymbol{\omega}^{(j)} - \hat{\boldsymbol{\omega}} \end{bmatrix}$ $P_k \approx \sum_{j=1}^N \mathfrak{W}_k^{(j)} \tilde{\underline{\boldsymbol{x}}}_k^{(j)} \left(\tilde{\underline{\boldsymbol{x}}}_k^{(j)}\right)^T$ $\hat{\boldsymbol{q}}_k^- = \hat{\boldsymbol{q}}_k^-(\delta\hat{\boldsymbol{\theta}}) \otimes \boldsymbol{q}^{(i)}$

Table 7.11: Measurement update equations for attitude BPF for uncontrolled spacecraft

Calculate expected measurements	$\hat{\boldsymbol{y}}^{(j)} = h(\hat{\boldsymbol{x}}^{(j)})$
Calculate weights	$\mathfrak{w}_k^{(j)} = \tilde{\boldsymbol{y}}_k - \hat{\boldsymbol{y}}_k^{(j)}$ $\tilde{\boldsymbol{w}}_k^{(j)} = \frac{1}{(2\pi)^{\frac{n}{2}}|R_k|^{\frac{1}{2}}} \exp\left[\frac{\mathfrak{w}_k^{(j)^T} R_k^{-1} \mathfrak{w}_k^{(j)}}{2}\right]$ $\mathfrak{W}_k^{(j)} = \frac{\tilde{\mathfrak{w}}_k^{(j)}}{\sum_{j=1}^N \tilde{\mathfrak{w}}_k^{(j)}}$
Measurement update	$\delta \boldsymbol{q}_e^{(j)} = \boldsymbol{q}^{(j)} \otimes \left(\boldsymbol{q}^{(i)}\right)^*$ $\delta \boldsymbol{q}_e \rightarrow \delta \boldsymbol{\theta}$ $\hat{\underline{\boldsymbol{x}}}_k = \sum_{j=1}^N \mathfrak{W}_k^{(j)} \underline{\boldsymbol{x}}_k^{(j)}$ $\tilde{\underline{\boldsymbol{x}}}_k = \begin{bmatrix} \delta\hat{\boldsymbol{\theta}} \\ \boldsymbol{\omega}^{(j)} - \hat{\boldsymbol{\omega}} \end{bmatrix}$ $P_k \approx \sum_{j=1}^N \mathfrak{W}_k^{(j)} \tilde{\underline{\boldsymbol{x}}}_k^{(j)} \left(\tilde{\underline{\boldsymbol{x}}}_k^{(j)}\right)^T$ $\hat{\boldsymbol{q}}_k^+ = \hat{\boldsymbol{q}}_k^+(\delta\hat{\boldsymbol{\theta}}) \otimes \boldsymbol{q}^{(i)}$
Calculate N_eff	$N_{eff} \approx 1/\sum_1^N (\mathfrak{w}_k^{(j)})^2$
Resample using algorithm in table 6.3 (optional)	
Roughen particles using algorithm in table 7.9 (optional)	

7.4 Summary

This chapter provides an overview of how extended Kalman Filter, the unscented Kalman filter, and the bootstrap particle filter can be adjusted to account for the quaternion being used to represent the attitude state. In addition, the equations for implementing these algorithms for the two different cases of attitude dynamics used in this work are also shown with accompanying tables summarizing the algorithms. With the information presented in this chapter, it is now possible to use the filters to estimate the attitude of a spacecraft using light curve measurements.

CHAPTER 8

REFLECTION PARAMETER ESTIMATION

Thus far, all of the equations related to estimating the attitude of a satellite have been presented under the assumption that the reflection parameters of the spacecraft are known perfectly. However, in reality this is never the case. The space environment is harsh; radiation and vacuum can affect the physical properties of many objects. Thus, even knowing the full BRDF of a spacecraft's facet model before launch may result in inaccuracies after launch when trying to observe the spacecraft. Therefore, it is necessary to also find a means to estimate the change in measurements due to the change in the reflection parameters of the spacecraft.

8.1 Measurement bias

In the work of Holzinger et al. [9], it was shown that the bias of the apparent magnitude measurement at time j can be represented as

$$b_{m,j} = \sum_{i=1}^{N_f} \frac{\partial M_{\Lambda,j}(\boldsymbol{\theta}_I^B)}{\partial p_i} \delta p_i + b_{c,j} \tag{8.1}$$

where M_Λ is the apparent magnitude measurement, $\boldsymbol{\theta}_I^B$ is the attitude representation for the transformation from the inertial to body frame, p is the term representing the different reflection parameters, and b_c is the measurement bias. If it is assumed that the total measurement bias is only a factor of the shape parameters, then this can be reduced to the following equation.

$$b_m = \sum_{i=1}^{N_f} \frac{\partial M_{\Lambda,j}(\boldsymbol{\theta}_I^B)}{\partial p_i} \delta p_i \tag{8.2}$$

In the remainder of their derivation, Holzinger et al. [9] presented a model in which the dynamics of the bias were reduced to Brownian motion, or a random walk,

$$\dot{b}_m = \eta_{\dot{b}_m} \tag{8.3}$$

with the noise term $\eta_{\dot{b}_m} \sim N(\mathbf{0}, Q_{\dot{b}_m})$. The model for the strength of the noise is

$$Q_{\dot{b}_{m,j}} = \sum_{i=1}^{N_f} \left\{ (\boldsymbol{\omega}_\mu^T F_i + (\dot{\boldsymbol{o}} - \dot{\boldsymbol{r}}^T) G_i^T) Q_{p,i} (G_i(\dot{\boldsymbol{o}} - \dot{\boldsymbol{r}}) + F_i \boldsymbol{\omega}_\mu) + Tr[F_i^T Q_{p,i} F_i Q_\omega] \right\} \tag{8.4}$$

where

$$F_i = \left. \frac{\partial M_{\Lambda,j}}{\partial p_i \partial \boldsymbol{\theta}_I^B} \right|_i B(\boldsymbol{\theta}_I^B) \tag{8.5}$$

and

$$G_i = \left. \frac{\partial M_{\Lambda,j}}{\partial p_i \partial \boldsymbol{v}} \right|_i \tag{8.6}$$

with ω_μ being the mean angular velocity, $\boldsymbol{o}$ the vector of the location of the observatory, $\boldsymbol{r}$ the position vector of the spacecraft, Q_p the shape model facet uncertainty, Q_ω the uncertainty in the maneuver angular rates, $B(\boldsymbol{\theta}_I^B)$ the rotation matrix that transforms from the inertial to body coordinate frames, and $\boldsymbol{v}$ the vector from the spacecraft to the observer (called $\boldsymbol{v}_r$ in the notation of this work). The derivation of this noise model is included in the appendix of [9].

This model for the noise has the bias uncertainty increasing for cases where the relative velocity between the spacecraft and the observer increases, the angular velocity rate increases, or the uncertainties in the shape model parameters and angular rate increase. This matches what one would expect in this type of estimation process. If a spacecraft moves away from the observer or changes its rate of rotation, or if the uncertainties of the parameters change, it makes sense that the uncertainties in the bias estimate would also

increase.

However, as the dynamics of the bias are a random walk, the uncertainty in the bias would increase unbounded. The variance grows linearly with time [55]. Furthermore, this includes a case with zero relative velocity between the spacecraft and observer, and a non-rotating spacecraft. This case could be somewhat approximated by a nadir-pointing GEO spacecraft over a short observation period. Under these conditions, it is counterintuitive for the uncertainty in the bias to grow, as the spacecraft would be maintaining the same orientation relative to the observer. For these reasons, this work presents alternative models that could be used to represent the bias in the measurement model due to the uncertainties in the spacecraft reflection parameters.

8.2   Proposed models for bias representation

The purpose of this section is to present different models that could serve as an alternative to that presented by Holzinger et al. in [9]. The aim of the proposed models is to provide a means to account for the uncertainty in the reflection parameters and their effect on the apparent magnitude measurement in such a way that the uncertainty of the bias terms or other states is somewhat bounded. One clear approach is directly estimating the reflection parameters themselves. However, this is a very computationally expensive approach, thus it is preferable to explore other options that might reduce the computational burden. The following sections present the different proposed models. The first two models are different methods of modeling the bias shown in Eq. 8.2, and the third is the direct estimation of the reflection parameters. The effectiveness of the different models is evaluated and presented in Chapter 10.

8.2.1   Model 1—traditional bias

The first proposed model is that of a traditional bias, where the value of the bias is constant. With this case the measurement model is

$$\tilde{M} = M + b_m + \nu \tag{8.7}$$

The model for the bias is the same as Eq. 8.2 (time indices and function terms have been removed for brevity):

$$b_m = \sum_{i=1}^{N_f} \frac{\partial M_i}{\partial p_i} \delta p_i \tag{8.8}$$

However, instead of the dynamics being driven by noise like in Eq. 8.3, the bias for this model is assumed to be constant:

$$\dot{b}_m = 0 \tag{8.9}$$

The variance of the bias is

$$\sigma_{b_m}^2 = E\left[b_m^2\right] = \sum_{i=1}^{N_f} \left(\frac{\partial M}{\partial p_i}\right)^2 \sigma_{p_i}^2 \tag{8.10}$$

Some of the benefits include that this model is easy to implement. Only a single additional state needs to be added to the estimation algorithms, and the dynamics are very straightforward, as the bias is constant. However, there are some limitations to using this model. Unlike the model of Holzinger et al. [9], this approach of modeling the bias as constant means that the uncertainty in the bias doesn't increase for the instances where the relative velocity increases between the observer and the spacecraft, nor does it increase for different levels of the angular velocity. This narrows the scope of the possible applications of this model. This model is likely best used for the cases where the same facets of the spacecraft are being observed over short observation periods, such as for the case of a satellite in GEO that is nadir pointing. However, as this does not seem well-suited for general application, there are other models that are proposed.

8.2.2   Model 2—first-order Markov process bias model

This model is similar to the previous model except that instead of modeling the bias as a constant, the dynamics of the bias are modeled as a first-order Markov process as shown in the following equation.

$$\dot{b}_m = \frac{-b_m}{\tau} + \kappa \tag{8.11}$$

The term τ is a time constant and for this model is defined as

$$\tau = 0.1(\frac{2\pi}{\omega}) \tag{8.12}$$

The strength of the noise driving the first-order Markov is

$$Q_\kappa = \frac{2\sigma_{b_m}^2}{\tau} \tag{8.13}$$

where σ_{b_m} in the equation above is the same as defined in Eq. 8.10.

Modeling the dynamics as a first-order Markov process offers some improved modeling capability over the model presented in the previous section. Setting the time constant inversely proportional to the angular velocity allows for the uncertainty to grow relative to the changing of the facets of the spacecraft while still remaining nearly constant for the instances where the same facets are not showing. If the rate of rotation is small, the time constant is large, and the bias model is essentially that of the previous model. Whereas when the spacecraft is spinning at higher angular rates, the uncertainty of the bias will grow to a steady-state value.

It is important to note that these first two models are observatory dependent. If utilizing multiple observatories, then the state vector will require additional terms. For models 1 and 2, there is a single state per observatory that needs to be added to the filter state vector.

8.2.3 Model 3—direct parameter estimation

Unlike the other models that estimate the bias for the measurement as a whole, this third model estimates the reflection parameters directly. the purpose of the model presented in this section is to estimate the bias on the reflection parameters themselves. The required components added to the states are the facet area A, diffuse albedo term a, microfacet slope parameter m, and the specular/diffuse weighting term ξ for each facet.

the measurement model for this case is

$$\tilde{M} = M + \nu \tag{8.14}$$

The benefits of this model are that as the parameters are being estimated directly, they are independent of the number of observatories. This means that there is a fixed number of components in the state vector for a given shape model regardless of how many observatories are used. In addition, each of the parameters are for a given facet, so if the attitude and angular rate are well-known the parameters can be estimated.

The downside of this model is that it greatly increases the number of states to be estimated. Here there are four reflection parameters per facet, so a cubic shape model results in an additional 24 states, which in turn relate to an increased computational burden. If employing a particle filter with each particle having different attitude states, this can be very computationally expensive as the number of particles needed often increases with the number of states. This computational burden is the main downside of this approach and may make models 1 and 2 more favorable in some situations.

8.3 Measurement partial derivatives

Computing the bias uncertainty for models 1 and 2 requires the partial derivative of the apparent magnitude measurement with respect to the individual reflection parameters as shown in Eq. 8.10. As mentioned previously, here these are the facet area, the specular/diffuse weighting factor, the facet slope parameter, and the diffuse albedo term. This section briefly presents the partial derivative of the measurement model with respect to

these parameters. From Chapter 5 the apparent magnitude measurement is

$$M_{sat} = -2.5 \log_{10} \left(\frac{I_\Lambda}{I_{sun}} \right) - 26.74 \tag{8.15}$$

where the flux of the satellite received by the observer is

$$I_{sat} = \frac{1}{\bm{v}_r^T \bm{v}_r} I_{sun}(\bm{s}) \sum_{i=1}^{N_f} A_{i,vis} \mathcal{R}_i \left(\hat{v}_r^b, \hat{s}^b, p_i, \right) \tag{8.16}$$

For more details about these different terms, refer to Chapter 5. For these derivatives, the notation denoting an individual facet will be dropped, as each of the facets has its own reflection parameters. For a single facet, the magnitude equation is

$$M = -2.5 \log_{10} \left(\frac{1}{\bm{v}_r^T \bm{v}_r} A_{vis} \mathcal{R} \left(\hat{\bm{v}}_r^b, \hat{\bm{s}}^b, p \right) \right) - 26.74 \tag{8.17}$$

Taking the derivative of the measurement function with respect to the area can be obtained by using the change of base formula and changing the base 10 logarithm to the natural logarithm. With this change of base, the magnitude equation becomes

$$M = \frac{-2.5 \ln \left(\frac{1}{\bm{v}_r^T \bm{v}_r} A_{vis} \mathcal{R} \left(\hat{\bm{v}}_r^b, \hat{\bm{s}}^b, p \right) \right)}{\ln 10} - 26.74 \tag{8.18}$$

With this form the partial derivative with respect to the area can be found.

$$\frac{\partial M}{\partial A} = \frac{-2.5}{A \ln 10} \tag{8.19}$$

The other reflection parameters are contained within the $\mathcal{R}$ term of Eq. 8.18. Finding the partial derivative with respect to the other parameters is facilitated using the chain rule, starting with the diffuse albedo term. This appears in the equations for both the specular and the diffuse reflection components. In the diffuse component, the reflection is a direct function of this term, in the specular component, it is used for the zero-incidence Fresnel

equation value. In accounting for all of these terms, the measurement partial with respect to the diffuse albedo term is given by the following equations.

$$\frac{\partial M}{\partial a} = \frac{\partial M}{\partial \mathcal{R}} \left(\frac{\partial \mathcal{R}}{\partial \mathcal{R}_d} \frac{\partial \mathcal{R}_d}{\partial a} + \frac{\partial \mathcal{R}}{\partial \mathcal{R}_s} \frac{\partial \mathcal{R}_s}{\partial F} \frac{\partial F}{\partial g} \frac{\partial g}{\partial n} \frac{\partial n}{\partial a} \right) \tag{8.20}$$

$$\frac{\partial M}{\partial \mathcal{R}} = \frac{-2.5}{\mathcal{R} \ln 10} \tag{8.21}$$

$$\frac{\partial \mathcal{R}}{\partial \mathcal{R}_d} = \xi \tag{8.22}$$

$$\frac{\partial \mathcal{R}_d}{\partial a} = \frac{\left(\hat{\boldsymbol{n}}^b \cdot \hat{\boldsymbol{s}}^b \right)}{\pi} \tag{8.23}$$

$$\frac{\partial \mathcal{R}}{\partial \mathcal{R}_s} = (1 - \xi) \tag{8.24}$$

$$\frac{\partial \mathcal{R}_s}{\partial F} = \frac{DG}{4 \left(\hat{\boldsymbol{n}}^b \cdot \hat{\boldsymbol{s}}^b \right) \left(\hat{\boldsymbol{n}}^b \cdot \hat{\boldsymbol{v}}_r^b \right)} \tag{8.25}$$

$$\begin{aligned} \frac{\partial F}{\partial g} = & \frac{(g-c)^2(cg-c^2+1)^2(2c^2g+2c^3-2c)}{2(g+c)^2 \left(cg - c^2 + 1 \right)^4} \\ & - \frac{(g-c)^2(cg+c^2-1)^2(2c^2g-2c^3+2c)}{2(g+c)^2 \left(cg - c^2 + 1 \right)^4} \\ & + \left[1 + \frac{(cg+c^2-1)^2}{(cg-c^2+1)^2} \right] \left[\frac{(g+c)^2(g-c) - (g-c)^2(g+c)}{(g+c)^4} \right] \end{aligned} \tag{8.26}$$

$$\frac{\partial g}{\partial n} = \frac{n}{\sqrt{c^2 + n^2 - 1}} \tag{8.27}$$

$$\frac{\partial n}{\partial a} = \frac{1}{\sqrt{a}(1 - \sqrt{a})^2} \tag{8.28}$$

A similar approach can be taken for the other parameters. For the facet slope parameter, the partial is

$$\frac{\partial M}{\partial m} = \frac{\partial M}{\partial \mathcal{R}} \frac{\partial \mathcal{R}}{\partial \mathcal{R}_s} \frac{\partial \mathcal{R}_s}{\partial D} \frac{\partial D}{\partial m} \tag{8.29}$$

where the $\frac{\partial M}{\partial \mathcal{R}}$ and $\frac{\partial \mathcal{R}}{\partial \mathcal{R}_s}$ terms are the same in the above equation as in Eqs. 8.21 and 8.24.

The remaining terms are shown below.

$$\frac{\partial \mathcal{R}_s}{\partial D} = \frac{FG}{4\left(\hat{\boldsymbol{n}}^b \cdot \hat{\boldsymbol{s}}^b\right)\left(\hat{\boldsymbol{n}}^b \cdot \hat{\boldsymbol{v}}_r^b\right)} \tag{8.30}$$

$$\frac{\partial D}{\partial m} = 2e^{\frac{-\tan^2 \gamma}{m^2}}\left[\frac{\tan^2 \gamma - m^2}{\pi m^5 \cos^4 \gamma}\right] \tag{8.31}$$

The partial of the measurement function with the specular/diffuse weighting term is

$$\frac{\partial M}{\partial \xi} = \frac{\partial M}{\partial \mathcal{R}}\frac{\partial \mathcal{R}}{\partial \xi} \tag{8.32}$$

$$\frac{\partial \mathcal{R}}{\partial \xi} = \mathcal{R}_d - \mathcal{R}_s \tag{8.33}$$

The $\frac{\partial M}{\partial \mathcal{R}}$ term from Eq. 8.32 is the same as Eq. 8.21.

With all of these partial derivatives, it is now possible to compute the $\frac{\partial M_i}{\partial p_i}$ term that is used in some of the models above so that they can be included in the estimation process.

If using an extended Kalman filter to estimate the bias terms, the derivative of the measurement with respect to the biases is also required for models 1 and 2. From Eq. 8.7 this would simply be 1 for each bias.

8.4   Incorporating models into a filter

The purpose of this section is to denote how the different proposed models could be incorporated into a filter so that they could be estimated by processing the light curves.

8.4.1   Models 1 and 2 filter setup

For models 1 and 2, the differences between them are in the dynamics or when propagating them forward in time. The other parts of incorporating them in a filter are identical.

The filter states for these models consist of the bias terms for each observatory.

$$\boldsymbol{x} = \begin{bmatrix} b_{m,1} \\ \vdots \\ b_{m,n} \end{bmatrix}, \quad P_{b_m} = \begin{bmatrix} \sigma_{b_{m1}}^2 & 0 & 0 \\ 0 & \ddots & 0 \\ 0 & 0 & \sigma_{b_{mn}}^2 \end{bmatrix} \tag{8.34}$$

Here n is the number of observatories. If estimating the measurement bias terms in addition to the attitude and angular velocity, then this becomes

$$\boldsymbol{x} = \begin{bmatrix} \boldsymbol{q}_{I \to b} \\ \boldsymbol{\omega}^b \\ b_{m,1} \\ \vdots \\ b_{m,n} \end{bmatrix}, \quad P_x = \begin{bmatrix} P_{\boldsymbol{\theta}} & 0 & 0 \\ 0 & P_{\boldsymbol{\omega}} & 0 \\ 0 & 0 & P_{b_m} \end{bmatrix} \tag{8.35}$$

The dynamics models for the attitude and angular velocity are the same as those presented in previous chapters, and the dynamics models for bias of model 1 and model 2 are shown in Eqs. 8.9 and 8.11, respectively. The process for propagating, or the time update of the state, is the standard form for the bias terms.

If utilizing an EKF for the bias estimation, the derivatives of the state dynamics with respect to state variables is needed for propagating the covariance matrix. For the bias terms from models 1 and 2, these would be 0 and $1/\tau$ respectively.

The measurement update has to be adjusted to consider the measurement bias. This change takes place in the computing of the expected measurement. From 8.7 the expected measurements at time k can be calculated as

$$\hat{M}_k = h(\hat{\boldsymbol{x}}_k) = M(\hat{\boldsymbol{q}}_k) + \hat{b}_{m,k,j} \tag{8.36}$$

where the j term on the bias denotes the specific observatory that made the measurement.

8.4.2   Model 3 Filter Setup

As previously mentioned, for model 3, the elements being estimated are the reflection parameters themselves. The items added to the state vector are these individual parameters for each of the facets of the desired shape model. Let $\boldsymbol{p}_i \equiv \begin{bmatrix} A_i & a_i & m_i & \xi_i \end{bmatrix}^T$ then the state and covariance matrix for the parameters are

$$\boldsymbol{x} = \begin{bmatrix} \boldsymbol{p}_1 \\ \vdots \\ \boldsymbol{p}_{N_f} \end{bmatrix}, \quad P_x = \begin{bmatrix} P_{\boldsymbol{p}_1} & 0 & 0 \\ 0 & \ddots & 0 \\ 0 & 0 & P_{\boldsymbol{p}_{N_f}} \end{bmatrix} \tag{8.37}$$

with

$$P_{\boldsymbol{p}_i} = \begin{bmatrix} \sigma_{A_i}^2 & 0 & 0 & 0 \\ 0 & \sigma_{a_i}^2 & 0 & 0 \\ 0 & 0 & \sigma_{m_i}^2 & 0 \\ 0 & 0 & 0 & \sigma_{\xi_i}^2 \end{bmatrix} \tag{8.38}$$

For this model it is assumed that the rate of change of the actual physical reflection parameters is slow enough that they are constant over the observation time.

$$\dot{\boldsymbol{p}} = 0 \tag{8.39}$$

Eq: Model3paramMeasModel From Eq. 8.14 the measurement model for the filter updates is

$$\hat{M}_k = h(\hat{\boldsymbol{x}}_k) = M(\hat{\boldsymbol{x}}_k) \tag{8.40}$$

The other parts of the filtering algorithms are the same as those presented in earlier chapters.

When calculating the perturbations on the parameters themselves, it is important to note that there are limits as to what values the parameters can be. Recall from Chapter 5 that the area must be positive, ξ is on the interval $[0,1]$, a is on the interval $(0,1)$, and m is restricted to $(0,1]$. In simply adding a bias or other term to these it is possible to violate these bounds. If needed, Holzinger et al. [9] provide a set of parameterizations to ensure that the domains are not violated. They define a new set of parameters, $\tilde{A}_i$, $\tilde{a}_i$, $\tilde{m}_i$, and $\tilde{\xi}_i$, that are only required to be real numbers, and they relate to the original reflection parameters through the following equations.

$$A_i = exp(\tilde{A}_i) \tag{8.41}$$

$$a_i = \frac{1}{2}\tanh \tilde{a}_i + \frac{1}{2} \tag{8.42}$$

$$m_i = \frac{1}{2}\tanh \tilde{m}_i + \frac{1}{2} \tag{8.43}$$

$$\xi_i = \frac{1}{2}\tanh \tilde{\xi}_i + \frac{1}{2} \tag{8.44}$$

8.5 Summary

This chapter proposes three alternative approaches to estimating the magnitude measurement bias than that presented by Holzinger et al. [9]. In addition, the closed-form equations for computing the partial derivatives of the magnitude measurement function with respect to the reflection parameters are given. Finally, this chapter presents the information needed to be able to fully incorporate these reflection parameter models into some sort of estimation algorithm.

CHAPTER 9

RESULTS: ATTITUDE ESTIMATION

This chapter presents the setup for all of the different test scenarios examined for estimating the attitude and angular velocity of a simulated spacecraft using the filter models from Chapter 7 and the measurement model from Chapter 5. A general overview of the chapter is as follows. First the different parameters of interest and error sources that are being investigated in this work are defined. Next the specific values and simulation parameters needed to run the tests are shown. These include the parameters common to all of the different tests as well as the specific orbit parameters needed to generate the results. After the different tests are explained, the results, major conclusions, and value of the analyses performed are presented.

9.1 Parameters of interest

In studying the performance of the different algorithms in estimating the attitude and angular velocity of the spacecraft, there are numerous variables that may affect the overall filter performance. In order to better understand how these variables can affect the ability of the filters to estimate the spacecraft attitude, multiple test scenarios are investigated in this work. The parameters of interest are:

- spacecraft orbital regime

- spacecraft spin rate

- spacecraft dynamics (controlled versus uncontrolled)

- size of the spacecraft

- number of observatories

In addition, the different levels of the initial uncertainty in the spacecraft state estimate are considered along with different levels of accuracy in the measurements.

The different parameters are discussed and explained in the following sections.

9.1.1 Orbital regime

The orbital regime used in this context describes the altitude of the orbit. For instance LEO, MEO, and GEO are examples of different orbital regimes. The goal of this research is to determine how well lightcurves can be utilized to obtain actionable information about the attitude of the spacecraft. The orbit of the object has a major effect on how well that information can be obtained.

Recall from Chapter 5 that the apparent magnitude measurement is a function of the square of the distance from the object to the observer (see Eq. 5.2). As the distance between the observer and the object increases, the dimmer the object appears to the observer. This means that objects in GEO or MEO will have a higher magnitude measurement than those in LEO (recall that dimmer objects have a larger magnitude value).

The ability to determine the attitude of spacecraft in high-altitude orbits is very desirable. Radar systems can be used to track the motion of objects in LEO, but they are expensive to use compared to electro-optical sensors [2]. Furthermore, they are limited in their use, as power constraints make them impractical for observing MEO or GEO spacecraft. However, EO sensors are already one of the more commonly used methods for tracking resident space objects in MEO or GEO, as they are able to view these objects in high-altitude orbits. Thus, investigating the ability of the estimation algorithms to estimate the attitude of a spacecraft using light curve measurements is important, as it can either become a cheaper alternative to current systems, or it can be utilized in regions where it isn't currently possible to use other methods to estimate the attitude of an uncooperative space object.

For this work the orbital regimes of interest are limited to LEO, MEO, and GEO. Transfer orbits going between these regimes are not considered. The specific test cases associated with each of the orbital regimes is shown in later sections.

9.1.2   Size of the spacecraft

As mentioned in the previous section, the different orbit altitudes affect how bright the object appears to an observer. The objects in higher altitudes are generally dimmer than those in the lower altitudes. To gain insight into just how the combined motion of the spacecraft attitude and orbit affect the apparent magnitude measurements and the estimation process, spacecraft of multiple sizes are used in the different test scenarios.

The general shape model dimensions are that of a 1U CubeSat. The dimensions of the CubeSat used are $10cm \times 10cm \times 10cm$, and the mass is 1.33 kg. This same shape model is used for test cases in LEO, MEO, and GEO. However, a second and a third shape model are used for additional test cases in MEO and GEO, respectively. These models are scaled up in area and volume such that if the same observation angles were used, the scaled-up version of the satellite would give the same measurements as the regular 1U CubeSat model in LEO. Furthermore, their mass is also scaled up so that the perturbations affecting the spacecraft would be more like that of a real-world satellite at that size.

From Eq. 5.6 the flux contributions to the apparent magnitude measurement due to the distance of the observer to the spacecraft and due to the shape model area (assuming the same area for each facet, which is true for a cube), simplify to

$$\frac{A}{\boldsymbol{v}_r^T \boldsymbol{v}_r} \tag{9.1}$$

with $\boldsymbol{v}_r$ being the vector from the spacecraft to the observatory.

The scaled value of the area can be found in the following manner.

$$A_2 = \left(\frac{A_1}{\boldsymbol{v}_{r,1}^T \boldsymbol{v}_{r,1}} \right) (\boldsymbol{v}_{r,2}^T \boldsymbol{v}_{r,2}) \tag{9.2}$$

Scaling the area in this manner allows for the same contribution to the measurement for different orbit altitudes.

9.1.3   Spacecraft spin rate

The speed and directions in which an object is spinning can greatly affect the results of an estimation process. Two vectors or 3 rotation/Euler angles are required to be able to fully define an attitude state. If an object were rotating such that only a single facet was continually visible to the observer, it follows that there wouldn't be enough information to fully define the attitude of the object, as there would be no information as to the directions of the other facets. There wouldn't be sufficient information to determine how the object would rotate about the axis pointed at the observer.

Similarly, if a spacecraft were to rotate in such a manner that all of its facets were visible to the observer over some observation time, then it would follow that there would be more information available from which the full attitude and rotation rates could be determined.

To determine the degree to which the spin rate affects the attitude estimation process, three different spin rates are used in the different test cases: A fast-spinning spacecraft that is spinning along all three axes to reveal multiple facets; a nadir-pointing, or slow-spinning spacecraft; and a spacecraft that is maintaining an inertially fixed attitude. These separate cases of the spin rates are used in the different tests to determine the attitude of the spacecraft. However, as the inertially fixed attitude would require some degree of control on the part of the spacecraft, it is used only in conjunction with the controlled dynamics, while the fast-spinning and slow-spinning cases are examined with both the controlled and uncontrolled dynamics.

9.1.4   Controlled or uncontrolled dynamics

Another variable is the rotational dynamics of the spacecraft. As has been discussed in previous chapters, there are two types of dynamics being used to model the rotational motion of the spacecraft. The first is the case where the spacecraft is controlling its own attitude, and the second case is where the spacecraft is tumbling freely due to the disturbance torques affecting it. More information about how the dynamics affect the estimation algorithms can be found in Chapter 7. For all but the inertially fixed spacecraft cases, the different tests are

performed twice, once with the controlled dynamics models, and once with the uncontrolled dynamics models.

9.1.5 Number of observatories

A final parameter is the number of observatories being used to obtain measurements. Specifically, each test case will be performed using either one or two observatories. This analysis is being done because, depending on the locations of the observatories, it is possible that the spacecraft can be viewed at different angles, resulting in different facets being visible. This may result in an improved estimate of the spacecraft attitude. Unlike previous work by the author [62] [63] where the measurements from multiple observatories were mostly simultaneous, this analysis will focus on the cases with measurements from the two sites taken at different times.

9.2 Error sources

In addition to the different parameters that are being varied for the test cases, other major factors impacting the performance of the estimation algorithms are the error sources included in the setup of the different test scenarios. The purpose of this section is to define the different error sources and explain how they are incorporated into the estimation process.

The different error sources considered for the different test cases consist of the following.

- initial uncertainty in the knowledge of the state parameters

  - position vector uncertainty

  - velocity vector uncertainty

  - attitude state uncertainty

  - angular velocity state uncertainty

- measurement noise

- attitude dispersion due to control system errors (controlled cases only)

- process noise applied during integration to represent the unmodeled torques (uncontrolled cases)

Each of these error sources is discussed in greater detail in the following sections.

9.2.1 State uncertainties

The state errors are the errors associated with the state variables, due to the fact that they aren't known perfectly in real-world applications. Here the state variables that can contribute to the uncertainties in the estimation process consist of the orbital position and velocity of the spacecraft and the uncertainty of the attitude states and angular velocity.

In this work, it is assumed that the orbital position and velocity of the spacecraft are known to the extent that the error contributions of these variables are negligible. The orbital parameters are not being estimated as states in the estimation algorithm. They are assumed known.

While the errors in the position and velocity vectors are not considered, the uncertainties associated with the attitude and angular velocity are a major factor in the analyses performed here. The initial attitude and angular velocity knowledge error is specified by the respective attitude and angular velocity standard deviations. Six separate values for attitude knowledge error and two values for angular velocity knowledge error are examined. Table 9.1 lists all of the possible considered values for the initial uncertainties in the attitude and angular velocity states. This is shown ot present the possible test cases. In some instances not all of the different tests were examined because the results were very poor for a case with lower uncertainties and it did not make sense to increase the initial uncertainties. Furthermore, for the sake of brevity only, select results will be shown in this chapter.

9.2.2 Measurement noise

Another major contributor to the errors in the system is the noise of the apparent magnitude measurements. In this work the noise on the apparent magnitude measurement

Table 9.1: Possible sets of initial conditions for attitude states

	$\sigma_\theta = 3°$	$\sigma_\theta = 5°$	$\sigma_\theta = 10°$	$\sigma_\theta = 20°$	$\sigma_\theta = 30°$g	$\sigma_\theta = 60°$
$\sigma_\omega = 0.02$ deg/s						
$\sigma_\omega = 0.2$ deg/s						

is modeled as a function of measured magnitude. A percentage of the measurement is taken and then is used to apply noise to the measurement:

$$R_k = (\frac{M_k r_{percent}}{3})^2 \tag{9.3}$$

where $r_{percent}$ is the desired percentage of the magnitude.

The reasons for applying the measurement noise in this way are, first, that the photometric noise isn't usually time invariant [22]; the noise can even vary between successive frames of the same object [64]. Second, for some of the measurement error sources, the error in magnitude decreases with a stronger signal or a brighter object [65]. This approach to modeling the measurement noise in this manner accounts for the variability in the magnitude measurement. Note that this noise model is intended to be a simplifying assumption; more complex models generally take place at the radiometric level and require more information about the EO sensor and locations where the measurements are taking place [22]. This percentage-based measurement model is deemed sufficient for the purposes of this dissertation.

Two different percentage levels are used for the value of $r_{percent}$: 1% and 10%.

9.2.3   Attitude control system error

The error in the attitude control system is another source of error for the controlled cases. The manner in which this error is applied to the different filters is discussed in detail in Chapter 7. For all of the different controlled cases, the error in the control system has a standard deviation of 0.1 degrees.

9.2.4 Dynamics process noise

The process noise is used in the cases with uncontrolled dynamics and is meant to account for any modeling errors in the torques acting on the spacecraft. The manner in which the process noise is incorporated into these filters is also shown in Chapter 7. The actual value used for the process noise was set for each of the different orbital regimes and the size of the shape model used. For the LEO cases, the process noise was sized to give 2 degrees of error in the attitude state after one orbit; for the MEO cases, the process noise gives 10 degrees of error after one orbit; and for the GEO cases, the noise was sized to give 15 degrees of error after one orbit. The MEO and GEO values are much larger due to their orbital periods being much larger than that of the LEO test cases.

9.3 Test cases setup

The purpose of this section is to present all of the specific test cases that were examined. As numerous tests were performed with many varying parameters, it is first essential to define some items that are common to all of the different test setups. These are explained in the following section.

9.3.1 General test setup

There are some items that are common to all of the different test cases. These are presented here so that they do not need to be shown for all of the individual test cases. The first commonality between all of the different tests is the reflection parameters on the shape model used, or rather all of the reflection parameters except the area, as that varies. All of the different test scenarios utilize a cubic shape model with the reflection parameters given in Table 9.2

In each of the different orbital regimes, tests were performed where the shape model is assumed to be a 1U CubeSat, and the area for all of the different facets for this case were set to 0.01 m^2. The MEO and GEO tests also had additional runs with a shape model with increased facet areas to provide insight into the effects of processing brighter

Table 9.2: Shape model reflection parameters

Axis	ξ	a	m
+X	0.1	0.95	0.04
-X	0.5	0.95	0.08
+Y	0.1	0.5	0.5
-Y	0.5	0.8	0.5
+Z	0.1	0.7	0.4
-Z	1	0.95	0.6

measurements. These scaled shape models are presented later when discussing the specific test setups related to MEO and GEO spacecraft.

The shape parameters shown in table 9.2 are an idealized set of shape parameters. The axis refers to the direction of the facet normal in the spacecraft body frame. The values were selected so that each facet would yield a distinct apparent magnitude measurement when the facet normal was aligned with the bisector (giving the greatest specular reflection).

For each of the different test cases, the total measurement time is 360 seconds, with measurements taken every 5 seconds during the measurement times. Any instances in which the timing differs from this will be noted in the individual case. In addition, the epoch for all of the different test cases was set to 8 hours, 8 minutes, and 40 seconds on March 1, 2020, UTC. For each test setup, the results from a single site are presented first, followed by the results from two observatories. The timing of the different sites, and which sites are used, will be presented on a case-by-case basis.

There are two types of analyses performed for all of the different tests. The first is a single run where the performance of all of the different filters is compared, and the second is where a Monte Carlo–type approach is taken to determine if the EKF and UKF are even viable options for the specific test. In each of the cases, the truth model is specified beforehand, and the filter estimates are defined based on the initial uncertainties in the state variables. To better provide consistent results, all of the filters were initialized to the same values for the state estimates.

The filters were tuned only once for a given test setup. For an example, all of the LEO fast-spinning, controlled dynamics, single-observatory cases had the same tuning for the filters. However, if the dynamics, spin conditions, or number of observatories changed, then the filters (mainly the BPF, which was tuned by adjusting the particle roughening parameter, $\mathcal{G}$,) would have to be retuned. The tuning was performed using a low initial uncertainty case and a larger initial uncertainty case, so that the filter performance would be robust for the different levels of uncertainty in the initial conditions. Unless explicitly stated otherwise, all of the BPF results presented here were computed using 10,000 particles.

In carrying out this research it was observed that the filter initial conditions had a major effect on the performance of the overall estimation. This was especially true for the EKF and UKF. To determine how effective these filters are for a given test setup, a Monte Carlo approach is used. For the specific test cases, the filters are run 100 times with the initial conditions and the measurement noise varying in the same manner as for the single-run tests. At the end of the simulation time, a count is taken of the samples where the final error is larger than the 3σ covariance bound.

The different tests are grouped primarily by orbital regime. Then they are further broken down by spin rate, controlled versus uncontrolled dynamics, and number of observatories.

9.3.2 Metrics for evaluating filter performance

The purpose of this section is to define the criteria, or the metrics, which are used to evaluate the filter performance for different scenarios (orbital regime, spin rate, etc).

True error and covariance bounds

As all of the results here are done in simulation, the truth model is known. The true error is the difference between the truth model and the mean estimate from the filter at the same instances in time. For the attitude state, the error between the quaternion and true estimate is calculated in the following manner.

$$\delta \boldsymbol{q}_\epsilon = \boldsymbol{q}_{I \to b} \otimes \hat{\boldsymbol{q}}_{I \to b} \tag{9.4}$$

The error is then converted to an error vector by extracting the axis and angle from the quaternion (see Eq. 3.15) and then multiplying them together.

$$\boldsymbol{\theta}_\epsilon = \theta_\epsilon \hat{\boldsymbol{e}} \tag{9.5}$$

This vector comprises the individual errors of the different states.

$$\boldsymbol{\theta}_\epsilon = \begin{bmatrix} \epsilon_{\theta_x} \\ \epsilon_{\theta_y} \\ \epsilon_{\theta_z} \end{bmatrix} \tag{9.6}$$

The error in the angular velocity is the difference between the true angular velocity and the mean estimate of the angular velocity.

$$\boldsymbol{\omega}_\epsilon^b = \boldsymbol{\omega}^b - \hat{\boldsymbol{\omega}}^b \tag{9.7}$$

$$\boldsymbol{\omega}_\epsilon^b = \begin{bmatrix} \epsilon_{\omega_x} \\ \epsilon_{\omega_y} \\ \epsilon_{\omega_z} \end{bmatrix} \tag{9.8}$$

The 3σ covariance bounds are plotted along with the calculated state errors. These are found by taking the square root of the diagonal elements of the covariance matrix output by the different filters. This approach to calculating the error gives the error and covariance bounds for each of the individual components of the state. For the attitude and angular velocity, this results in six separate plots of the error. This true error and the covariance bounds are the criteria used to evaluate the filter performance for both the single-run cases and for the Monte Carlo runs.

Root sum squared error and covariance

In addition to the individual component error and covariance bounds, the root sum squared (RSS) error is also computed to provide a general overview of the error value for the attitude and angular velocity states as a whole. The root sum squared error is computed using the individual error components. At each time step the RSS error is computed in the following manner for the attitude and angular velocity.

$$\epsilon_{\theta_{RSS}} = \sqrt{\epsilon_{\theta_x}^2 + \epsilon_{\theta_y}^2 + \epsilon_{\theta_z}^2} \tag{9.9}$$

$$\epsilon_{\omega_{RSS}} = \sqrt{\epsilon_{\omega_x}^2 + \epsilon_{\omega_y}^2 + \epsilon_{\omega_z}^2} \tag{9.10}$$

The σ_{RSS} is computed using the covariance matrix. It is found by taking the square root of the trace of the covariance matrix of the specific state.

$$\sigma_{RSS_\theta} = \sqrt{tr(P_\theta)} \tag{9.11}$$

$$\sigma_{RSS_\omega} = \sqrt{tr(P_\omega)} \tag{9.12}$$

For the RSS plots, the RSS error is plotted along with the $3\sigma_{RSS}$ bound.

Measurement residuals

Another method that is used to help determine the performance of the filters is looking at the measurement residuals. The residual is the difference between the measurement and the expected measurement calculated by the filter during the estimation process.

$$\boldsymbol{y}_{resid} = \tilde{\boldsymbol{y}} - \hat{\boldsymbol{y}} \tag{9.13}$$

For the UKF, the value of the mean measurement $\hat{\boldsymbol{y}}^-$ (see Eq. 7.76), as opposed to the measurements from each of the sigma points, is used in Eq. 9.13 to calculate the residual, as that gives the same residual as what is used in the update portion of the filter. For the BPF, the residuals that are plotted are the expected measurements from each of the different particles at the given time.

Accompanying the value of the residuals on the plots is the 3σ value of the measurement noise at the given time. This is done to illustrate how close the expected measurement is to the actual measurement.

Measurement plots

While not necessarily used to evaluate the filter performance, another plot that is presented with the results is a plot of the measurements, or the light curve, for the given observation times. In these plots the true measurement, computed using the truth model, is plotted as a solid line. The noisy measurements, the ones that are used for the filter updates, are plotted at the same time steps as discrete points.

Plot colors

Again, while not a metric that is used to measure filter performance, the colors used on the plots are consistent for the different cases so that the results can be evaluated quickly. The results from each of the different filters are plotted with separate colors for the covariance bounds. The EKF results are blue, the UKF results are green, and the BPF results are magenta. Cases differing from this have an accompanying legend or explanation for clarity.

9.3.3   LEO tests

This section presents all of the different test cases for the LEO spacecraft. For all of the tests the spacecraft had the same orbit and observatories collecting measurements. The Keplerian orbital elements of the spacecraft at the given epoch are semi-major axis $a = 6871.14$ km, eccentricity $e = 0.01$, inclination $i = 83°$, right ascension of the ascending node

$\Omega = 0°$, argument of perigee $\omega = 0°$, and true anomaly $\nu = 126.264°$. Figure 9.1 provides an illustration of the spacecraft ground track and the location of the two observatories.
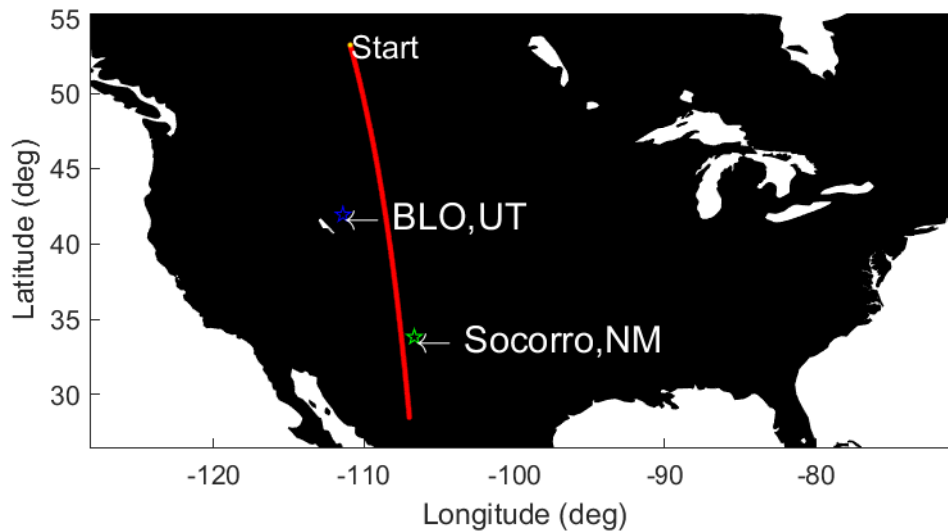
Fig. 9.1: Ground track of LEO satellite and observatory locations

The two observatories used in the LEO test cases are Socorro, New Mexico (NM), and the Bear Lake Observatory (BLO) located near Garden City, Utah (UT). The Utah State University Space Situational Awareness Telescope for Astrodynamics Research (USU-STAR) housed at USU's Bear Lake Observatory is a newly constructed (as of 2016) EO telescope built with the intent to observe RSOs. It is maintained and operated by Utah State University. (The author assisted in the setup and operation of this telescope.) Socorro, New Mexico, is one of the locations of the Ground-based Electro-Optical Deep Space Surveillance (GEODSS) network, which is used to observe resident space objects. The latitude, longitude, and altitude used for these two sites are shown in Table 9.3.

Table 9.3: LEO test cases observatory locations

Name	Latitude (deg)	Longitude (deg)	Altitude (m)
Socorro, NM	33.8173	-106.66	1500
BLO, UT	41.93	-111.4	1815

For the single-site test cases, Socorro, NM, was the only observatory collecting the measurements. Both observatories were used for the two-site cases. The tasking of the different sites in collecting observations of the spacecraft is another parameter that was varied, and the specific timing of the measurements with the two will be presented on a case-by-case basis.

As mentioned previously, there were three different spin rates examined in the LEO spacecraft test cases. These are the fast-spinning, nadir-pointing, and inertially fixed spacecraft. With the fast-spinning and nadir-pointing spacecraft, cases with both the controlled and uncontrolled dynamics were examined. However, only the controlled dynamics were used for the inertially fixed spacecraft.

For the fast-spinning spacecraft, the initial attitude is set so that the bisector for the +X facet is initially aligned with the observatory at Socorro, NM, and the +Z facet is aligned as closely as possible with the angular momentum vector of the orbit. The initial conditions for the attitude can be expressed as a 3-2-1 Euler angle sequence with the angles $\phi = -42.4122°$, $\theta = 59.1601°$, and $\psi = 48.9897°$. The values for the initial angular velocity are $\boldsymbol{\omega}^b = [2 \quad 1 \quad 3.6]^T$ deg/s.

For the nadir-pointing, or slow-spinning case, the spacecraft's initial orientation was set to where the +Z axis was aligned with the position vector, resulting in the -Z axis nadir pointing, and +Y axis was aligned with the orbit angular momentum vector. The +X axis pointed in the along-track direction to complete the triad. The 3-2-1 Euler angle sequence for this initial attitude state is $\phi = -174.911°$, $\theta = 35.9513°$, and $\psi = 8.6586°$. The angular velocity was set so that the spacecraft rotated about the body +Y axis at the rate of the orbital mean motion to maintain the nadir-pointing orientation. The initial angular velocity vector was set to $[0 \quad 0.0635 \quad 0]^T$ deg/s.

For the inertially fixed cases, the angular velocity is set to $[0 \quad 0 \quad 0]^T$. To better understand if there was an impact on the results based on the initial conditions used, tests were performed using three different initial attitude states called LIIC1, LIIC2, and LIIC3. (LIIC stands for LEO inertial initial condition). These three sets of initial conditions are the the initial conditions for the fast-spinning cases (LIIC1), the initial attitude states for the nadir-pointing spacecraft (LIIC2), and the final set is where the body frame was set to align with the ECI frame at the given epoch (LIIC3). This was done to investigate the effects of the initial conditions on the performance of the filters for the inertially-fixed test cases.

With each of these different test cases the parameters were varied in the manner explained in the previous sections.

9.3.4 MEO tests

This section presents all of the different test cases and results for the MEO spacecraft. Throughtout all of the different test scenarios, the spacecraft had the same orbit. The Keplerian orbital elements of the spacecraft at the given epoch are semi-major axis $a = 26378.14$ km, eccentricity $e = 0.$, inclination $i = 89°$, right ascension of the ascending node $\Omega = 179°$, argument of perigee $\omega = 0°$, and true anomaly $\nu = 39.511°$. The MEO cases are carried out using the same two observatories as the LEO cases. These are Socorro, NM, and BLO, UT. The locations of these observatories are shown in Table 9.3. Figure 9.2 shows the ground track of the spacecraft and the location of these observatories.

For the MEO spacecraft the different tests were performed twice. First they were performed with the same CubeSat shape model used for generating the LEO results, and then again with a shape model with the facet area scaled up so that the measurements can be as bright as the CubeSat in LEO.

For the fast-spinning cases, the MEO spacecraft was oriented such that the +X facet was aligned with the bisector between the satellite-to-observatory vector for Socorro, NM, and the satellite-to-Sun vector. The -Z body axis was set to align as closely as possible to the orbital-specific angular momentum vector. The 3-2-1 Euler angles that define the initial
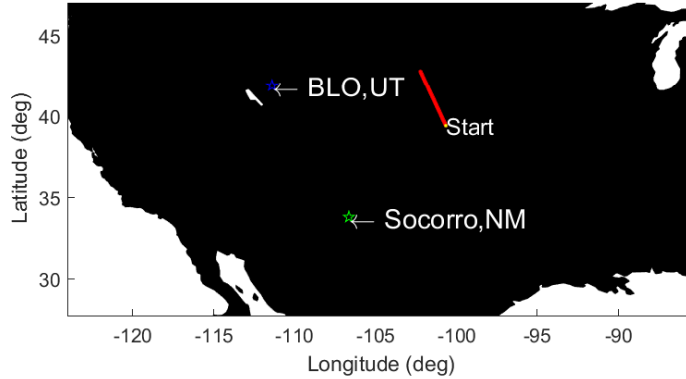
Fig. 9.2: Ground track of MEO satellite and observatory locations

state are $\phi = -8.8009°$, $\theta = 24.7231°$, and $\psi = 92.7882°$. The values for the initial angular velocity are the same as for the LEO fast-spinning case: $\boldsymbol{\omega}^b = \begin{bmatrix} 2 & 1 & 3.6 \end{bmatrix}^T$ deg/s.

With the nadir-pointing test cases it was observed that the higher altitude orbits were much more sensitive to the attitude initial conditions than for the LEO case. For this reason, three different sets of initial conditions were examined to determine their effect on the spacecraft attitude estimation. The first case, MEO IC1, had the +Z facet aligned with the position vector so that the -Z facet was nadir pointing, and the +Y axis was aligned with the LVLH cross-track direction. The +X axis was used to complete the triad. The initial 3-2-1 Euler angles for this initial orientation was $\phi = -1.2134°$, $\theta = -50.4784°$, and $\psi = 1.5715°$. The angular velocity for the nadir was set so that the spacecraft attitude rotated about the body +Y axis at the same rate as the orbital mean motion: $\boldsymbol{\omega}^b = \begin{bmatrix} 0 & 0.0084 & 0 \end{bmatrix}^T$ deg/s.

The second set of initial conditions for the nadir-pointing spacecraft, MEO IC2, had the +X axis nadir pointing, the +Y body axis aligned with the LVLH cross-track direction, and the +Z completing the triad. In this case the initial angular velocity was set to the same value as that of the MEO IC1. The 3-2-1 Euler angle sequence for this initial attitude is $\phi = 0.8236°$, $\theta = 39.5038°$, and $\psi = 1.2961°$.

The final set of initial conditions, MEO IC3, is again where the ECI frame and body frame are aligned at the observation epoch. With this setup, the MEO spacecraft wasn't exactly nadir pointing, but rather the angular velocity was set up so that the vector magnitude was the same as the orbital mean motion, and the direction of the rotation was about the angular momentum vector expressed in the body frame at the observation epoch. This case was more of a slow-rotation case rather than a true nadir-pointing case. The angular velocity vector was set to $\omega^b = [1.473 \times 10^{-7} \quad 0.0084 \quad 0.000147]^T$ deg/s.

Like what was done with the LEO test cases, with the MEO spacecraft inertial test cases three sets of initial conditions were also examined. The first set was for the same initial conditions as the fast-spinning spacecraft. This was done to provide an example where the satellite reflects specularly like with MEO IC2. The second set of initial conditions had the body frame equal to the ECI coordinate frame in order to provide an intermediate case, and the final set of initial conditions was the same as MEO IC1 which is where the reflection is mostly diffuse. As all of these cases were inertially fixed, the angular velocity was set to 0 for all of the components.

9.3.5 GEO tests

In this section the setup for the GEO spacecraft test cases is presented. For all of the different tests, the spacecraft had the same orbit. For this case, the initial orbit is defined by the position and velocity vectors. At the epoch the position vector is $r^I = [-35529.95 \quad 23098.15 \quad 68.34]^T$ km, and the velocity vector is $r^I = [-1.672 \quad -2.571 \quad 0.0032]^T$ km/s. As the GEO is at a much higher altitude than the other orbits, observatories with a larger baseline distance between them were used for this analysis. These observatories were Socorro, NM, as before, but the second observatory is Maui, Hawaii (HI). The latitude, longitude, and altitude data used for these sites are shown in Table 9.4, and the figure showing the spacecraft ground track and the observatory locations is Fig. 9.3.

As is to be expected for a GEO spacecraft, the ground track in this instance isn't a line like for the MEO and LEO cases, but rather, it maintains the same orientation relative to the observatories throughout the observation time. As with the MEO spacecraft, a scaled

Table 9.4: GEO test cases observatory locations

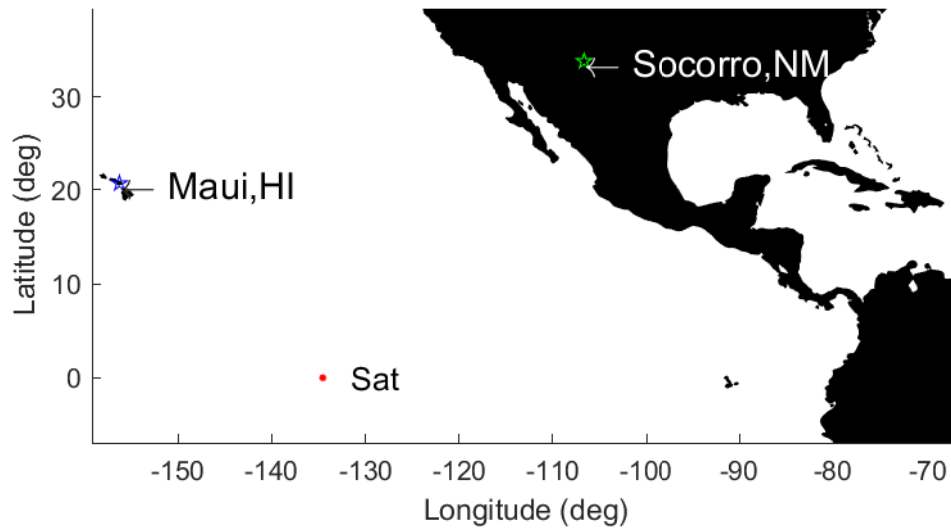| Name	Latitude (Deg)	Longitude (Deg)	Altitude (m)
Socorro, NM	33.8173	-106.66	1500
Maui, HI	20.7081	-156.257	3059

Fig. 9.3: Ground track of GEO satellite and observatory locations

shape model is also used for all of the different test cases in GEO along with the CubeSat model used in all three orbital regimes.

As before there are three different spin rates with different initial conditions that need to be defined for the GEO spacecraft. Again, these are the fast-spinning spacecraft; the nadir-pointing, or slow-spinning spacecraft; and the inertially fixed GEO spacecraft. For the fast-spinning spacecraft the initial orientation was set such that the body +X facet normal vector was aligned with the bisector between the vector from the spacecraft to the observatory at Socorro, NM, and the spacecraft-to-Sun vector. The attitude is further defined by the body +Z facet normal aligning with the orbital angular momentum as closely as possible. The rotation rate for the fast-spinning cases was the same as for the LEO and MEO fast-spinning cases, and the 3-2-1 Euler angle sequence for the initial attitude is $\phi = -27.2326°$, $\theta = 1.1295°$, and $\psi = -0.050061°$.

As was explained with the MEO test setup, the attitude estimation for the slow-spinning/nadir cases were sensitive to the attitude initial conditions. Thus, for the GEO slow-spinning/nadir case there were three sets of initial conditions used, which are called GEO IC1, GEO IC2, and GEO IC3. The first set of initial conditions has the +Z vector aligned with the spacecraft radial position vector, the +Y axis is aligned with the LVLH cross-track direction, and the +X axis is used to complete the triad. The initial Euler angle sequence (all Euler angle sequences in this section are 3-2-1 sequences) is $\phi = -123.03°$, $\theta = -0.05969°$, and $\psi = 89.908°$. The rotation rate for this case is again the orbital mean motion about the +Y body vector which gives $\boldsymbol{\omega}^b = \begin{bmatrix} 0 & 0.0041465 & 0 \end{bmatrix}^T$ deg/s.

GEO IC2 has the spacecraft oriented so that the +X axis is nadir pointing and the +Y axis is aligned with the LVLH cross-track direction. The rotation rate is the same as for GEO IC1, and the the Euler angle sequence to initialize the spacecraft to this attitude is $\phi = -33.028°$, $\theta = 0.092397°$, and $\psi = 89.94°$.

The final set of initial conditions for the slow-spinning/nadir-pointing cases has the +Y axis aligned with the radial direction (meaning the -Y axis is nadir pointing), the +Z axis is aligned with the cross-track direction, and the +X axis is used to complete the triad.

For this case the magnitude of the angular velocity vector is the same, but the rotation is about the +Z axis instead of the +Y axis. The Euler angle sequence to define the initial attitude is $\phi = 56.972°$, $\theta = 0.05969°$, and $\psi = 0.092397°$.

As with the MEO test cases, the inertial cases with the GEO spacecraft also examined three sets of initial conditions. The first set is the same as the fast-spinning case, the second set was the same as GEO IC2, and the third set of initial conditions was where the body frame was set equal to the ECI frame.

For the sake of brevity, the results from all of these numerous test cases are not presented in this work. Rather, the general conclusions that were obtained from examining all of these different cases are presented along with select results that provide good examples of the conclusions being shown.

9.4   Results and conclusions

As the previous section makes clear, numerous tests with varying parameters were performed in order to get a better understanding of the conditions affecting the performance of the different filters in estimating the attitude and angular velocity of a spacecraft. The purpose of this section is to summarize these numerous test cases and present the conclusions drawn from analyzing the results of the individual tests. The main conclusions from this analysis are summed up in the following list.

- Of the three filters examined, the BPF is the most robust in estimating the attitude of the spacecraft but it is often not as accurate as the UKF for cases of low initial uncertainty.

- The EKF and UKF are not suitable for this application for initial attitude uncertainty larger $\sigma_\theta > 10°$.

- Higher accuracy attitude estimates are more readily obtained in LEO than in MEO or GEO.

- Better attitude estimates are generally obtained with the faster spinning spacecraft.

- A second observatory offers significant improvement in attitude estimation for the slow-spinning cases but not the fast-spinning cases.

- The difference in dynamics between the controlled and uncontrolled dynamics cases produced a difference in the performance of the filters and light curve measurements only for the fast-spinning spacecraft.

- Scaling the size of the GEO spacecraft produced markedly different results only for the cases with larger uncertainty in the measurements.

This list constitutes a brief overview of the main conclusions of all the different test case results. To relate this list back to the parameters of interest, these different conclusions can be grouped in the following categories: filter type (EKF,UKF,and BPF), the effects of the orbital regime, the effects of the spacecraft spin rate, number of observatories, and the effects of the different dynamics models. The following sections expand upon these conclusions and present the supporting results which led to their formulation.

9.4.1 Filter performance

The purpose of this section is to present the results and conclusions obtained related to the performance of the three different filters in estimating the attitude of the spacecraft using light curve measurements. Recall that these three filters are the bootstrap particle filter (BPF), the unscented Kalman filter (UKF), and the extended Kalman filter (EKF). Note that in this chapter these filters are the versions presented in Chapter 7. This means that here EKF can be used interchangeably with the MEKF of the Chapter 7. As was stated in the previous section, the BPF is the most robust of the filters, but sometimes at the cost of accuracy for cases with low initial uncertainty. The UKF is often more accurate for these cases, but the UKF starts to break down when the initial uncertainty in the attitude grows larger than $\sigma_\theta = 10°$. The EKF is generally not the best choice for this application.

To begin it is first necessary to establish the methods in which the filter performance was evaluated. For the EKF and the UKF the Monte Carlo runs are used to determine whether the filter is a viable option for a given test case setup. The EKF and UKF did

poorly in the nadir-pointing and inertially fixed test cases for all levels of initial uncertainty in the attitude. Thus, the Monte Carlo results are not shown for these test cases. However, with the fast spinning cases the results varied with the different test parameters. The Monte Carlo runs were performed for the fast-spinning cases with the levels of initial uncertainty presented in Table 9.1 and for the cases where the measurement noise is calculated based on either 1% or 10% of the measurement value.Additional single-run results will be confined to those of the BPF. Note that the BPF is a Monte Carlo–type estimation algorithm, so it was not included in the Monte Carlo analysis of the EKF and UKF, but its filter performance is determined instead from the individual filter run for the specific test setup.

A summary of the Monte Carlo results is presented in Fig. 9.4, with the results for the other test cases shown in Appendix B. The example shown is for the fast-spinning LEO spacecraft. The colors of the boxes correspond to the number of Monte Carlo samples that finished with the error larger than the 3σ covariance bounds. The red boxes correspond to the runs where more than ten samples were outside of the covariance bounds for any of the six state components.The green boxes are the cases where there were fewer than five samples that left the covariance bounds for the majority of the state variables. The yellow boxes are an intermediate case. They correspond to the instances where any component has six to nine samples leave the covariance bound. In addition, if there are two or more components with exactly five samples that left the covariance bounds the box is colored yellow. The gray squares are where the tests weren't run, as both filters had already performed poorly at a lower level of initial uncertainty.

From the Monte Carlo results shown here and in the appendix, it is apparent that the EKF is generally not a very reliable choice for this application. The UKF tends to do better in most cases, although it fails in its reliability when the initial attitude uncertainty grows larger than $10°$ 1σ, or even before that in some cases. However, this does not mean that there is no merit in using the UKF in estimating the attitude of the spacecraft using light curve measurements. It often performed better than the other filters in the cases of low initial state uncertainty.

| | $r_{percent}$ | Single Observatory | | | | | | Two Observatories | | | | | |
| | | $\sigma_\theta = 3°$ | | $\sigma_\theta = 5°$ | | $\sigma_\theta = 10°$ | | $\sigma_\theta = 3°$ | | $\sigma_\theta = 5°$ | | $\sigma_\theta = 10°$ | |
		EKF	UKF	EKF	UKF	EKF	UKF	EKF	UKF	EKF	UKF	EKF	UKF
Controlled $\sigma_\omega = 0.02\frac{deg}{s}$	1%												
	10%												
Controlled $\sigma_\omega = 0.2\frac{deg}{s}$	1%												
	10%												
Uncontrolled $\sigma_\omega = 0.02\frac{deg}{s}$	1%												
	10%												
Uncontrolled $\sigma_\omega = 0.2\frac{deg}{s}$	1%												
	10%												

Fig. 9.4: Error counts summary of Monte Carlo results from fast-spinning LEO spacecraft

Figure 9.5 presents a direct comparison of the performance of the different filters. The results shown are for the controlled, fast-spinning LEO spacecraft with $\sigma_\omega = 0.02$ deg/s and $r_{percent} = 1\%$. Figures 9.5a and 9.5b are the results for the test case where the initial uncertainty in the attitude was set to $\sigma_\theta = 3°$. Note that the referenced figure shows only the RSS attitude and angular velocity plots. In this case these plots provide an overview of the filter performance as a whole. For each of the different test cases, all of the different metrics presented in section 9.3.2 were computed. However, for the sake of brevity, only the RSS values will be shown for the different test cases unless the individual result plots reveal information that cannot be readily determined from the RSS results. An example of this would be the case where only one or two of the angle components remain consistent while the error increases for the other angles.

For the results shown in Fig. 9.5 the seed in this instance was such that all three filters were able to converge. From these two figures it can be seen that the BPF had a larger covariance bound than both the EKF and UKF. This is due to the particle roughening increasing the uncertainty in the BPF at each time step. However, this added step helps to make the BPF more robust. This is apparent in the remaining parts of the figure.
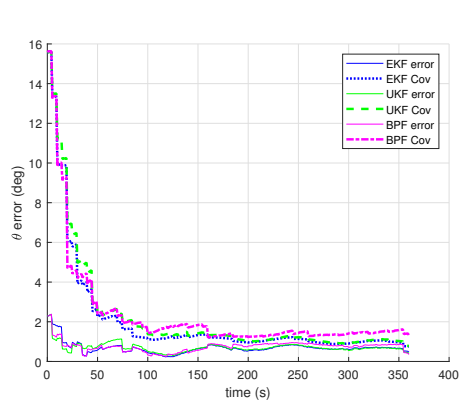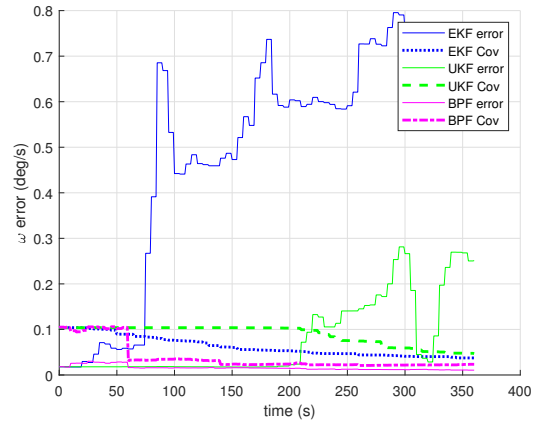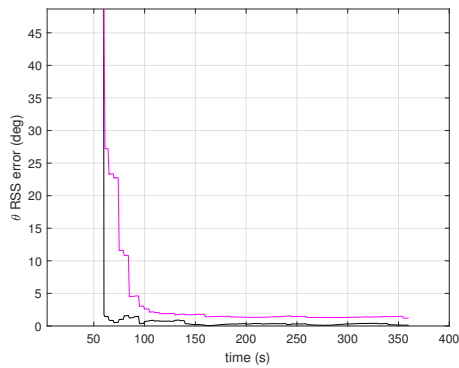
(a) RSS attitude results, $\sigma_\theta = 3°$
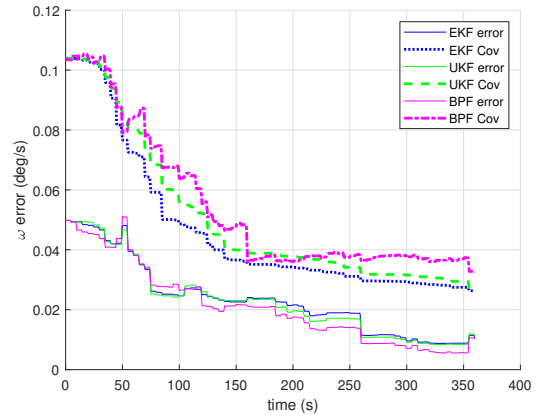
(b) RSS angular velocity results, $\sigma_\theta = 3°$
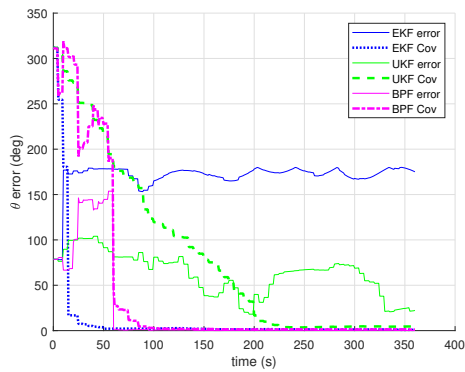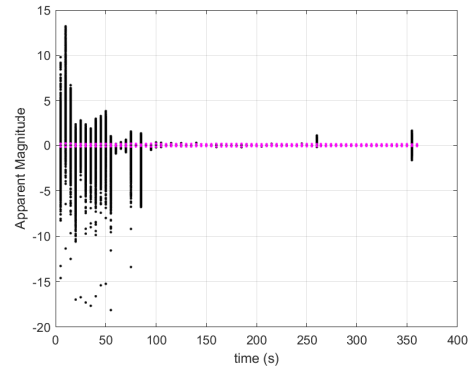
(c) RSS attitude results, $\sigma_\theta = 60°$

(d) RSS angular velocity results, $\sigma_\theta = 60°$

(e) Zoomed-in BPF RSS attitude results

(f) BPF measurement residuals $\sigma_\theta = 60°$

Fig. 9.5: Filter Comparison for the fast-spinning LEO spacecraft with $\sigma_\omega = 0.02$ deg/s and $r_{percent} = 1\%$

Figures 9.5c and 9.5d present the results for the case where $\sigma_\theta = 60°$. This case represents the worst-case initial uncertainty for estimating the attitude of a spacecraft. In this instance the EKF and UKF both diverged. The BPF, however, was still able to accurately estimate the spacecraft attitude and angular velocity. A good estimate of the angular velocity is necessary to obtain a good estimate of the attitude. In later figures only the attitude will be shown to demonstrate the performance and accuracy of the filters. Figure 9.5e shows the zoomed-in BPF attitude results from Fig. 9.5c, and Fig. 9.5f shows the residuals of the particle states illustrating how the BPF was able to converge. These figures illustrate that in this case the BPF was able to obtain a very accurate estimate of the spacecraft attitude even in cases with large uncertainty in the initial estimate of the spacecraft attitude.

To gain some insight into the reasoning behind why the BPF performed well when the EKF and UKF both diverged, the plots of the particle distributions over time are presented in Fig. 9.6. For the attitude states, it is difficult to interpret the components of the quaternion, especially as an attitude is not uniquely represented by a single quaternion. Thus, to provide more insight into the particle distribution, the attitude distributions shown in Fig. 9.6 are the error rotation vectors between the truth state and the individual particle attitude quaternions at the given time step. For these plots, 0 is where the truth state would lie. The angular velocity plots are the actual distributions of the particles' angular velocity components. The angular velocity components of the truth state are shown with the thick black line.

It can be seen, especially from examining the attitude components of 9.6, that there are occasions in which the particles are distributed in different groups. This is showing instances where the distribution is multimodal (this may also inflate the covariance estimate of the BPF over the other filters). As more information is received, the distribution converges. Both the EKF and UKF are not well-suited for cases where the underlying distribution is multimodal. Furthermore, it is possible that the uncertainty is just too large for the filters to be able to converge, so only the BPF was effective for these levels of uncertainty in the
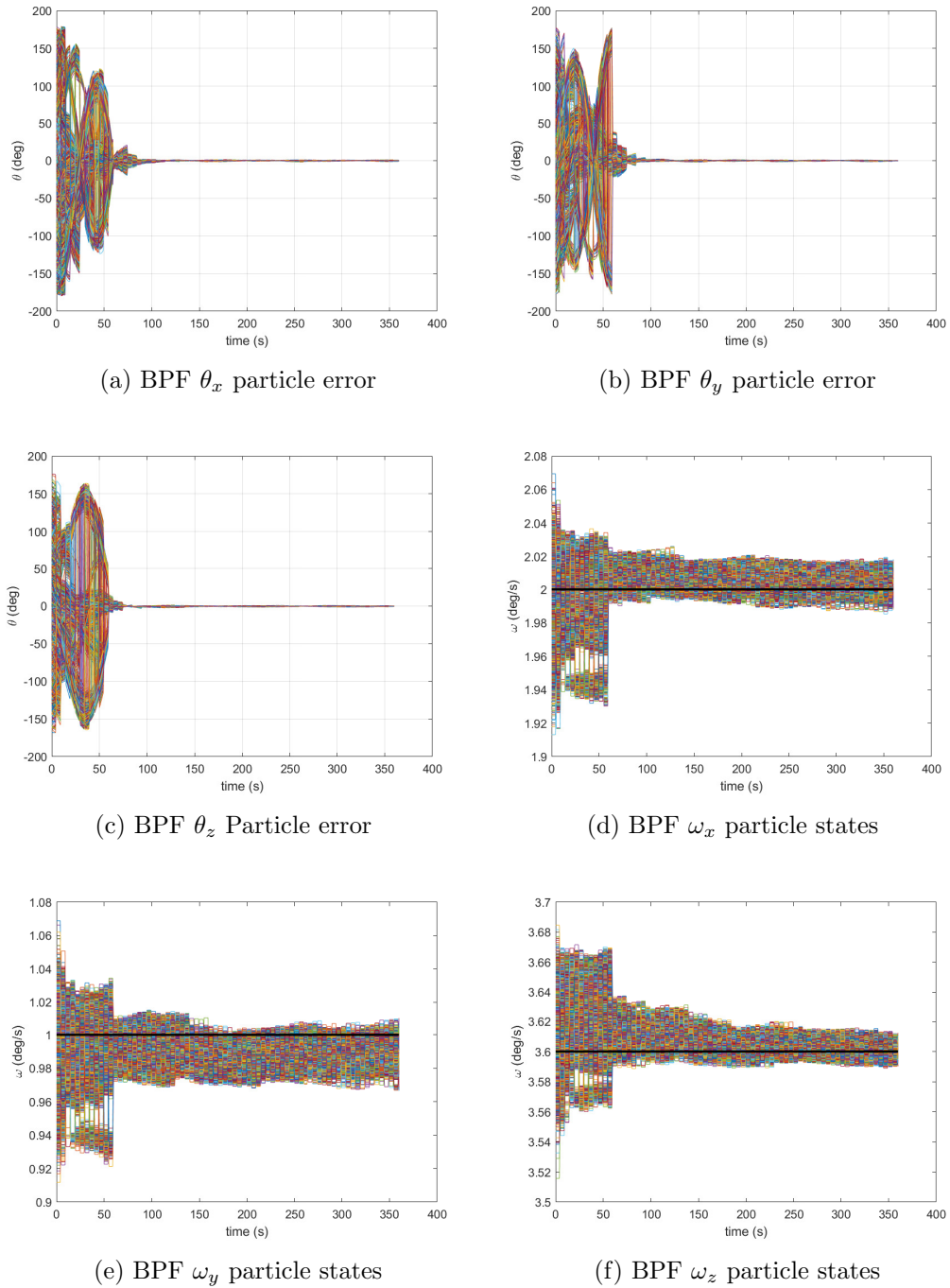
(a) BPF θ_x particle error

(b) BPF θ_y particle error

(c) BPF θ_z Particle error

(d) BPF ω_x particle states

(e) BPF ω_y particle states

(f) BPF ω_z particle states

Fig. 9.6: BPF results for the fast-spinning LEO spacecraft with $\sigma_\omega = 0.02$ (deg/s), $\sigma_\theta = 60°$, and $r_{percent} = 1\%$

initial conditions.

It is important to note, however, that the BPF was not able to estimate the attitude of the spacecraft to this extent for the given level of state uncertainties for all of the different test cases. It is generally more robust than the other filters. However, in many instances none of the filters were able to obtain a good estimate of the attitude after the completion of the observation time. Some of these cases are discussed in greater detail in the proceeding sections. However, one such example is shown here to give an example of when the BPF fails. For this same test setup (the controlled fast-spinning LEO spacecraft being observed with just one observatory), increasing the initial uncertainty in the angular velocity was enough to cause the BPF to diverge as shown in Fig. 9.7.

In this figure the test setup was the same as for the previous results shown but with the state initial uncertainties set to $\sigma_\omega = 0.2$ deg/s and $\sigma_\theta = 30°$. In this particular case the BPF results might have been improved by some adjustments to the tuning, but that would change the earlier results, so it was not done.

Returning to Fig. 9.7, this was presented to illustrate that there are cases where even the BPF fails to perform well. However, for this test setup, the filter performed well for the different cases of initial conditions up through $\sigma_\theta = 20°$ and only failed for the larger initial uncertainties. Referring again to Fig. 9.4, the EKF and UKF both started to fail regularly at the attitude state uncertainty of $\sigma_\theta = 5°$. While the bootstrap particle filter may not be as accurate as the UKF (and sometimes EKF, though it is generally unsuited for this application), for some of the low initial uncertainty conditions it is more robust in that it is able to estimate the attitude of the spacecraft for cases in which the other filters might diverge. This is especially true for when there are large initial estimates of the state uncertainties.

While the BPF tends to perform better than the other filters for many of the different cases, there are still drawbacks associated with using this filter. In running all of the different test cases, the BPF was much more computationally expensive than the other two filters. All of the attitude results here used 10,000 particles, which required a much larger
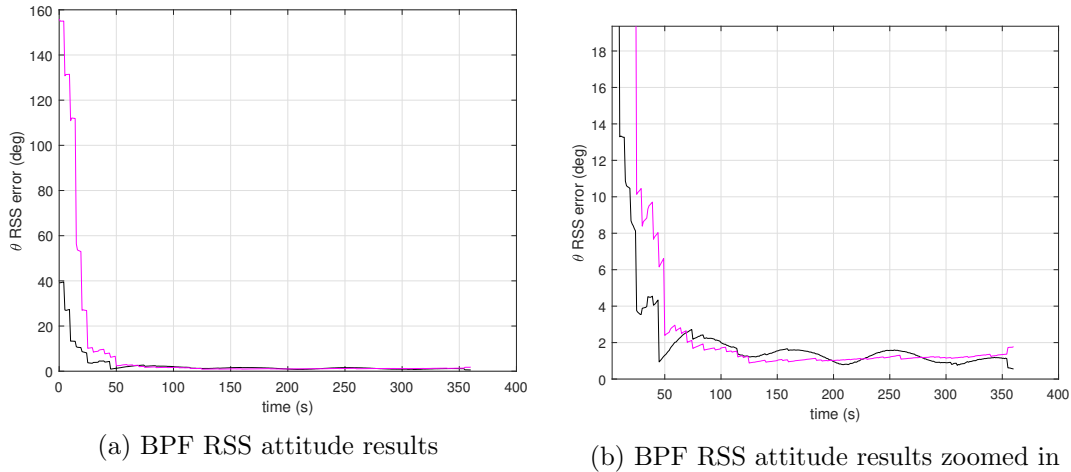
(a) BPF RSS attitude results

(b) BPF RSS attitude results zoomed in

Fig. 9.7: BPF RSS Attitude results for the fast-spinning LEO spacecraft with $\sigma_\omega = 0.2$ (deg/s), $\sigma_\theta = 30°$, and $r_{percent} = 1\%$

computation time than for the EKF and UKF. In addition, the UKF was more robust in its tuning. The tuning for the UKF did not have to be changed for all of the different test cases, while the BPF had to be retuned for each of the different setups as explained in section 9.3. However, once tuned for a given setup, the BPF performed well.

In this section it has been shown that the EKF is generally not a good option for estimating the attitude of the spacecraft using light curve measurements, and the UKF is not a very viable option for cases with large initial uncertainties in the attitude. However, if the uncertainties are low it can yield a smaller covariance than the BPF, and since it is more computationally efficient could be used at the very least to help set up the initial distribution for running the BPF. The BPF has been shown to be robust in its estimation of the attitude. It is often able to perform in cases where the other filters fail, though it is computationally expensive to implement.

The purpose of this section was to present and compare the behavior of the different filters for this application. It was not intended to be an in-depth discussion of the actual estimation of the attitude under a variety of different conditions. The actual discussion and analysis of the attitude results dependent on the different parameters is found in the subsequent sections.

9.4.2 Effects of the orbital regime

The effects of the different orbital regimes on performance of estimating the attitude of a spacecraft are presented in this section. The different orbital regimes can affect the performance of the filters, as the measurement function is a function of the vector from the observatory to the spacecraft. The same object in a lower altitude would appear brighter in a lower orbit than if it had the same observational geometry in a higher orbit. In addition, the altitude of the orbit can affect the result, as it is possible that more of the spacecraft facets may be seen for a low altitude orbit that flies past the observatory than might be seen for something like a GEO spacecraft which appears to be unmoving for an observer on Earth.

From the numerous tests that were performed, it was observed that the performance of the attitude estimation was generally better for the spacecraft in LEO than for the other orbital regimes. In addition, in investigating whether this improved performance was related to the brightness of the object at the given measurement times, this section also presents the results obtained from scaling up the size of the shape model for the MEO and GEO cases so that the measurements would be at the same level as the LEO spacecraft. From these different tests, it became apparent that the scaling of the spacecraft produced markedly different results only for the cases with the large uncertainty in the measurements. The remainder of the section will present the results helping to support these conclusions.

The best attitude determination results were achieved for the fast-spinning spacecraft cases with the lower measurement noise. To determine the different levels of performance between the different filters, the results for the fast-spinning controlled spacecraft with the lower measurement noise and σ_ω are shown for the LEO case in Fig 9.5 and for the MEO and GEO cases in Fig. 9.8. These are shown in order to establish what the best-case performance of the filters looks like for the different orbital regimes.

From the figures, it is clear that the LEO test case is able to obtain a more accurate result than with the MEO or GEO test cases. In the case of the LEO spacecraft, the filters are able to obtain an accurate estimate of the attitude down to the level of $2°$ for the 3σ
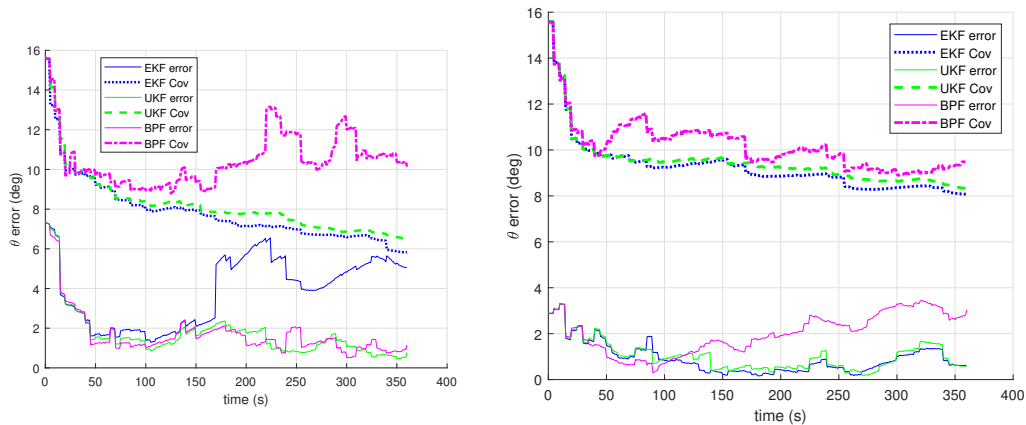
(a) MEO $\sigma_\theta = 3°$

(b) GEO $\sigma_\theta = 3°$
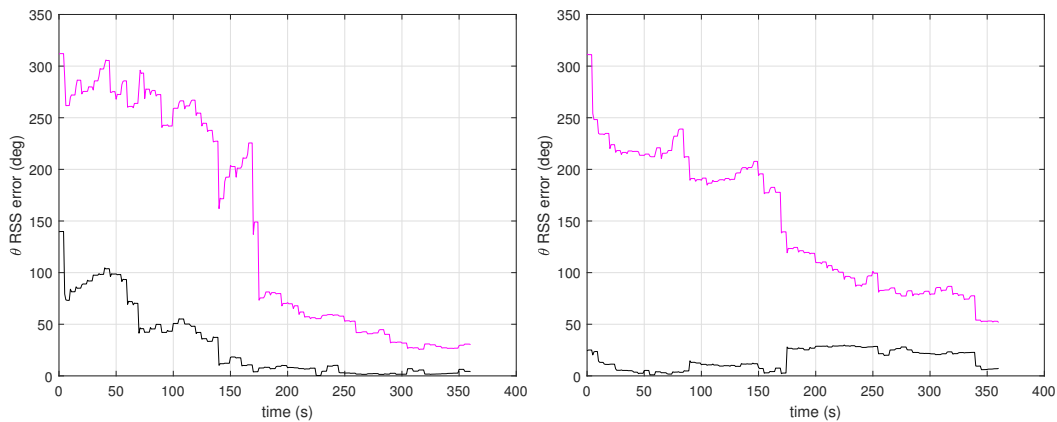
(c) MEO $\sigma_\theta = 60°$

(d) GEO $\sigma_\theta = 60°$

Fig. 9.8: Attitude results for the controlled fast-spinning MEO and GEO spacecraft with $\sigma_\omega = 0.02$ deg/s and $r_{percent} = 1\%$ and controlled dynamics

RSS bound. The best cases for the MEO and GEO spacecraft are only able to obtain an estimate down to 6° and 8°, respectively. Furthermore, while the LEO spacecraft was able to obtain the same level of accuracy from $\sigma_\theta = 3°$ to $\sigma_\theta = 60°$, with the MEO and GEO test cases the attitude RSS covariance bound increased with the initial attitude uncertainty. From these results it is clear that the LEO test case is obtaining more accurate results than either the MEO or GEO test cases. To provide some insight into why this occurring, the lightcurves used for these runs are presented in Fig. 9.9.

From examining the LEO measurement plot shown in Fig 9.9a and the plot of the BPF residuals shown in Fig. 9.5f, the particles start to converge when the sharp peaks and valleys on the measurement plot occur. This is due to the specular nature of some of the spacecraft facets, and it allows for narrowing in on the actual attitude. One other item of note from the measurement curve is the general positive slope of the graph over time. This is due to the spacecraft moving closer to the observatory as the observation time progresses, as can be seen from Fig. 9.1.

The light curve measurement for the MEO spacecraft is presented in Fig. 9.9b. This light curve differs greatly from that of the LEO spacecraft. In this instance, there isn't a gradual positive slope in the data over the measurement time. Rather, there is a small negative slope in the magnitude of the specular spikes which is likely due to the spacecraft moving away from the observatory. This is further supported by the absence of a trend in the GEO light curve shown in Fig. 9.9c. In GEO the object appears fixed to the observer. These trends from the movement of the spacecraft in its orbit may provide the filter additional information related to the attitude of the spacecraft as different facets may become more visible. This is further supported by the results for the cases with the slow-spinning spacecraft.

Unlike the fast-spinning spacecraft, which expose many facets to the observatory, making it easier to obtain a good attitude estimate, the nadir-pointing spacecraft are oriented so that the same facet points earthward continually. This reduces the number facets that can be viewed, especially for the objects in high-altitude orbits.
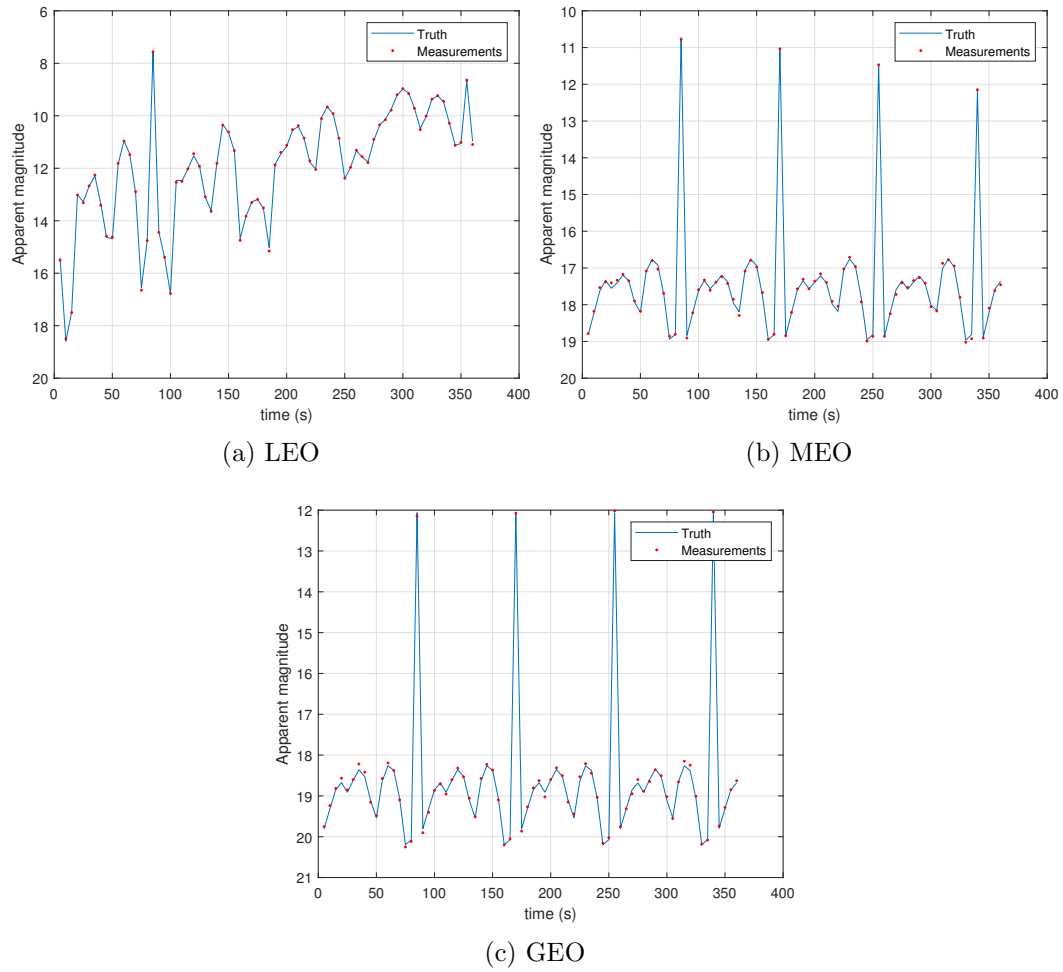
(a) LEO

(b) MEO

(c) GEO

Fig. 9.9: Magnitude measurements and residuals for the fast-spinning LEO, MEO, and GEO spacecraft with controlled dynamics, $\sigma_\omega = 0.02$ deg/s and $r_{percent} = 1\%$

The measurements and best-case results for the uncontrolled nadir-pointing spacecraft with $\sigma_\omega = 0.02$ deg/s and $r_{percent} = 1\%$ are shown in Figs. 9.10 and 9.11 for LEO, MEO, and GEO. In this instance the best cases for MEO and GEO correspond to using the initial conditions MEO IC3 and GEO IC2. Furthermore, for these results the scaled models were used for the GEO and MEO cases. This was done to better compare the performance of the attitude estimation when the lightcurves are at similar levels.

In looking at the lightcurves for this case, again the LEO and MEO spacecraft had slight trends to the data which in this case corresponded to the spacecraft moving closer or farther away from the observatory. For the GEO case shown in Fig. 9.10c, the nadir-pointing facet was very specular, and the slight trend in the light curve is from the small changes in reflection geometry. It is clear from looking at the different figures that the LEO spacecraft has a much larger range of magnitudes over the same observation time than the other two orbital regimes. The additional movement of the LEO spacecraft in this case allows for more accurate estimates of the attitude state which can be seen from the results in Fig. 9.11.

From the figure it is clear that while not all of the attitude components were able to be fully estimated with this test scenario, the attitude estimates of the LEO spacecraft were superior to those of the MEO and GEO spacecraft for both the case when $\sigma_\theta = 3°$ and $\sigma_\theta = 10°$. Indeed, for the latter case the attitude estimate for LEO was able to converge, while the filter diverged for both the MEO and GEO cases. From these results, and those of the fast-spinning spacecraft, it is clear that the attitude is better able to be estimated for the LEO spacecraft than for the higher altitude orbital regimes.

It is important to note that the presentation of these results is not to discount the ability of the filters to improve an estimate of the spacecraft's attitude state. Rather, the results here simply show that for the given application, more accurate results can be obtained in LEO than in the other two orbital regimes that were examined. It is clear from examining the results from the fast-spinning spacecraft that the filters were able to improve the attitude estimate during the observation period. This shows that there is some gain
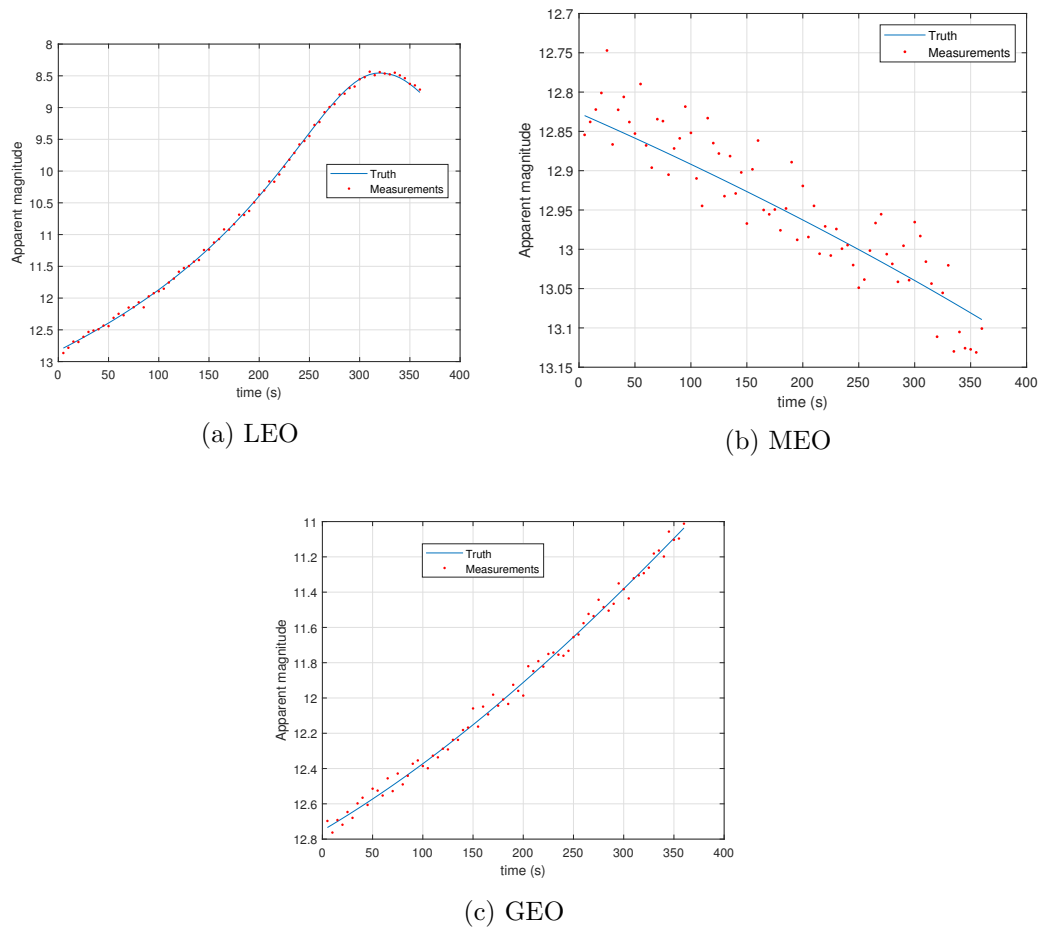
(a) LEO

(b) MEO

(c) GEO

Fig. 9.10: Magnitude measurements for uncontrolled nadir-pointing LEO, MEO, and GEO spacecraft with $\sigma_\omega = 0.02$ deg/s, $r_{percent} = 1\%$, and scaled facet shape models
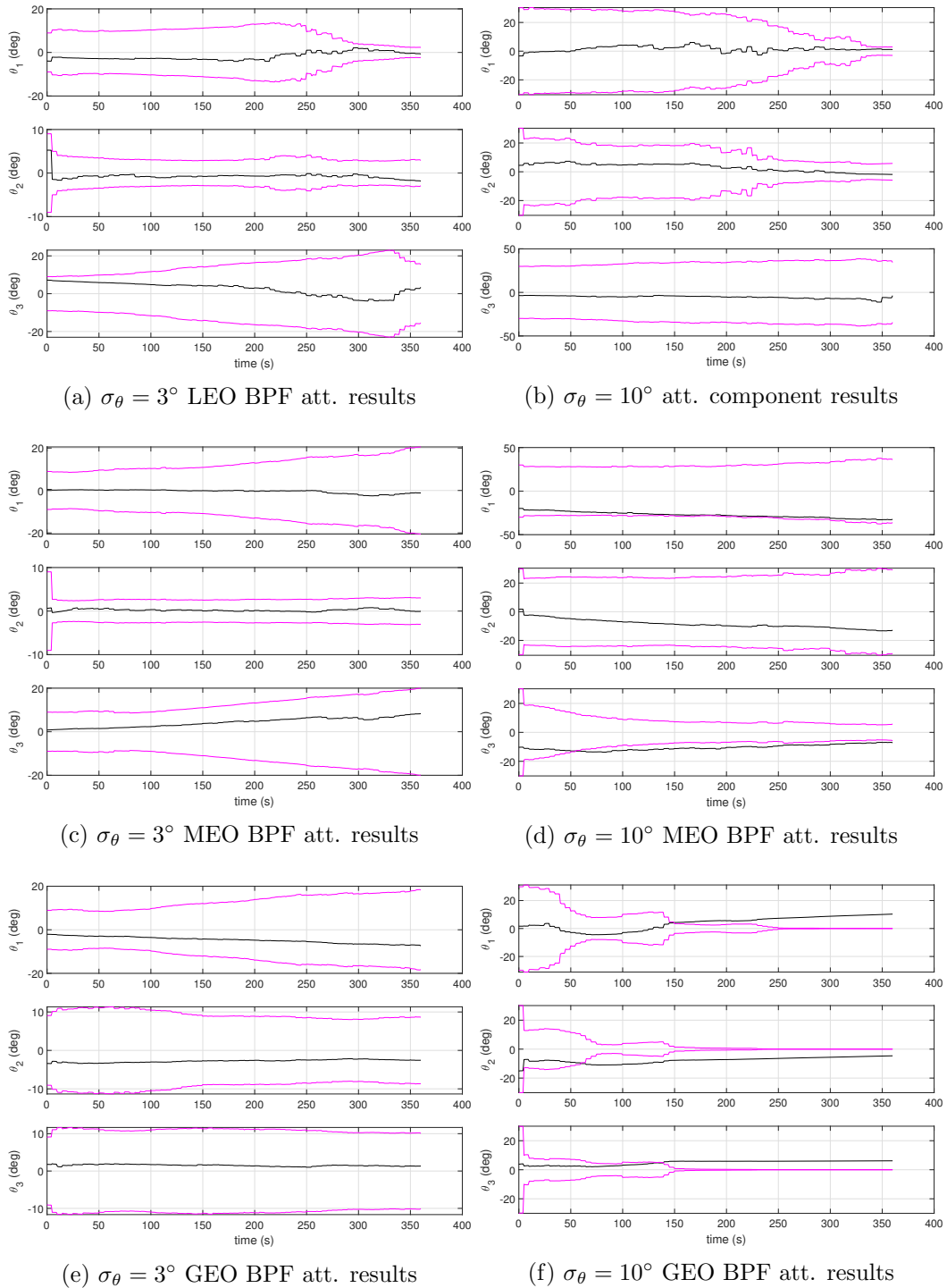
(a) $\sigma_\theta = 3°$ LEO BPF att. results

(b) $\sigma_\theta = 10°$ att. component results

(c) $\sigma_\theta = 3°$ MEO BPF att. results

(d) $\sigma_\theta = 10°$ MEO BPF att. results

(e) $\sigma_\theta = 3°$ GEO BPF att. results

(f) $\sigma_\theta = 10°$ GEO BPF att. results

Fig. 9.11: Attitude results for uncontrolled nadir-pointing LEO, MEO, and GEO spacecraft with $\sigma_\omega = 0.02$ deg/s and $r_{percent} = 1\%$ and the scaled facet area shape models (MEO and GEO)

in utilizing the lightcurves to estimate the attitude of the spacecraft even in these higher orbital regimes.

One final item of note is that the results presented in 9.11 used the scaled shape model for both the MEO and GEO spacecraft. It was observed that, generally, the scaled shape model did not do much to help improve the performance of the attitude estimation. As has been discussed, it is the general shape of the light curve, the peaks and valleys, and the changing between them that aid in determining the attitude of the filter. With the scaled shape model, the general shape of the light curve is the same, with the difference being in the scale of the magnitude measurements. This can be seen from looking at the comparison between the lightcurves for the uncontrolled fast-spinning MEO spacecraft with both the CubeSat and scaled facet shape models that is presented in Fig. 9.12.

From looking at the figure, it can be seen that the light curve is very similar for the two different shape models. In general, it was observed that the CubeSat and scaled shape models produced similar results in estimating the attitude except in the cases with the larger uncertainty in the magnitude measurements. This is because in this case the actual lightcurves were noticeably different from one another. This is shown in Figs. 9.12b and 9.12d. As the measurement noise is computed as a percentage of the magnitude measurement, when $r_{percent}$ is larger the scaled shape model produces better results, as the scaled model is brighter, which results in a lower magnitude. If the measurement noise were computed with a fixed covariance rather than a percentage, then it is unlikely that there would be a significant difference between the results of the CubeSat and scaled spacecraft shape models.

This section presented the key conclusions related to the effects of the test scenario orbital regime on the performance of the attitude estimation. The key conclusions were that the most accurate attitude results can be obtained in LEO as opposed to MEO or GEO. The other key conclusion is that the shape of the scaled shape models didn't greatly change the accuracy estimate, as it tends to be the shape of the light curve that determines the performance of the filter as opposed to the scale of the measurements.
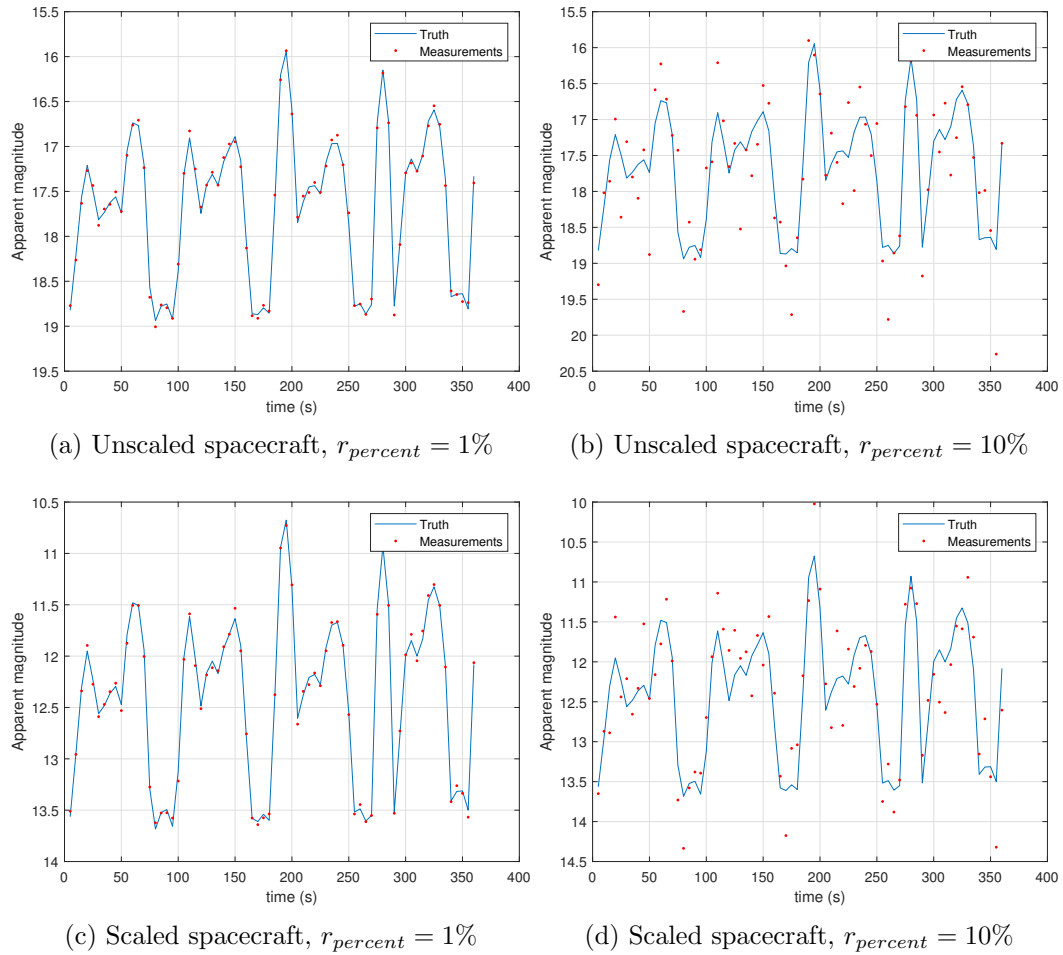
(a) Unscaled spacecraft, $r_{percent} = 1\%$

(b) Unscaled spacecraft, $r_{percent} = 10\%$

(c) Scaled spacecraft, $r_{percent} = 1\%$

(d) Scaled spacecraft, $r_{percent} = 10\%$

Fig. 9.12: The fast-spinning uncontrolled MEO spacecraft measurement curves for both the scaled and CubeSat shape models

9.4.3 Effects of the spin rate

From the results that have been presented in the previous sections it can be seen that the spin rate greatly impacts the accuracy of the attitude results that are obtained. From the different tests that have been performed, the general conclusion related to the effect of the spacecraft spin rate is that the more accurate results are obtained with the fast-spinning spacecraft.

The reasons for this occurrence can be understood by examining Fig. 9.13. The figure shows the value of the dot products between the spacecraft-to-observatory vector and the shape model facet normal vectors. It is the same as the cosine of the angle between the different vectors. The three different cases are for the controlled GEO spacecraft when it is fast spinning, nadir pointing, and inertially fixed over the observation time. The initial conditions for the nadir-pointing and inertially fixed case are GEO IC2.

In the figure, when the dot product between the spacecraft-to-observatory vector and the facet normal are positive, the facet is visible to the observatory at that time. For the fast-spinning case shown in Fig. 9.13a, all of the facets become visible to the observatory at some point, while for the other cases the same facets are visible over the whole of the observation time. The fast-spinning cases are able to show all of the facets repeatedly, which allows for an accurate estimation of the attitude components. For the slow-spinning or inertially fixed cases, the number of facets that can be seen and the rate at which they change are different. Furthermore, if only the same facets are visible, it can result in only

(a) Fast-spinning   (b) Nadir   (c) Inertial
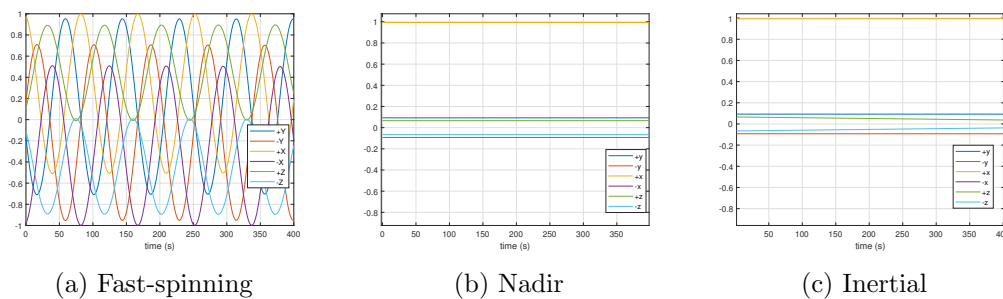
Fig. 9.13: Dot product of the vector from the satellite to the observatory at Socorro, NM, and the facet normal vectors for GEO spacecraft

some of the attitude components being observable over the observation time. This can be seen in the slow-spinning results shown in the previous section.

One final thing to note related to the slow-spinning or inertially fixed spacecraft is that due to the slow rotation rate of the spacecraft these test scenarios require good initial knowledge of the state and accurate measurements. As the initial state uncertainty or measurement error became large, it became difficult to obtain an accurate estimate of the state. The best results were obtained for cases with $\sigma_\theta \leq 10°$. Results were generally unreliable for all filters as the uncertainty in the attitude state increased.

The spacecraft spin rate has an effect on the estimate of the spacecraft attitude. The faster spinning the spacecraft, the more the facets can be seen by the observatory, which generally results in an improved attitude estimate. For this reason the fast-spinning cases resulted in much more accurate attitude estimates than the slow-spinning or inertially fixed test cases and scenarios.

9.4.4   Effects of using two observatories

The previous sections have presented the results and conclusions drawn from looking at the performance of the different filters and the effects that the orbital regime and spacecraft spin rate can have on the ability to estimate the attitude of a spacecraft using light curve measurements. This section provides further insight in presenting the results and conclusions pertaining to the use of a second observatory in collecting light curve measurements and estimating the attitude of the spacecraft.

The main conclusions related to the use of a second observatory are that when the spacecraft is spinning very rapidly, there is not much improvement in the attitude estimate from using a second observatory, but when the spacecraft is rotating slowly, then a second observatory can greatly increase the accuracy of the estimate. This is discussed further in the following sections.

Two-site photometry with fast-spinning spacecraft

As the last section established, when the spacecraft is spinning rapidly it is better able to estimate the attitude of the spacecraft, as all the different facets are seen by the observatory. However, when a second site is added, but the measurements are not taken at the same time, there is little improvement to the attitude estimation, as there is not much additional information about the spacecraft attitude that is gained. This can be seen from comparing the facets that are visible to the observer at Socorro, NM, and at the BLO, UT, for the controlled fast-spinning LEO case shown in Fig. 9.14.

(a) Socorro, New Mexico

(b) Bear Lake Observatory, Utah
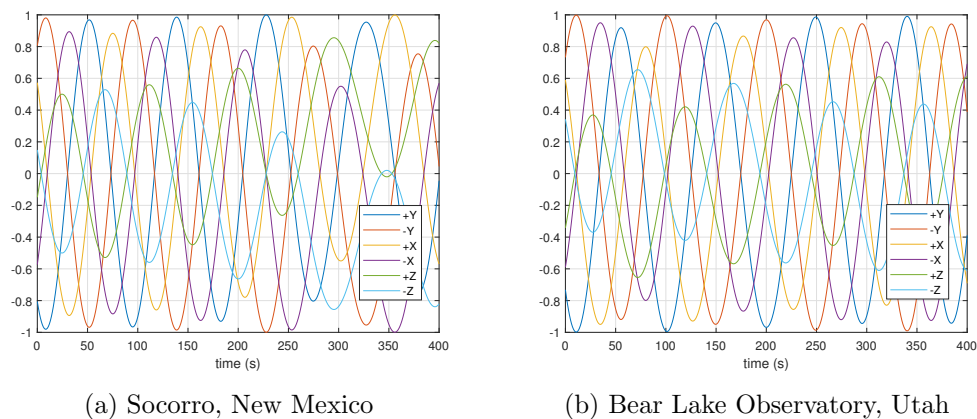
Fig. 9.14: Cosine of the angle between the facet normal vectors and the satellite-to-observatory vectors

It can be seen from the figure that the same facets are visible to the observer and follow a similar pattern in which they are most visible. This results in the light curve including the second site being very similar to the light curve for a single site, which can be seen by comparing the lightcurves from two observatories shown in Fig. 9.15a to that of the single-site lightcurves shown in Fig. 9.9a. In this case the setup for the measurements was that the BLO first observed the spacecraft from 0 to 260 seconds, with follow-on observations from Socorro, NM, from 300 to 400 seconds after the start of the observation epoch.

As the lightcurves are very similar, the attitude estimation results are also very similar for the single-observatory and two-observatory cases. The results for the controlled, fast-

spinning LEO spacecraft with $\sigma_\omega = 0.02$ deg/s and $r_{percent} = 1\%$ are presented in Fig. 9.15. From the figures, it is clear that the performance of the filters in this case does not differ greatly from that of the single-site case shown in Fig. 9.5. It is possible that simultaneous measurements from both sites could improve the overall attitude estimation, but that was not examined in this work.
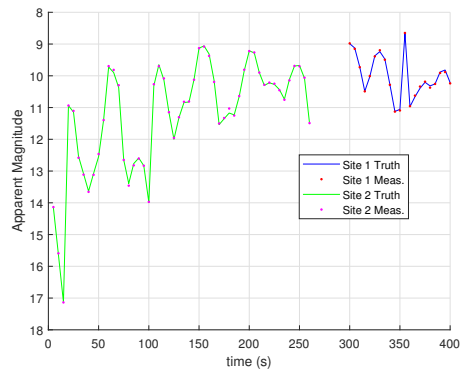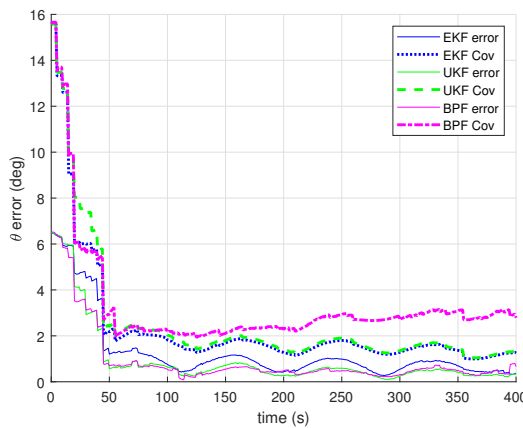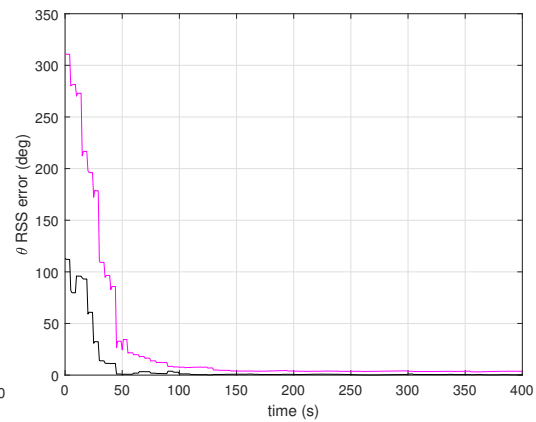

(a) Two-observatory measurements

(b) $\sigma_\theta = 3°$

(c) $\sigma_\theta = 60°$

Fig. 9.15: Two-observatory measurements and attitude estimation results for the fast-spinning controlled LEO spacecraft with $\sigma_\omega = 0.02$ deg/s, and $r_{percent} = 1\%$

Two-site photometry with nadir-pointing and inertially fixed spacecraft

Recall from Fig. 9.13 that unlike the fast-spinning cases which have multiple facets visible to the observer over the observation time, the slow-spinning/nadir-pointing and the inertially-fixed cases often have the same facets visible at a given time or have a much slower rate of change between the different facets. Two observatories that are viewing the spacecraft will have different measurement geometries resulting in additional information about the state. However, for the high-altitude orbits, where the reflection geometry is similar for both observatories, the best results are obtained when a specular facet is visible. This is due to the Lambertian diffuse reflection model which reflects equally in all directions. The only directional reflectance with the measurement model of Chapter 5 is the specular reflection.

This conclusion can be reached by examining the results for the nadir-pointing GEO spacecraft. For the results presented in this section, the uncertainty in the angular velocity was set to $\sigma_\omega = 0.02$ deg/s, and the measurement noise was computed with $r_{percent} = 1\%$. The first set of results examines the nadir-pointing GEO spacecraft with initial conditions IC1. The measurements and results for both the one- and two-observatory cases are shown in Fig. 9.16.

For the two-observatory results shown in the figure, the scenario was such that the observatories switched off collecting measurements over the observation time as opposed to just having one observatory collect measurements followed by a single follow-on collection by the second observatory. In this instance Maui, HI, collected from 0–100 seconds and 205–260 seconds after the start of the observation epoch, and Socorro, NM, collected measurements from 105–200 and 300–400 seconds after the start of the collection time. It was observed that switching multiple times between the observatories could often improve the attitude estimation results, as it gave multiple points where the different reflection geometries could be used to provide additional information about the spacecraft orientation.

However, in this specific instance it can be seen that the single-site results do not differ greatly from the two-site results. This is largely due to the choice of the spacecraft initial

(a) Single-site measurements

(b) Two-site measurements

(c) One-site, $\sigma_\theta = 3°$

(d) One-site, $\sigma_\theta = 10°$

(e) Two-site $\sigma_\theta = 3°$
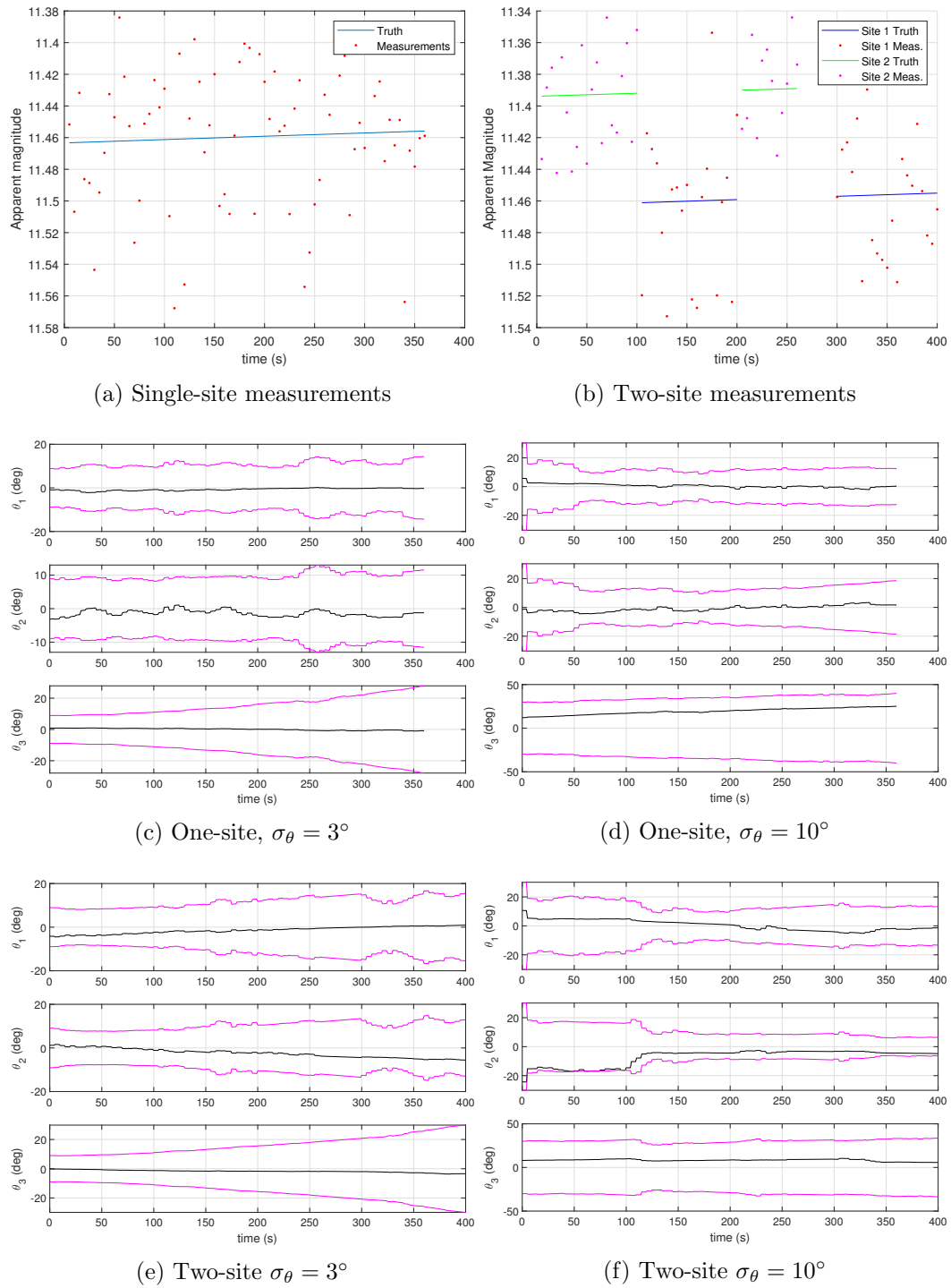
(f) Two-site $\sigma_\theta = 10°$

Fig. 9.16: Measurements and attitude component results for GEO IC1 with one and two observatories collecting measurements

conditions. Recall that the setup for GEO IC1 has the -Z body frame axis nadir pointing, the +Y body axis is aligned with LVLH cross-track direction, and the +X body axis is used to complete the triad. From Table 9.2 the -Z facet is the most diffuse out of all of the facets. The diffuse reflection model used is a Lambertian reflection model where the light reflects equally in all directions. This results in the measurements being very similar between the two sites, and in very similar results for one- and two-site cases.

The next set of results is for the same test setup, but with the initial conditions GEO IC2. In this case the most specular facet, the +X axis, is nadir pointing. This means that there is a much larger directional dependency in the light reflected by the spacecraft.

The single-site results for these initial conditions, GEO IC2, were presented in Figs. 9.11e and 9.11f. The results for the two observatories (with the same measurement setup as for the GEO IC1 case) are presented in Fig. 9.17. In this instance there is a significant difference in the lightcurves from each of the observatories. This difference in the lightcurves is a result of the largely specular nature of the facet that is nadir pointing. There is a large directional dependence resulting in largely different lightcurves from the two observatories.

The variation in the lightcurves allows for an improved estimate of the attitude state for the case when $\sigma_\theta = 3°$, as can be seen in Fig. 9.17b. From this figure it is apparent that while not all of the attitude components were able to be estimated, the estimate of two of the components greatly increased. With the nadir-pointing cases, the same facet is facing toward Earth over the entire observation time, which makes it difficult to estimate all three angle components. It is clear, however, that the use of the two sites greatly improved the overall attitude estimation compared to that of the single site case.

With the larger initial attitude state uncertainty, the performance was somewhat different. In this instance the filter collapsed to a result very quickly once the observatories switched for the first time. This led to the filter diverging at the end of the observation time. This also occurred in the single-site case for this setup. The manner in which the solution collapses down in Fig. 9.17c is indicative of the particles suffering from the impoverishment problem. It is possible that the performance in this case could be improved by adjusting
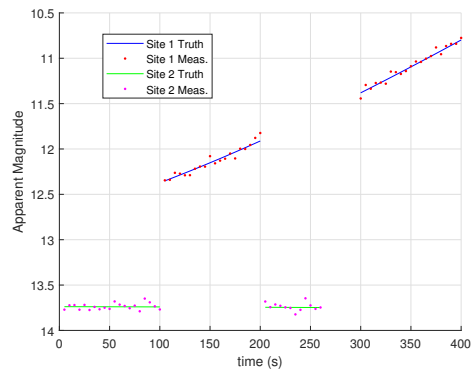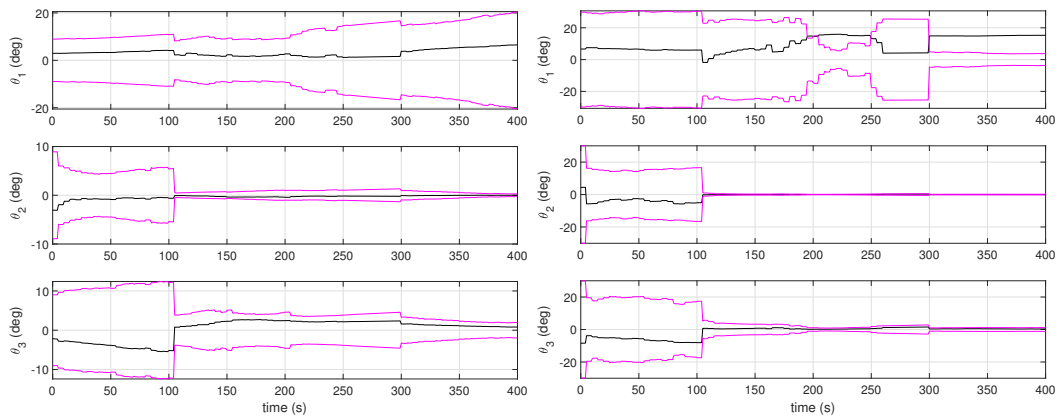
(a) Two-site measurements

(b) $\sigma_\theta = 3°$ BPF att. results

(c) $\sigma_\theta = 10°$ BPF att. results

Fig. 9.17: Two-site measurements and attitude results for the uncontrolled, nadir-pointing GEO spacecraft with $\sigma_\omega = 0.02$ deg/s, $r_{percent} = 1\%$, initial conditions GEO IC2, and scaled facet shape model

the roughening of the particles, but that could affect the performance for the lower levels of uncertainty. As the filters were only tuned once for the different test scenarios, this was not done and is left to future work. The solution would be to tune the filter for each of the different levels of uncertainty.

The next set of results demonstrates the effects of using two sites in the case of an inertially fixed spacecraft. The effects of two observatories on the inertially fixed spacecraft were similar to that of adding a second observatory for the nadir-pointing spacecraft. The lightcurves and attitude results for the single-observatory and two-observatory cases are shown in Fig. 9.18.

From the figure it is clear that the addition of a second site greatly improved the overall attitude estimation results. The covariance was lower for two of the three attitude components for the case when $\sigma_\theta = 3°$, and as the uncertainty increased, the second observatory helped to prevent the filter from diverging and resulted in an improved estimate for all three attitude components.

In this section, the results related to the effects of adding a second observatory were presented. It was shown that the addition of a second observatory did not greatly improve results for the fast-spinning spacecraft but did greatly improve the attitude estimates of the nadir-pointing and inertially-fixed spacecraft. Furthermore, it was shown that for the nadir-pointing spacecraft in high altitudes, the second observatory is only able to improve the estimate for the cases where the shape model reflection has a large directional component to it. If the light reflects equally in all directions, there isn't much to be gained by adding a second observatory. The next section discusses the effects that the dynamics models used have on the performance of the spacecraft attitude estimation.

9.4.5   Effects of the dynamics models

This section discusses the effects on the attitude estimation of the spacecraft when using either the controlled or uncontrolled dynamics models. From looking at the different test-case data, it was observed that there was not a large difference between the controlled or uncontrolled dynamics case. The only exception was for the fast-spinning cases in which

(a) Single site Measurements

(b) Two-site measurements

(c) Single-site BPF att. results, $\sigma_\theta = 3°$

(d) Single-site BPF att. results, $\sigma_\theta = 10°$

(e) Two-site BPF att. results, $\sigma_\theta = 3°$

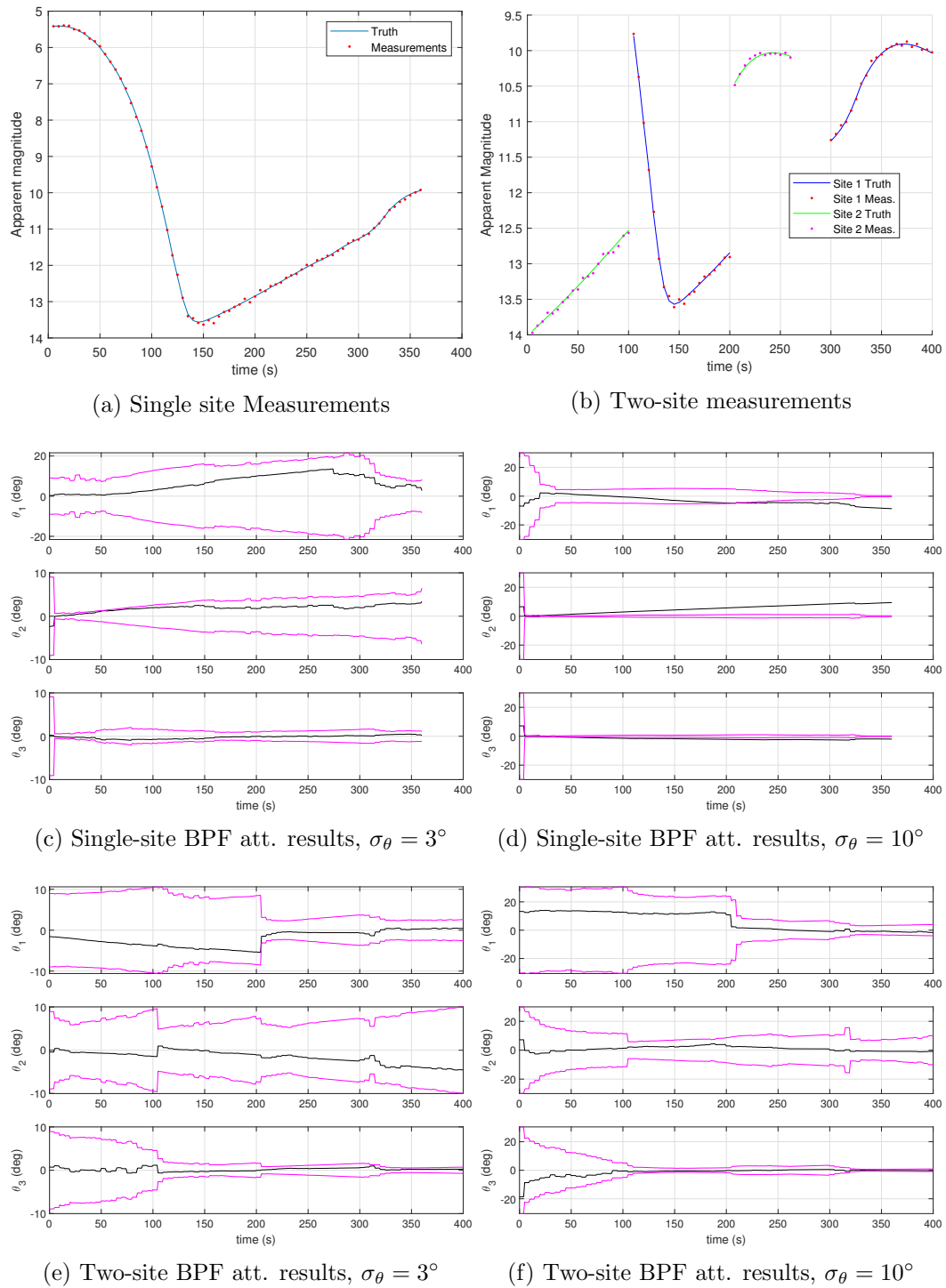(f) Two-site BPF att. results, $\sigma_\theta = 10°$

Fig. 9.18: One- and two-observatory lightcurves and attitude results for the inertially fixed LEO spacecraft with initial conditions LIIC1

the disturbance torques caused some of the specular peaks and valleys to change somewhat. This can be seen by examining the GEO fast-spinning results.

For these test cases, the shape model used is the CubeSat shape model with the areas of 0.01 m^2. The angular uncertainty in the angular velocity is $\sigma_\omega = 0.02$ deg/s, and the measurements are computed using $r_{percent} = 1\%$. The light curve for the controlled case was shown earlier in the chapter in Fig. 9.9c, and the lightcurve for the controlled case is shown in Fig. 9.19.
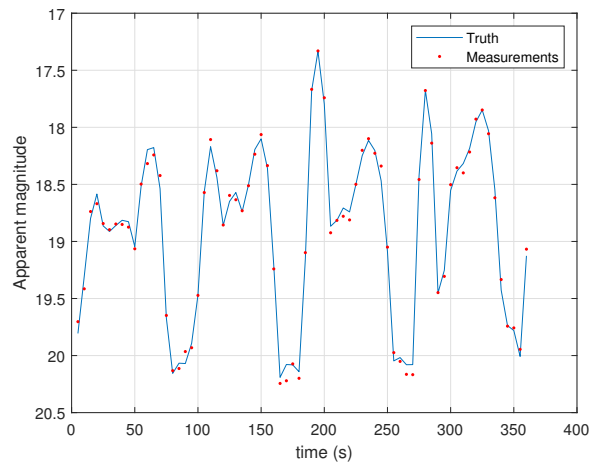
Fig. 9.19: Measurements for uncontrolled, fast-spinning GEO spacecraft

The measurements for the uncontrolled case are very different from the measurements for the controlled case. Both are at about the same magnitude, but the large spikes found in the controlled case are not present in the uncontrolled case. As has been discussed previously, the shape of the light curve has a large impact on the accuracy of the attitude estimation. Thus, the results are somewhat different between the controlled and uncontrolled dynamics models.

The reason why the fast-spinning cases are affected more than the slow-spinning cases is that the initial conditions of the fast-spinning cases are set up so that the facet normal of the most specular facet is aligned with the bisector between the observatory and Sun at the start of the observation time. Aligning the facet normal with the bisector results in the ideal conditions for specular reflection. With the fast-spinning cases, the satellite

is rotating so quickly the disturbance torques can perturb the attitude enough so that the specular peaks don't occur at the ideal conditions. With the slow-spinning cases the disturbance torques don't cause as great an effect, so the results don't differ much between the controlled dynamics and uncontrolled dynamics cases.

9.4.6 General effects of increased uncertainty and measurement noise

Thus far, the majority of the results that have been presented were for the case where the angular velocity is well-known and the measurements are very accurate. This was done to illustrate the effects of the different parameters, which were best shown in the cases where the attitude was well-estimated. The purpose of this section is to provide some insight into the differences in filter performance for the cases with increased measurement noise or an increased uncertainty in the angular velocity state.

Increasing the state uncertainty in the angular velocity or the measurement noise affected the results in two different ways: the overall covariance of the attitude and angular velocity increased, or the filters were less robust in estimating the attitude of the spacecraft. Less robust here means that the filter is not able to estimate the attitude at as large a value of initial uncertainty in the attitude state as it had previously done. These two behaviors can be seen in the following examples for the fast-spinning LEO spacecraft.

Recall, from the results shown in Fig. 9.5, that for the controlled fast-spinning LEO spacecraft with $\sigma_\omega = 0.02$ deg/s and $r_{percent} = 1\%$ the BPF was able to obtain a good estimate of the attitude state for all the different values of the initial attitude state uncertainty from $\sigma_\theta = 3°$ through $\sigma_\theta = 60°$. However, it was also shown in Fig. 9.7 that simply increasing the initial uncertainty in the angular velocity from $\sigma_\omega = 0.02$ deg/s to $\sigma_\omega = 0.2$ deg/s resulted in the filter being less robust and diverging when $\sigma_\theta = 30°$.

Increasing the measurement noise also greatly affects the performance of the filter. With the increased measurement noise the attitude results have a larger covariance bound. This can be seen in Fig. 9.20. In each of the cases shown in the figure, there is an increased covariance bound from what was seen for the earlier results with the low measurement noise and uncertainty in the angular velocity. For the case with the increased angular velocity

uncertainty and measurement noise, the increased covariance bound prevented the filter from diverging, as happened with the measurement noise in Fig. 9.7, but again this came at the cost of greater uncertainty in the system overall.

The main conclusions from this section are that increasing the measurement noise or initial angular velocity state uncertainty will affect the performance of the filters by either increasing the uncertainty in the state estimate or by causing the filter to be less robust. However, despite the increased uncertainty or decrease in the performance of the filter, the results show that there is still some potential and application for estimating the attitude of the spacecraft using light curve measurements. It is just important to be cognizant of the different error sources and how that will affect the overall performance of the attitude estimation.

9.5 Summary

In this chapter the setup for each of the different test cases was presented. The detail about the test setup included defining all of the different parameters that were examined, as well as explaining the manner in which these parameters were varied for the different test cases. In addition, the different sources of error were defined, and their application was explained. The orbital-regime-specific observatories and initial conditions were also defined.

After defining all of the test setup information, the key conclusions regarding the parameters were presented. These conclusions were the general conclusions taken from examining the test results as a whole along with details of some of the major effects related to the performance of the filters, orbital regime, spacecraft spin rate, number of observatories, dynamics, and the effects of the different error sources.

From the results, it was found that the BPF is most robust in performing the spacecraft attitude estimation, though tuning the filter can be tedious and can come at the cost of accuracy for the cases with low initial uncertainty in the state estimates. Furthermore, it was shown that the UKF isn't very reliable, as the state uncertainty increased. In addition, the most accurate results were generally associated with the fast-spinning and LEO spacecraft, but the use of two observatories had a larger impact on the results of the
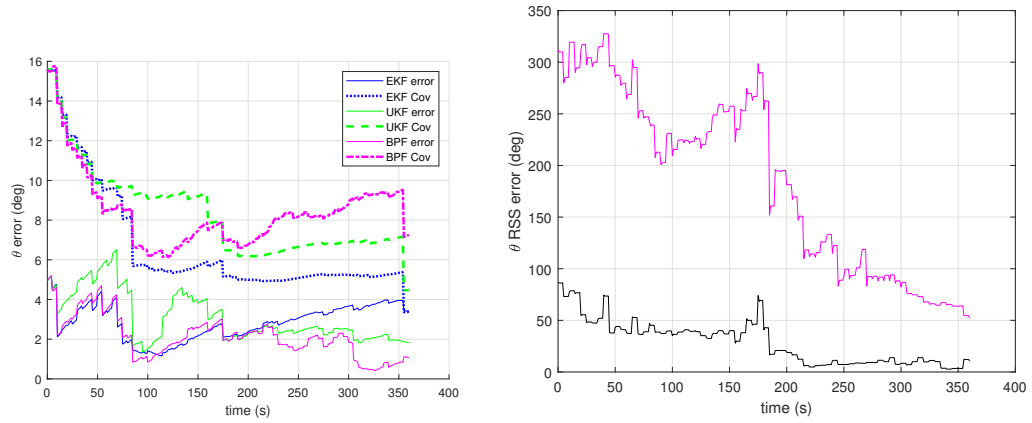
(a) $\sigma_\omega = 0.02$ deg/s, $r_{percent} = 10\%$, $\sigma_\theta = 3°$

(b) $\sigma_\omega = 0.02$ deg/s, $r_{percent} = 10\%$, $\sigma_\theta = 60°$
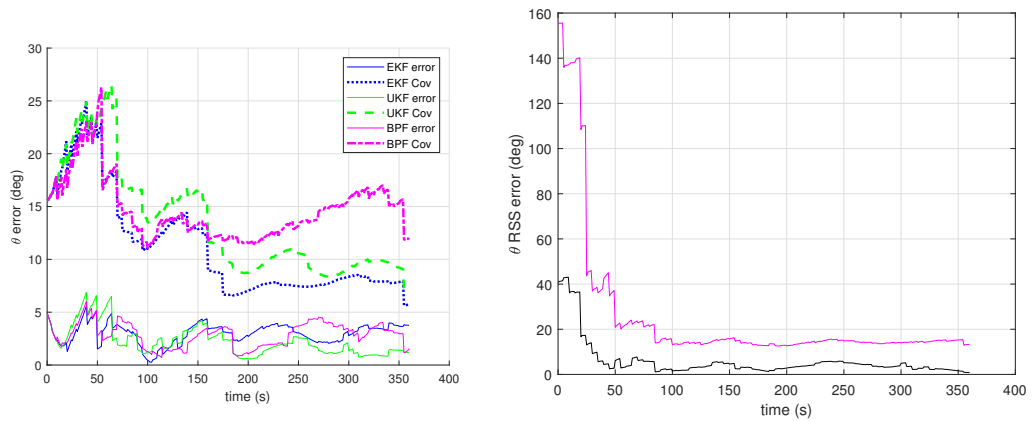
(c) $\sigma_\omega = 0.2$ deg/s, $r_{percent} = 10\%$ $\sigma_\theta = 3°$

(d) $\sigma_\omega = 0.2$ deg/s, $r_{percent} = 10\%$, $\sigma_\theta = 30°$

Fig. 9.20: Attitude results for controlled, fast-spinning spacecraft with $r_{percent} = 10\%$ and varying values for initial state uncertainties

slow-spinning spacecraft than on these fast-spinning ones. Finally, it was shown that the different dynamics had a larger impact on the fast-spinning spacecraft than on the slow-spinning spacecraft, but the ability to estimate the attitude was fairly close for both sets of dynamics.

These results have shown that there is a lot of potential in utilizing this type of approach for estimating the attitude of real-world spacecraft. However, it is important to note that these results were obtained under a number of assumptions. These assumptions include that the orbital state of the spacecraft and its shape parameters are perfectly well-known so that the error from these sources can be neglected. There were also some simplifying assumptions made when defining the measurement model in Chapter 5. These assumptions may not hold in real-world applications, so there is a need to examine them further. The next chapter explores some of the effects of relaxing the knowledge of the shape parameters, but the other items remain as work that can be better explored in the future.

CHAPTER 10

RESULTS: REFLECTION PARAMETER ESTIMATION

In this chapter the testing scenarios and results are presented for evaluating the effectiveness of the different approaches for modeling the uncertainties in the reflection parameters. These different approaches are the models presented in Chapter 8.

The chapter first discusses the setup of the different test cases along with the different criteria used to evaluate the performance of each model. Next, the main conclusions from this work are presented along with the results from the individual models that show how these conclusions were obtained. Finally, any additional conclusions or insights gained from the different tests are presented and discussed.

10.1 Test setup

This section presents the methods used to set up and run the different test cases in order to evaluate the performance of filters in estimating the parameters associated with the individual reflection parameter models. The overall setups for the different tests were selected from scenarios which yielded good results for the attitude-only estimation (see Chapter 9). The cases that were selected are the fast-spinning LEO spacecraft, the inertially fixed LEO spacecraft, and a nadir-pointing GEO spacecraft. The controlled dynamics models were used for each of these cases. In the instances in which the results associated with these test cases have multiple sets of initial conditions, the case where the initial conditions that provided the best attitude result were selected. For the LEO inertial cases, LIIC1 was used, and for the GEO nadir-pointing cases, GEO IC2 were chosen to set up the test scenarios.

A detailed description of the setup for these different scenarios is included in the previous chapter, Chapter 9. However, a brief description of the different test cases is provided here. For the LEO cases, the two observatories that are used are Socorro, NM, and the

BLO, UT. For the GEO case the two observatories are Socorro, NM, and Maui, HI. For all of the two-site cases the observatories followed a switching pattern. The first, Socorro, NM, would observe the spacecraft from 105–200 seconds and 300–400 seconds after the start of the observation epoch, and the second site would view the spacecraft from 0–100 seconds and 205–260 seconds after the start of the epoch. For reference, the light curves for these different runs are presented all together in Fig. 10.1.

Before attempting to estimate the combined reflection parameters and attitude information, the different models were first tested to determine if the reflection parameters could be estimated on their own when combined with a perfect knowledge of the attitude state.

For each of the different runs, for both the parameters on their own and the combined parameters and attitude estimation, the initial estimate of the shape model parameters are the same that were used for generating the attitude results in Chapter 9. A truth model was found by perturbing the reflection parameters with a value drawn from $N(0, \sigma_p$, where $\sigma_p)$ was set to 10% of the parameter value. The parameters here are referring to the facet area,A, specular/diffuse weighting term, ξ, diffuse albedo term, a, and the microfacet slope parameter,m. After generating the truth model, the measurements were computed using this truth model and the same measurement noise model used previously. Then filters for the different models could be implemented following the methods laid out in Chapter 8. The attitude portion of the truth model and filters is the same as that of Chapter 9, with the exception of the fast-spinning LEO spacecraft. For this case the initial conditions were changed to where the body frame was aligned with the ECI frame at the initial epoch. The angular velocity vector for the fast-spinning case and the other parts of the dynamics were all the same as in the previous chapter.
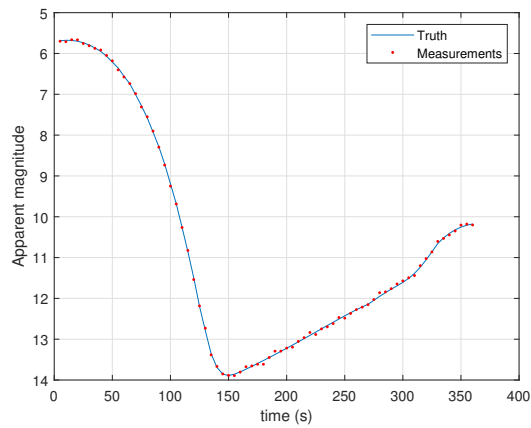
10.2 Error sources

For all of the different test scenarios, there were associated error sources affecting the results. The purpose of this section is to define these error sources and explain the manner in which they were accounted for and incorporated into the simulation and estimation process. First the error sources common to all of the different test setups are discussed. Following
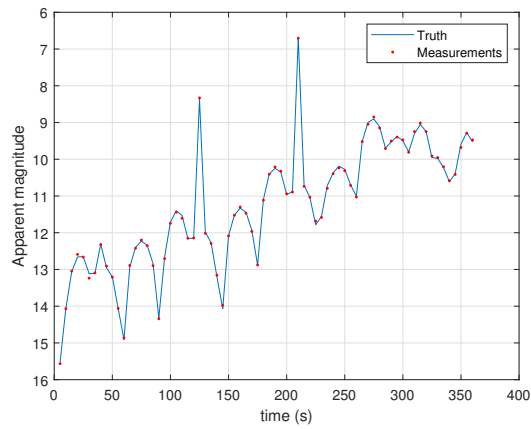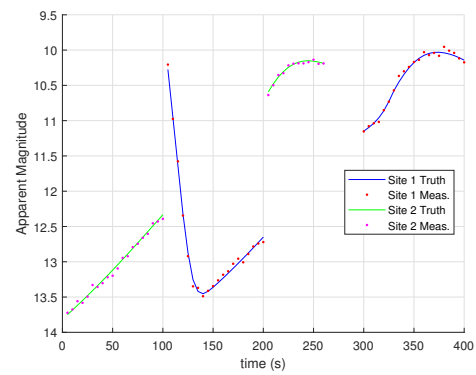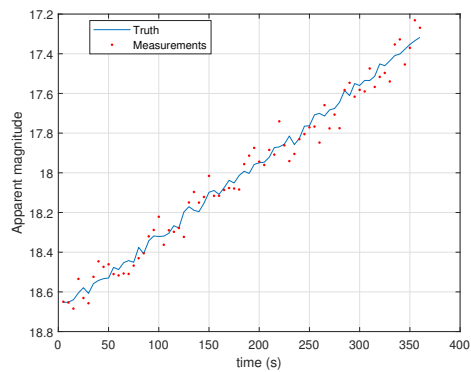
(a) LEO fast case 1 obs.
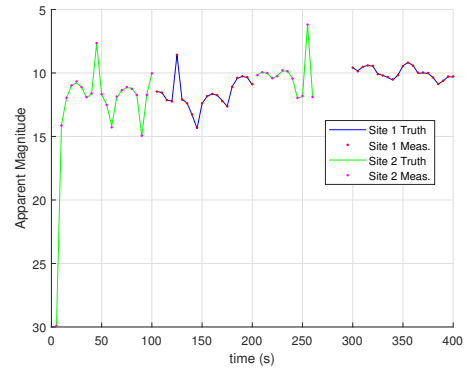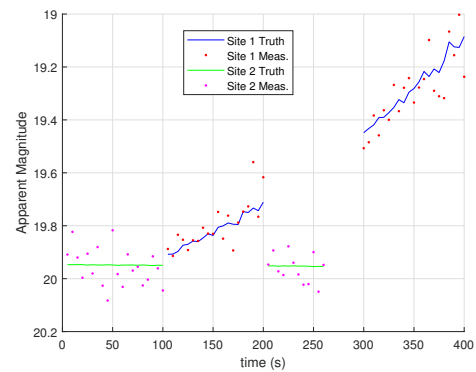
(b) LEO fast case 2 obs.

(c) LEO inertial case 1 obs.

(d) LEO inertial case 2 obs.

(e) GEO nadir case 1 obs.

(f) GEO nadir case 2 obs.

Fig. 10.1: Light curves for the different test cases discussed in this chapter

are the model-specific error sources.

The error sources common to all of the different test scenarios are identical to those associated with the attitude estimation. These include the following sources:

- initial uncertainty in the knowlege of the state parameters

    - position vector uncertainty

    - velocity vector uncertainty

    - attitude state uncertainty

    - angular velocity state uncertainty

- measurement noise

- attitude control system errors

In addition to the errors common to all of the previous test cases, in estimating the reflection parameters there is an additional error affecting the estimation results:

- Uncertainty in shape model reflection parameters

The three proposed reflection parameter estimation models are implemented to account for the effects of this uncertainty.

For all of the different test cases, as before, the position and velocity vectors are assumed to be known with enough knowledge that the error contributions are deemed negligible. Furthermore, for the cases where the reflection parameters alone are being estimated, the angular velocity and attitude state uncertainties are neglected. For the measurement noise, it is applied the same way for the attitude cases but with all of the tests performed with $r_{percent} = 1\%$, as this provided the best results for the attitude estimation. The shape model uncertainty is the difference between the reflection parameter estimates and the true shape parameters as explained in the previous section. All of the different test cases for this chapter were for the controlled dynamics, and the uncertainty in the attitude control system is used in the manner explained in previous chapters. These error sources are those

that are common for all of the different tests. The following section explains the methods used to evaluate the results of the estimation process.

10.3 Metrics for evaluating filter performance

In order to evaluate the performance of the different filters, it is requisite to first define the metrics used for this assessment. Unlike with the attitude estimation, the truth state for Models 1 and 2 are unknown. Thus, different metrics will have to be used for evaluating the performance of Models 1 and 2. For these models, the plot of the mean bias will be used along with the 3σ covariance bounds. The convergence of the covariance bounds helps to illustrate the behavior of the filter for those states. In addition, as the purpose of these models is to estimate the error in the measurements, the measurement residuals will be used as an indication of the filter performance for these terms. If the bias estimation is performing well, then the measurement residuals between the expected measurements and the actual measurement used for the state update should fall around the levels of the measurement noise.

For Model 3, and when the attitude states are also being estimated, the true values of the states are known, and so the true error can be used to evaluate the performance of these filters. For these states, the true error is plotted along with the 3σ covariance bound. This allows for the performance of the filter to be gauged. Now, with these different metrics defined, the following sections present the the general conclusions from all of the different test cases, and the results for the different models.

10.4 General results conclusions

When first presenting the different reflection parameter models, it was acknowledged that the most direct method would be to just estimate the parameters directly. However, the additional states for all of the different reflection parameters makes the direct estimation approach quite costly. This was the motivation in presenting Models 1 and 2. The estimation of a bias term requires many fewer states than trying to estimate the reflection parameters for all of the different facets composing the spacecraft shape model. However,

after carrying out the different test cases and analyzing the performance of the different model, the following conclusions were reached.

- Models 1 and 2 are not suitable for combined bias and attitude estimation.

- Model 3 is the most suitable for combined attitude and parameter estimation with some caveats.

    - Not all of the parameters have improved estimates after processing all the measurements.

    - Due to ambiguities in the measurement models, the filter may converge to parameters that aren't the truth value but yield similar measurements.

    - The attitude estimates obtained with the combined parameter and attitude estimation are not as accurate as when there was a perfect knowledge of the shape model reflection parameters.

The following sections present the results for the individual models that will demonstrate the veracity of the conclusions listed above.

10.5   Model 1—bias results and discussion

The first model evaluated is the model with the constant bias, Model 1. When initially defining the models in Chapter 8, it was hypothesized that this straight bias could be a good fit for the cases where the spacecraft is rotating slowly, but as it doesn't have any terms to account for the rotation rate of the spacecraft, it may perform poorly as the spin rate of the spacecraft increases. To gauge the performance of the filter with the different spin rates, the results for estimating the bias with a perfect knowledge of the attitude are examined first.

10.5.1   Bias-only results

The first set of results examines the test case with the fast-spinning spacecraft. For the test cases presented in this section, all of the runs have the uncertainty in the angular

velocity set to $\sigma_\omega = 0.02$ deg/s and $\sigma_\theta = 3°$, respectively, and the measurement noise is computed with $r_{percent} = 1\%$. Figure 10.2 presents the results for the fast-spinning LEO test case.
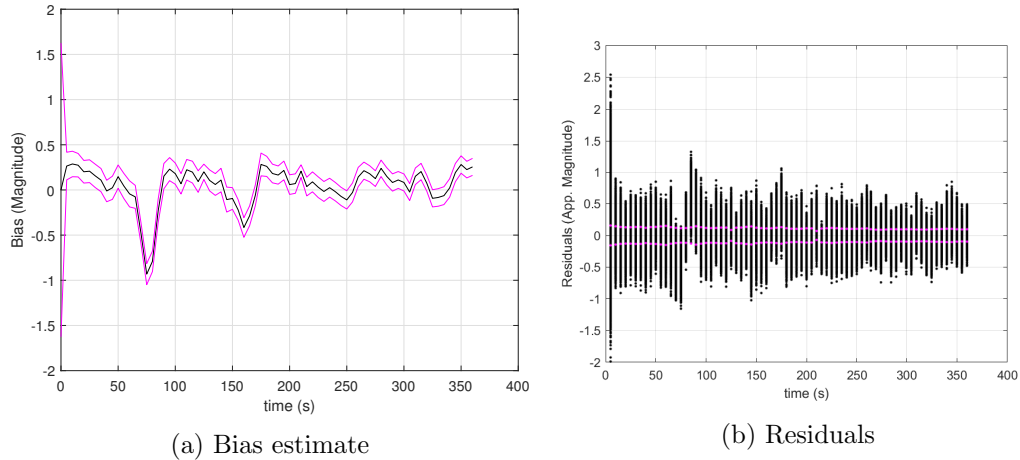

(a) Bias estimate

(b) Residuals

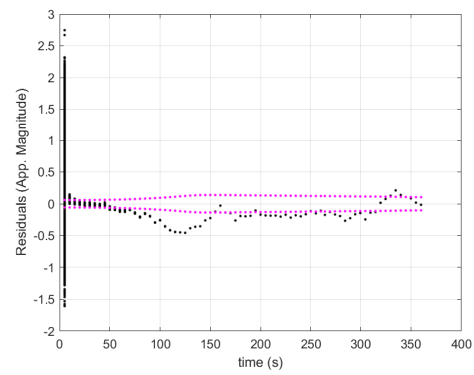Fig. 10.2: Model 1 bias estimation results for fast-spinning LEO spacecraft

On the left-hand side of the figure is the estimate of the measurement bias with its 3σ covariance bounds, and on the right is the difference between the expected measurement from all of the particles and the actual measurement

From the results shown in Fig. 10.3, the results for the GEO spacecraft showed that the spacecraft performed well in that instance. With the nadir-pointing GEO spacecraft, the same facet is visible over the the observation time, and so it makes sense that the filter can obtain an estimate for the bias due mainly to the one facet. However, for the inertially fixed LEO spacecraft, the filter performed poorly. It appears that the sharp change in the values of the measurements that can be seen in Fig. 10.1c resulted in the filter becoming impoverished and being unable to accurately model the bias on the measurements.

With the way that the bias is computed and initialized, the addition of a second site doesn't improve the estimate of the bias at all, as the bias terms are site dependent. They are computed using the measurement geometry and line-of-sight vector for a given observatory. The effects of a second observatory can be seen by looking at the two-site results for the nadir GEO case as shown in Fig. 10.4.
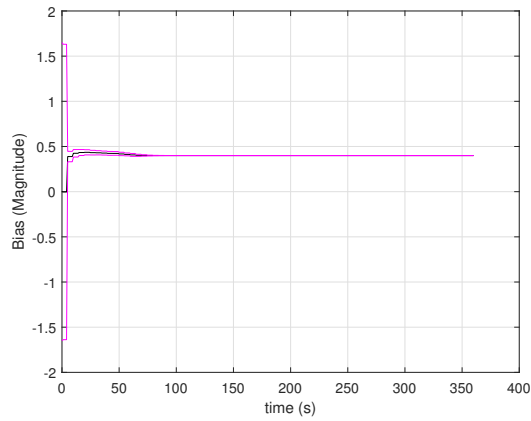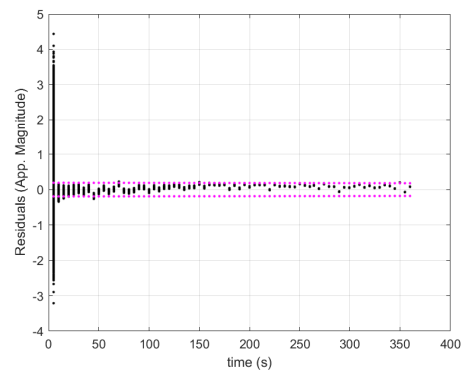
(a) Inertially fixed LEO, bias

(b) Inertially fixed LEO, residuals
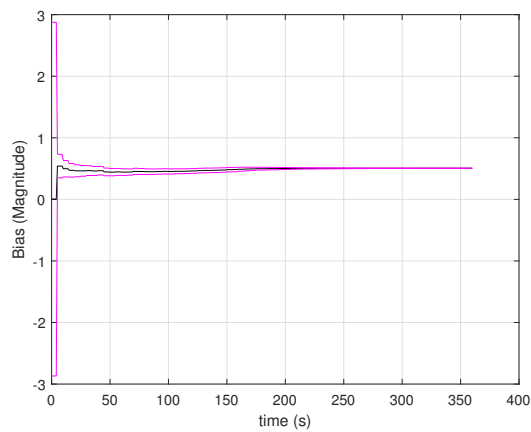
(c) GEO nadir, bias

(d) GEO nadir, residuals

Fig. 10.3: Model 1 bias-only estimation results for the inertially fixed LEO case and the nadir-pointing GEO spacecraft case
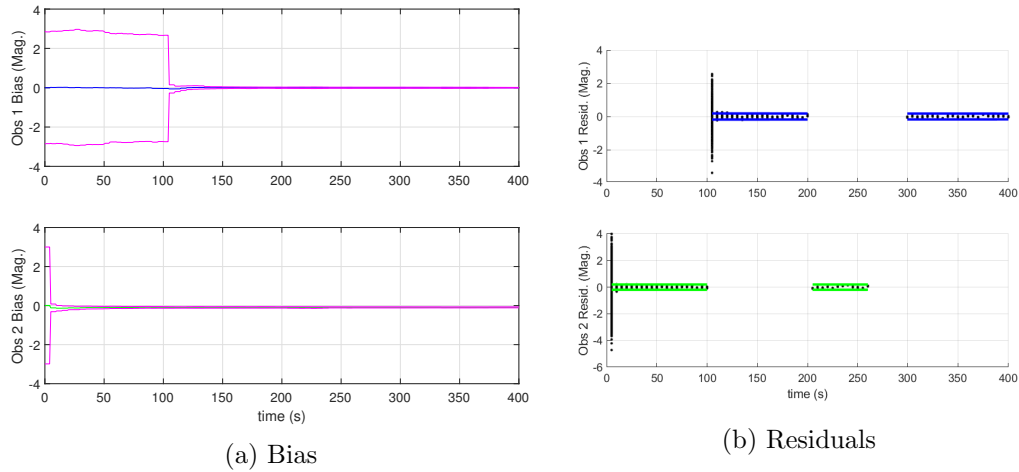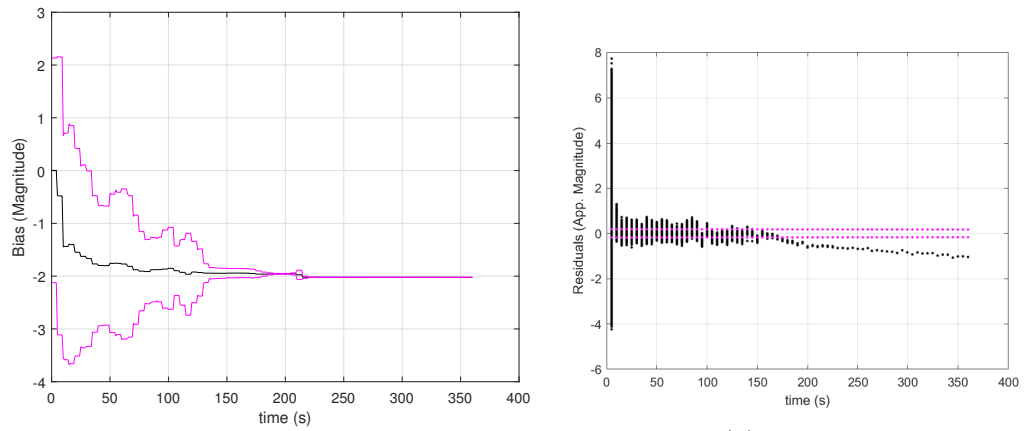
(a) Bias
(b) Residuals

Fig. 10.4: Model 1 bias results for the nadir-pointing GEO spacecraft with measurements from two observatories

Here in the figure it can be seen that the results are very similar to that of the single-site case. However, the fact is that the bias estimate doesn't improve with the addition of a second observatory. In the last chapter, it was established that in some instances the addition of a second observatory can help improve the estimate of the spacecraft attitude. This next section investigates the performance of the filter in estimating the bias terms along with the attitude states.

### 10.5.2 Combined bias and attitude estimation

From the conclusions of Chapter 9 it was established that the attitude estimation performance for the fast-spinning case doesn't improve with the addition of a second observatory. Furthermore, as the filter was unable to obtain an accurate estimate for the bias with a perfect knowledge of the attitude state for this case, it follows that it won't be able to perform well with the case when the attitude is unknown. Thus, this section for the combined estimation of the bias and attitude states will solely examine the results from the nadir-pointing GEO spacecraft. The results for a single observatory are shown in Fig. 10.5.

As can be seen from Fig. 10.5, for the single site, the BPF converges for the bias but is unable to obtain a good estimate for the attitude of the spacecraft. There is too much uncertainty in the system for a good estimate. For this case the best attitude estimates

(a) Bias

(b) Residuals
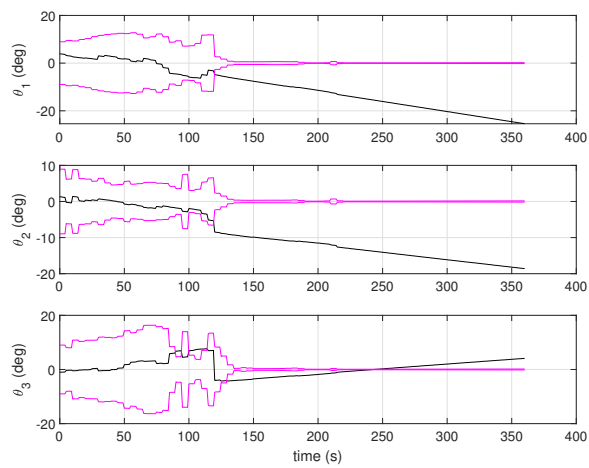
(c) Attitude

Fig. 10.5: Model 1 attitude and bias results for the nadir-pointing GEO spacecraft with measurements from a single observatory

were only obtained when using two observatories to view the spacecraft. To determine whether the improved attitude will aid in the combined attitude and bias estimation, Fig. 10.6 presents the results obtained using the two sites to observe the spacecraft.

(a) Bias

(b) Residuals
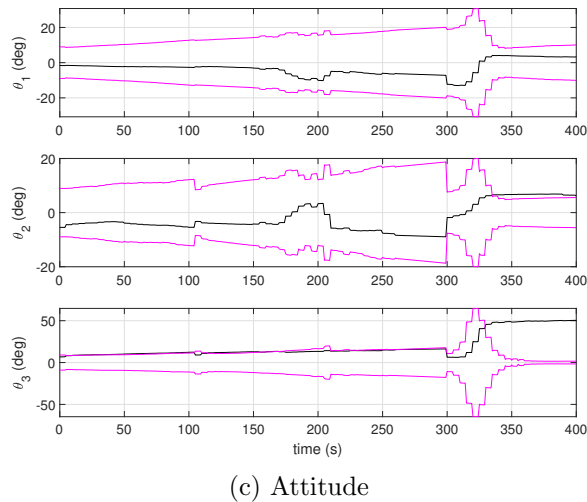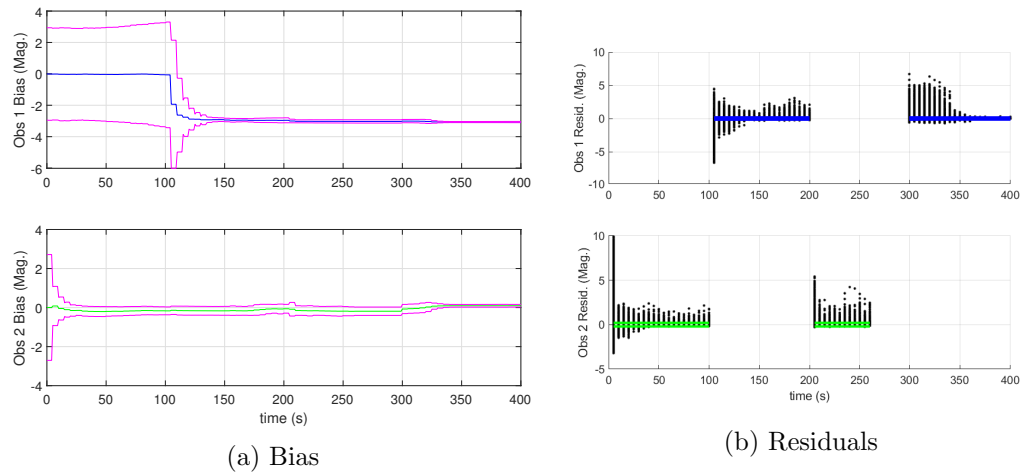
(c) Attitude

Fig. 10.6: Model 1 attitude and bias results for the nadir-pointing GEO spacecraft with measurements from two observatories

The addition of a second observatory did not affect a great change to the results. As before, the biases were able to converge, but did not yield a good estimate of the spacecraft attitude.

From all of the test results, the following conclusions can be made regarding Model 1. First, the model is able to obtain a good estimate of the measurement bias due to the

change in the reflection parameters when viewing the spacecraft rotating slowly so that the same facet is in view, which in turn results in only small changes to the measurement curves. The filter doesn't perform as well in estimating the bias if there is a sharp change in the measurement curve due to the specularity of the dominant facet (as seen with the inertial case) or if the facets are changing rapidly. A second conclusion to be made is that this model is not a good choice when attempting to estimate the attitude in conjunction with the bias. The filter failed to obtain a good estimate of the attitude, and the filter diverged when estimating the bias and attitude. This means that this model may be a good choice for estimating the measurement bias for something like a nadir-pointing spacecraft, but only for the cases where the attitude is known *a priori*. There may be applications where this might be the case, but as for general application, this filter isn't suitable.

10.6 Model 2—bias results and discussion

The second model to provide a potential alternative to having to estimate the reflection parameters directly is the bias modeled as an ECRV, Model 2. Unlike the previous bias model where the bias was constant, this model has dynamics that change with time. The time constant for this model is a function of the spacecraft angular velocity. This means that the covariance can grow with the rotation rate of the spacecraft to account for the changes in the facets. Making the time constant a function of the angular velocity has the effect of the bias being modeled similarly to the constant bias of Model 1 when the spacecraft is spinning very slowly, and being a constant bias when the spacecraft isn't rotating like for the inertially-fixed spacecraft. For that reason the results for the inertially fixed LEO spacecraft will not be examined in this section.

10.6.1   Bias-only results

The results for the parameter-only estimation for the fast-spinning LEO and the nadir-pointing GEO cases are shown in Figs. 10.7 and 10.8, respectively.
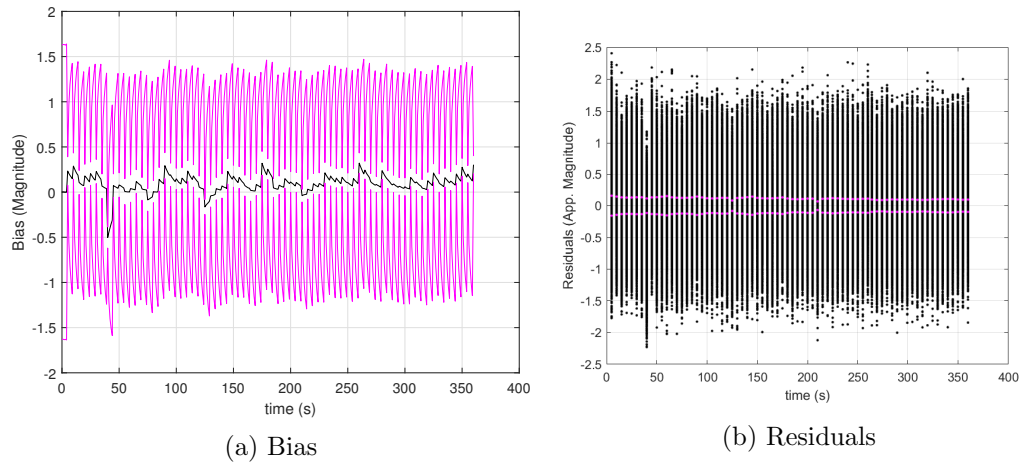

(a) Bias

(b) Residuals

Fig. 10.7: Model 2 bias results for the fast-spinning LEO spacecraft with measurements from a single observatory

As can be seen from the figures, for the fast-spinning LEO cases, the covariance decreases slightly after the first set of measurements, but beyond that point, the process noise of the ECRV causes the distribution of the expected measurements, or the bias distribution, to become very large. This is a direct result of large magnitude of the angular velocity vector. If the rotation rate is smaller, the noise will not be increased to such an extent. An example of this is the GEO spacecraft for which the results are shown in 10.8. For this case, the filter is able to obtain a very accurate estimate of the bias, and in 10.8b it can be seen that the expected measurement distribution falls very closely to the measurement noise, meaning that the filter was able to home in on the value of the bias.

10.6.2   Bias and attitude estimation results

This next set of results illustrates the performance of the filter when trying to estimate the spacecraft attitude along with the measurement bias. As the filter didn't perform well for the fast-spinning LEO case, the combined estimation will focus on the GEO nadir-
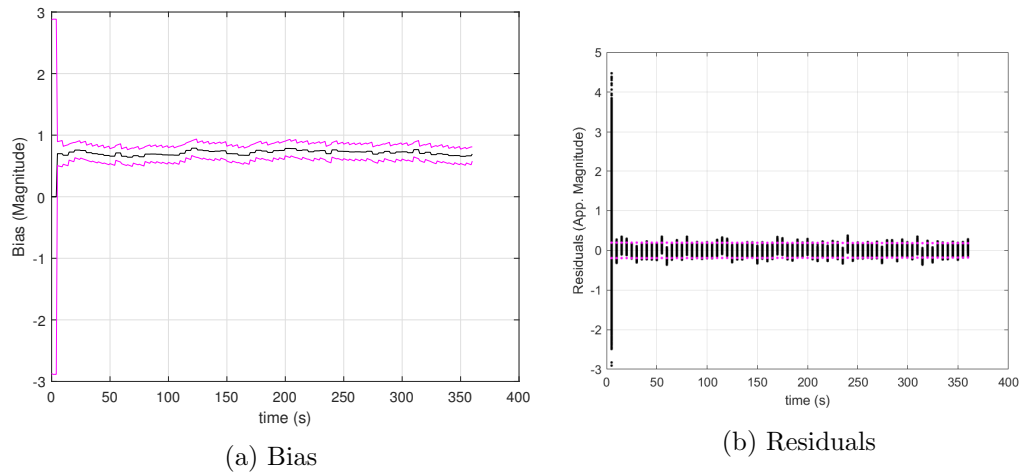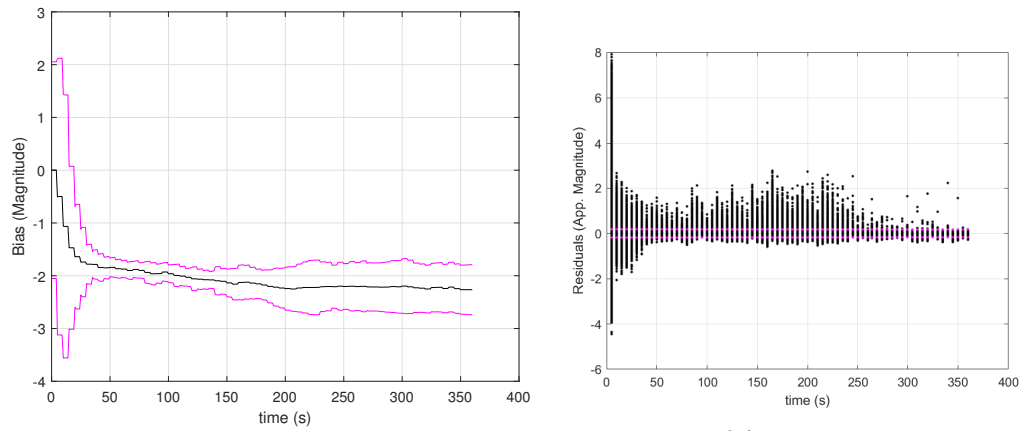
(a) Bias

(b) Residuals

Fig. 10.8: Model 2 results for the nadir-pointing GEO spacecraft with measurements from one observatory

pointing spacecraft. The results obtained from using only a single observatory are shown in Fig. 10.9.

In this set of results there are some interesting things to note. From 10.9c it is very clear that the filter is unable to estimate the spacecraft attitude in this case. The covariance bounds for all the cases grow over time, and in one case the filter diverges, or leaves the covariance bounds. The bias estimate is also unable to be well-determined, as can be seen in Fig. 10.9a. Previously in the bias-only estimation, the covariance stayed constant after being reduced initially once the first measurement was processed. However, in this case, the covariance drops down but then increases over time. It is lower than the initial value, but it doesn't support that the filter is really able to obtain a good estimate.

From the previous chapter, this setup for the attitude performed best when two different observatories were collecting the measurements. The results obtained when using two observatories to collect measurements are shown in Fig. 10.10.

From the figure it is again clear that in this case the filter is unable to determine the attitude of the spacecraft. The covariance grows for the whole observation period for all three of the angles. The covariance on the bias terms did decrease from the initial value, but the residuals show that the expected measurements are closely matching the measurement used to update the filter, and it is unable to help improve the estimate of the

(a) Bias

(b) Residuals
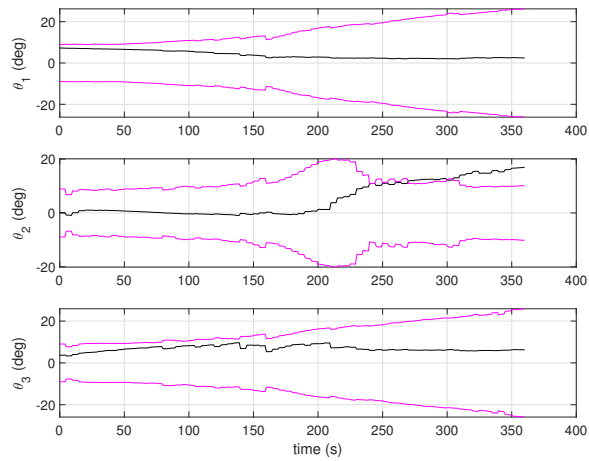
(c) Attitude

Fig. 10.9: Model 2 attitude and bias results for the nadir-pointing GEO spacecraft with measurements from a single observatory

(a) Bias

(b) Residuals

(c) Attitude

Fig. 10.10: Model 2 attitude and bias results for the nadir-pointing GEO spacecraft with measurements from two observatories

spacecraft attitude. Recall from Chapter 9 that the effectiveness of estimation process with the nadir-pointing GEO spacecraft is sensitive to the initial conditions of the attitude and the reflection parameters. Despite this mo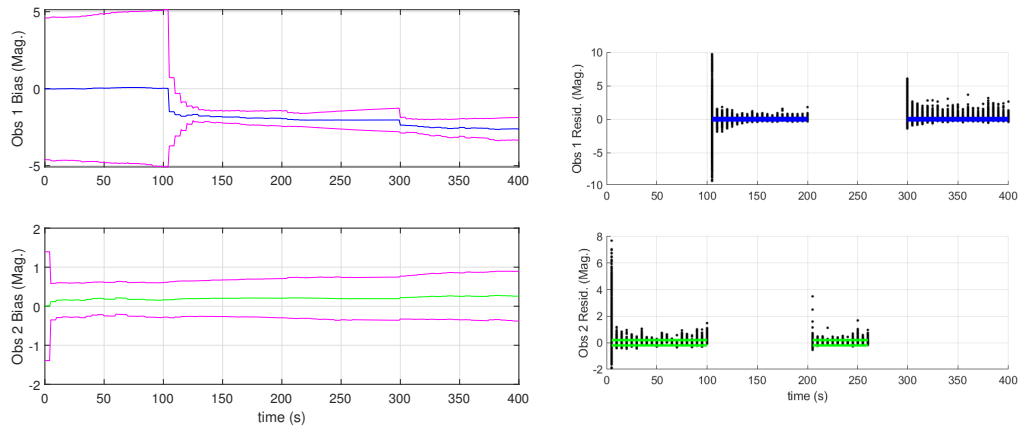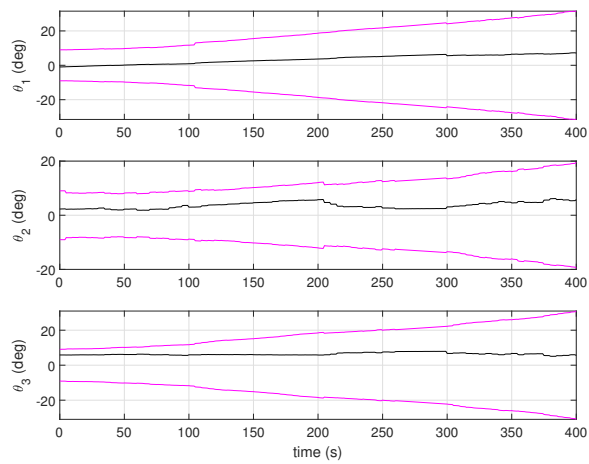del performing well when estimating the reflection parameters on their own, the combined uncertainties in the attitude and parameters makes the filter unable to estimate the attitude in this instance.

The two different bias models were very computationally efficient when compared to the direct estimation of the reflection parameters. However, as has been shown here and in the last section, they are not suitable for use when trying to estimate the attitude of the spacecraft along with the bias.

10.7   Model 3 - Parameter-only estimation results

Model 3 is the direct estimation of the reflection parameters themselves. This section presents the results obtained when estimating the different reflection parameters with a perfect knowledge of the attitude state. The combined attitude and reflection parameter results are presented in the following section.

The first set of results is for the test cases where the spacecraft attitude is assumed to be known perfectly, and only the reflection parameters are being estimated. This is done to determine whether this model is even a viable candidate for estimating the reflection parameters with the spacecraft attitude states. The first test investigated is that of the fast-spinning LEO spacecraft. Intuitively, it makes sense that the slow-spinning cases should be able to provide some improved estimate of the reflection parameters, as only a few facets are visible but are visible for a long period of time. For the fast-spinning cases, it seems less intuitive that there would be opportunities to extract the reflection parameters, as the individual facets are only visible for short periods of time and are changing rapidly. However, the results shown in Fig. 10.11 show that this is not the case and that the filter is able to estimate the values of the parameters even for the fast-spinning cases.

It is important to note that these results were generated with the accurate measurements, $r_{percent} = 1\%$, and for this instance in which only the parameters are being estimated, the uncertainties due to the other state variables are not considered.

(a) +X facet

(b) -X facet

(c) +Y facet
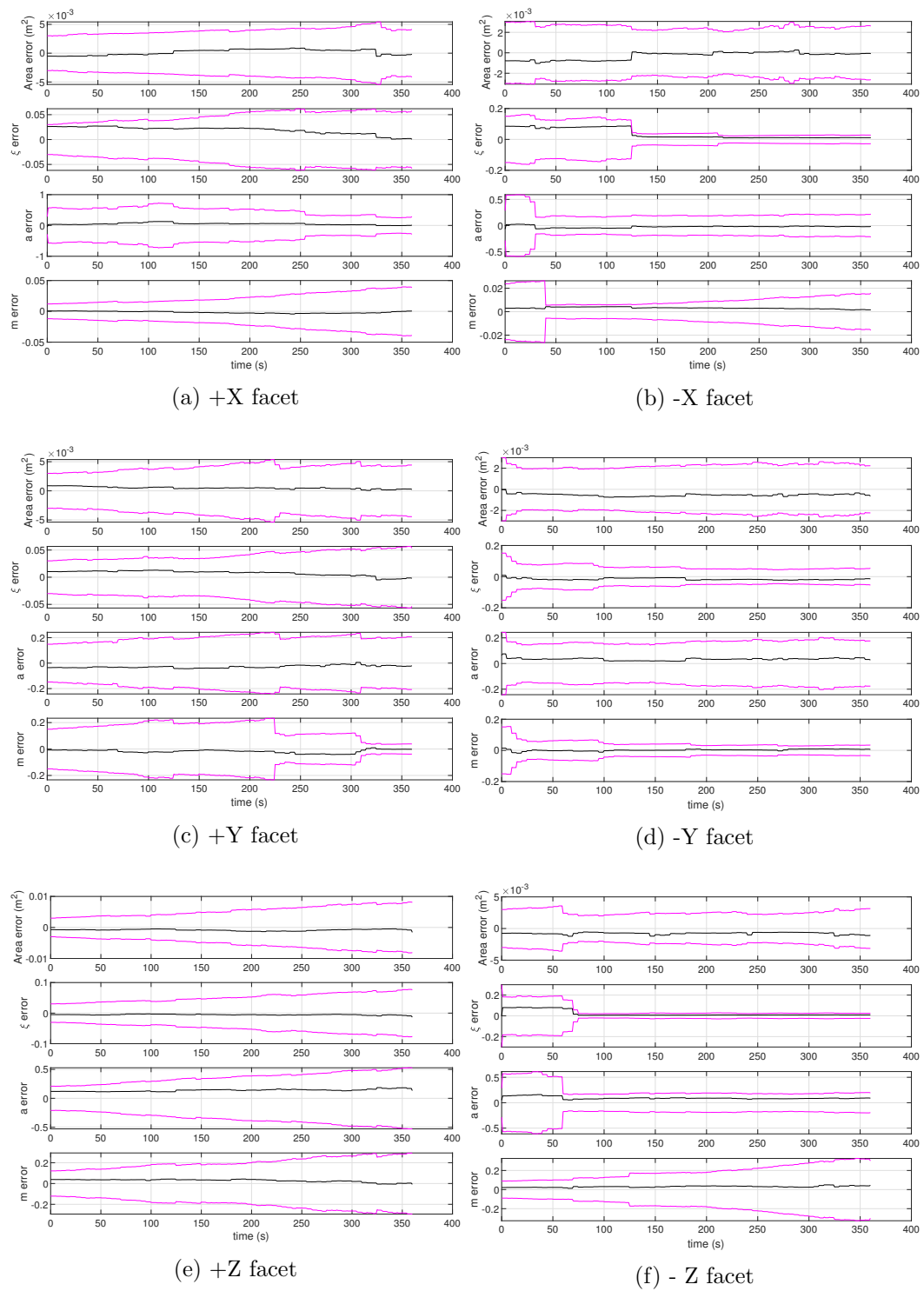
(d) -Y facet

(e) +Z facet

(f) - Z facet

Fig. 10.11: Single-site reflection parameter estimation results for the fast-spinning LEO spacecraft test case

From the figure it is clear that the filter was able to estimate some of the parameters. The parameters that are estimated are consistent with the times when the facets were visible, as is shown in Fig. 10.12.

In this fast-spinning case, it actually turned out that some of the facets were visible over much of the observation time. However, it is clear that the error in some of the facet parameters began to decrease as the facets became temporarily visible to the observer, which means that the parameter errors can be decreased with the fast-spinning cases.

The filter was able to improve the estimates of some of the parameters for all of the test cases where the parameter values were being estimated on their own without the attitude states also being estimated.

It is interesting to note that even for the visible facets, not all of the parameters were able to be estimated. In some cases the covariance bounds remained at the same level or actually increased over the observation time due to the effects of particle roughening. To better understand which parameters are able to be estimated while others are not, it is important to look at the different parameters for each of the different facets. All of the different runs for this case were completed with the CubeSat shape model shown below.

Table 10.1: Shape model for scaled GEO spacecraft

Axis	Area (m^2)	ξ	a	m
+X	0.01	0.1	0.95	0.04
-X	0.01	0.5	0.95	0.08
+Y	0.01	0.1	0.5	0.5
-Y	0.01	0.5	0.8	0.5
+Z	0.01	0.1	0.7	0.4
-Z	0.01	1	0.95	0.6

The general behavior for all of these different cases is that the error in the facet area wasn't really able to be estimated in any of the cases. It is likely that the other parameters had a larger effect on the change in the measurements than the area for this case, which is why it couldn't be estimated. The most diffuse facet is the -Z facet. From 10.11f it can
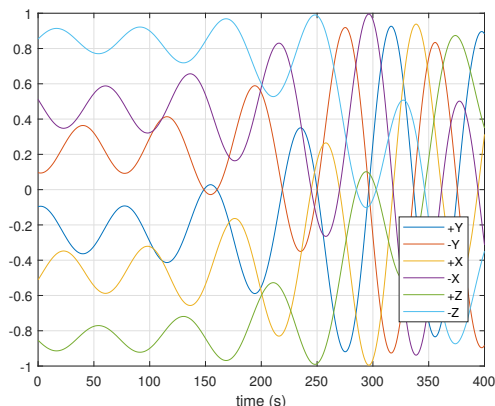
Fig. 10.12: Dot product between vector from spacecraft to Socorro, NM, and the facet normal vectors for the observation time

be seen that the two parameters that were able to be estimated were the specular diffuse weighting term ξ and the diffuse albedo term. It make sense in this case that the facet slope parameter would be unestimated, as specular reflection isn't used in this case.

One other interesting case is that the facets that are most specular by ξ are the $+X$, $+Y$, and $+Z$ facets, but in none of these cases does the estimate for ξ improve. The $+Z$ axis didn't really have much improvement at all in any of the parameters, because it was not very visible to the observer until the very end of the simulation. The facets, other than the $-Z$ facet, that were able to obtain good estimates for ξ were the $-X$ and the $-Y$ facet. This is an interesting result, as these two parameters had equal weighting for the specular and diffuse components.

The other parameter that greatly affects the specular component of reflection is the facet slope parameter, m. The two facets with the lowest value of m and, therefore, the most directional dependence in their measurements are the $\pm X$ facets. It is notable that the estimate of m didn't improve at all for the $+X$ facet and only improved temporarily for the $-X$ facet at the beginning of the observation time. It seems likely that the specular nature of the $+X$ facet wasn't seen in the latter half of the observation time, as the other facets could contribute to the measurement curve quickly. Indeed, in the measurement curve shown in Fig. 10.1a, there doesn't appear to be the specular spikes associated with that facet in the

part where the +X facet became visible. Instead the amount of light that was reflected back was a large factor, which is why the diffuse albedo estimate improved for that case.

The slow-spinning GEO spacecraft results support some of these conclusions. Recall from that for the GEO IC2 case, which was used for the nadir-pointing tests here, the +X facet is the most visible facet for the entirety of the observation time. This is facet that is pointing earthward. When estimating the reflection parameters, only the +X facet had any improvement in the estimates by the end of the observation time. The results for just this facet are shown in Fig. 10.13.
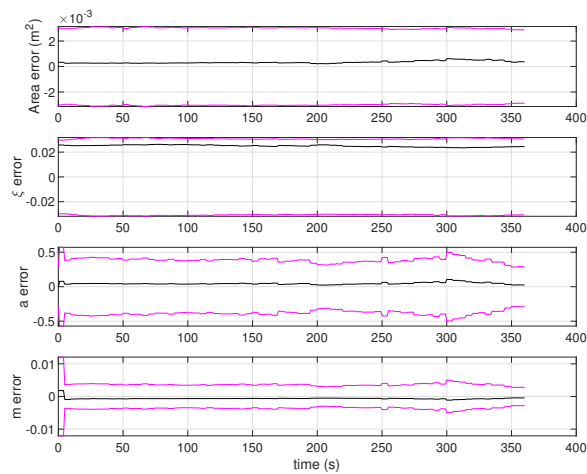
Fig. 10.13: +X facet estimation results for the nadir-pointing GEO spacecraft case

This case is when this facet is dominating the measurements, and the directional behavior of the facet is clear due to the changes in the light curve (see Fig 10.1e) that are due to slight changes in the measurement geometry. In this instance, the estimate of the microfacet slope parameter improves over time. The conclusion that can be drawn from these figures is that the ability to estimate the particular facet parameters depends on the contributions of the facet to the overall measurements and whether or not the measurement contribution is able to reveal information about the specular or diffuse contributions to the measurement. A more in-depth analysis could investigate the measurement contributions of the specular and diffuse components of each facet, but that is left as future work.

10.8   Model 3 - Combined parameter and attitude estimation

The goal of this dissertation is to investigate how well the attitude can be estimated in conjunction with the different reflection parameters. Thus far it has been established that the direct estimation of the reflection parameters can be accomplished in the case when the attitude is known perfectly. The next set of results investigates how well the reflection parameters and the attitude can be estimated together.

This section presents the results and conclusions obtained for estimating the full reflection parameters in conjunction with the spacecraft attitude and angular velocity. In addition to presenting an overview of the performance of the filters for the different orbital regimes and test cases, this section also presents results for both single- and two-observatory cases. Unlike the bias models presented earlier in which the addition of a second observatory simply added another state to the filter that did not do much to provide information about the other observatory bias, with estimating the parameters directly, the measurements from both observatories should be able to provide more information about the parameters, since they are the same for both observatories.

The first set of results to be presented is the fast-spinning LEO results. Recall from the previous chapter that the fast-spinning cases generally yielded the more accurate results. The following analysis is to determine if it is still possible to obtain the accurate attitude results even in the case where the parameters are unknown. For this first set of results, the initial uncertainties in the attitude and angular velocity states are $\sigma_\theta = 3°$ and $\sigma_\omega = 0.02$ deg/s, respectively, and only the more accurate measurement setup is used. Figure 10.14 shows the attitude and angular velocity results for this test case.

As can be seen from the figures, the filter is able to obtain a good estimate of both the attitude and the angular velocity of the spacecraft. Recall that a good estimate of the attitude is a result of a good estimate of the angular velocity, so from this point forward, only the attitude results will be shown unless the angular velocity is needed to provide additional insight. The results for the reflection parameter estimation are shown in Fig. 10.16.
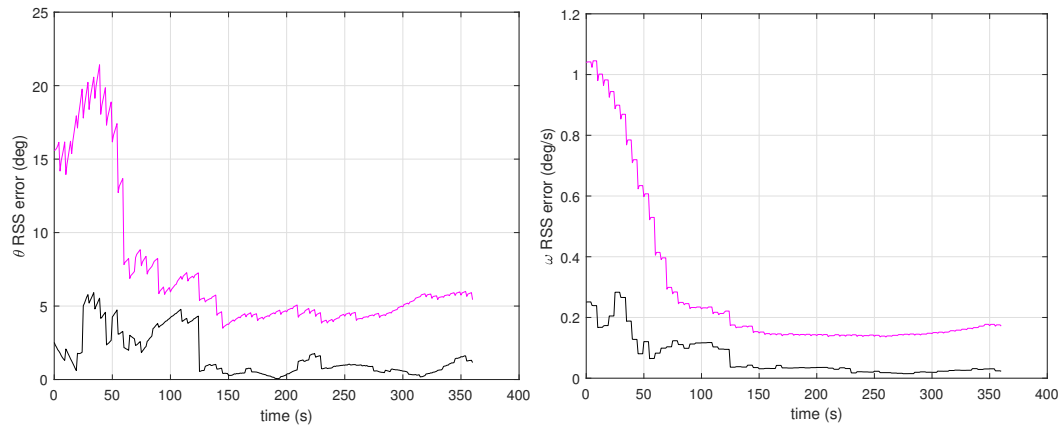
(a) RSS attitude results

(b) RSS angular velocity results
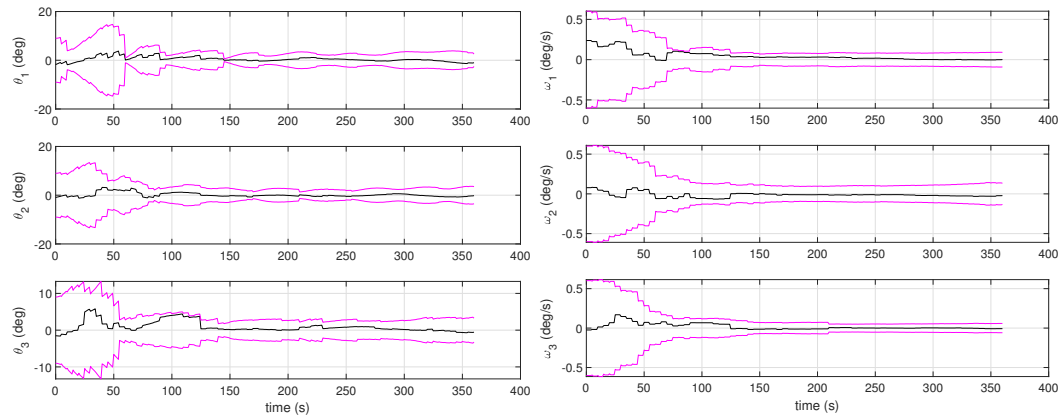
(c) Attitude component results

(d) Angular velocity component results

Fig. 10.14: Attitude and angular velocity results

(a) +X facet

(b) -X facet

(c) +Y facet

(d) -Y facet

(e) +Z facet

(f) -Z facet
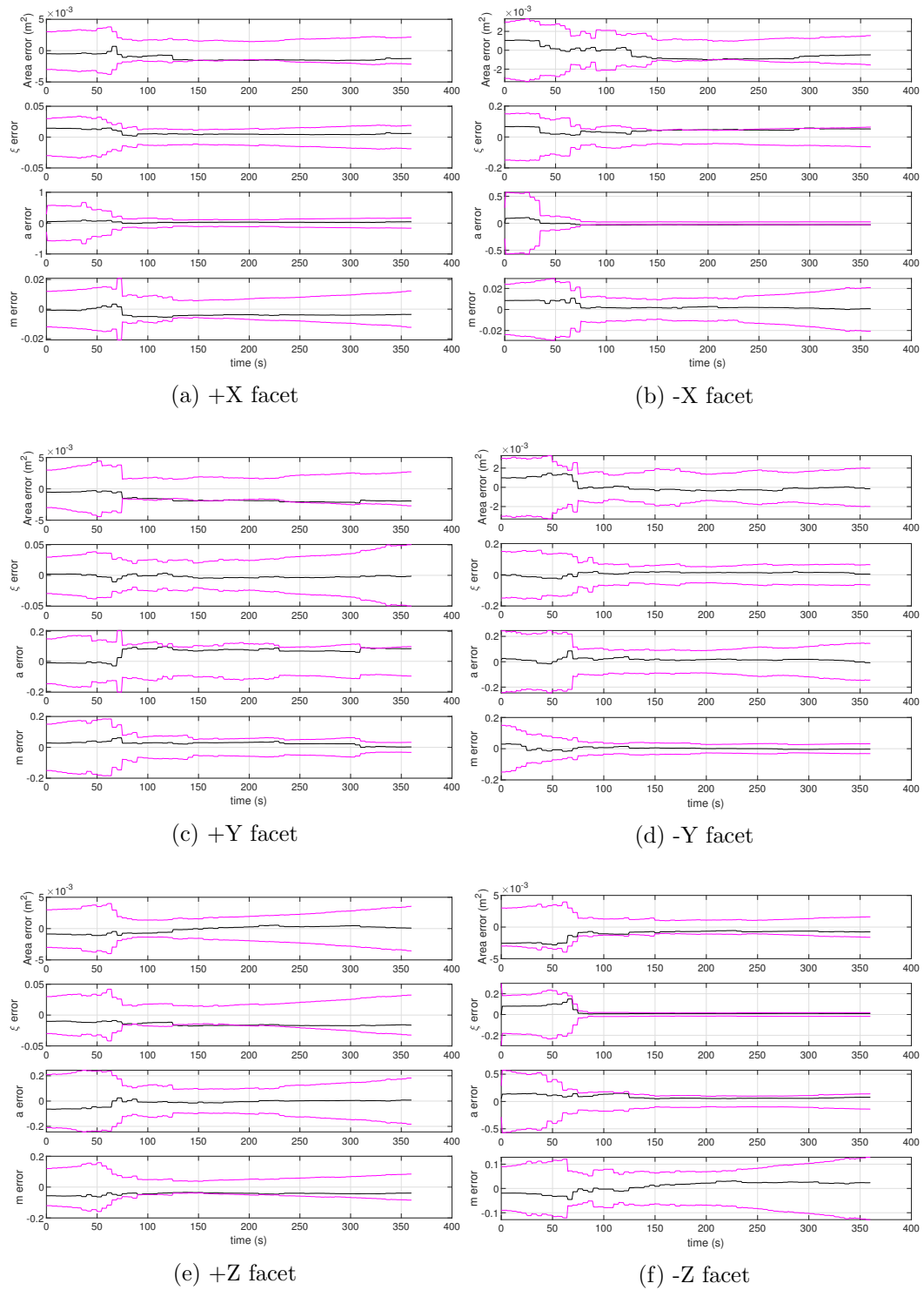
Fig. 10.15: Single-site fast-spinning LEO spacecraft reflection parameter results for combined parameter and attitude estimation case

This set of results is different from the results for just the reflection parameters shown in Fig. 10.11. The covariance decreases for some of the parameters even at a time when that facet isn't visible to the observer. The reasons for this can be seen from examining the residuals from the expected measurements of all of the particles and the measurement used to update the filter. These are shown in Fig. 10.16.
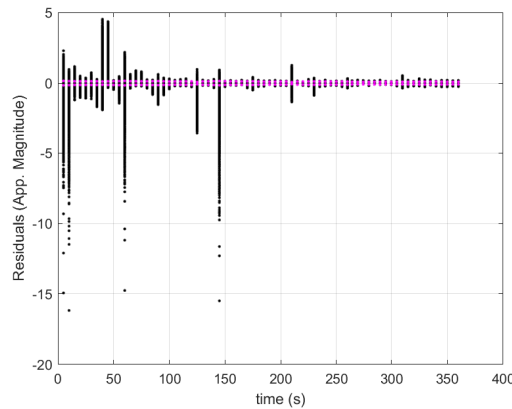
Fig. 10.16: Measurement residuals for combined attitude and reflection parameter estimation for fast-spinning LEO spacecraft

In looking at the residuals, there is a large distribution of measurements that occurred between 50 and 100 seconds, the times corresponding to the drop in covariance values for the different reflection parameters. The magenta dots at that point are the 3σ measurement covariance bounds, and the particles outside of these bounds are likely to be rejected in favor of those particles within the bounds. Since the distribution was so large compared to the actual measurement values, the diversity of all of the different particles was reduced at once. This is why the covariance bounds of the parameter estimates dropped at that point in time.

Another item to consider when looking at the residuals is that with the reflection model used, it is possible in some instances to obtain the same measurement with different combinations of parameters. Thus, the residuals are a key metric here as well, since they give the capability to see how well the particles with their state estimates are able to

generate measurements close to that of the measurement used to update the state. It is possible that the error could leave the covariance bounds, but the combination of the filter parameters could reproduce the same measurement value. If the expected measurements of the different particles falls along very close to or just outside the magenta covariance bounds of the residuals plot, then the estimates are at least able to somewhat predict the measurement behavior and could be used to obtain better estimates of the state variables.

The next set of results is for the same test setup but with two observatories switching off in collecting measurements. The setup for the two-site results is that observatory 2, BLO, UT, in this case, is collecting measurements from 0–100 seconds and 205–260 seconds after the epoch, and the first observatory, Socorro, NM, collects measurements from 105–200 seconds and from 300–400 seconds. It is the same setup as the switching cases of the attitude results. The attitude results are shown in Fig. 10.17, and the parameter results are presented in Fig. 10.18.

When comparing the attitude results shown in 10.17 to those in 10.14, the filters performed at about the same level in estimating the attitude of the spacecraft. The covariance bound for the two-site case didn't grow as large initially as that of the single-site case. Furthermore, while not dropping off as quickly as they did for the single-site case, the reflection parameter covariance has the general trend of decreasing somewhat at the points when they are visible to the observatory. The times when this occurs can be seen from examining Figs. 10.12 and 10.17c.

Overall, while there were some changes in the attitude estimates from the different test cases, the final covariance of the attitude components is very close to that of the initial covariance. To determine if there is a limit to what can be estimated with the given levels of uncertainty in the measurements, the test case where the initial uncertainty, σ_θ, in the attitude was increased from $3°$ to $10°$. The attitude and parameter estimation results are presented in Figs. 10.19 and 10.20.

From the plots of the attitude results shown in Fig. 10.19a, it is clear that the filter is able to bring the covariance of the attitude down over the observation time. This shows

(a) Attitude results

(b) Measurement residuals
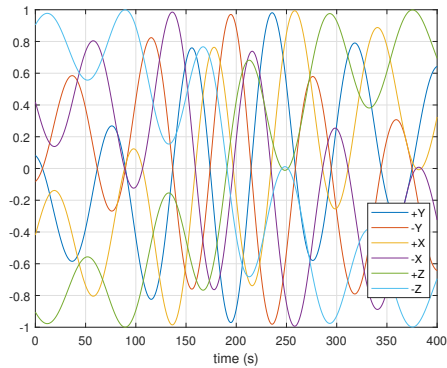
(c) Cosine of the angle between spacecraft normals and the spacecraft-to-observatory vector

Fig. 10.17: Attitude results for the combined attitude and reflection parameter estimation for the two-observatory fast-spinning LEO spacecraft case
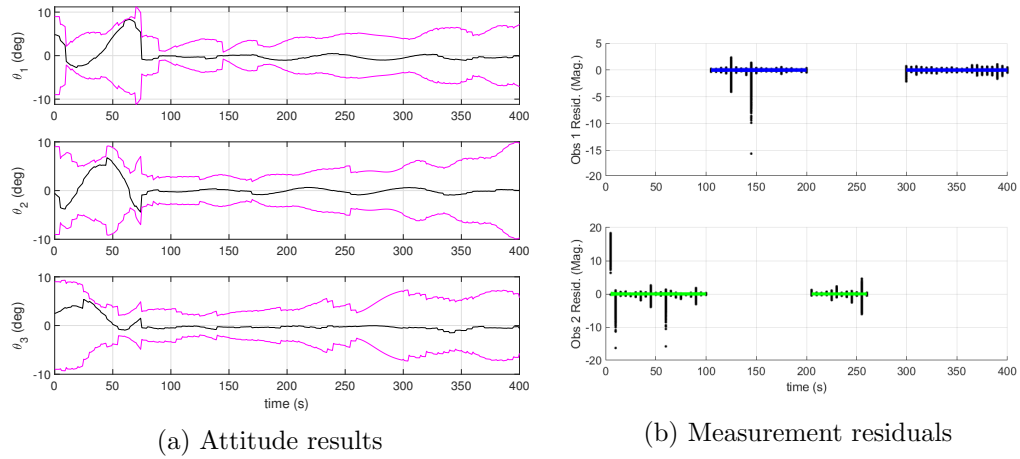
(a) +X facet

(b) -X facet

(c) +Y facet

(d) -Y facet

(e) +Z facet

(f) -Z facet

Fig. 10.18: Two-site fast-spinning LEO spacecraft reflection parameter results for combined parameter and attitude estimation case and $\sigma_\theta = 3°$

(a) Attitude results

(b) Measurement residuals

Fig. 10.19: Attitude results for the combined attitude and reflection parameter estimation for the two-observatory fast-spinning LEO spacecraft case with $\sigma_\theta = 10°$

that the filter is working and that there is some limit to the accuracy that is attainable with the given level of noise in the measurements. The accuracy of the reflection parameters themselves didn't change much with the increase of the uncertainty in the spacecraft attitude. For the case of the fast-spinning spacecraft, it is clear that the attitude can be estimated along with the direct estimation of the reflection parameters.

The next set of results was for the inertially fixed LEO spacecraft. Recall that the initial conditions for this case were the same for the fast-spinning spacecraft results from the previous chapter (not the ones for the fast-spinning LEO cases of this chapter). The attitude-only results from the single- and two-observatory cases are shown in Fig. 9.18, respectively. From the figures, it is clear that the filter was unable to obtain accurate estimates of all of the attitude elements, but was at least able to obtain an improved estimate for one of the angles for the single-site case, and two angles for the two-site case. This means that even for the best-case scenario with the combined parameter and attitude estimation case, it is unrealistic to expect the covariance to converge for all of the different attitude components. The single-observatory results for the combined attitude and parameter estimation are shown in Fig. 10.21.

Unlike the attitude-only estimation, adding the reflection parameters in addition to the attitude resulted in the covariance growing throughout the whole observation time. The

(a) +X facet

(b) -X facet

(c) +Y facet

(d) -Y facet
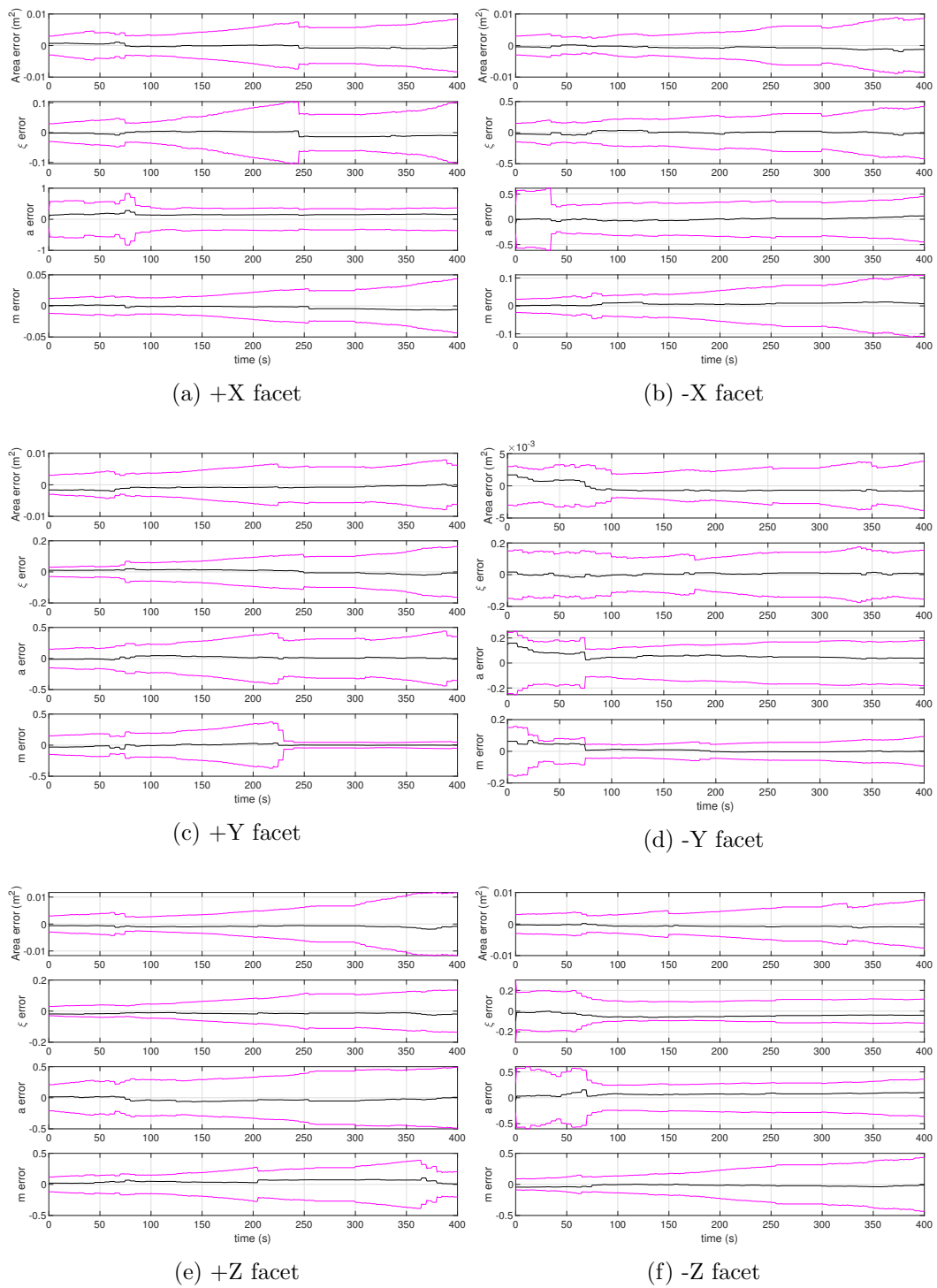
(e) +Z facet

(f) -Z facet

Fig. 10.20: Two-site fast-spinning LEO spacecraft reflection parameter results for combined parameter and attitude estimation case and $\sigma_\theta = 10°$
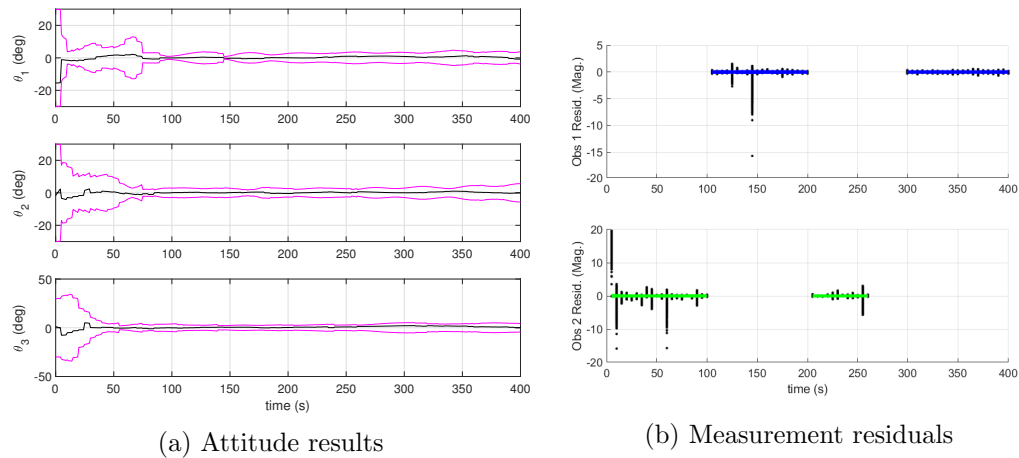
(a) Attitude results

(b) Measurement residuals

Fig. 10.21: Attitude results for the combined attitude and reflection parameter estimation for the single observatory, inertially fixed LEO spacecraft case with $\sigma_\theta = 3°$

uncertainty in the reflection parameters made it so that the filter was unable to operate at the same level as before. When adding a second site, however, the performance of the filter improved greatly. These results are shown in Fig. 10.22.

(a) Attitude results

(b) Measurement residuals

Fig. 10.22: Attitude results for the combined attitude and reflection parameter estimation for the two-observatory inertially fixed LEO spacecraft with $\sigma_\theta = 3°$

The results for the accompanying reflection parameters are presented in Fig. 10.23. For both the attitude and the reflection parameters, there was not a severe drop in the covariance bounds like there was for the fast-spinning LEO case. However, it is clear that the estimates of some of the parameters and attitude states improved over the course of the

observation time.

As there wasn't a sharp decrease in the covariance bounds, this test case was also run a second time with an increased value of the initial uncertainty in the initial spacecraft attitude estimate. The attitude and reflection parameter results for the case when $\sigma_\theta = 10°$ are shown in Figs. 10.24 and 10.25.

Once again, the increased uncertainty in the attitude state makes it clear that some of the attitude components are able to be estimated using the filter. If these results are compared to the results with the perfect knowledge of the reflection parameter, the attitude components' covariance bounds are much larger for the case presented here. That is to be expected with additional uncertainties in the system. However, these results show that there is potential in using this approach to determine the attitude and reflection parameters of a spacecraft.

The final set of results is for the nadir-pointing GEO spacecraft. In this case, one facet, the +X facet, dominates the list of the facets visible to the observer. As with the inertially fixed test case, the attitude-only estimation results weren't able to obtain an improved estimate for all three of the attitude components. So in the best case here, with the uncertain reflection parameters, it is improbable that the complete attitude state will be estimated by the filter. The single-site attitude results for this case are shown in Fig. 10.26, and the parameter results are shown in Fig. 10.27.

For this case, the results show that the filter produced an improved estimate of the attitude state and reflection parameters. To determine if adding a second observatory in this case could be helpful, the same test case was run, but with two observatories. These results are shown in Figs. 10.28 and 10.29.

For this test setup, the performance of the filter was actually worse for the two-site case. The attitude estimates didn't converge to the same level as before, and the covariance was slightly larger for the reflection parameters. The reason for why this occurred likely has to do with the specific light curves for the different observatories. In Fig. 10.1e the light curve increases steadily, and the change in magnitude is a result of the slight change in the

(a) +X facet

(b) -X facet

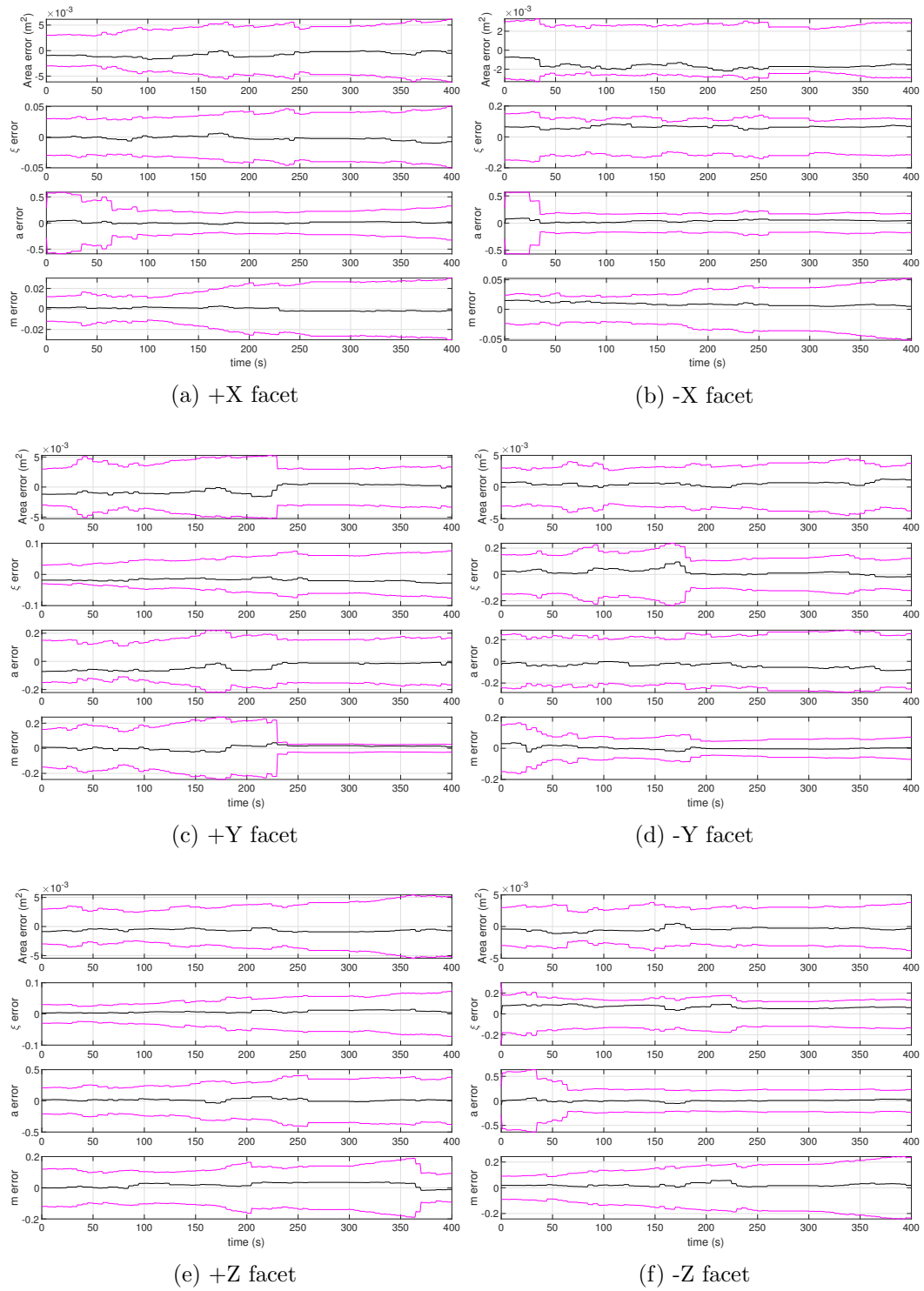(c) +Y facet

(d) -Y facet

(e) +Z facet

(f) -Z facet

Fig. 10.23: Two-site inertially fixed LEO spacecraft reflection parameter results for combined parameter and attitude estimation case with $\sigma_\theta = 3°$
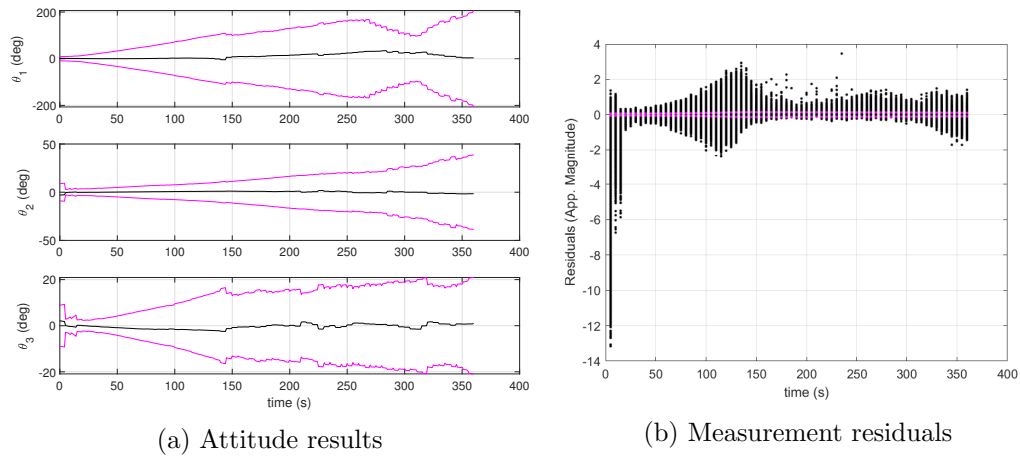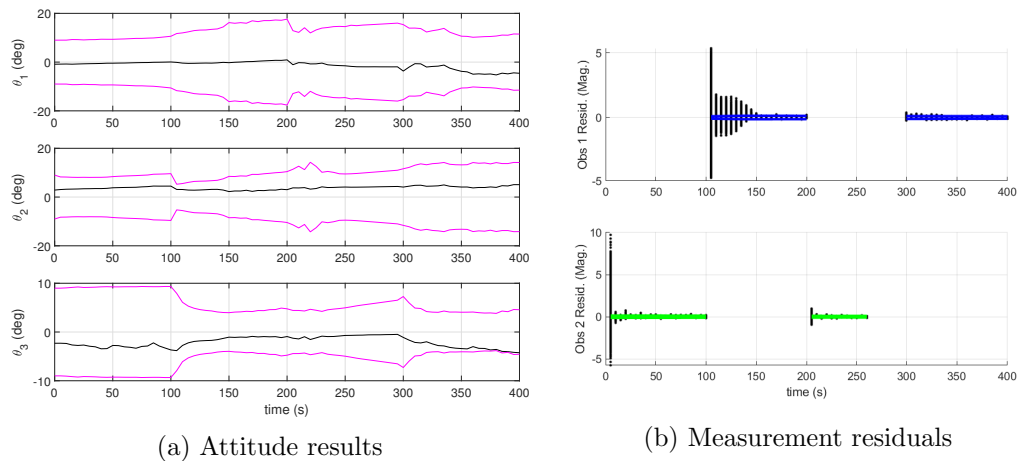
(a) Attitude results
(b) Measurement residuals

Fig. 10.24: Attitude results for the combined attitude and reflection parameter estimation for the two-observatory inertially fixed LEO spacecraft with $\sigma_\theta = 10°$

system reflection geometry. However, for the two-site case shown in Fig. 10.1f, the second site doesn't give the same drastic change, and the magnitude remains dim. This results in a poorer performance overall. However, even the two-site case provided an improved attitude estimate.

This section has shown that the direct estimation of the reflection parameters, while computationally expensive, can be estimated in a filter along with the spacecraft attitude parameters.

10.9   Summary and conclusion

This chapter presented the results and major conclusions obtained from investigating the estimation of the reflection parameter terms in addition to the spacecraft attitude. It was shown that the direct estimation of the reflection parameters yielded the best results. However, as the direct estimation of the reflection parameters is computationally expensive, one of the goals was to determine if a single bias on the measurement could be used as an alternative way to capture the change in measurements due to uncertainties in the reflection parameters. The results of the different test cases showed this to not be the case. The bias models were only effective when uncoupled from the estimation of the spacecraft attitude, and not for every case.

(a) +X facet

(b) -X facet
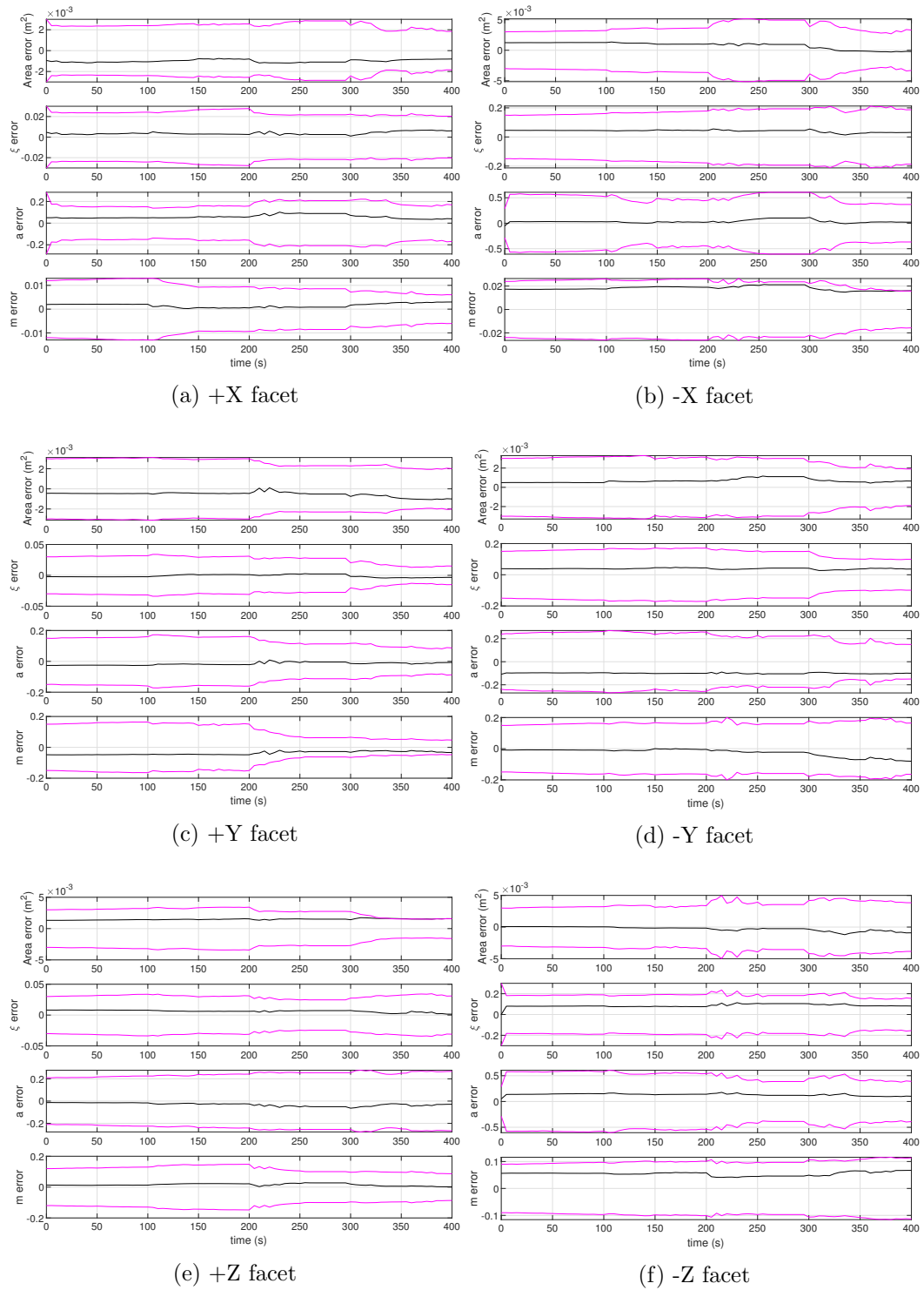
(c) +Y facet

(d) -Y facet

(e) +Z facet

(f) -Z facet

Fig. 10.25: Two-site inertially fixed LEO spacecraft reflection parameter results for combined parameter and attitude estimation case with $\sigma_\theta = 10°$
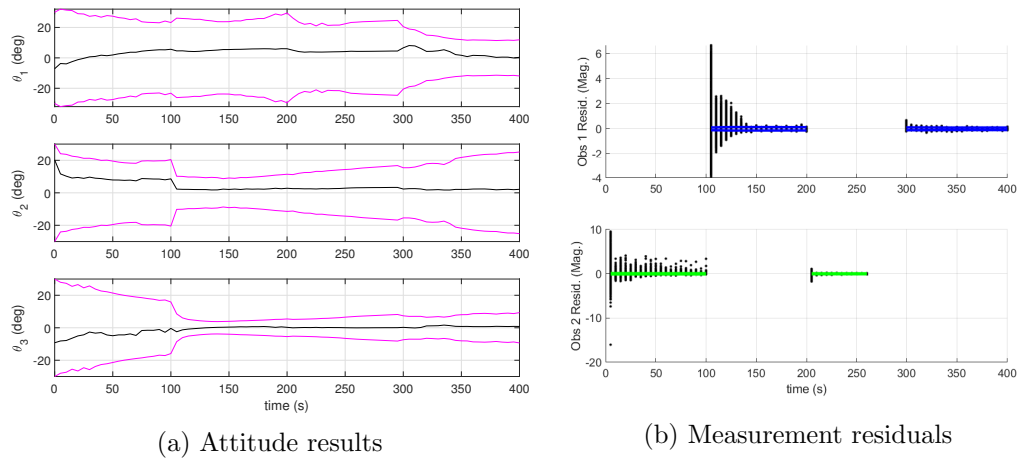
(a) Attitude results

(b) Measurement residuals

Fig. 10.26: Attitude results for the combined attitude and reflection parameter estimation for the single-observatory, nadir-pointing GEO spacecraft

While computationally expensive, the direct estimation of the reflection parameters provided good results when estimating the attitude and the reflection parameters themselves. However, there were some drawbacks associated with this approach. The first being that the attitude results weren't always as accurate as before when the shape model was known. In addition, Some of the parameters were unable to be estimated when processing the light curves. There just wasn't enough information to bring down the uncertainty values. Furthermore, due to ambiguities in the measurements, there were some instances where the filter would converge to a value for a parameter, but it did not match the truth value. This could make it difficult to know if the true parameter is being estimated or not.

One method that might be able to help provide a better estimate of the parameters is using the uncontrolled dynamics models, as some of the perturbations are functions of the reflection parameters. Another item to consider would be estimating the bias due to each facet rather than a single bias on the whole magnitude measurement. That might allow for more robust results. However, both of these considerations are left as future work.

(a) +X facet

(b) -X facet

(c) +Y facet

(d) -Y facet

(e) +Z facet

(f) -Z facet
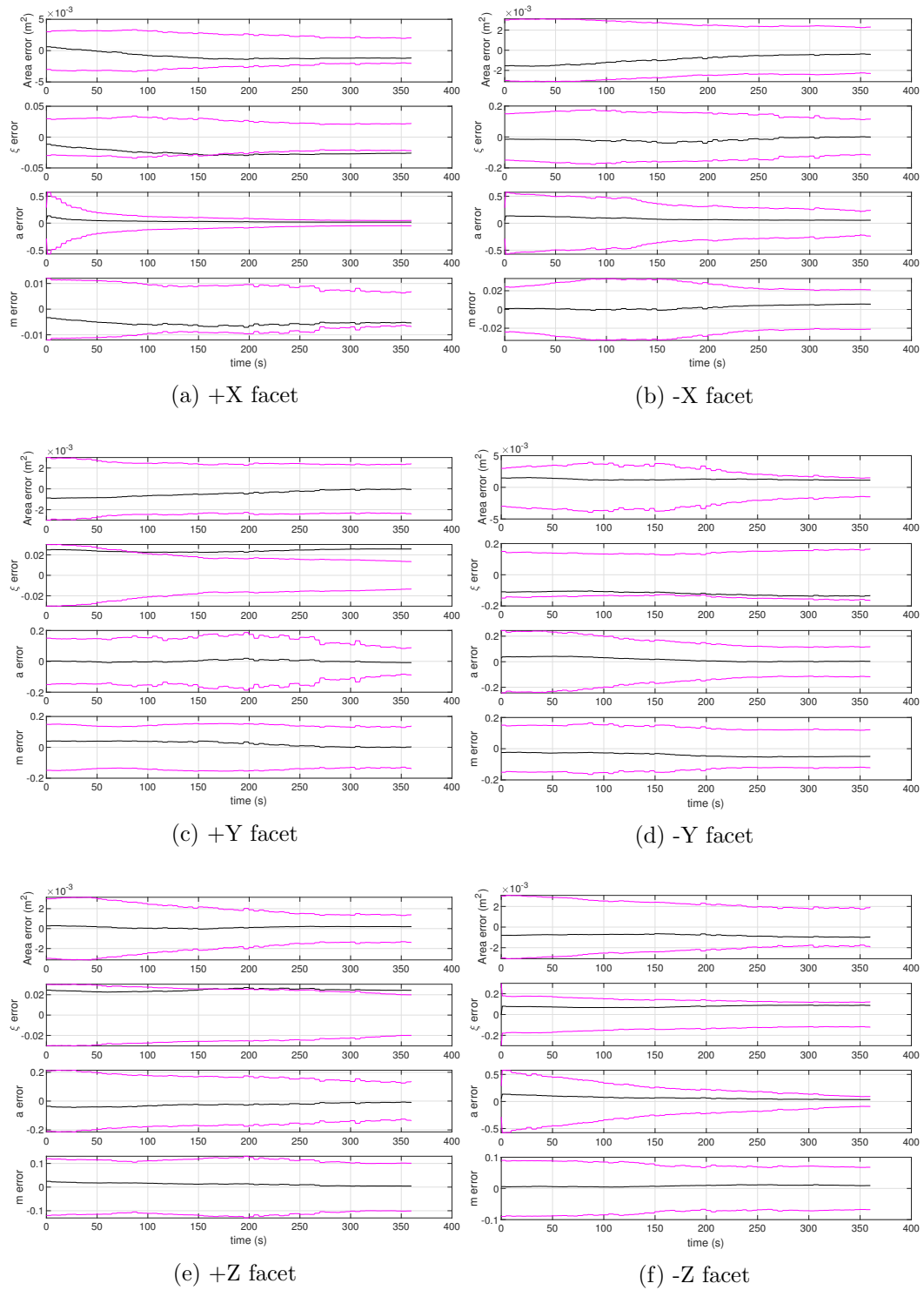
Fig. 10.27: Nadir-pointing GEO spacecraft reflection parameter results for combined parameter and attitude estimation case
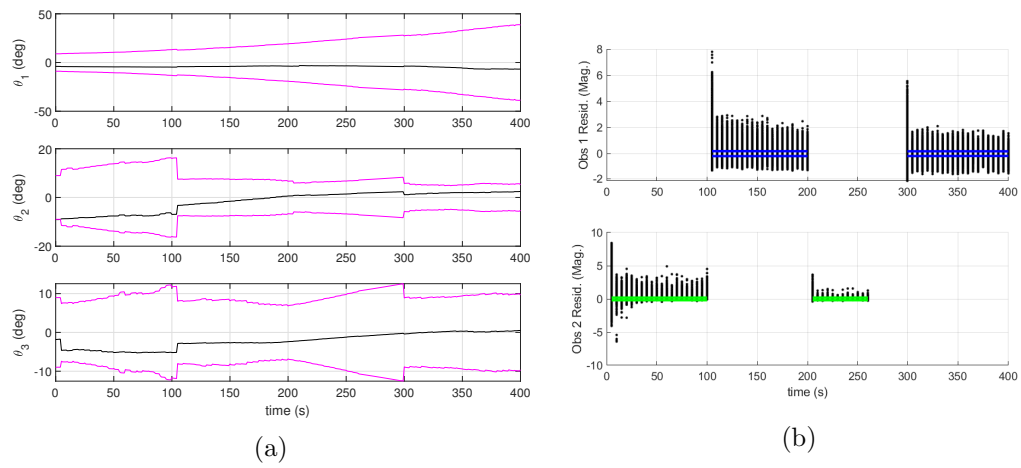
Fig. 10.28: Attitude results for the combined attitude and reflection parameter estimation for the two-observatory case with the nadir-pointing GEO spacecraft

(a) +X facet

(b) -X facet

(c) +Y facet

(d) -Y facet

(e) +Z facet

(f) -Z facet
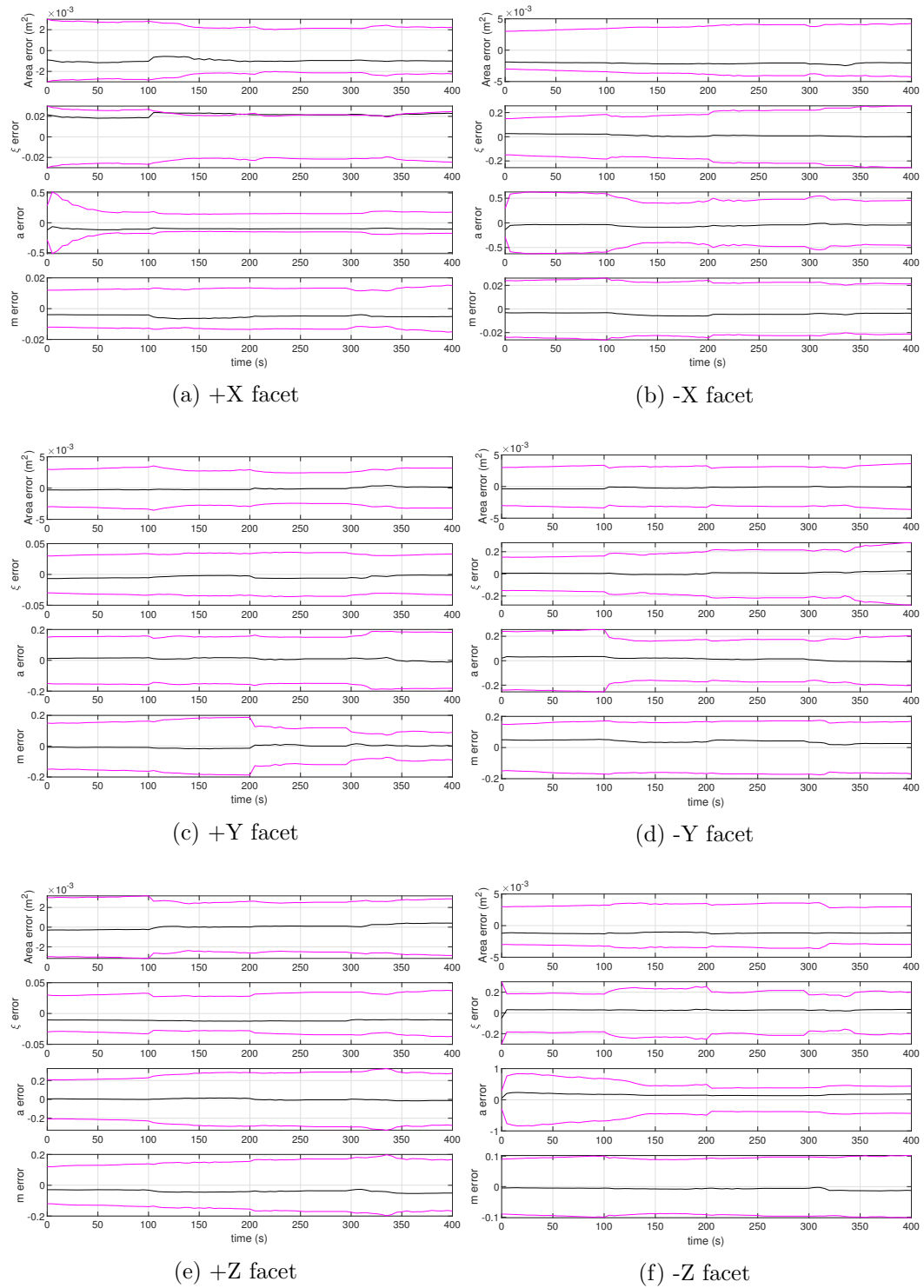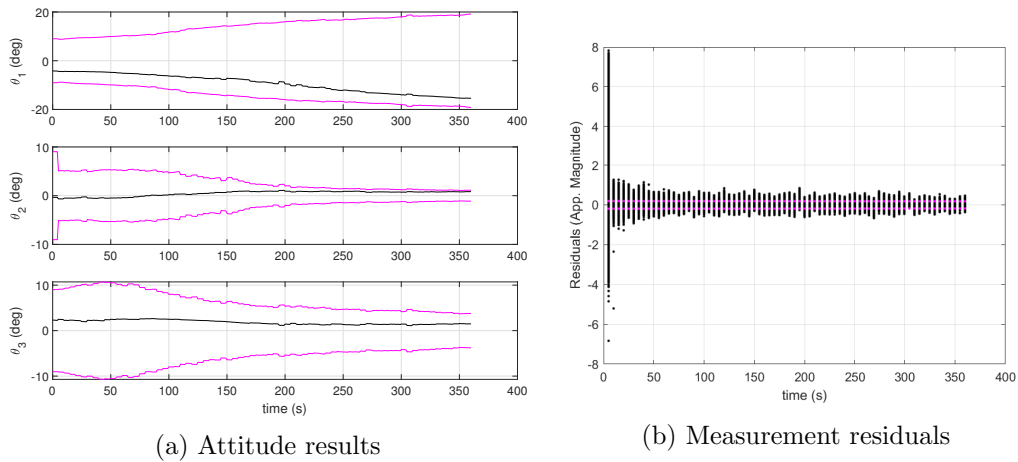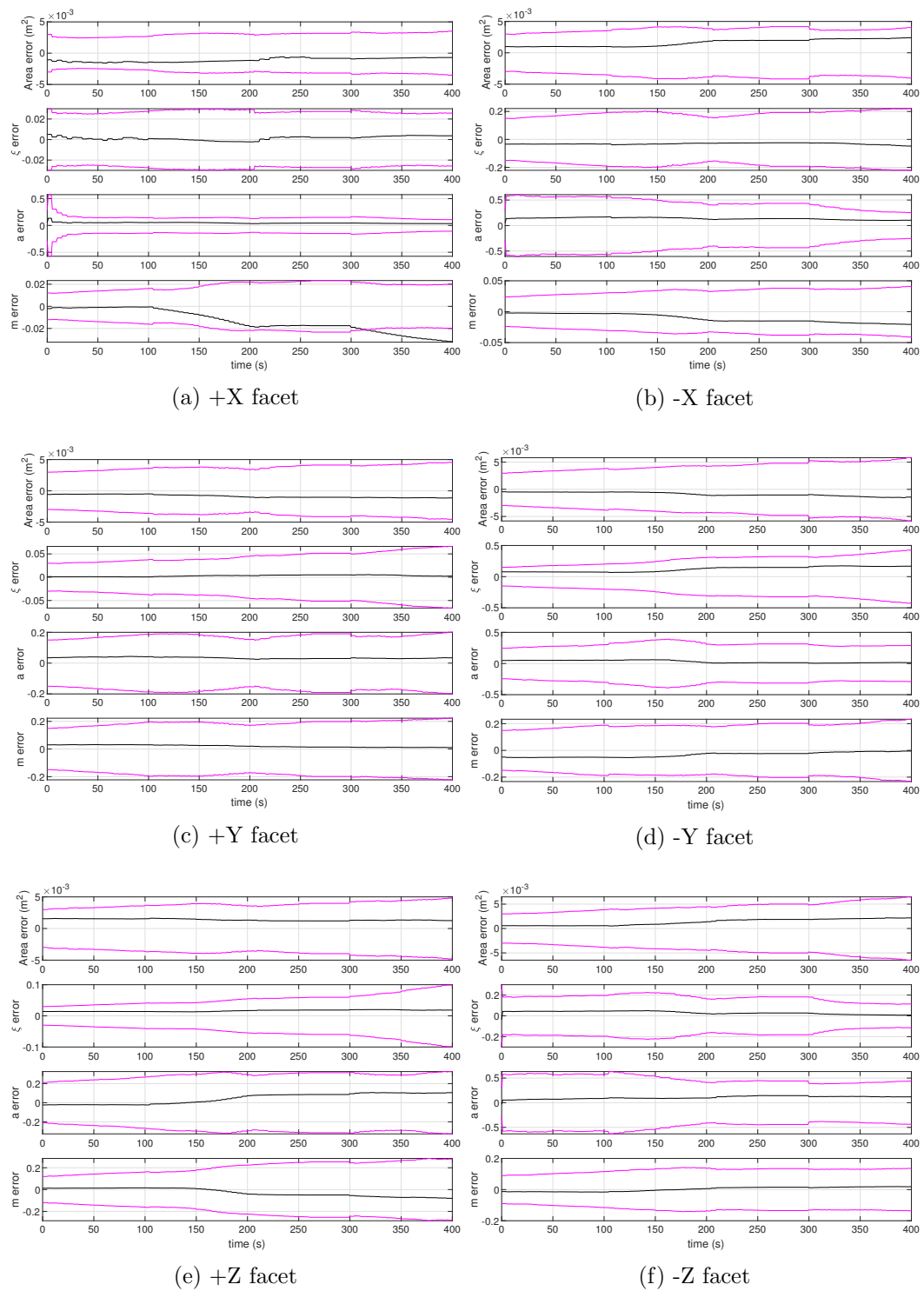
Fig. 10.29: Two-site nadir-pointing GEO spacecraft reflection parameter results for combined parameter and attitude estimation case

CHAPTER 11

SUMMARY AND CONCLUSIONS

The purpose of this chapter is to summarize the key contributions and conclusions that were arrived at in completing this research and were presented in the previous chapters. In addition, possible applications of this work are enumerated, and further research topics related to those of this dissertation are presented.

11.1   Summary

There are two key contributions of this work. The first is an in-depth analysis of the effects of different spacecraft variables and scenarios on the performance of various filters in estimating the attitude of a spacecraft with light curve measurements. The second contribution is the presentation, analysis, and evaluation of three models used to account for the effects of uncertainties in the reflection parameters of the spacecraft shape model.

Pertaining to the first item, there were a number of key findings related to the different scenarios and variables used in estimating the attitude of the spacecraft with light curve measurements. Out of the three different filters tested, it was found that the bootstrap particle filter (BPF) provided the most robust results when realizing the attitude estimation. Furthermore, it was found that out of LEO, MEO, and GEO scenarios, the most accurate results were obtained for the spacecraft in LEO. In addition, rotation rate of the spacecraft played a major role in the accuracy of the results obtained; the most accurate results were obtained for the fast-spinning spacecraft, which revealed multiple spacecraft facets to the observer collecting measurements. However, due to this, the addition of a second observatory did not much improve the attitude results for the fast-spinning spacecraft, but it did affect a change in the accuracy of the results obtained for the slower spinning spacecraft.

For the models used to simulate the effects of the uncertainties in the spacecraft shape model reflection parameters, Models 1 and 2 were two separate approaches used to model the bias on the apparent magnitude measurement, and Model 3 was the direct estimation of the parameters. It was shown that Models 1 and 2 were ill-suited to estimate the spacecraft attitude along with the bias terms, while Model 3 was able to estimate the reflection parameters along with the spacecraft attitude.

Despite the fact that Model 3 performed better than the other two filters when estimating the attitude and the parameters, it still had limitations affecting its overall performance. With each of the different runs, not all of the parameters were able to be estimated. Furthermore, on some occasions the filter would lock onto an erroneous solution for some of the parameters, but the measurements would still be at the same level as the truth model due to nature of the measurement model. While the measurement residuals may come out to a similar level for the filter updates, if the goal is to use the shape parameters estimates in other models such as SRP models, the erroneous parameters could prove problematic.

11.2   Applications

This section briefly presents some of the applications of the work presented in this dissertation. This helps to establish the context and limitations of the research in preparation for discussing the potential future extensions to this line of work. The potential future work is presented in the next section.

In the course of performing this research, a number of simplifying assumptions were made. Some of these assumptions include having prior knowledge of the shape model of the spacecraft, having a perfect knowledge of the spacecraft orbit, and the simplifying assumptions presented with the shape and measurement model in Chapter 5. These assumptions limit the different possible real-world applications of this work.

One of the best-use case scenarios that could be implemented considering all of these assumptions is the case when a satellite operator loses contact with their satellite and would like to determine the attitude in order to improve their ability to reestablish contact with the satellite. In this case the operator could have very good estimates of the spacecraft's shape

parameters, orbit, and attitude before the moment that they could no longer communicate with the satellite. Under these conditions, light curve measurements could be used to better improve the spacecraft attitude estimates.

Another use case for application is for a satellite operator to better determine the attitude of a satellite that is no longer operational. In this case the operator would have knowledge of the shape of the spacecraft, but may not have a very accurate attitude estimate. Light curves could be used to improve the spacecraft attitude estimate, which in turn could lead to a better orbit estimate and aid in later debris removal or collision analysis. However, before this can be widely applied, it may first be necessary to further investigate this topic of research to improve the overall attitude and reflection parameter estimation presented in this work.

11.3   Future work

To make this work more applicable to real-world situations, there are a number of items that have been left as future work or continuations to this research. One of these items is the combined estimation of the spacecraft attitude and its orbit. Along with the magnitude of an object, electro-optical telescope images can provide angle data that are used in the estimation of the spacecraft orbit. It is possible that the combined orbit and attitude estimation could lead to better estimates of the spacecraft reflection parameters. This is especially true of high-altitude spacecraft, as the solar radiation pressure is one of the larger perturbations in those regimes.

For the combined estimation of a satellite's attitude and orbit to be most effective, the instances of the reflection parameter estimation with the uncontrolled spacecraft dynamics would have to be implemented. The results presented in Chapter 10 were strictly for the controlled dynamics models. Further extension of this work includes incorporating the perturbations that couple the attitude and orbit together for their joint estimation.

In addition to the dynamics models used, it is left to future work to investigate the performance of different shape models. All of the results presented in this dissertation were for a spacecraft with a cubic shape model. It is possible that cylinders representing

rocket bodies, or flat plates for solar panels, could yield different forms of light curves that could be easily identifiable and aid later in the characterization of objects of known shape. Furthermore, many spacecraft have solar panels or other components that make their shape nonconvex, so it would be helpful to investigate the performance of the spacecraft attitude using light curves for the case where the shape model is nonconvex, or in approximating a nonconvex shape as convex shape.

To improve the estimation of the reflection parameters, there are two avenues that could prove useful in the future. The first is adjusting the measurement model to account for telescope filters being used to generate the measurement, and the second is to examine the feasibility of using a single bias for the individual facets of the spacecraft.

Generally, when taking photometric measurements, filters are used on the EO telescope to provide for better comparison with known stars, and thus provide more accurate magnitude measurements [50]. The reflectance of the different objects can occur differently at different wavelengths; thus, investigating different combinations of filters and observatories could prove insightful and provide more detailed information about the physical reflection properties of the spacecraft.

While not improving the actual knowledge of the values of the spacecraft reflection properties, there is another set of models that could possibly reduce computation time when trying to estimate the spacecraft attitude while also accounting for the uncertainties in the shape model reflection parameters. Recall that Models 1 and 2 used only a single measurement bias to try to account for the effects of uncertainties in all of the different facets of the spacecraft shape model. While this was sufficient for the cases when the attitude was known perfectly, these models failed when trying to jointly estimate the attitude and the measurement bias. It is possible that a model where each of the facets has a unique bias that is estimated could provide useful for modeling the effects of the uncertainties in the reflection parameters while incorporating a much-reduced number of states in the filter. This approach would potentially greatly speed up each of the individual filter runs.

The final item left to future work is the actual implementation of these algorithms with real-world spacecraft and measurements. All of the analyses presented in this work were performed in simulation. Using actual spacecraft and operator data, these algorithms could be tested and validated so that they could become more widespread in their use. The testing of these results against actual spacecraft data would be very beneficial and would provide a lot of information about the accuracy of these models.

As more and more objects are launched into space each year, there is a commensurate increase in the need to be able to provide accurate and timely information about these spacecraft—a need for increased space situational awareness. This research can aid in this effort in allowing for better estimation of the attitude and reflection parameters of a spacecraft.

REFERENCES

[1] Piergentili, F., Santoni, F., and Seitzer, P., "Attitude Determination of Orbiting Objects from Lightcurve Measurements," *IEEE Transactions on Aerospace and Electronic Systems*, Vol. 53, No. 1, 2017, pp. 81–90.

[2] Yanagisawa, T. and Kurosaki, H., "Shape and motion estimate of LEO debris using light curves," *Advances in Space Research*, Vol. 50, No. 1, 2012, pp. 136–145.

[3] Linares, R., Jah, M. K., Crassidis, J. L., and Nebelecky, C. K., "Space object shape characterization and tracking using light curve and angles data," *Journal of Guidance, Control, and Dynamics*, Vol. 37, No. 1, 2013, pp. 13–25.

[4] Kaasalainen, M., Torppa, J., and Muinonen, K., "Optimization methods for asteroid lightcurve inversion: II. The complete inverse problem," *Icarus*, Vol. 153, No. 1, 2001, pp. 37–51.

[5] Silha, J., Schildknecht, T., Pittet, J.-N., Bodenmann, D., Kanzler, R., Kärräng, P., and Krag, H., "Comparison of ENVISATs attitude simulation and real optical and SLR observations in order to refine the satellite attitude model," *AMOS Technical Papers*, 2016.

[6] Battin, R. H., *An introduction to the mathematics and methods of astrodynamics*, Aiaa, 1999.

[7] Bond, V. R. and Allman, M. C., *Modern astrodynamics: fundamentals and perturbation methods*, Vol. 51, Princeton University Press, 1996.

[8] Markley, F. L. and Crassidis, J. L., *Fundamentals of spacecraft attitude determination and control*, Vol. 33, Springer, 2014.

[9] Holzinger, M. J., Alfriend, K. T., Wetterer, C. J., Luu, K. K., Sabol, C., and Hamada, K., "Photometric attitude estimation for agile space objects with shape uncertainty," *Journal of Guidance, Control, and Dynamics*, Vol. 37, No. 3, 2014, pp. 921–932.

[10] Hall, D., Calef, B., Knox, K., Bolden, M., and Kervin, P., "Separating attitude and shape effects for non-resolved objects," *The 2007 AMOS Technical Conference Proceedings*, Maui Economic Development Board, Inc. Kihei, Maui, HI, 2007, pp. 464–475.

[11] Linares, R., Jah, M. K., Crassidis, J. L., Leve, F. A., and Kelecy, T., "Astrometric and photometric data fusion for inactive space object mass and area estimation," *Acta Astronautica*, Vol. 99, 2014, pp. 1–15.

[12] Linares, R., Crassidis, J. L., Wetterer, C. J., Hill, K. A., and Jah, M. K., "Astrometric and photometric data fusion for mass and surface material estimation using refined bidirectional reflectance distribution functions-solar radiation pressure model," Tech. rep., PACIFIC DEFENSE SOLUTIONS LLC KIHEI HI, 2013.

[13] Richardson, M., *Mass Estimation Through Fusion of Astrometric and Photometric Data Collection with Application to High Area-to-mass ration objects*, Master's thesis, California Polytechnic State University, 2017.

[14] Linares, R., Leve, F. A., Jan, M. K., and Crassidis, J. L., "Space object mass-specific inertia matrix estimation from photometric data," *Advances in the Astronautical Sciences*, Vol. 144, 2012, pp. 41–54.

[15] Henderson, L. S., *Modeling, estimation, and analysis of unresolved space object tracking and identification*, Ph.D. thesis, The University of Texas at Arlington, 2014.

[16] Linares, R., Jah, M. K., and Crassidis, J. L., "Inactive space object shape estimation via astrometric and photometric data fusion," *Adv. Astronaut. Sci.*, Vol. 143, 2012, pp. 217–232.

[17] Wetterer, C. J., Hunt, B., Hamada, K., Crassidis, J. L., and Kervin, P., "Shape, surface parameter, and attitude profile estimation using a multiple hypothesis unscented Kalman filter," *Adv. Astronaut. Sci.*, Vol. 152, 2014, pp. 1475–1484.

[18] Linares, R. and Crassidis, J. L., "Space-Object Shape Inversion via Adaptive Hamiltonian Markov Chain Monte Carlo," *Journal of Guidance, Control, and Dynamics*, 2017, pp. 1–12.

[19] Bradley, B. and Axelrad, P., "Lightcurve Inversion for Shape Estimation of GEO Objects from Space-Based Sensors," *Univ. of Colorado. International Space Symposium for Flight Dynamics*, 2014.

[20] Früh, C. and Schildknecht, T., "Analysis of observed and simulated light curves of space debris," *Proceedings of the international Astronautical Congress*, 2010.

[21] Jah, M. and Madler, R. A., "Satellite characterization: angles and light curve data fusion for spacecraft state and parameter estimation," *Proceedings of the Advanced Maui Optical and Space Surveillance Technologies Conference*, Vol. 49, 2007.

[22] Coder, R. D., Holzinger, M. J., and Linares, R., "3DOF Estimation of Agile Space Objects Using Marginalized Particle Filters," *AIAA Journal of Guidance, Control, and Dynamics, Submitted*, 2016.

[23] Hinks, J. C., Linares, R., and Crassidis, J. L., "Attitude observability from light curve measurements," *AIAA Guidance, Navigation, and Control (GNC) Conference*, 2013, p. 5005.

[24] Dianetti, A. D., Weisman, R., and Crassidis, J. L., "Observability Analysis for Improved Space Object Characterization," *Journal of Guidance, Control, and Dynamics*, 2017, pp. 1–12.

[25] Fulcoly, D. O., Kalamaroff, K. I., and Chun, F., "Determining basic satellite shape from photometric light curves," *Journal of Spacecraft and Rockets*, Vol. 49, No. 1, 2012, pp. 76–82.

[26] Calef, B., Africano, J., Birge, B., Hall, D., and Kervin, P., "Photometric signature inversion," *Unconventional Imaging II*, Vol. 6307, International Society for Optics and Photonics, 2006, p. 63070E.

[27] Kucharski, D., Kirchner, G., Flegel, S. K., Jah, M. K., and Bennett, J. C., "High-definition Photometry–an optical method for remote detection of MMOD impacts on satellites," *LPI Contributions*, Vol. 2109, 2019, pp. 6075.

[28] Wetterer, C. J., Chow, C. C., Crassidis, J. L., Linares, R., and Jah, M. K., "Simultaneous position, velocity, attitude, angular rates, and surface parameter estimation using astrometric and photometric observations," *Proceedings of the 16th International Conference on Information Fusion*, IEEE, 2013, pp. 997–1004.

[29] Kurt, M. and Edwards, D., "A Survey of BRDF Models for Computer Graphics," *SIGGRAPH Comput. Graph.*, Vol. 43, No. 2, May 2009, pp. 4:1–4:7.

[30] Ashikhmin, M. and Shirley, P., "An anisotropic phong BRDF model," *Journal of graphics tools*, Vol. 5, No. 2, 2000, pp. 25–32.

[31] Cook, R. L. and Torrance, K. E., "A reflectance model for computer graphics," *ACM Transactions on Graphics (TOG)*, Vol. 1, No. 1, 1982, pp. 7–24.

[32] He, X. D., Torrance, K. E., Sillion, F. X., and Greenberg, D. P., "A comprehensive physical model for light reflection," *ACM SIGGRAPH computer graphics*, Vol. 25, ACM, 1991, pp. 175–186.

[33] Ceniceros, A., Gaylor, D. E., Anderson, J., Pinon III, E., Dao, P., and Rast, R., "Comparison of BRDF-predicted and observed light curves of GEO satellites," Tech. rep., University of Arizona Tucson United States, 2015.

[34] Ashikhmin, M. and Premoze, S., "Distribution-based brdfs," *Unpublished Technical Report, University of Utah*, Vol. 2, 2007, pp. 6.

[35] Crassidis, J. L. and Junkins, J. L., *Optimal estimation of dynamic systems*, CRC press, 2011.

[36] Gordon, N. J., Salmond, D. J., and Smith, A. F., "Novel approach to nonlinear/non-Gaussian Bayesian state estimation," *IEE Proceedings F (Radar and Signal Processing)*, Vol. 140, IET, 1993, pp. 107–113.

[37] Du, X., Wang, Y., Hu, H., Gou, R., and Liu, H., "The attitude inversion method of geostationary satellites based on unscented particle filter," *Advances in Space Research*, 2018, pp. –.

[38] Doucet, A., De Freitas, N., and Gordon, N., *Sequential Monte Carlo Methods in Practice. Series Statistics For Engineering and Information Science*, Springer New York, 2001.

[39] Schaub, H. and Junkins, J. L., *Analytical mechanics of space systems*, American Institute of Aeronautics and Astronautics, 2009.

[40] Markley, F. L., "Attitude error representations for Kalman filtering," *Journal of guidance, control, and dynamics*, Vol. 26, No. 2, 2003, pp. 311–317.

[41] Schaub, H., Junkins, J. L., et al., "Stereographic orientation parameters for attitude dynamics: A generalization of the Rodrigues parameters," *Journal of the Astronautical Sciences*, Vol. 44, No. 1, 1996, pp. 1–19.

[42] Crassidis, J. L. and Markley, F. L., "Unscented filtering for spacecraft attitude estimation," *Journal of guidance, control, and dynamics*, Vol. 26, No. 4, 2003, pp. 536–542.

[43] Vallado, D. A., *Fundamentals of astrodynamics and applications*, Vol. 12, Springer Science & Business Media, 2001.

[44] Curtis, H. D., *Orbital mechanics for engineering students*, Butterworth-Heinemann, 2013.

[45] Montenbruck, O. and Gill, E., *Satellite orbits: models, methods and applications*, Springer Science & Business Media, 2012.

[46] Marsh, J., Lerch, F., Putney, B., Christodoulidis, D., Smith, D., Felsentreger, T., Sanchez, B., Klosko, S., Pavlis, E., Martin, T., et al., "A new gravitational model for the Earth from satellite tracking data: GEM-T1," *Journal of Geophysical Research: Solid Earth*, Vol. 93, No. B6, 1988, pp. 6169–6215.

[47] Wertz, J., *Spacecraft Attitude Determination and Control*, Astrophysics and Space Science Library, Springer Netherlands, 1978.

[48] Rieke, G. H., *Measuring the universe: a multiwavelength perspective*, Cambridge University Press, 2012.

[49] Walsh, J. W., "Photometry," *phot*, 1958.

[50] Warner, B. D. et al., *A practical guide to lightcurve photometry and analysis*, Vol. 300, Springer, 2006.

[51] Pogson, N., "Magnitudes of Thirty-six of the Minor Planets for the first day of each month of the year 1857," *Monthly Notices of the Royal Astronomical Society*, Vol. 17, Nov. 1856, pp. 12–15.

[52] Beckmann, P. and Spizzichino, A., "The scattering of electromagnetic waves from rough surfaces," *Norwood, MA, Artech House, Inc., 1987, 511 p.*, 1987.

[53] Blinn, J. F., "Models of light reflection for computer synthesized pictures," *Proceedings of the 4th annual conference on Computer graphics and interactive techniques*, 1977, pp. 192–198.

[54] Torrance, K. E. and Sparrow, E. M., "Theory for off-specular reflection from roughened surfaces," *Journal of the Optical Society of America*, Vol. 57, No. 9, 1967, pp. 1105–1114.

[55] Maybeck, P. S., *Stochastic models, estimation, and control*, Vol. 1, Academic press, 1979.

[56] Kalman, R. E., "A new approach to linear filtering and prediction problems," *Journal of basic Engineering*, Vol. 82, No. 1, 1960, pp. 35–45.

[57] Van Der Merwe, R., *Sigma-point Kalman filters for probabilistic inference in dynamic state-space models*, Ph.D. thesis, Oregon Health & Science University, 2004.

[58] Ristic, B., Arulampalam, S., and Gordon, N., *Beyond the Kalman filter: Particle filters for tracking applications*, Artech house, 2003.

[59] Julier, S. J. and Uhlmann, J. K., "New extension of the Kalman filter to nonlinear systems," *Signal processing, sensor fusion, and target recognition VI*, Vol. 3068, International Society for Optics and Photonics, 1997, pp. 182–193.

[60] Julier, S. J., "The scaled unscented transformation," *Proceedings of the 2002 American Control Conference (IEEE Cat. No. CH37301)*, Vol. 6, IEEE, 2002, pp. 4555–4559.

[61] Linares, R., Crassidis, J. L., and Jah, M. K., "Particle filtering light curve based attitude estimation for non-resolved space objects," *AAS/A1AA Space Flight Mechanics Meeting*, Vol. 14, 2014, p. 210.

[62] Bernard, A. and Geller, D., "Attitude Determination of Rotating Spacecraft Using Light Curve Measurements," *2018 AAS/AIAA Astrodynamics Specialist Conference*, 2018.

[63] Bernard, A. and Geller, D., "Attitude Determination Using Light Curves From Multiple Observation Sites," *1st IAA Conference on Space Situational Awareness*, 2017.

[64] Koppelman, M., "Uncertainty analysis in photometric observations," *Society for Astronomical Sciences Annual Symposium*, Vol. 24, 2005, p. 107.

[65] Newberry, M., "Increasing precision and accuracy in photometric measurements," *Precision CCD Photometry*, Vol. 189, 1999, p. 74.

APPENDICES

APPENDIX A

DERIVATION OF LINEARIZED DYNAMICS

When using the extended Kalman filter, the propagation of the state covariance matrix is found using the linearized state dynamics. The following sections are the derivations of the linearized state dynamics for the quaternion kinematics, and the dynamics equation for the angular velocity of the uncontrolled satellite.

A.1 Quaternion dynamics

The true quaternion is defined as being a small-angle rotation away from the estimated quaternion. In terms of the inertial and spacecraft body frames this is shown in the following equation:

$$\boldsymbol{q}_{I \to b} = \delta \boldsymbol{q}_{\hat{b} \to b} \otimes \boldsymbol{q}_{I \to \hat{b}} \tag{A.1}$$

Note that the term $\boldsymbol{q}_{I \to \hat{b}}$ is the same as $\hat{\boldsymbol{q}}_{I \to b}$ in earlier parts of this document. The notation is changed slightly here to help provide clarity in how the quaternions cascade together. Using the product rule, the time derivative of this equation is

$$\dot{\boldsymbol{q}}_{I \to b} = \delta \dot{\boldsymbol{q}}_{\hat{b} \to b} \otimes \boldsymbol{q}_{I \to \hat{b}} + \delta \boldsymbol{q}_{\hat{b} \to b} \otimes \dot{\boldsymbol{q}}_{I \to \hat{b}} \tag{A.2}$$

The equation for the quaternion kinematics is

$$\dot{\boldsymbol{q}}_{I \to b} = \frac{1}{2} \boldsymbol{q}_{\boldsymbol{\omega}} \otimes \boldsymbol{q}_{I \to b} \tag{A.3}$$

where

$$\boldsymbol{q}_{\boldsymbol{\omega}} \equiv \begin{bmatrix} 0 \\ \boldsymbol{\omega}^b \end{bmatrix} \tag{A.4}$$

and similarly, the equation kinematics of the quaternion state estimate are

$$\dot{\hat{q}}_{I \to \hat{b}} = \frac{1}{2} q_{\hat{\omega}} \otimes \hat{q}_{I \to \hat{b}} \tag{A.5}$$

Substituting the above equation and equation A.3 into equation A.2 yields

$$\frac{1}{2} q_{\omega} \otimes q_{I \to b} = \delta \dot{q}_{\hat{b} \to b} \otimes q_{I \to \hat{b}} + \delta q_{\hat{b} \to b} \otimes \frac{1}{2} q_{\hat{\omega}} \otimes \hat{q}_{I \to \hat{b}} \tag{A.6}$$

Now, using the definition of equation A.1, this can be rewritten as

$$\frac{1}{2} q_{\omega^b} \otimes \delta q_{\hat{b} \to b} \otimes q_{I \to \hat{b}} = \delta \dot{q}_{\hat{b} \to b} \otimes q_{I \to \hat{b}} + \delta q_{\hat{b} \to b} \otimes \frac{1}{2} q_{\hat{\omega}^b} \otimes \hat{q}_{I \to \hat{b}} \tag{A.7}$$

Now post quaternion multiplying each term by $\hat{q}_{\hat{b} \to I}$ gives

$$\frac{1}{2} q_{\omega^b} \otimes \delta q_{\hat{b} \to b} = \delta \dot{q}_{\hat{b} \to b} + \delta q_{\hat{b} \to b} \otimes \frac{1}{2} q_{\hat{\omega}^b} \tag{A.8}$$

Now grouping similar terms

$$\delta \dot{q}_{\hat{b} \to b} = \frac{1}{2} \left(q_{\omega^b} \otimes \delta q_{\hat{b} \to b} - \delta q_{\hat{b} \to b} \otimes q_{\hat{\omega}^b} \right) \tag{A.9}$$

Now substituting in the error for the angular velocity, $\omega^b = \hat{\omega}^b + \delta \omega^b$ this becomes

$$\delta \dot{q}_{\hat{b} \to b} = \frac{1}{2} \left(q_{\hat{\omega}^b} \otimes \delta q_{\hat{b} \to b} - \delta q_{\hat{b} \to b} \otimes q_{\hat{\omega}^b} \right) + \frac{1}{2} q_{\delta \omega^b} \otimes \delta q_{\hat{b} \to b} \tag{A.10}$$

Now due to quaternion multiplication (see equation 3.20), the above equation can be rewritten as

$$\delta \dot{q}_{\hat{b} \to b} = \begin{bmatrix} 0 \\ -\hat{\omega}^b \times \delta \bar{q}_{\hat{b} \to b} \end{bmatrix} + \frac{1}{2} q_{\delta \omega^b} \otimes \delta q_{\hat{b} \to b} \tag{A.11}$$

Here $\bar{q}$ denotes the vector components of the quaternion ($q_{(2:4)}$ from equation 3.14. The notation has been changed to prevent confusion with the other subscripts).

Now assuming that $\delta q_{\hat{b} \to b}$ is small, ($\approx [1\ 0\ 0\ 0]^T$), this reduces down to

$$\delta \dot{\boldsymbol{q}}_{\hat{b} \to b} = \begin{bmatrix} 0 \\ -\hat{\boldsymbol{\omega}}^b \times \delta \bar{\boldsymbol{q}}_{\hat{b} \to b} \end{bmatrix} + \frac{1}{2} \begin{bmatrix} 0 \\ \delta \boldsymbol{\omega}^b \end{bmatrix} \tag{A.12}$$

Now ignoring the scalar component, $\delta \dot{q}_{\hat{b} \to b}(1)$, this gives

$$\delta \dot{\bar{\boldsymbol{q}}}_{\hat{b} \to b} = -\hat{\boldsymbol{\omega}}^b \times \delta \bar{\boldsymbol{q}}_{\hat{b} \to b} + \frac{1}{2} \delta \boldsymbol{\omega}^b \tag{A.13}$$

Now by how the quaternion is defined (see equation 3.15)

$$\bar{\boldsymbol{q}}_{\hat{b} \to b} = \sin\left(\frac{\delta \theta}{2}\right) \hat{\boldsymbol{e}} \tag{A.14}$$

where $\delta \theta$ is the magnitude of the error rotation vector, and $\hat{\boldsymbol{e}}$ is the unit vector of rotation (the hat here denotes a unit vector rather than an estimate). Then using small angle approximations

$$\delta \bar{\boldsymbol{q}}_{\hat{b} \to b} \approx \frac{\delta \theta}{2} \hat{\boldsymbol{e}} = \frac{\delta \boldsymbol{\theta}}{2} \tag{A.15}$$

which gives

$$\frac{\delta \dot{\boldsymbol{\theta}}}{2} = -\hat{\boldsymbol{\omega}}^b \times \frac{\delta \boldsymbol{\theta}}{2} + \frac{1}{2} \delta \boldsymbol{\omega}^b \tag{A.16}$$

Multiplying the entire equation by two gives

$$\delta \dot{\boldsymbol{\theta}} = -\hat{\boldsymbol{\omega}}^b \times \delta \boldsymbol{\theta} + \delta \boldsymbol{\omega}^b \tag{A.17}$$

or equivalently

$$\delta \dot{\boldsymbol{\theta}} = \begin{bmatrix} -[\hat{\boldsymbol{\omega}} \times] & I_{3\times 3} \end{bmatrix} \delta \boldsymbol{x} \tag{A.18}$$

where

$$\delta \boldsymbol{x} = \begin{bmatrix} \delta \boldsymbol{\theta} \\ \delta \boldsymbol{\omega}^b \end{bmatrix} \quad (A.19)$$

A.2 Angular velocity dynamics

The purpose of this section is to define the spacecraft angular velocity linearized dynamics. The original state vector is

$$\boldsymbol{x} = \begin{bmatrix} \boldsymbol{q}_{I \to b} \\ \boldsymbol{\omega}^b \end{bmatrix} \quad (A.20)$$

with the error state defined as

$$\delta \boldsymbol{x} = \begin{bmatrix} \delta \boldsymbol{\theta} \\ \delta \boldsymbol{\omega}^b \end{bmatrix} \quad (A.21)$$

The perturbation model for the angular velocity is

$$\boldsymbol{\omega}^b = \hat{\boldsymbol{\omega}}^b + \delta \boldsymbol{\omega}^b \quad (A.22)$$

which means that

$$\dot{\boldsymbol{\omega}}^b = \dot{\hat{\boldsymbol{\omega}}}^b + \delta \dot{\boldsymbol{\omega}}^b \quad (A.23)$$

The differential equation governing the angular velocity of the spacecraft is given by Euler's rotational equation with noise added:

$$\dot{\boldsymbol{\omega}}^b = J^{-1} \left[\sum \boldsymbol{T}^b(\boldsymbol{x}) - \omega^b \times J\omega^b \right] + G_w w \quad (A.24)$$

The differential equation for the estimated angular velocity is

$$\dot{\hat{\boldsymbol{\omega}}}^b = f(\hat{\boldsymbol{x}}, t) = J^{-1} \left[\sum \boldsymbol{T}^b(\hat{\boldsymbol{x}}) - \hat{\omega}^b \times J\hat{\omega}^b \right] \quad (A.25)$$

This means that

$$\dot{\boldsymbol{\omega}}^b = \dot{\hat{\boldsymbol{\omega}}}^b + \delta\dot{\boldsymbol{\omega}}^b = f(\hat{\boldsymbol{x}}, t) + \delta\dot{\boldsymbol{\omega}}^b \tag{A.26}$$

Now plugging equation A.24 into the left-hand side of the previous equation gives

$$J^{-1}\left[\sum \boldsymbol{T}^b(\boldsymbol{x}) - \boldsymbol{\omega}^b \times J\boldsymbol{\omega}^b\right] + G_w\boldsymbol{w} = f(\hat{\boldsymbol{x}}, t) + \delta\dot{\boldsymbol{\omega}}^b \tag{A.27}$$

Now using the relationship from equation A.22 this can be rewritten as

$$f(\hat{\boldsymbol{x}} + \delta\boldsymbol{x}, t) + G_w\boldsymbol{w} = f(\hat{\boldsymbol{x}}, t) + \delta\dot{\boldsymbol{\omega}}^b \tag{A.28}$$

Using a Taylor series expansion, it can be shown that

$$\delta\dot{\boldsymbol{\omega}}^b = \left.\frac{\partial f}{\partial \boldsymbol{x}}\right|_{\hat{\boldsymbol{x}}} \delta\boldsymbol{x} + G_w\boldsymbol{w} \tag{A.29}$$

It can be seen from equation A.25 that f is a function of the spacecraft angular velocity and possibly other state variables, depending on the torques that are applied. The only torques considered in this work are the gravity gradient torque and the torques due to aerodynamic drag and solar radiation pressure (SRP). The linearization of these torques is presented in the proceeding sections. As these torques are a function of attitude only, and not angular velocity, the remainder of this section is dedicated to taking the partial of f with respect to the angular velocity of the spacecraft: $\left.\frac{\partial f}{\partial \boldsymbol{\omega}^b}\right|_{\delta\hat{\boldsymbol{x}}} \delta\omega$. The sections after will illustrate how the specific torques are linearized with respect to attitude.

Using the product rule, the term

$$\frac{\partial f}{\partial \boldsymbol{\omega}^b} = J^{-1}\left[\frac{\partial \boldsymbol{\omega}^b}{\partial \boldsymbol{\omega}^b} \times J\boldsymbol{\omega}^b + \boldsymbol{\omega}^b \times J\frac{\partial \boldsymbol{\omega}^b}{\partial \boldsymbol{\omega}^b}\right] \tag{A.30}$$

Using the properties of cross products this can be rewritten as

$$\frac{\partial f}{\partial \boldsymbol{\omega}^b} = J^{-1}\left[-[J\boldsymbol{\omega}^b\times]\frac{\partial \boldsymbol{\omega}^b}{\partial \boldsymbol{\omega}^b} + [\boldsymbol{\omega}^b\times]J\frac{\partial \boldsymbol{\omega}^b}{\partial \boldsymbol{\omega}^b}\right] \tag{A.31}$$

As the derivative of a vector with respect to itself is identity, this evaluates to

$$\frac{\partial f}{\partial \boldsymbol{\omega}^b} = J^{-1} \left[-[J\boldsymbol{\omega}^b \times] + [\boldsymbol{\omega}^b \times] J \right] \tag{A.32}$$

And thus,

$$\left. \frac{\partial f}{\partial \boldsymbol{\omega}^b} \right|_{\delta \hat{\boldsymbol{x}}} \delta \boldsymbol{\omega} = J^{-1} \left[-[J\hat{\boldsymbol{\omega}}^b \times] + [\hat{\boldsymbol{\omega}}^b \times] J \right] \delta \boldsymbol{\omega} \tag{A.33}$$

With the above equation, the only term remaining that is needed to express the full linearized angular velocity equation is the term

$$\left. \frac{\partial f}{\partial \boldsymbol{\theta}} \right|_{\delta \hat{\boldsymbol{x}}} \delta \boldsymbol{\theta} \tag{A.34}$$

From A.25 the different terms contributing to this are the different torques being used. It was explained earlier that the torques used are all a function of attitude and not angular velocity, so the term needed to finish linearizing the angular velocity dynamics is as follows.

$$\left. \frac{\partial f}{\partial \boldsymbol{\theta}} \right|_{\delta \hat{\boldsymbol{x}}} \delta \boldsymbol{\theta} = J^{-1} \left[\frac{\partial \sum \boldsymbol{T}}{\partial \boldsymbol{\theta}} \right] \delta \boldsymbol{\theta} \tag{A.35}$$

The following sections show the process for obtaining $\frac{\partial \sum T}{\partial \boldsymbol{\theta}}$ for the different torques modeled.

Gravity gradient torque

The purpose of this section is to provide the derivation of the linearized gravity gradient torque with respect to the attitude of the spacecraft. The equation for the gravity gradient torque is

$$\boldsymbol{T}_{gg}^b = \frac{3\mu}{||\boldsymbol{r}^b||^5} \left[\boldsymbol{r}^b \times \left(J\boldsymbol{r}^b \right) \right] \tag{A.36}$$

The idea is to be able to find the linearized torque with respect to the state variables. Using a Taylor series approach, the linearized torque can be expressed as

$$\delta \boldsymbol{T}_{gg}^b = \frac{\partial \boldsymbol{T}_{gg}^b}{\partial \boldsymbol{x}} \delta \boldsymbol{x} \tag{A.37}$$

In the given equation, the only variable that is a function of the state is the $\boldsymbol{r}^b$, as it is the position of the satellite in the body frame which requires some attitude knowledge. However, as the magnitude of a vector is the same, independent of what coordinate frame it is expressed in, the only two terms needing to be accounted for are those in the cross product. Furthermore, the gravity gradient torque is a function of the attitude only, so the only term that needs to be computed is $\frac{\partial \boldsymbol{T}_{gg}^b}{\partial \boldsymbol{\theta}}$.

The calculation of this term is simplified by employing the chain rule to take the derivative.

$$\frac{\partial \boldsymbol{T}_{gg}^b}{\partial \boldsymbol{\theta}} = \frac{\partial \boldsymbol{T}_{gg}^b}{\partial \boldsymbol{r}^b} \frac{\partial \boldsymbol{r}^b}{\partial \boldsymbol{\theta}}\bigg|_{\hat{x}} \tag{A.38}$$

Starting with the first term on the right-hand side of the previous equation

$$\frac{\partial \boldsymbol{T}_{gg}^b}{\partial \boldsymbol{r}^b} = \frac{3\mu}{||\boldsymbol{r}||^5} \frac{\partial \left(\left[\boldsymbol{r}^b \times \left(J\boldsymbol{r}^b\right)\right]\right)}{\partial \boldsymbol{r}^b} \tag{A.39}$$

Finding this partial derivative can be simplified using the derivative multiplication rule.

$$\frac{\partial}{\partial \boldsymbol{r}^b}\left(\left[\boldsymbol{r}^b \times \left(J\boldsymbol{r}^b\right)\right]\right) = \left[\frac{\partial}{\partial \bar{\boldsymbol{r}}^b}\boldsymbol{r}^b \times \left(J\boldsymbol{r}^b\right)\right] + \left[\boldsymbol{r}^b \times \frac{\partial}{\partial \boldsymbol{r}^b}\left(J\boldsymbol{r}^b\right)\right] \tag{A.40}$$

Now rewriting the previous equation in terms of cross-product matrices facilitates taking these derivatives

$$\frac{\partial}{\partial \boldsymbol{r}^b}\left(\left[\boldsymbol{r}^b \times \left(J\boldsymbol{r}^b\right)\right]\right) = -\left[\left(J\boldsymbol{r}^b\right)\times\right]\frac{\partial \boldsymbol{r}^b}{\partial \boldsymbol{r}^b} + \left[\boldsymbol{r}^b\times\right]J\frac{\partial \boldsymbol{r}^b}{\partial \boldsymbol{r}^b} \tag{A.41}$$

As $\frac{\partial \boldsymbol{r}^b}{\partial \boldsymbol{r}^b} = I_{3\times3}$, equation A.41 becomes

$$\frac{\partial}{\partial \boldsymbol{r}^b}\left(\left[\boldsymbol{r}^b \times \left(J\boldsymbol{r}^b\right)\right]\right) = -\left[\left(J\boldsymbol{r}^b\right)\times\right] + \left[\boldsymbol{r}^b\times\right]J \tag{A.42}$$

Substituting this back into equation A.39

$$\frac{\partial T_{gg}^b}{\partial \boldsymbol{r}^b} = \frac{3\mu}{||\boldsymbol{r}||^5} \left(-\left[\left(J\boldsymbol{r}^b \right) \times \right] + \left[\boldsymbol{r}^b \times \right] J \right) \tag{A.43}$$

Substituting the above equation into equation A.38 gives

$$\frac{\partial T_{gg}^b}{\partial \boldsymbol{r}^b} = \frac{3\mu}{||\boldsymbol{r}||^5} \left(-\left[\left(J\boldsymbol{r}^b \right) \times \right] + \left[\boldsymbol{r}^b \times \right] J \right) \frac{\partial \boldsymbol{r}^b}{\partial \boldsymbol{\theta}} \tag{A.44}$$

Now the only derivative that remains is the partial derivative of the satellite position vector in the body frame with respect to the small-angle rotation of the attitude about a reference state (here, the state estimate will be used). In terms of quaternions, this can be represented as

$$\boldsymbol{q}_{I \to b} = \begin{pmatrix} 0 \\ \delta\boldsymbol{\theta}/2 \end{pmatrix} \otimes q_{I \to \hat{b}} \tag{A.45}$$

In terms of rotation matrices, this can be written as

$$R_{I \to b} = R_{\hat{b} \to b}(\delta\boldsymbol{\theta}) R_{I \to \hat{b}} \tag{A.46}$$

This means that the transformation of the position vector from the inertial frame to the spacecraft body frame can be written as

$$\boldsymbol{r}^b = R_{\hat{b} \to b}(\delta\boldsymbol{\theta}) R_{I \to \hat{b}} \boldsymbol{r}^I \tag{A.47}$$

Assuming small angles, this can be approximated as

$$\boldsymbol{r}^b = \left[I_{3x3} - \left[\delta\boldsymbol{\theta} \times \right] \right] R_{I \to \hat{b}} \boldsymbol{r}^I \tag{A.48}$$

Distributing the right-hand terms into the brackets yields

$$\boldsymbol{r}^b = R_{I \to \hat{b}} \boldsymbol{r}^I - \left[\delta\boldsymbol{\theta} \times \right] R_{I \to \hat{b}} \boldsymbol{r}^I \tag{A.49}$$

Now applying cross-product properties, this can be rewritten as

$$\boldsymbol{r}^b = R_{I \to \hat{b}} \boldsymbol{r}^I + \left[\left(R_{I \to \hat{b}} \boldsymbol{r}^I \right) \times \right] \delta \boldsymbol{\theta} \qquad \text{(A.50)}$$

As $R_{I \to \hat{b}} \boldsymbol{r}^I = \boldsymbol{r}^{\hat{b}}$, with the equation in this form, the derivative $\frac{\partial \boldsymbol{r}^b}{\partial \delta \boldsymbol{\theta}}$ can be found

$$\frac{\partial \boldsymbol{r}^b}{\partial \delta \boldsymbol{\theta}} = \left[\boldsymbol{r}^{\hat{b}} \times \right] \qquad \text{(A.51)}$$

which expression is equivalent to

$$\frac{\partial \boldsymbol{r}^b}{\partial \delta \boldsymbol{\theta}} = \left[\hat{\boldsymbol{r}}^b \times \right] \qquad \text{(A.52)}$$

Substituting everything back into equation A.38 and evaluating at the state estimate gives

$$\frac{\partial T_{gg}^b}{\partial \boldsymbol{\theta}^b} = \frac{3\mu}{||\hat{\boldsymbol{r}}||^5} \left(- \left[\left(J \hat{\boldsymbol{r}}^b \right) \times \right] + \left[\hat{\boldsymbol{r}}^b \times \right] J \right) \left[\hat{\boldsymbol{r}}^b \times \right] \qquad \text{(A.53)}$$

A.3 Solar radiation pressure torque

The torque on a spacecraft due to solar radiation pressure is

$$\boldsymbol{T}_{SRP} = \sum_{i=1}^{N} \boldsymbol{r}_{cm}^i \times \boldsymbol{F}_{SRP}^i \qquad \text{(A.54)}$$

where

$$\boldsymbol{F}_{SRP}^i = -P_{SR} A_i \left[2 \left(\frac{\mathcal{R}_d^i}{3} + \mathcal{R}_s^i \cos \theta_{SRP}^i \right) \hat{\boldsymbol{n}}^b + (1 - \mathcal{R}_s^i) \hat{\boldsymbol{s}}^b \right] \max(\cos \theta_{SRP}^i, 0) \qquad \text{(A.55)}$$

As the term $\bar{\boldsymbol{r}}_{cm}^i$ is not dependent on the state variables, the derivative of the solar radiation pressure torque is

$$\frac{\partial \boldsymbol{T}_{SRP}}{\partial \boldsymbol{x}} = \boldsymbol{r}_{cm}^i \times \frac{\partial \boldsymbol{F}_{SRP}}{\partial \boldsymbol{x}} \qquad \text{(A.56)}$$

Attention will first be given to the term $\frac{\partial \boldsymbol{F}_{SRP}}{\partial \boldsymbol{x}}$. As with the gravity gradient torque, the torque and force due to solar radiation pressure is a function of the attitude and not angular velocity. Only the derivatives with respect to the linearized attitude state are considered, $\frac{\partial \boldsymbol{F}_{SRP}}{\partial \delta \boldsymbol{\theta}}$.

To simplify, the subscript i will be dropped from the different terms, and let $\beta \equiv -P_{SR}A$ and $u \equiv \cos \theta_{SRP} \equiv \hat{\boldsymbol{s}}^b \cdot \hat{\boldsymbol{n}}$. Furthermore, if $u \leq 0$, then the whole derivative will be 0. Thus, this derivation will focus on the cases when this doesn't occur. In these instances, the force due to solar radiation pressure is

$$\boldsymbol{F}_{SRP} = \beta \left[2 \left(\frac{\mathcal{R}_d}{3} + \mathcal{R}_s u \right) \hat{\boldsymbol{n}}^b + (1 - \mathcal{R}_s) \hat{\boldsymbol{s}}^b \right] u \qquad (A.57)$$

As u is a dot product of two vectors, it is a scalar and can be moved around as such. Distributing the terms through, the above equation becomes

$$\boldsymbol{F}_{SRP} = \frac{2\beta \mathcal{R}_d}{3} \hat{\boldsymbol{n}}^b u + 2\beta \mathcal{R}_s \hat{\boldsymbol{n}}^b u^2 + \beta (1 - \mathcal{R}_s) \hat{\boldsymbol{s}}^b u \qquad (A.58)$$

Now substituting back in the definition of u this becomes

$$\boldsymbol{F}_{SRP} = \frac{2\beta \mathcal{R}_d}{3} \hat{\boldsymbol{n}}^b \left(\hat{\boldsymbol{s}}^b \cdot \hat{\boldsymbol{n}}^b \right) + 2\beta \mathcal{R}_s \hat{\boldsymbol{n}}^b \left(\hat{\boldsymbol{s}}^b \cdot \hat{\boldsymbol{n}}^b \right)^2 + \beta (1 - \mathcal{R}_s) \hat{\boldsymbol{s}}^b \left(\hat{\boldsymbol{s}}^b \cdot \hat{\boldsymbol{n}}^b \right) \qquad (A.59)$$

Now with the equation in this form, the only term that is a function of the attitude is the $\hat{\boldsymbol{s}}^b$ term. Using the chain rule, the desired derivative is

$$\frac{\partial \boldsymbol{F}_{SRP}}{\partial \delta \boldsymbol{\theta}} = \frac{\partial \boldsymbol{F}_{SRP}}{\partial \hat{\boldsymbol{s}}^b} \frac{\partial \hat{\boldsymbol{s}}^b}{\partial \delta \boldsymbol{\theta}} \bigg|_{\hat{x}} \qquad (A.60)$$

Using properties of the dot product, $\left(\hat{\boldsymbol{s}}^b \cdot \hat{\boldsymbol{n}} \right)$ can be rewritten as $\left(\hat{\boldsymbol{n}}^B \right)^T \hat{\boldsymbol{s}}^b$. Now A.59 can be rewritten as

$$\boldsymbol{F}_{SRP} = \frac{2\beta \mathcal{R}_d}{3} \hat{\boldsymbol{n}}^b \left(\left(\hat{\boldsymbol{n}}^b \right)^T \hat{\boldsymbol{s}}^b \right) + 2\beta \mathcal{R}_s \hat{\boldsymbol{n}}^b \left(\left(\hat{\boldsymbol{n}}^b \right)^T \hat{\boldsymbol{s}}^b \right)^2 + \beta (1 - \mathcal{R}_s) \hat{\boldsymbol{s}}^b \left(\left(\hat{\boldsymbol{n}}^b \right)^T \hat{\boldsymbol{s}}^b \right) \quad (A.61)$$

Now as the term $\left(\hat{\boldsymbol{n}}^B\right)^T \hat{\boldsymbol{s}}^b$ appears in every term on the right-hand side (RHS) of equation A.61, it is helpful to define the derivative of this with respect to $\hat{\boldsymbol{s}}^b$

$$\frac{\partial \left(\hat{\boldsymbol{n}}^B\right)^T \hat{\boldsymbol{s}}^b}{\partial \hat{\boldsymbol{s}}^b} = \left(\hat{\boldsymbol{n}}^b\right)^T I_{3\times 3} = \left(\hat{\boldsymbol{n}}^b\right)^T \tag{A.62}$$

Now the partial derivatives of each of the RHS terms in A.61 can be found. For simplicity each term is shown separately.

Using equation A.62 the derivative of the first term is

$$\frac{\partial \left(\frac{2\beta\mathcal{R}_d}{3}\hat{\boldsymbol{n}}^b \left(\left(\hat{\boldsymbol{n}}^B\right)^T \hat{\boldsymbol{s}}^b\right)\right)}{\partial \hat{\boldsymbol{s}}^b} = \frac{2\beta\mathcal{R}_d}{3}\hat{\boldsymbol{n}}^b \left(\hat{\boldsymbol{n}}^b\right)^T \tag{A.63}$$

The partial derivative of the second term can be found through application of the chain rule and equation A.62

$$\frac{\partial \left(2\beta\mathcal{R}_s\hat{\boldsymbol{n}}^b \left(\left(\hat{\boldsymbol{n}}^b\right)^T \hat{\boldsymbol{s}}^b\right)^2\right)}{\partial \hat{\boldsymbol{s}}^b} = 4\beta\mathcal{R}_s \left(\left(\hat{\boldsymbol{n}}^b\right)^T \hat{\boldsymbol{s}}^b\right) \hat{\boldsymbol{n}}^b \left(\hat{\boldsymbol{n}}^b\right)^T \tag{A.64}$$

The derivative of the final RHS term of A.61 can be found using the multiplication rule and equation A.62.

$$\frac{\partial \left(\beta(1 - \mathcal{R}_s)\hat{\boldsymbol{s}}^b \left(\left(\hat{\boldsymbol{n}}^b\right)^T \hat{\boldsymbol{s}}^b\right)\right)}{\partial \hat{\boldsymbol{s}}^b} = \beta(1 - \mathcal{R}_s) \left[\left(\left(\hat{\boldsymbol{n}}^b\right)^T \hat{\boldsymbol{s}}^b\right) I_{3\times 3} + \hat{\boldsymbol{s}}^b \left(\hat{\boldsymbol{n}}^b\right)^T\right] \tag{A.65}$$

Now following the same approach as was done for $\boldsymbol{r}^b$ in A.2, the term $\frac{\partial \hat{\boldsymbol{s}}^b}{\partial \delta\boldsymbol{\theta}}$ can be written as

$$\frac{\partial \hat{\boldsymbol{s}}^b}{\partial \delta\boldsymbol{\theta}} = \left[(R_{I\to\hat{b}}\hat{\boldsymbol{s}}^I) \times\right] \tag{A.66}$$

where $R_{I\to\hat{b}}$ is the transformation matrix from the inertial to some reference body frame that is close to the true spacecraft body frame (in this case it is the rotation matrix from the attitude state estimate $R_{I\to\hat{b}}(\hat{\boldsymbol{q}}_{I\to b})$), and $[\times]$ denotes the skew-symmetric cross-product matrix.

With all of these terms defined, equation A.60 can now be written as

$$
\begin{aligned}
\frac{\partial \boldsymbol{F}_{SRP}}{\partial \delta \boldsymbol{\theta}} = {}& \frac{2\beta \mathcal{R}_d}{3} \hat{\boldsymbol{n}}^b \left(\hat{\boldsymbol{n}}^b \right)^T \left[(R_{I \to \hat{b}} \hat{\boldsymbol{s}}^I) \times \right] \\
& + 4\beta \mathcal{R}_s \left(\left(\hat{\boldsymbol{n}}^b \right)^T \hat{\boldsymbol{s}}^b \right) \hat{\boldsymbol{n}}^b \left(\hat{\boldsymbol{n}}^b \right)^T \left[(R_{I \to \hat{b}} \hat{\boldsymbol{s}}^I) \times \right] \\
& + \beta(1 - \mathcal{R}_s) \left[\left(\left(\hat{\boldsymbol{n}}^b \right)^T \hat{\boldsymbol{s}}^b \right) I_{3 \times 3} + \hat{\boldsymbol{s}}^b \left(\hat{\boldsymbol{n}}^b \right)^T \right] \left[(R_{I \to \hat{b}} \hat{\boldsymbol{s}}^I) \times \right] \quad \text{(A.67)}
\end{aligned}
$$

Now as the torque due to SRP is solely a function of the attitude of the spacecraft, the linearized torque for a given facet is

$$
\frac{\partial \boldsymbol{T}_{SRP}}{\partial \boldsymbol{x}} = \left[\boldsymbol{r}_{cm} \times \frac{\partial \boldsymbol{F}_{SRP}}{\partial \delta \boldsymbol{\theta}} \quad \boldsymbol{0} \right] \tag{A.68}
$$

which can be rewritten in an equivalent form as

$$
\frac{\partial \boldsymbol{T}_{SRP}}{\partial \boldsymbol{x}} = \left[[\boldsymbol{r}_{cm} \times] \frac{\partial \boldsymbol{F}_{SRP}}{\partial \delta \boldsymbol{\theta}} \quad \boldsymbol{0} \right] \tag{A.69}
$$

Thus, the linearized torque for a given facet can be found by substituting equation A.67 into equation A.69. The total values could then be found by summing up the different contributions of the individual facets.

A.4 Atmospheric drag torque

As was shown in Chapter 4, the torque due to atmospheric drag is

$$
T_{drag}^b = \sum_{i=1}^{N} \boldsymbol{r}_{cm,i}^b \times \boldsymbol{F}_{aero,i}^b \tag{A.70}
$$

where the i denotes the individual facets, $\boldsymbol{r}_{cm}$ is vector to the application of the force from the center of mass, and $\boldsymbol{F}_{aero}^b$ is the aerodynamics force.

Out of the state variables considered (attitude and angular velocity), the torque is only a function of the spacecraft attitude. The linearized form of this torque is thus

$$\frac{\partial T^b_{drag}}{\partial \delta \boldsymbol{x}} = \begin{bmatrix} \frac{\partial T^b_{drag}}{\partial \delta \boldsymbol{\theta}} & \mathbf{0} \end{bmatrix} \tag{A.71}$$

The only term in the torque equations dependent on the attitude of the spacecraft is in the dot product between the velocity vector and the normal vector of a given facet, as the velocity vector must be converted to the body frame to perform this dot product. Thus,

$$\frac{\partial T^b_{drag}}{\partial \delta \boldsymbol{\theta}} = \frac{\partial T^b_{drag}}{\partial \hat{\boldsymbol{v}}^b} \left. \frac{\partial \hat{\boldsymbol{v}}^b}{\partial \delta \boldsymbol{\theta}} \right|_{\hat{x}} \tag{A.72}$$

Differentiating Eq. 4.21 with respect to the velocity vector and plugging it back into Eq. A.70 gives

$$\frac{\partial T^b_{drag}}{\partial \hat{\boldsymbol{v}}^b} = \sum_{i=1}^{N} \left[\boldsymbol{r}^i_{cm} \times \right] \left[-\frac{1}{2}\rho C_{D,i} A_i |\boldsymbol{v}|^2 \hat{\boldsymbol{n}}^b \left(\hat{\boldsymbol{n}}^b \right)^T \right] \tag{A.73}$$

Following the manner of the previous sections, the derivative of the velocity vector in the body frame is

$$\frac{\partial \hat{\boldsymbol{v}}^b}{\partial \delta \boldsymbol{\theta}} = \left[(R_{I \to \hat{b}} \hat{\boldsymbol{v}}^I) \times \right] \tag{A.74}$$

Thus, the total linearized torque due to atmospheric drag is

$$\frac{\partial T^b_{drag}}{\partial \delta \boldsymbol{\theta}} = \sum_{i=1}^{N} \left[\boldsymbol{r}^i_{cm} \times \right] \left[-\frac{1}{2}\rho C_{D,i} A_i |\boldsymbol{v}|^2 \hat{\boldsymbol{n}}^b \left(\hat{\boldsymbol{n}}^b \right)^T \right] \left[(R_{I \to \hat{b}} \hat{\boldsymbol{v}}^I) \times \right] \tag{A.75}$$

APPENDIX B

MONTE CARLO RESULTS FOR ATTITUDE ESTIMATION USING THE EKF AND
UKF

This appendix presents the tabulated results of the Monte Carlo runs for the different fast-spinning cases. These data are presented here to show the instances where the EKF or UKF might not be the best choice for the attitude estimation of the spacecraft.

The summary tables for the fast spinning MEO cases are shown in Figs. B.1 and B.2, and the Monte Carlo summary tables for the GEO cases are shown in Figs. B.3 and B.4. The red boxes correspond to the runs where more than ten samples were outside of the covariance bounds for any of the six state components.The green boxes are the cases where there were fewer than five samples that left the covariance bounds for the majority of the state variables. The yellow boxes are an intermediate case. They correspond to the instances where any component has six to nine samples leave the covariance bound. In addition, if there are two or more components with exactly five samples that left the covariance bounds the box is colored yellow. The gray squares are where the tests weren't run, as both filters had already performed poorly at a lower level of initial uncertainty.

IN examining these tables, it can be seen that in some instances the number of boxes in the green increased with the larger uncertainties in the state and measurements. These occurrences are due to the fact that the increased uncertainty in the state or measurements inflates the covariance bounds which then results in fewer samples leaving the covariance bounds. For this reason it is suggested that if considering utilizing either the EKF or UKF for attitude estimation, that scenario first be completed in simulation with a BPF also included to help validate the results.

		Single Observatory						Two Observatories					
		$\sigma_\theta = 3°$		$\sigma_\theta = 5°$		$\sigma_\theta = 10°$		$\sigma_\theta = 3°$		$\sigma_\theta = 5°$		$\sigma_\theta = 10°$	
	$r_{percent}$	EKF	UKF	EKF	UKF	EKF	UKF	EKF	UKF	EKF	UKF	EKF	UKF
Controlled $\sigma_\omega = 0.02\dfrac{deg}{s}$	1%	red	green	red	yellow	red	red	red	green	red	green	red	red
	10%	red	green	red	green	red	yellow	red	green	red	green	red	yellow
Controlled $\sigma_\omega = 0.2\dfrac{deg}{s}$	1%	red	green	red	yellow	red	red	red	yellow	red	red	red	red
	10%	red	green	red	red	red	red	red	yellow	red	red	gray	gray
Uncontrolled $\sigma_\omega = 0.02\dfrac{deg}{s}$	1%	green	green	green	green	red	red	green	green	yellow	green	red	green
	10%	green	green	green	green	green	green	green	green	green	green	green	green
Uncontrolled $\sigma_\omega = 0.2\dfrac{deg}{s}$	1%	red	green	red	green	red	yellow	red	green	red	green	red	yellow
	10%	green	green	green	green	yellow	green	red	green	red	green	red	green

Fig. B.1: Monte Carlo results summary for the fast-spinning MEO spacecraft with CubeSat shape model

		Single Observatory						Two Observatories					
		$\sigma_\theta = 3°$		$\sigma_\theta = 5°$		$\sigma_\theta = 10°$		$\sigma_\theta = 3°$		$\sigma_\theta = 5°$		$\sigma_\theta = 10°$	
	$r_{percent}$	EKF	UKF	EKF	UKF	EKF	UKF	EKF	UKF	EKF	UKF	EKF	UKF
Controlled $\sigma_\omega = 0.02\dfrac{deg}{s}$	1%	red	green	red	green	red	red	red	green	red	green	red	red
	10%	red	green	red	green	red	yellow	green	green	green	green	red	yellow
Controlled $\sigma_\omega = 0.2\dfrac{deg}{s}$	1%	red	yellow	red	red	gray	gray	red	yellow	red	red	gray	gray
	10%	red	yellow	red	green	gray	gray	red	red	red	yellow	red	red
Uncontrolled $\sigma_\omega = 0.02\dfrac{deg}{s}$	1%	green	green	yellow	green	red	green	green	green	green	yellow	red	red
	10%	green	green	green	green	yellow	green	green	green	green	green	red	green
Uncontrolled $\sigma_\omega = 0.02\dfrac{deg}{s}$	1%	red	green	red	green	red	green	yellow	green	red	green	red	yellow
	10%	yellow	green	yellow	green	yellow	green	green	green	yellow	green	red	yellow

Fig. B.2: Monte Carlo results summary for the fast-spinning MEO spacecraft with scaled shape model

	$r_{percent}$	Single Observatory						Two Observatories					
		$\sigma_\theta = 3°$		$\sigma_\theta = 5°$		$\sigma_\theta = 10°$		$\sigma_\theta = 3°$		$\sigma_\theta = 5°$		$\sigma_\theta = 10°$	
		EKF	UKF	EKF	UKF	EKF	UKF	EKF	UKF	EKF	UKF	EKF	UKF
Controlled $\sigma_\omega = 0.02\frac{deg}{s}$	1%												
	10%												
Controlled $\sigma_\omega = 0.2\frac{deg}{s}$	1%												
	10%												
Uncontrolled $\sigma_\omega = 0.02\frac{deg}{s}$	1%												
	10%												
Uncontrolled $\sigma_\omega = 0.02\frac{deg}{s}$	1%												
	10%												

Fig. B.3: Monte Carlo results summary for the fast-spinning GEO spacecraft with CubeSat shape model

	$r_{percent}$	Single Observatory						Two Observatories					
		$\sigma_\theta = 3°$		$\sigma_\theta = 5°$		$\sigma_\theta = 10°$		$\sigma_\theta = 3°$		$\sigma_\theta = 5°$		$\sigma_\theta = 10°$	
		EKF	UKF	EKF	UKF	EKF	UKF	EKF	UKF	EKF	UKF	EKF	UKF
Controlled $\sigma_\omega = 0.02\frac{deg}{s}$	1%												
	10%												
Controlled $\sigma_\omega = 0.2\frac{deg}{s}$	1%												
	10%												
Uncontrolled $\sigma_\omega = 0.02\frac{deg}{s}$	1%												
	10%												
Uncontrolled $\sigma_\omega = 0.02\frac{deg}{s}$	1%												
	10%												

Fig. B.4: Monte Carlo results summary for the fast-spinning GEO spacecraft with scaled shape model

CURRICULUM VITAE

Arun Bernard

Education

PhD Aerospace Engineering, May 2021

Utah State University, Logan, Utah

Dissertation project—Attitude and Reflection Parameter Estimation of Resident Space Objects Using Ground-based Photometry

BS Mechanical Engineering, May 2016

Utah State University, Logan, Utah

Graduated Magna cum Laude

Work Experience

Technician/Graduate Research Assistant, January 2019–June 2020

Space Dynamics Laboratory, Logan, Utah

Research Assistant, May 2016–Present

Utah State University—Space Awareness, Guidance, and Navigation Lab, Logan, Utah

Undergraduate Research Assistant, February 2016–May 2016

Utah State University—Orbit Dynamics and Inference Lab, Logan, Utah

Mechanical Engineering Intern, Summers 2014 and 2015

Hill Air Force Base, Utah

Awards and Honors

Utah NASA Spacegrant Consortium Fellowship, May 2016 - April 2019

Utah State Presidential Scholarship, Aug. 2010 - May 2016

Thomas A. Berghoff Memorial Scholarship, Aug. 2015 - May 2016

Engineering Scholarship from Dean, Aug. 2015 - May 2015

Harold R. Kepner Memorial Scholarship, Aug. 2013 - May 2014

Elks National Foundation Scholarship, Aug. 2010 - Dec 2010

Published Conference Papers

Bernard, A. J. and Geller, D.K., "Spacecraft Attitude Determination Using Ground Based Photometry: A Comparison of Estimation Algorithms," *Utah NASA Space Grant Consortium Fellowship Symposium*, 2019

Bernard, A. and Geller, D., "Attitude Determination of Rotating Spacecraft Using Light Curve Measurements," 2018 *AAS/AIAA Astrodynamics Specialist Conference*, 2018.

Bernard, A., Nafi, A. M., and Geller, D., "Using Triangulation in Optical Orbit Determination," *2018 AAS/AIAA Astrodynamics Specialist Conference*, 2018.

Bernard, A. and Geller, D., "A Comparison of the Bootstrap Particle Filter and the Extended Kalman Filter and the Effects of Non-Linear Measurements in Spacecraft Attitude Determination Using Light Curves," *Utah NASA Space Grant Consortium Fellowship Symposium*, 2018.

Bernard, A. and Geller, D., "Attitude Determination Using Light Curves From Multiple Observation Sites," *1st IAA Conference on Space Situational Awareness*, 2017.

Bernard, A., and Geller, D., "Simultaneous Two-Site Photometry in Attitude Determination of Resident Space Objects," *Utah NASA Space Grant Consortium Fellowship Symposium*, 2017

Nafi, A. M., Bernard, A., and Fujimoto, K., "A unified approach for optical survey strategy design of resident space objects," *AIAA/AAS Astrodynamics Specialist Conference*, 2016.

Fujimoto,K., Bernard, A., and Nafi, A. M. "Assessing Two-Track Initial Orbit Determination Methods for Resident Space Object Catalog Initialization," *AIAA/AAS Astrodynamics Specialist Conference*, 2016.